ANALYTICAL MODELING AND VERIFICATION WITH NUMERICAL METHODS AND EXPERIMENTS OF THREE PHASE REACTIVE MATERIALS, DRILLING, CEMENTING AND PERFORMANCE OF SMART CEMENTED MODEL OIL WELLS

A Thesis

Presented to

the Faculty of the Department of Civil & Environmental Engineering

University of Houston

In Partial Fulfillment

of the Requirements for the Degree

Doctor of Philosophy

in Civil Engineering

by

Bahareh Basirat

December 2016

ANALYTICAL MODELING AND VERIFICATION WITH NUMERICAL METHODS AND EXPERIMENTS OF THREE PHASE REACTIVE MATERIALS, DRILLING, CEMENTING AND PERFORMANCE OF SMART CEMENTED MODEL OIL WELLS

____

Bahareh Basirat

Approved:

____

Chair of the Committee
Cumaraswamy Vipulanandan, Professor,
Civil and Environmental Engineering

Committee Members:

____

Kalyan. B. Nakshatrala, Assistant Professor,
Civil and Environmental Engineering

____

Bill Rixey, Associate Professor,
Civil and Environmental Engineering

____

Robello Samuel, Adjunct Faculty,
Petroleum Engineering

____

Gino J. Lim, Professor,
Department of Industrial Engineering

____

Suresh K. Khator, Associate Dean,
Cullen College of Engineering

____

Roberto Ballarini, Professor and Chair,
Civil and Environmental Engineering

ACKNOWLEDGEMENTS

This study would not have been possible without valuable assistances of several individuals throughout my research. I realized though only my name appears on the cover of this dissertation, a great many people including my family members, well-wishers, my friends, my professors and my colleagues (CIGMAT group) have contributed to accomplish this task.

My parents, who have always loved me unconditionally. Their support and encouragement motivating and inspiring every bit of me towards new possibilities in life. To my brother, thank you for encouraging me in all of my pursuits and inspiring me to follow my dreams. Special thanks to my husband, Pedram for his selfless love, care and dedicated efforts during this journey. This would not have been possible without the support of my family specially my grandfather who taught me to work hard for the things that I aspire to achieve, my friends who have always supported me and directed my ambitions toward my goals.

I would like to express my sincere gratitude to my advisor, Dr. C. Vipulanandan, for his valuable guidance and encouragement throughout my study. I would like to extend my appreciation to Dr. Kalyan. B. Nakshatrala, Dr. Bill Rixey, Dr. Robello Samuel and Dr. Gino J. Lim for serving in my thesis committee and taking time for exchanging valuable suggestions.

The financial support provided by the CIGMAT and THC-IT at the University of Houston is gratefully acknowledged.

ANALYTICAL MODELING AND VERIFICATION WITH NUMERICAL METHODS AND EXPERIMENTS OF THREE PHASE REACTIVE MATERIALS, DRILLING, CEMENTING AND PERFORMANCE OF SMART CEMENTED MODEL OIL WELLS

A Thesis

Presented to

the Faculty of the Department of Civil & Environmental Engineering

University of Houston

In Partial Fulfillment

of the Requirements for the Degree

Doctor of Philosophy

in Civil Engineering

by

Bahareh Basirat

December 2016

ABSTRACT

In this study new analytical models were developed based on using a nonlinear rheological model to predict the drilling and cementing of the oil well. Also, the long term performance of a model field well that was cemented using the smart cement was predicted using a nonlinear piezoresistive model and numerical model.

The new reactive three phase material model was developed to characterize the three phase material with reactive constituents and to introduce the six independent reactive material parameters that depend on the curing time, temperature and pressure which contribute to the phase transition. This model can be used for any material with three phases such as cement, drilling mud, filter cake, oil rich rocks and medicines. In order to verify the model, cement slurry with water-cement ratio of 0.4 was tested for over 800 days. The changes in the weight, volume and the moisture content with the curing time was monitored to quantify the change in the three phases. Influence of the six material parameters on the shrinkage, porosity and electrical resistivity of the solidified cement were verified. The resistivity of the cement was influenced by the one reactive model parameter that represented the direct reaction of the liquid phase with the solid phase. The fracture behavior of smart cement was also evaluated using the electrical property monitoring tools in addition to the crack mouth opening displacement (CMOD) gauge. Also, Vipulanandan failure model for material was compared with Drucker–Prager criterion and verified with experimental results.

In this study, well drilling and casing installation was investigated analytically using the new shear thinning rheological model. The analytical model predictions were compared to the Newtonian model. The Newtonian model over predicted the flow velocities and shear stress by 300%. Also, the analytical solutions were verified using numerical method. The effects of eccentricity for axial flow is investigated numerically while the eccentricity effect is analyzed analytically for the vortex flow. Later on, a new kinetic model has been developed assuming that the permeability and solid content during the filter cake is changing with time, temperature and pressure using Hyperbolic Model. The new kinetic model was verified with results from of fluid loss and compared with the API model. Also pumping of cement slurry during the well installation was investigated in terms of shear stress developed at the casing and geological formation interfaces.

Three physical models simulating the cemented wells (including small model, large model and field model) were tested. During the test, the pressure applied inside the casing in small and large model test and the change of resistivity in smart cement were measured and p, q model was used to correlate the casing pressure to the cement resistivity changes. The numerical model analyzed to define the stresses and displacement along and around the wellbore and verified with the stress predicted from piezoresistivity effects. The smart cement will also predict the pressure inside the well.

TABLE OF CONTENTS

LIST OF FIGURES

LIST OF TABLES

CHAPTER 1. INTRODUCTION

1.1. General

Most of the natural and artificial materials are three phase (solid, liquid, gas) materials with the constituents reacting over time based on the chemical compositions, pressure and temperature. The geological rock and soil formations with various types of oil and gases in them representing the natural three phase reactive materials in place for millions of years. These three phases materials are under varying temperature and pressures undergoing chemicals, physical and biological reactions. In the material characterization of this study a three phase interaction model proposed can be used in different field. The medicines used in the medical field, chemicals used in the science and materials used in the engineering field can be characterized as three phase materials.

Medical Field

Various types of medicate\ions and manufactured using foams and solid particles. The interaction depends on interfacial energy, temperature and pressure.

A study has been investigated in the US National library of medicine. In this research, as europium monoxide (EuO) has its highest potential when integrated with spintronic-relevant semiconductors, the requirements with respect to the structural perfection of EuO films are basically the same as for all other semiconductor applications. Decades of technological innovation make it possible to fabricate silicon and other mainstream semiconductors with unrivalled perfection. For thin films, the standard methods all involve epitaxy—utilizing liquids (liquid-phase epitaxy), gases (vapour-phase epitaxy) or solids (solid-phase epitaxy). In this process, the atoms in the film inherit their crystalline arrangement from the underlying single crystal on which they are deposited and with which they do not react. If the depositing materials react with the substrate, the result is often disastrous to the crystalline perfection of the product formed, but an exception exists:

topotaxy. Here the product inherits its highly oriented structure from the single crystal it replaced (Mairoser, et al., 2015).

Science Field

Lithium cobalt oxide ($LiCoO_2$) electrodes contain three phases, or domains, each having specific-intended function: ion-conducting pore space, lithium-ion-reacting active material, and electron conducting carbon-binder domain (CBD) (Zielke, et al., 2014).

Fluidized-bed bioreactors have been shown to outperform such existing wastewater treatment systems as the activated-sludge process, rotating biological contactor, and trickling filter. Various modes of fluidized-bed bioreactor operations have been attempted for aerobic treatment of wastewater containing phenol, e.g., the tapered three-phase fluidized bed (TTFB), the conventional liquid-solid fluidized bed (CFB) coupled with a preaerator, the conventional three-phase fluidized bed (CTFB), and the external-loop three phase fluidized bed (ETFB). Studies of the hydrodynamics and transport behavior of a draft tube gas-liquid-solid fluidized-bed (DTFB) bioreactor showed that gas holdup and volumetric gas-liquid mass transfer coefficient in a DTFB is higher than that in a CTFB (Fan, et. al, 1987).

Engineering Field

In the oil and gas industry, knowing the characteristics of the cement is very important due to challenges related to oil well cement. Shrinkage of the cement, chemical reaction between the water and cement content, specific weight, porosity and weight loss are all affecting the behavior of the cement.

There are three stages for the performing the oil well, drilling, cementing and long term performance of the cemented casing. In the first stage, the rheological models such as Newtonian, Bingham and Power law has the limitation on the stress, which goes to infinity when the strain rate reached to very high numbers. Here a new model proposed to eliminate this limitation which is verified by numerical modeling with COMSOL Multiphysics. The effects of the eccentricity are investigated for an axial flow numerically. The eccentricity effects of Newtonian and Hyperbolic model are compared for concentric and various eccentric cases. While the eccentricity effects are analyzed analytically for vortex flow using the complex potential function theory.

Drilling muds are used in oil, gas, and geothermal well drilling, and fluid loss and filter cake formation are critical issues related to successful operations. Also, the filter cake formation and fluid loss are affected by pressure in the borehole. Rate and total fluid loss from drilling mud can affect the performance of the drilling mud and well safety. Hence, it is critical to quantify not only the rate of fluid loss process but also the changes in the filter cake formation during the fluid loss process. Past studies have assumed that the permeability and solid fraction in the filter cake remained unchanged during the formation of the cake and the fluid loss was directly propositional to the square-root of time (API Model). The new kinetic model prediction was also compared to the API model, and it predicted fluid losses very well. Hence, the new kinetic model can be used to better model the filter cake formation and filter loss in real time as functions of changes in permeability and solid content in the filter cake.

The numerical method was done using COMSOL Multiphysics for cemented casing. In the experimental evaluation, three physical models build to investigate the piezoresistive behavior of the cemented casing due to internal pressure inside the casing. The vertical stress from numerical model validated with field test using the piezoresistive effects.

1.2. Problem Statement

In the material characterization of this project three phase interaction of the material proposed. Three phase (solid, liquid and gas) representation is the most general case for all the natural and artificial materials that are commonly used in the field of medicine, science and engineering. In this study, chemically reactive three phase material model with six independent variables changes with time representing the chemical based on the composition of the solid, liquid and gas in the three phase material, there will be reaction between the three phases changing the compositions and density in the material. Knowledge of the phase interaction of a hardening cement paste is necessary to describe the chemical and physical properties of a cement based material. In order to verify the application of the model, cement slurry samples with initial water – to – cement ratio (moisture content) of 0.4 were investigated for over 800 days cured under room condition. Influence of the six material parameters on the shrinkage, porosity and electrical resistivity of the solidified cement was quantified. The volume shrinkage was influenced by the liquid – solid reactive model parameter. The resistivity of the cement was influenced by the "b(t)" reactive model parameter.

There are three stages in performing the oil well, drilling, cementing and cemented casing. The new models proposed in these stages.

In the first stage, the rheological models including, Newtonian, Power law and Bingham models have the limitation of the stress goes to infinity when the strain rate is very high. A new model developed to eliminate this characteristic and introduce new analytical solution which is verified with the numerical solution with COMSOL Multiphysics software. This model can be used in the second stage (cementing) as well. One of the challenges in the drilling and cementing stage is the eccentricity which may occur due to so many effect such as weight of the casing in the deviated wellbore. The effects of eccentricity for axial flow is investigated numerically while the eccentricity effect is analyzed analytically for the vortex flow. As an element of the drilling the filter cake properties have been investigated. The API model presents the filter cake properties such as permeability and solid content as constant while in the reality these parameters are time dependent characteristics. Therefore, new kinetic model proposed to express the filter cake permeability and solid content as a time dependent functions.

Real time monitoring of the cementing (third stage) is necessary to prevent failures in the oil wells. Finding the stresses and strains around the wellbore while pressurizing the casing is a challenge. There are three physical model built in the lab and the energy research park in which the pressure correlated with the resistivity changes. The vertical stress from numerical model validated with field test using the piezoresistive effects. Hence, by monitoring and measuring the resistance the stresses and strain can be predicted.

1.3. Objectives

The objective of this study is to introduce new models proposed for different stages of the performance of the oil well, such as drilling, cementing and cemented casing.

- The three phase interaction between material elements leads this study to have a better insight of material behavior. The material can be any three phase material including cement, drilling mud or filter cake in the oil and gas study. Medicine in the medical field and materials in other scientific studies.
- The new rheological model proposed to eliminate the limitation of Newtonian, Power law and Bingham model which is verified by numerical model using COMSOL Multiphysics. The eccentricity is investigated numerically for axial flow and analytically for vortex flow.
- A new kinetic model proposed for the filter cake to make the permeability and filter cake solid content as time dependent functions compared with the API model.

- Three test models including small model, large model and field model test were built. The real time monitoring of the cement behavior along the piezoresistivity characteristics was done to prove the relationship of the pressure and resistivity changes.
- The modeling of the oil well is an important fact to estimate the stress and strain around the wellbore in long term performance for maintenance of the wellbore integrity which is verified with the numerical methods and by correlating the pressure with resistivity changes, the stresses can be predicted by monitoring the resistivity changes.

1.4. Organization

This thesis is organized into six chapters. Chapter 1 is the introduction to this research study, which presents the research problem that was the focus of this study. Chapter 2 summarizes background and literature review. In Chapter 3, materials and methods procedures are broadly discussed. Chapter 4 is material modeling including three phase and modeling. Chapter 5 discusses the rheological model for drilling fluid and also a kinetic model for filter cake. Chapter 6 expresses physical models and also analytical solution of the smart cemented oil well. A numerical model performed to investigate the stress and displacement around the wellbore verified with the piezoresistivity effects of the cement.

.

CHAPTER 2. BACKGROUND AND LITERATURE REVIEW

2.1. Introduction

The main purpose of this chapter is to provide a review on the topics that are closely related to the proposed study. This chapter summarizes the background to the past research on the three phase material modeling, the rheological model developed for the drilling and API model for the filter cake and also the research developed analytical models for developing stress, strain and displacement around the wellbore.

2.2. General

In oil and gas industry, knowing the characteristics the drilling mud, cement and other elements of the wellbore is very important.

Knowledge of the phase interaction of a hardening cement paste is necessary to describe the chemical and physical properties of a cement based material. Powers and Brownyard Studied the physical properties of hardened Portland cement paste (Brouwers, 2004). They presented an empirical model for the phase distribution of a hardening cement paste in 1948. This model is a benchmark due to quantitative calculations ability of the volumetric composition of cement based materials. In the following years, Powers modified the model referred to as Powers' model (Powers, 1947 and 1960).

Jensen and Hansen described the water-entrained cement based materials (Jensen and Hansen, 2000). In 1980's Hansen expressed the unit volume of hardened Portland cement paste and fractional volume of capillary pores, cement gel, gel water and unhydrated cement. He showed how the fractional volumes of all major constituents in the physical structure of room temperature cured

Portland cement paste can be estimated from information on water-cement ratio and degree of hydration of the cement (Hansen, 1986).

The porosity of a material exerts influence on its physical properties. For hardened cement paste a large volume of pores is inherent in the set structure. Backscattered electron image has been used as a tool (Mellas et al., 2003) to capture the porosity of the harden cement. Pycnometry technique is another tool to identify the specific weight of the cement (Shahrouzi et al., 2012) also the porosity has been estimated using the density method (Takagi and Chow, 2001).

Proposed model for phase transition can be represent all the parameters interacting in different physical and chemical changes inside the material. Moreover, the porosity and shrinkage of the material can be predicted.

Table 2 - 1: Three phase reactive material literature review

Reference	Title	Remarks
Mairoser, et al., 2015	High-quality EuO thin films the easy way via topotactic transformation	Three phase material in medical field
Zielke, et al., 2014	Three-Phase Multiscale Modeling of a LiCoO2 Cathode: Combining the Advantages of FIB–SEM Imaging and X-Ray Tomography	Three phase material in science field
Fan, et. al, 1987	Bioreactor with Immobilized Living Cells for Phenol Degradation	
Powers. 1958	Structure and Physical properties of Hardened Portland Cement Paste.	Quantitative calculations ability of the volumetric composition of cement based materials
Powers, 1947	A discussion of cement hydration in relation to the curing of concrete	
Powers, 1960	Physical properties of cement paste	
Brouwers, 1948	Studies of the physical properties of hardened Portland cement paste,	An empirical model for the phase distribution of a hardening cement paste
Brouwers, 2004	The work of Powers and Brownyard revisited: Part 1.	Studied the physical properties of hardened Portland cement paste
Brouwers, 2011	A Hydration Model of Portland Cement,	
Brouwers, 2012	Paste models for hydrating calcium sulfates, using the approach by Powers and Brownyard	

Table 2 - 1: Three phase reactive material literature review

Reference	Title	Remarks
Hansen, 1986	Physical structure of hardened cement paste. A classical approach.	Expressed the unit volume of hardened Portland cement paste and fractional volume of capillary pores, cement gel, gel water and unhydrated cement
Jensen and Hansen, 2000	Water-entrained cement-based materials I. Principle and theoretical background	Described the water-entrained cement based materials
Mellas, et al., 2003	Estimation of the Porosity of Portland Cement Pastes Using Backscattered Electron Image	Backscattered electron image has been used as a tool to capture the porosity of the harden cement.
Shahrouzi, et al., 2012	The Effect of Paste Concentration on Mechanical and Setting Properties of Calcium Phosphate Bone Cements	Pycnometry technique is another tool to identify the specific weight of the cement
Vipulanandan et al., 2014	Behavior of Piezoresistive Smart Cement Contaminated with Oil Based.	Electrical resistivity is one of the method can be used to investigate the piezoresistive behavior of the oil well cement
Li and Wei, 2003	The Electrical Resistivity of Cement Paste Incorporated with Retarder	Accuracy, ease of testing and nondestructive characteristics electrical resistivity
Wong and Buenfeld, 2009	Determining the water-cement ratio, cement content, water content and degree of hydration of hardened cement paste: Method development and validation on paste samples	Proposed a method first quantifies the composition of the hardened cement paste
Takagi and Chow, 2001	Formation of macro pores in calcium phosphate cement implants	The porosity has been estimated using the density method
Talabani, 1997	Gas Migration Eliminated Through Correct Cement Design Including Elastomers.	Gas migration investigation
Tang, Ge and Brus 2002	Gas-liquid-solid phase transition model for two-dimensional nanocrystal self-assembly on graphite.	The inter particle attractive force, phase separation kinetics, and critical coverage in this system can be revealed from aggregation spatial patterns at different kinetic stages
Brameshuber and Raupach, 2003	Nondestructive Determination of the Water Content in the Concrete Cover using the Multiring Electrode Part I: Aspects of Concrete Technology	The electrolytic resistivity of concrete essentially depends on the chemical composition of the pore solution and the pore structure
Garboczi, 2000	Conductivity of the Interfacial Transition Zone in Cement Mortars Introduction	MIP measures the overall porosity and approximate pore-size distribution of a material
Handin, 1965	Strength of Oil Well Cements at Downhole Pressure- Temperature Conditions	Oil Well Cements integrity
Khalid, 1998	Prevention of Shallow Gas Migration Through Cement	

As an important element of the oil well, cement sheath, placed in the annulus between casing and formation, provides zonal isolation and structural support to the casing throughout the life of a well (Abbas et al., 2002; Goodwin, 1997). The knowledge of the cement properties during time helps to maintain the zonal isolation in oil well (Boukhelifa et al., 2005).

In the oil industry, gas migration during cement setting and hardening is a very big challenge. These theories related to gas migration attribute this phenomenon to fluid loss during cementing and the differential pressure occurrence due to the gelation. The differential pressure leads gas to migrate into the pores of the cement structure. During the setting phase of cement, micro-fractures can be formed between cement and formation and within cement itself which leads to gas migration (Khandka, 2007; Talabani, 1997; Khalid, 1998 and McDaniel, 2014).

Fracture mechanics concepts have proved invaluable tools in both characterizing and explaining the failure processes in materials (Zerbst et al., 2015). Fatigue fracture mechanics properties (Korte et al., 2014) is also one of the characteristics which can be found in this area. Fracture mechanics introduces various parameters to describe the behavior of materials also under various loading condition.

Principles of fracture mechanics are finding increasing applications in concrete, cement mortar and cement paste, triggered to a large extent by the need to understand the behavior of those materials in different applications. However, literature on the fracture properties of oil well cements used in petroleum industry is limited and there is a need for detailed studies.

In the literature, researchers have used both linear elastic fracture mechanics (LEFM) parameters and elastic plastic fracture parameters in characterizing fracture resistance of cement paste, cement mortar, cement concrete, polymer concrete and rocks (Avci et al., 2004; Atkinson, 1987; Bazant, 1992; Dharmarajah et al., 1988; Vipulanandan et al., 1994; Wecharatna et al., 1982; Ziegeldorf et al., 1999).

The application of LEFM to cementitious materials was justified by treating crack branching and fracture process zone to be analogous to a small size plastic zone at the crack tip. LEFM is being used extensively in determining the critical stress intensity factor (KIC) based on measurements of the initial notch depth and load to failure (Ziegeldorf, 1999). Critical stress intensity factor is one of the most frequently used parameters in the literature to study the fracture properties of materials (Vipulanandan et al., 1994). Stress intensity factor, KI characterizes the crack tip conditions in a linear elastic material (Budynas 1999).

There is crack growth in the material when the stress intensity factor reaches the Critical Stress Intensity Factor based on the mode of loading (Roesler et al., 2007). Prior to fracture, the crack tip absorbs energy and generates local plastic deformation or forms micro cracks based on the type of material.

The critical stress intensity factor and crack displacement opening displacement of mortar and concrete using three-point bend test on notched beam have been investigated by many researchers (Shah, 1991; Yoshiyuki and Kazuo, 1976). Also ASTM-E399 includes Single Edge Notched Beams (SENB) tests for different type of material. The critical stress intensity factor (KI) for portland cement paste and mortar were investigated by many researches and the initial (KIC) varied from 0.4 to 1.9 Mpa.sqrt (m) (Zhu and Xu, 1990; Wittmann and Metzener-Gheorghita, 1985).

Different methods for determination of Crack Tip Opening Displacement (CTOD) including double clip method were compared on Single Edge Notched Tension (SENT) specimens (Philippa and Henryk, 2012). In this study, Elastic Crack Tip Opening Displacement (CTODe)is calculated as a function of Elastic Crack Mouth Opening Displacement, CMODe (Vipulanandan and Dharmarajan, 1989; Jenq and Shah, 1985)

The compositions of oil well cements are different from Portland cement based on the application conditions. Oil well cements are subjected to high temperature and pressures resulting in cracks. The Gulf of Mexico disaster (2010) showed that one of the main reason of failure was the cement job which is a challenge in oil and gas industry (Handin, 1965; Salim and Amani, 2013; Swayze, 1954).

Table 2 - 2: Fracture study literature review

Reference	Title	Remarks
Zerbst et al., 2015	Fracture mechanics as a tool in failure analysis – prospects and limitations	characterize and explain the failure processes in materials
Abbas et al., 2002	Solutions for Long-Term Zonal Isolation	Cement role in zonal isolation and structural support to the casing
Goodwin, 1997	Oilwell / Gaswell Cement-Sheath Evaluation.	Cement role in zonal isolation and structural support to the casing
Ravi et al., 2002	Improve the Economics of Oil and Gas Wells by Reducing the Risk of Cement Failure	Cement withstand high stresses under extreme service
Khandka, 2007	Leakage Behind Casing	Gas Migration due to micro fractures
Talabani, 1997	Gas Migration Eliminated Through Correct Cement Design Including Elastomers.	Controlling the Gas migration during cement setting
Khalid, 1998	Prevention of Shallow Gas Migration Through Cement	During the setting phase of cement, micro-fractures can be formed
McDaniel, 2014	Cement Sheath Durability: Increasing Cement Sheath Integrity to Reduce Gas Migration in the Marcellus Shale Play.	
Avci et al., 2004	Fracture behavior of glass fiber reinforced polymer composite	Researchers have used both linear elastic fracture mechanics (LEFM) parameters and elastic plastic fracture parameters in characterizing fracture resistance of cement paste, cement mortar, cement concrete, polymer concrete and rocks
Atkinson, 1987	Fracture Mechanics of Rock	
Vipulanandan et al., 1994	Fracture Behavior of Cement Grouted Sand	
Wecharatna et al., 1982	Slow Crack Growth in Cement Composites	
Ziegeldorf et al., 1999	A Model Law for the Notch Sensitivity of Brittle Materials	
Budynas, 1999	Advanced Strength and Applied Stress Analysis	Stress intensity factor, K_I characterizes the crack tip conditions in a linear elastic material

Table 2 - 3: Fracture study literature review

Reference	Title	Remarks
Roesler et al., 2007	Concrete fracture prediction using bilinear softening	Estimates the total fracture energy
Shah, 1991	Toughening mechanisms in quasi-brittle materials	The critical stress intensity factor and crack displacement opening displacement
Yoshiyuki and Kazuo, 1976	Stress Intensity Factors for Cracks in Notch Bend Specimens for Three Point Bending	
Zhu and Xu, 1990	Fracture properties of cement paste and mortar: an experimental investigation	The critical stress intensity factor (K_I) for Portland cement paste
Wittmann and Metzener-Gheorghita, 1985	Fracture toughness of concrete determined on large specimens	
Philippa and Henryk, 2012	Validation of Methods to Determine CTOD from SENT specimens	Different methods for determination of Crack Tip Opening Displacement
Vipulanandan and Dharmarajan, 1989	Critical crack tip opening displacement for polymer composites	Calculation of Crack Mouth Opening Displacement
Jenq and Shah, 1985	A Fracture Toughness Criterion for Concrete	
Handin, 1965	Strength of Oil Well Cements at Downhole Pressure-Temperature Conditions	Oil well cements are subjected to high temperature and pressures resulting in cracks
Salim and Amani, 2013	Special Considerations in Cementing High Pressure High	
Swayze, 1954	Effects of High Pressures and Temperatures on Strength of Oil-well Cements	

Several methods have been used to monitor the behavior of cementatious material such as X-ray diffraction, calorimetric analysis, scanning electron microscopy and ultrasonic methods. Different concrete properties including the transport properties of the concrete using various electrical resistivity test methods (Smith, 2006). Electrical resistivity is one of the method can be used to investigate the behavior of the oil well cement (Vipulanandan and Heidari, 2014) due to the accuracy, ease of testing and nondestructive characteristics (LI and WEI, 2003) of this method. Brameshuber and Raupach monitored the resistivity changes influence versus time and water content for concrete using multiring-electrode (Brameshuber and Raupach, 2003). Vipulanandan investigated the two probe method of measuring electrical resistivity in order to find the oil well cement properties. He introduced a new material called smart cement material with modifications which enhance the mechanical properties of the smart cement, without affecting the rheological properties. (Vipulanandan et al., 2015). In this study the two probe method has been selected as a nondestructive method to find the correlation of cement properties with resistivity changes.

There are three stages for performance of the oil well. The first stage is the drilling. The second stage is cementing and the third stage is the cemented casing in long term performance of the oil well. Empirical and time-independent rheological models including Power law, Bingham and Herschel–Bulkley, represent the shear stress shear, strain rate, yield stress and apparent viscosity relationship. The estimated rheological properties can vary significantly based on the models (Reddy and Riley, 2004). The two models which have been used widely in oil and gas industry (Guillot, 1990). The Bingham plastic model includes yield stress and a limiting viscosity at finite strain rates, while the Power law model fails to consider. Herschel–Bulkley model (Herschel and Bulkley, 1926) does not have such limitation and can predict the nonlinear shear-thinning/shear-thickening behavior of OWCs. The hyperbolic model was effective in predicting the shear stress–shear strain rate shear thinning behavior (Vipulanandan and Mohammed, 2015). Based on the root mean square error (RMSE), hyperbolic model was predicting the fluid characteristics better than Herschel–Bulkley and Casson models also the hyperbolic model predicted the maximum shear stress tolerance of drilling mud other two models predicted in-finite shear stress tolerance for the drilling mud (Vipulanandan and Mohammed, 2014). Azar and Samuel in 2007 proposed the analytical model for determination of the velocity generated by Newtonian, Power law and Bingham model for the fluid flow. The velocity predicted for these models. In this study hyperbolic model introduced for predicting the velocity of the drilling mud and cement slurry in an axial flow.

The eccentricity of the casing in the annular wellbore is a challenge while drilling and cementing. The weight of the casing in the deviated wellbore is one of the reasons for occurrence of the eccentricity. Nakayama and Boucher at 1998 suggested the theory of complex variable which combines the potential function and stream function. In this study this theory has been used to investigate the effects of the eccentricity. An analytical model is developed using the theory of complex variable to model the eccentricity for vortex flow. A numerical model also is provided to show the effect of eccentricity for the axial flow.

An elements of the drilling is filter cake which its properties is investigated. The drilling fluids are a mixture of solids, liquids, and chemicals, with the liquid being the continuous phase. To stabilize the wellbore, the drilling fluid forms a filter cake, which stabilizes the formation face. Some material such as cement, filter cake and any other material made up of three phases of solid, liquid and air can be modeled using the following method. Filter cake builds up over the face of the porous medium and filtrate overrun the formation (Civan, 1996). When the slurry contains particles of different sizes, the larger particles of the slurry form the skeleton of the filter cake and the smallest particles can migrate and deposit within the porous cake formed by the larger particles. Simultaneously, the cake may undergo a compaction process by the effect of the fluid drag as the suspension of smaller particles flows through the cake (Tien et al. 1997). Osisanya and Griffith (1997) developed an equation to determine filter cake permeability based on filtrate volume, shear stress, plastic viscosity, and yield point of the fluid. Past studies on the formation of filter-cake were focused on the model tests in the laboratory. Khatib (1994) claimed that the cake porosity varies with the applied pressure particularly for compressible particles and also the filter cake characteristics of the solids can be expressed by developing empirical permeability-porosity correlations. Fathi and Theliander (1995) developed a method for the local filtration charactristics such as specific filtration resistance and porosity. The filter cake was simulated by layer by layer model expressed by Theliander and Fathi (1996). Filter cake properties changes with time and loses water as well as cement and the characteristics is changing with time. In this study, the new kinetic model utilized hyperbolic model make the permeability and solid fraction of the filter cake as a function of time (Vipulanandan, Raheem, Basirat and Mohammed, 2014).

Table 2 - 4: Literature review for vortex and axial flow, stage 1 and 2 of the performance of oil well

Reference	Title	Remarks
Reddy and Riley, 2004	High Temperature Viscosifying and Fluid Loss Controlling Additives for Well Cements, Well Cement Composition Sand Methods	The estimated rheological properties can vary significantly based on the models
Guillot, 1990	Rheology of Well Cement Slurries.	The Bingham plastic model and the Power law model are widely used in the petroleum industry to describe the flow properties of cement slurries
Azar and Samuel, 2007	Drilling Engineering	Investigation of different velocity from different rheological models
Ochoa, 2006	Analysis of Drilling Fluid Rheology and Tool Joint Effect to Reduce Errors in Hydraulics Calculations	Non-Newtonian fluids do not conform to direct proportionality between shear stress and shear strain rate
Herschel and Bulkley, 1926	Konsistenzmessungen Von Gummi-Benzollösungen	Non-Newtonian fluids, Herschel and Bulkley
Vipulanandan and Mohammed, 2015	Smart Cement Modified with Iron Oxide Nanoparticles to Enhance the Piezoresistive Behavior and Compressive Strength for Oil Well Applications	Developed hyperbolic model for smart cement
Vipulanandan and Mohammed, 2014	Hyperbolic Rheological Model with Shear Stress Limit for Acrylamide Polymer Modified Bentonite Drilling Muds	Developed hyperbolic model for drilling muds
Nakayama and Boucher, 1998	Introduction to Fluid Mechanics	Utilize the theory of complex variable for eccentricity
Civan, 1996	A Multi-Purpose Formation Damage Model	Filter cake builds up over the face of the porous medium and filtrate overrun the formation

Table 2 - 3: Literature review for vortex and axial flow, stage 1 and 2 of the performance of oil well

Reference	Title	Remarks
Osisanya and Griffith, 1997	Evaluation of Cement Slurry Quality Using Filter Cake Permeability and Thickness	developed an equation to determine filter cake permeability based on filtrate volume, shear stress, plastic viscosity, and yield point of the fluid
Tien et al., 1997	Analysis of Cake Growth in Cake Filtration: Effect of Fine Particle Retention	Cake may undergo a compaction process by the effect of the fluid drag
Khatib, 1994	Prediction of Formation Damage Due to Suspended Solids: Modeling Approach of Filter Cake Buildup in Injectors	Claimed cake porosity is not constant
Fathi and Theliander, 1995	Determination of Local Filtration Properties at Constant Pressure	Developed local filtration properties such as specific filtration resistance and porosity
Theliander and Fathi, 1996	Simulation of the Build-up of a Filter Cake	filter cake was simulated by layer by layer model
Vipulanandan, Raheem, Basirat and Mohammed, 2014	New Kinetic Model to Characterize the Filter Cake Formation and Fluid Loss in HPHT Process	Utilized the hyperbolic model to introduce a kinematic model for permeability and soli fraction of the filter cake

The third stage of the performing oil well cement is cemented casing which its performance provides the zonal isolation of the wellbore (Sarap, et al., 2009). The utilizing the real time monitoring in boreholes increase the safety in the performance of the wellbore (Vipulanandan, et al., 2015), therefore, and the challenges can be recognized before disasters. Many researchers used the electrical resistivity to characterize the cement and concrete in other cement applications (Azhari and Banthia, 2012; Liao and Wei, 2014). Carter provided remote real-time data monitoring and application of emerging real-time technologies that utilizing data acquisition and performance optimization for safety (Carter, et al., 2014). John in 1992 introduced the most common cement type in oil and gas are cement Class G and H.

In this study, the smart cement was used to installed and cemented the field in order to enhance the piezoresistive properties. The field well was designed and built in the Energy Research Park (ERP) which is used to demonstrate the concept of real time monitoring of the flow of drilling mud and smart cement and hardening of the cement in place. The well was installed in soft swelling clay soils. A new method has been developed to measure the electrical resistivity of the materials using the two probe method (Vipulanandan et al., 2014). Change in the resistance of hardening cement was continuously monitored since the installation of the field well. Also, a method was developed to predict the changes in electrical resistance of the hardening cement outside the casing (Electrical Resistance Model - ERM) with time. The ERM predicted the changes in the electrical resistances of the hardening cement outside the cemented casing very well. In addition, the pressure testing showed the piezoresistive response of the hardened smart cement and a piezoresistive model has been developed to predict the pressure in the casing from the change in resistivity in the smart cement (Vipulanandan et al., 2016).

Table 2 - 5: Literature review for real monitoring of cemented casing, stage 3 of the performance of oil well

<table>
<tr><th>Reference</th><th>Title</th><th>Remarks</th></tr>
<tr><td>API Recommended Practice 10B, 1997</td><td>Recommended Practice for Testing Well Cements Exploration and Production Department,</td><td rowspan="2">Cement requirements and types in order to use in oil or gas well</td></tr>
<tr><td>API Recommended Practice 65, 2002</td><td>Cementing Shallow Water Flow Zones in Deepwater Wells.</td></tr>
<tr><td>Azhari and Banthia, 2012</td><td>Cement-based sensors with carbon fibers and carbon nanotubes for piezoresistive sensing</td><td rowspan="2">Electrical resistivity measurement has been used by many re- searchers to characterize the cement concrete and in other cement applications</td></tr>
<tr><td>Liao and Wei, 2014</td><td>Relationship between chemical shrinkage and electrical resistivity for cement pastes at early age</td></tr>
<tr><td>Carter, et al., 2014</td><td>Improved Regulatory Oversight Using Real- Time Data Monitoring Technologies in the Wake of Macondo</td><td>Through remote real-time data monitoring that aid in data acquisition and performance optimization for improved safety. Data sets and tools necessary for regulators to effectively monitor and regulate deepwater operations on a continuous basis are identified.</td></tr>
</table>

Table 2 - 6: Literature review for real monitoring of cemented casing, stage 3 of the performance of oil well

Reference	Title	Remarks
John, 1992	Class G and H Basic Oil Well Cements	Most common cement type in oil and gas, Cement Class G and H
Sarap, et al., 2009	The use of high performance spacers for zonal isolation in high temperature High-pressure wells	Zonal isolation of the cemented casing
Wei, et al., 2008	Electrical measurement to assess hydration process and the porosity formation	Limited studies have used electrical measurement methods to study the microstructural evolution in hydrating cement-based material systems
Zuo, et al., 2014	Hydration of cement with retarder characterized via electrical resistivity measurements and computer simulation	
Vipulanandan and Mohammed, 2015	Smart cement rheological and piezoresistive behavior for oil well applications	Investigating the piezoresistivity effect of smart cement
Vipulanandan and Sett, 2004	Development and Characterization of Piezoresistive Smart Structural Materials	A new method has been developed to measure the electrical resistivity of the materials using the two probe method. Also it predicts the changes in electrical resistance of the hardening cement outside the casing (Electrical Resistance Model - ERM) with time has been developed.
Vipulanandan et al., 2015	Real Time Monitoring of Oil Based Mud, Spacer Fluid and Piezoresistive Smart Cement to Verify the Oil Well Drilling and Cementing Operation Using Model Tests	
Vipulanandan et al., 2014	Development and Characterization of Smart Cement for Real Time Monitoring of Ultra-Deepwater Oil Well Cementing Applications	
Vipulanandan et al., 2016	Field Test for Real Time Monitoring of Piezoresistive Smart Cement to Verify the Cementing Operations	A field well was installed and cemented using the smart cement mixture

CHAPTER 3. MATERIALS AND METHODS

3.1. Sample Prepration

Cement slurry samples were prepared at a water-cement ratio of 0.4. Also, conductive filler up to 0.1% was added to make the cement piezoresistive. The specimens were cured at room condition. Four wires were placed in the mold specimen as shown in Fig. 3 - 1.

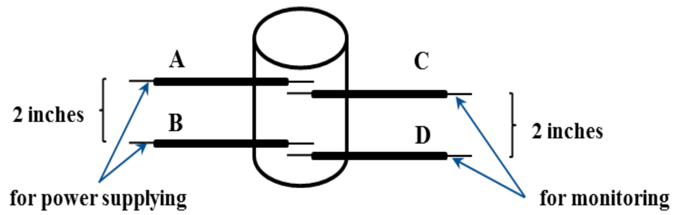

Fig. 3 - 1: Specimen for Electrical Properties Measurement

The LCR device was used in order to measure the resistance using two probe method (Fig. 3 - 2).

Fig. 3 - 2: Resistance Measurement Technique

3.2. Impedance Characterization

Studies have identified that measuring the resistance using two-probe method has some concerns associated with contact resistances at the interface of the wires and cement (Chung, 2001). Therefore, quantifying the contact resistance is important to obtain bulk resistance from apparent resistance to overcome this problem. Impedance characterization of materials is good tool to overcome the problem of quantifying the contact resistance and bulk resistance using equivalent circuit representation of the physical system that need to be studied.

Vipulanandan and Prashanth, (2013) proposed two possible equivalent electrical circuits for materials in order to find the most suitable equivalent circuit to represent the smart cement for the purpose of impedance characterization.

One of the equivalent circuit is shown in Fig. 3 - 3, which represents a general bulk material where the bulk material has both resistance (R_b) and capacitance (C_b). Contacts are connected in series with bulk and also have resistance (Rc) and capacitance (Cc).

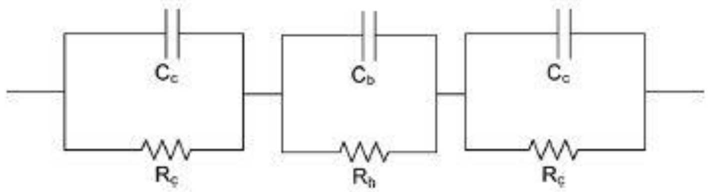

Fig. 3 - 3: Equivalent circuit 1
(Where the bulk material is represented by resistance and capacitance)

The total impedance Z_1 of this equivalent circuit can be given by Eq. (3 - 1). where ω is the angular frequency of the applied signal. When ω approaches zero, the impedance $Z_1=R_b+2R_c$. When ω approaches infinity then $Z_1 = 0$, as

$$Z_1 = \frac{R_b}{1+\omega^2 R_c^2 C_b^2} + 2\frac{Rc}{1+\omega^2 R_c^2 C_c^2} - j\left\{\frac{2\omega R_c^2 C_c}{1+\omega^2 R_c^2 C_c^2} + \frac{\omega R_b^2 C_b}{1+\omega^2 R_b^2 C_b^2}\right\}. \qquad \textbf{(3 - 1)}$$

The second possible equivalent circuit can be represented by assuming the capacitance of the bulk material, C_b, to be zero as shown in Fig. 3 - 4. It represents a special bulk material.

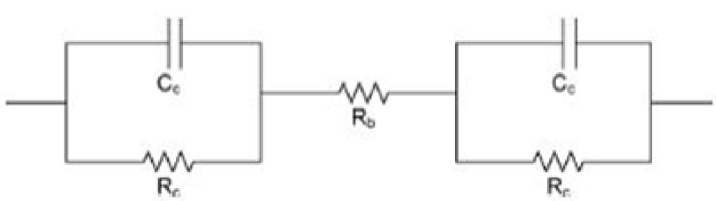

Fig. 3 - 4: Equivalent circuit 2
(Where the bulk material is represented by resistance only)

The total impedance of this equivalent circuit, Z_2, can be obtained by substituting C_b=0 in Eq. (3 - 1) and represented in Eq. (3 - 2) as

$$Z_2 = R_b + 2\frac{Rc}{1+\omega^2 R_c^2 C_c^2} - j\left\{\frac{2\omega R_c^2 C_c}{1+\omega^2 R_c^2 C_c^2}\right\}. \tag{3 - 2}$$

When ω reaches 0, resulting impedance $Z_2=R_b+2R_c$. When ω reaches infinity, then $Z_2= R_b$. Therefore, the variation of impedances Z_1 and Z_2 with the applied frequency (*f*) where $\omega = 2\pi f$, are shown in Fig. 3 - 5.

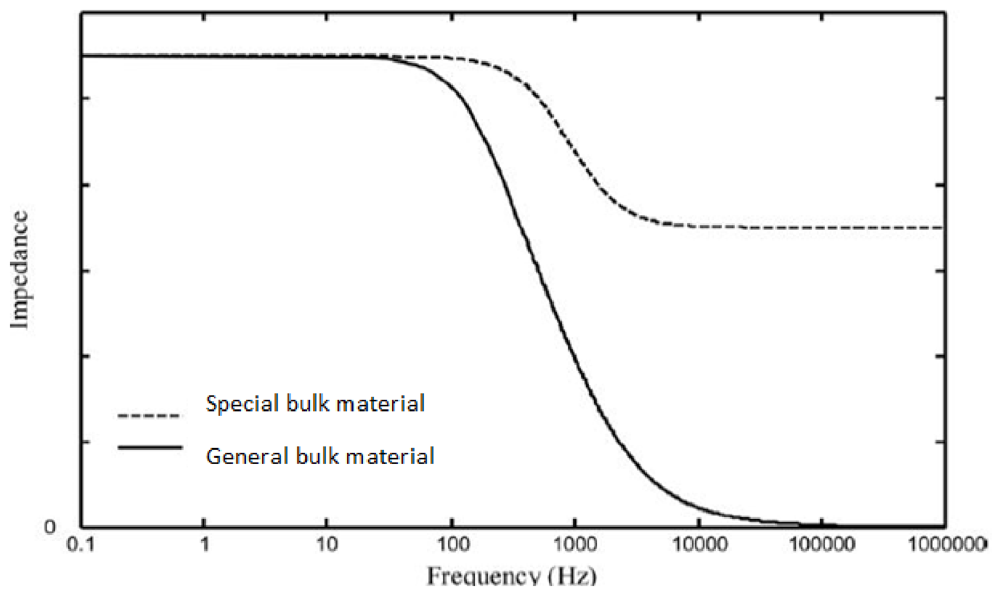

Fig. 3 - 5: Comparison of general bulk material and special bulk material

3.3. Characterization of the Smart Cement

Fig. 3 - 6 shows the typical piezoresistivity that was measured against compressive stress. Also, it was found the piezoresistivity was about 300% at the failure which is much higher than the piezoresistivity at failure of normal cement (Fig. 3 - 6).

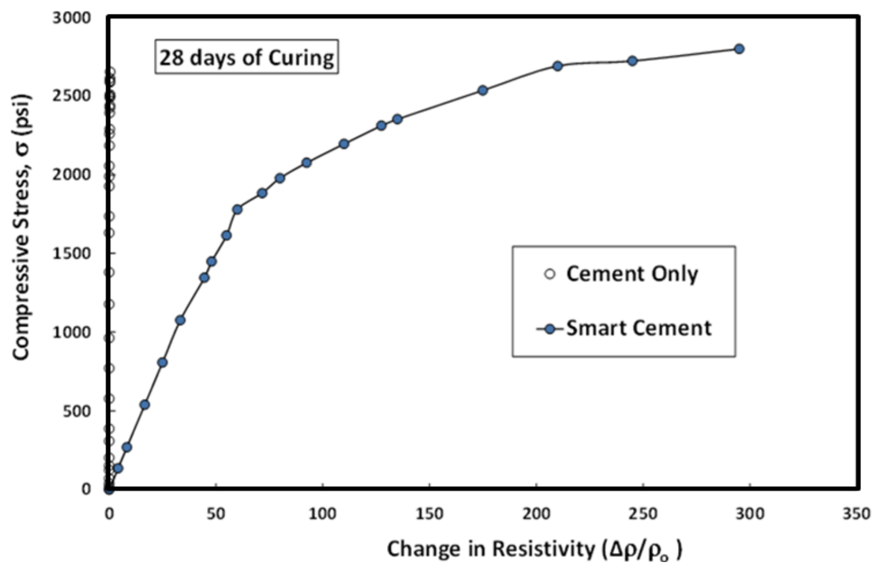

Fig. 3 - 6: Compressive stress versus change in resistivity relationship for neat cement and smart cement

3.3.1. Fracture Properties of Smart Oil Well Cements

Based on the Single Edge Notched Beams (SENB) tests fracture properties of piezoresistive smart oil well cement was investigated. The piezoresistive smart concrete was characterized as having a change in piezoresistivity of 200% for 25 MPa compressive strength after 28 days of curing. Mode I fracture behavior with varying notch-to-depth ratio under three-point loading system was invesrigated. The crack growth in the test specimens were determine by measuring the crack mouth opening displacement (CMOD) during loading and unloading the specimens. Also the changes in resistivity was measured during the testing and was correlated to the elastic and plastic crack growth. The elastic and plastic crack growth was related to the stresses and change in piezoresistivity using nonlinear relationship. The piezoresistivity changed by 4.2 % during the fracture test. The mode I critical stress intensity factor and critical crack tip opening displacement varied with the crack growth and was in the ranges of 0.3 to 2.2 MPa.√m and 0.5 to 28 μm, respectively.

(a) Stress Intensity Factor

The mode I stress intensity factor K_I for a bending loading can be represented as Eq. (3 - 3) (Shah 1990). where σ is bending stress and stress intensity factor represented as

$$K_I = \sigma\sqrt{a}F(\alpha). \qquad \textbf{(3 - 3)}$$

Where F(α) is a correction factor for finite width and loading geometry. For three-point loading bending test F(α) is given in the Eq. (3 - 4), where a factor α_e depends on the crack length and defined as $\alpha_e = (a_e+H_0)/(d+H_0)$. H_0 is the clip gauge holder thickness as shown in Fig. 3 - 8 (Shah 1990). Where F(α) is a correction factor defined as

$$F(\alpha_e) = \frac{\left[1.99-\alpha_e(1-\alpha_e)(2.15-3.93\alpha_e+2.7\alpha_e^{\,2})\right]}{\left[(1+2\alpha_e)(1-\alpha_e)^{\frac{3}{2}}\right]}. \qquad \textbf{(3 - 4)}$$

In Eq. (3 - 3), "a" has to be calculated from a numerical iteration procedure using Eq.(3 - 5), where initial compliance C_0 is given by C_0= CMOD/P and unloading compliance C_u was measured at loads and the effective crack length (a_e) and represented as

$$a_e = a_0\left[\frac{C_U}{C_0}\right]\left[\frac{V(\alpha_0)}{V(\alpha_e)}\right]. \qquad \textbf{(3 - 5)}$$

where a_0 is initial notch depth. V(α_e) is given as

$$V(\alpha_e) = 0.76-2.28\alpha_e+3.87\alpha_e^{\,2}-2.04\alpha_e^{\,3}+\frac{0.66}{(1-\alpha_e)^2}. \qquad \textbf{(3 - 6)}$$

(b) Load Versus CMOD

This schematic diagram of load versus CMOD explains the components of total CMOD ($CMOD^T$).

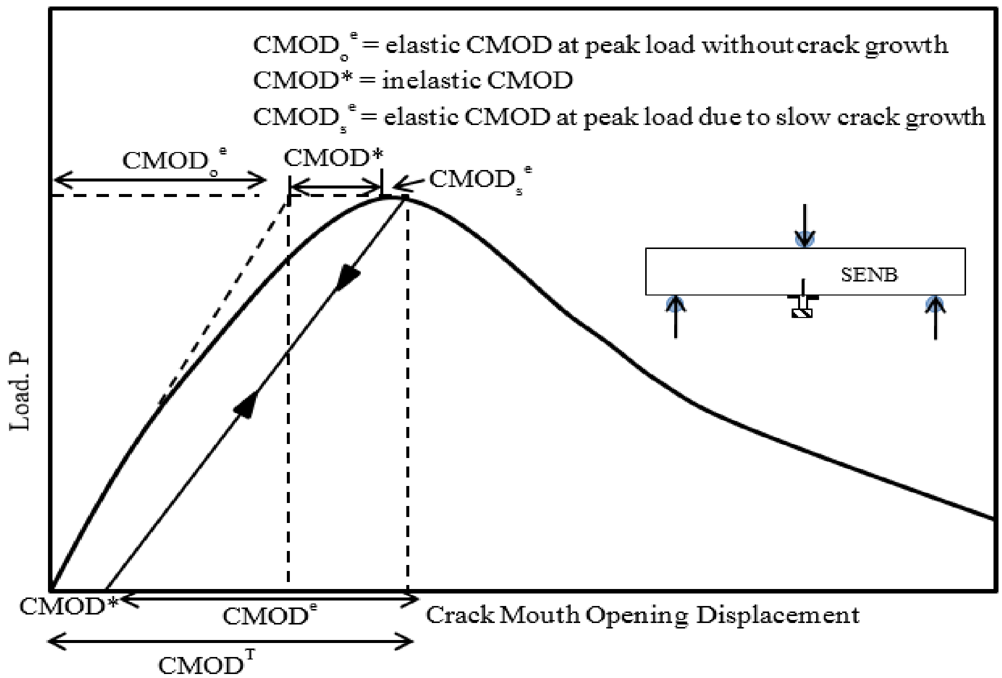

Fig. 3 - 7: Schematic diagram of load versus CMOD with the components of $CMOD^T$

If the material behaves elastically up to the peak load without any crack extension, the relationship between load and CMOD would be linear as shown in the Fig. 3 - 7. By unloading the specimen immediately after the peak load it can be seen that there is inelastic displacement (CMOD*). At peak load the $CMOD^T$ is composed of the elastic displacement (no crack extension, $COMD^e_o$), inelastic displacement (CMOD*) and the elastic displacement due to slow crack growth ($COMD^e_s$). In order to apply LEFM, the inelastic CMOD (CMOD*) should be extracted from the total COMD ($CMOD^T$) at peak load. The total elastic COMD ($COMD^e = COMD^e_o + COMD^e_s$) at peak load is obtained by unloading the specimen at 95% of the peak load. Finding the effective crack length is a point of interest to see the effect of the load on crack length.

3.3.2. Materials and Methods

(a) SENB Test

Single Edge Notched Beams (SENB) (size of S = 9", d = 3" and b = 3") using API class of H oil well cement was used in order to characterize the mode I fracture behavior. Specimens were cured for 28 days under relative humidity above 95% condition.

A clip on Crack Mouth Opening Displacement (CMOD) gauge was used to measure the CMOD. Fig. 3 - 8 shows the schematic diagram of experimental setup with clip on CMOD gauge. Knife edges were glued to the specimen.

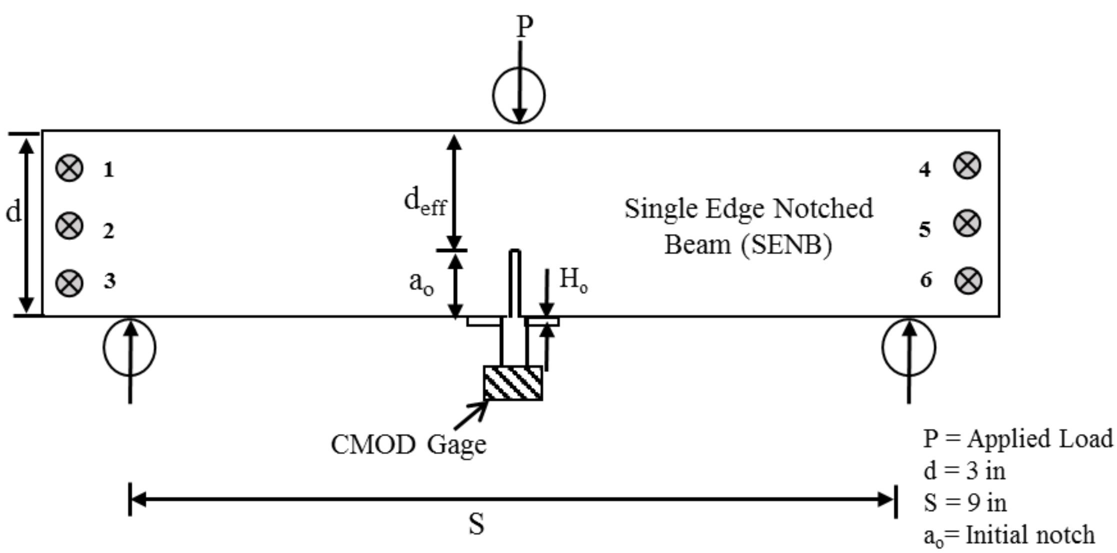

Fig. 3 - 8: Schematic diagram of experimental setup

Further, in order to monitor the crack, a nondestructive method, piezoresistive method was also used. The use of piezoresistive method and the necessity of using smart cement in the piezoresistive measurement are explained.

3.4. Impedance Characterization of Smart Cement

According to literature, researchers have been using two different methods to measure resistance for piezoresistive studies, which are two-probe method and four-probe method. Two-probe method is easy to be adopted in the field while four-probe method has limitations in applications.

The Class H smart cement used in this study was characterized for the above purpose under 20 Hz to 300 kHz .AC current using a LCR meter in order to find out whether the smart cement is general bulk material or special bulk material. Fig. 3 - 9 shows the impedance characterization of smart cement cured for 28 days under relative humidity above 95%.

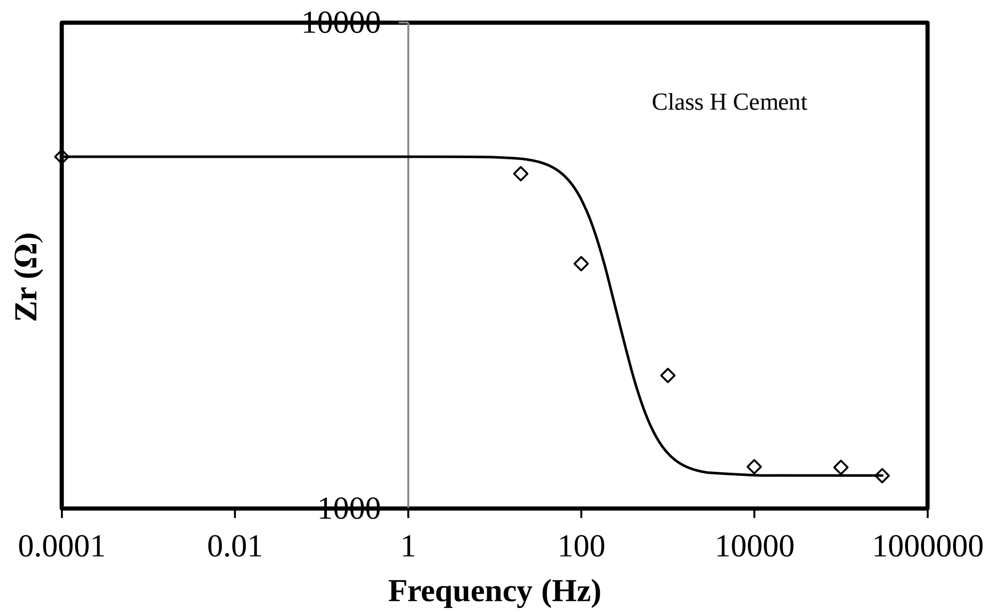

Fig. 3 - 9: Impedance characterization of different classes oil well cement at 28 days of curing

Class H cement tested in this study were characterized as special bulk material (resistance only bulk material). Fig. 3 - 9 compared with Fig. 3 - 5, justifies the use of two probes method for piezoresistivity studies at high frequency of Alternative Current (AC) which eliminates the contact resistance and measures only bulk resistance.

3.5. Summary

Self-sensing smart cement was used in this study with adding a conduct filler which makes the sensing properties much higher than normal cement. The impedance of the smart cement monitored and proved that the two probe measurements works perfectly at high frequency (300 kHz) and the effect of the contact resistance will be minimum. The fracture properties also evaluated in the side of electrical beside mechanical properties of the fracture as the knowledge of the cement crack is a vital task in the oil well cement.

1. Addition of 0.075% conduct filler enhance the piezoresistive sensing ability more than 30 times compared to neat cement and 750 times compared to strain measurement thus making it smart cement.
2. Impedance characterization of smart cements used in this study revealed that conduct filler modified smart cements to be special bulk (resistance only) material which enables the use of two probe method for piezoresistive study.

CHAPTER 4. THREE PHASE REACTIVE MATERIAL MODELING, FRACTURE THEORY AND ELECTRICAL CIRCUITS

4.1. Three Phase Reactive Material Modeling

Three phase (solid (S), liquid (L) and gas (G)) representation is the most general case for all the natural and artificial materials that are commonly used in the field of medicine, science and engineering. Current three phase model are very much focused on the changes in liquid content. In this study, chemically reactive three phase material model with six independent time dependent variables representing the chemical reactions occurring between the solid, liquid and gas in the three phase material. These reactions between the three phases will change the compositions and density of the material.

In order to determine the six independent reactive parameters, theoretically it is essential to have six independent measurements. But in this study the changes in the weight, volume and the moisture content with time and developing correlation between few selected parameters (based on the information available in the literature), the six independent material parameters were quantified. These six independent material parameters were also used to verify the influence on the changes in the physical (shrinkage, porosity) and electrical properties of the materials.

In order to verify the application of the model, cement slurry samples with initial water – to – cement ratio (moisture content) of 0.4 were investigated for over 800 days cured under room condition. Also, the influence of the six material parameters on the volume shrinkage, porosity and electrical resistivity of the solidified cement was quantified.

4.1.1. Reactive Parameters

In this study, the three phases material including gas (G), liquid (L) and solid (S) are interacting over time under varies curing environment (pressure and temperature).

(a) Solid Phase

There will be reaction between the solid phase, liquid phase and gas phase. Due to the reaction, part of the solid phase will become liquid phase and fractional parameter based on weight is represented as "b(t,T,P)". Unreacted fraction of the solid phase will be represented by a fractional parameter "a(t,T,P)" and the remaining fraction of solid phase will be transferred to the gas phase "c(t,T,P)". Hence, the solid parameters relationship is defined as

$$a(t,T,P) + b(t,T,P\ ) + c(t,T,P) = 1\ . \tag{4 - 1}$$

(b) Liquid Phase

Due to another reaction, a portion of the liquid phase will become solidified which the fractional parameter is called "p(t,T,P)". Unreacted fraction of the liquid phase is represented as "q(t,T,P)" and the remaining portion evaporates "r(t,T,P)". Finally, the liquid parameters can be shown as

$$p(t,T,P) + q(t,T,P) + r(t,T,P) = 1. \tag{4 - 2}$$

(c) Gas Phase

Due to two reactions one portion of the gas becomes solid "x(t,T,P)", one portion becomes liquid "y(t,T,P)" and the remaining portion is "z(t,T,P)". The gas parameters represented as

$$x(t,T,P) + y(t,T,P) + z(t,T,P) = 1. \tag{4 - 3}$$

In Fig. 4 - 1 the phase changes and the reactions parameters are shown.

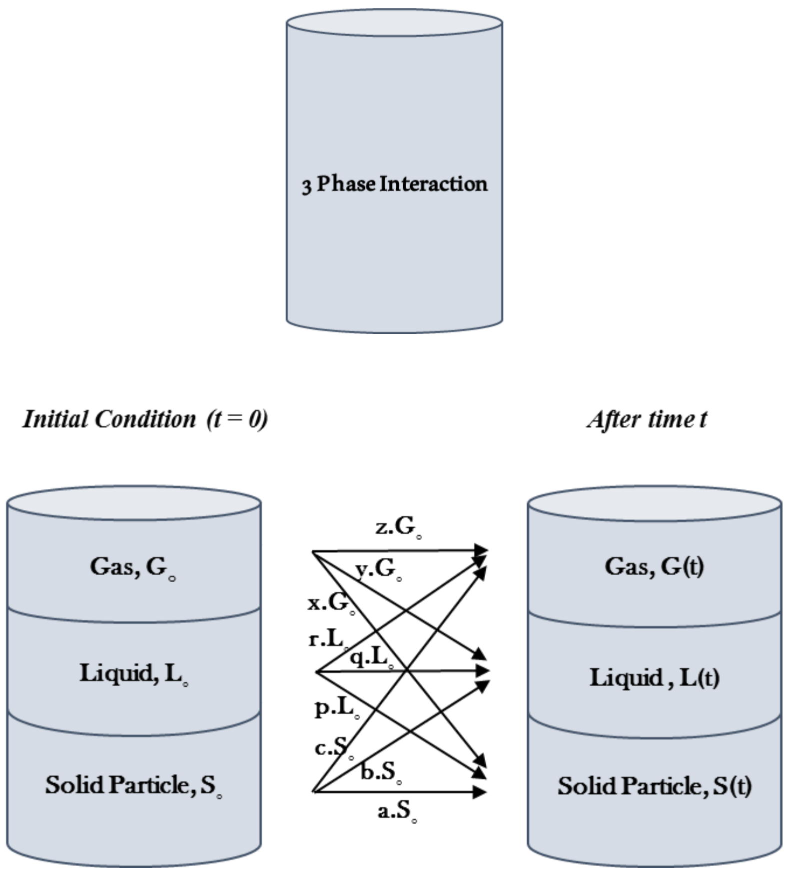

Fig. 4 - 1:Three phase parameters

After curing time t, the weight of the solid particles, $W_S(t,T,P)$**,** the weight of the liquid $W_L(t,T,P)$ and the weight of the air $W_G(t,T,P)$ can be written as portions of W_{S_0}**,** W_{L_0} and W_{G_0}**,** as following:

$$\begin{aligned} W_S(t,T,P) &= a(t,T,P).W_{S_0} + p(t,T,P).W_{L_0} + x(t,T,P).W_{G_0}, \\ W_L(t,T,P) &= b(t,T,P).W_{S_0} + q(t,T,P).W_{L_0} + y(t,T,P).W_{G_0}, \\ W_G(t,T,P) &= c(t,T,P).W_{S_0} + r(t,T,P).W_{L_0} + z(t,T,P).W_{G_0}\,. \end{aligned} \quad \textbf{(4 - 4)}$$

The three phase can be written in a matrix form as

$$\begin{bmatrix} W_S(t,T,P) \\ W_L(t,T,P) \\ W_G(t,T,P) \end{bmatrix} = \begin{bmatrix} a(t,T,P) & p(t,T,P) & x(t,T,P) \\ b(t,T,P) & q(t,T,P) & y(t,T,P) \\ c(t,T,P) & r(t,T,P) & z(t,T,P) \end{bmatrix} . \begin{bmatrix} W_{S_0} \\ W_{L_0} \\ W_{G_0} \end{bmatrix}. \quad \textbf{(4 - 5)}$$

The liquid fraction that becomes part of solid, "p(t,T,P)" and unreacted solid fraction "a(t,T,P)" which forms the solid phase of the material can be correlated using a time dependent parameter "m(t,T,P)" as

$$\frac{p(t,T,P)}{a(t,T,P)} = m(t,T,P). \quad \textbf{(4 - 6)}$$

The solid fraction that becomes part of liquid, "b(t,T,P)" and unreacted liquid fraction "q(t,T,P)" which forms the liquid phase can be correlated using a time dependent parameter "η(t,T,P)" as

$$\frac{b(t,T,P)}{q(t,T,P)} = \eta(t,T,P). \quad \textbf{(4 - 7)}$$

Due to the gas reaction with the liquid, a portion of the gas, "y(t,T,P)" reacts with the liquid can be represented as "ξ(t,T,P)" as

$$\frac{y(t,T,P)}{q(t,T,P)} = \xi(t,T,P). \quad \textbf{(4 - 8)}$$

The other reaction of the gas happens with solid particles, therefore, a part of gas "x(t,T,P)" reacts with solid particles "a(t,T,P)" called as "α(t,T,P)" and represented as

$$\frac{x(t,T,P)}{a(t,T,P)} = \alpha(t,T,P). \quad \textbf{(4 - 9)}$$

Hence, the current weight of the solid phase of the test sample can be represented as follows and by substituting assumptions in Eqs. (4 - 6) and (4 - 9) in the Eq. (4 - 4), which yields

$$W_S(t,T,P) = a(t,T,P).W_{S_0} + m(t,T,P)a(t,T,P).W_{L_0} + \alpha(t,T,P)a(t,T,P).W_{G_0}. \quad \textbf{(4 - 10)}$$

Parameter "a(t,T,P)" can be derived as

$$a(t,T,P) = \frac{W_S(t,T,P)}{W_{S_0} + m(t,T,P).W_{L_0} + \alpha(t,T,P).W_{G_0}}. \quad \textbf{(4 - 11)}$$

by substituting assumptions in Eqs. (4 - 7) and (4 - 8) in the Eq. (4 - 4), which results in

$$W_L(t,T,P) = \eta(t,T,P)q(t,T,P).W_{S_0} + q(t,T,P).W_{L_0} + \xi(t,T,P)q(t,T,P).W_{G_0}. \qquad \textbf{(4 - 12)}$$

Parameter "q(t,T,P)" can be derived as

$$q(t,T,P) = \frac{W_L(t,T,P)}{\eta(t,T,P).W_{S_0} + W_{L_0} + \xi(t,T,P).W_{G_0}}. \qquad \textbf{(4 - 13)}$$

By substituting parameter "a(t)" from Eq. (4 - 11) in Eqs. (4 - 6) and (4 - 9), parameter "p(t)" and "x(t,T,P)" can be found as

$$p(t,T,P) = \frac{m(t,T,P).W_S(t,T,P)}{W_{S_0} + m(t,T,P).W_{L_0} + \alpha(t,T,P).W_{G_0}}. \qquad \textbf{(4 - 14)}$$

And

$$x(t,T,P) = \frac{\alpha(t,T,P).W_S(t,T,P)}{W_{S_0} + m(t,T,P).W_{L_0} + \alpha(t,T,P).W_{G_0}}. \qquad \textbf{(4 - 15)}$$

By substituting parameter "q(t,T,P)" from Eq. (4 - 13) in Eqs. (4 - 7) and (4 - 8), parameter "b(t,T,P)" and "y(t,T,P)" can be found as

$$b(t,T,P) = \frac{\eta(t,T,P).W_L(t,T,P)}{\eta(t,T,P).W_{S_0} + W_{L_0} + \xi(t,T,P).W_{G_0}}. \qquad \textbf{(4 - 16)}$$

And

$$y(t,T,P) = \frac{\xi(t,T,P).W_L(t,T,P)}{\eta(t,T,P).W_{S_0} + W_{L_0} + \xi(t,T,P).W_{G_0}}. \qquad \textbf{(4 - 17)}$$

Using the mass conservation from Eqs (4 - 1), (4 - 2) and (4 - 3) the rest of the parameters can be determined.

By substituting parameter "a(t,T,P)" and "b(t,T,P)", parameter "c(t,T,P)" is defined as

$$c(t,T,P) = 1 - \frac{W_S(t,T,P)}{W_{S_0} + m(t,T,P).W_{L_0} + \alpha(t,T,P).W_{G_0}} - \frac{\eta(t,T,P).W_L(t,T,P)}{\eta(t,T,P).W_{S_0} + W_{L_0} + \xi(t,T,P).W_{G_0}}. \tag{4 - 18}$$

And by substituting parameter "p(t,T,P)" and "q(t,T,P)", parameter "r(t,T,P)" is defined as

$$r(t,T,P) = 1 - \frac{m(t,T,P).W_S(t,T,P)}{W_{S_0} + m(t,T,P).W_{L_0} + \alpha(t,T,P).W_{G_0}} - \frac{W_L(t,T,P)}{\eta(t,T,P).W_{S_0} + W_{L_0} + \xi(t,T,P).W_{G_0}}. \tag{4 - 19}$$

Finally, parameter "z(t,T,P)" is defined as following

$$z(t,T,P) = 1 - \frac{\alpha(t,T,P).W_S(t,T,P)}{W_{S_0} + m(t,T,P).W_{L_0} + \alpha(t,T,P).W_{G_0}} - \frac{\xi(t,T,P).W_L(t,T,P)}{\eta(t,T,P).W_{S_0} + W_{L_0} + \xi(t,T,P).W_{G_0}}. \tag{4 - 20}$$

In the case, the gas weight is neglected the parameter "α(t,T,P)" and "ξ(t,T,P)" will be zero as well as "x(t,T,P)", "y(t,T,P)" and "z(t,T,P)". Therefore, the solid particles' weight will be

$$W_S(t,T,P) = \frac{W(t,T,P)}{1 + \beta(t,T,P)}. \tag{4 - 21}$$

and the weight of the liquid can be derived as shown as

$$W_L(t,T,P) = \frac{\beta(t,T,P)}{1 + \beta(t,T,P)} W(t,T,P). \tag{4 - 22}$$

By having changes in volume and the initial volume we are able to find the amount of shrinkage, the ratio of changes in volume to the initial volume (shrinkage, "$s(t,T,P)$") can be expressed as a

$$s(t,T,P) = \frac{\Delta V(t,T,P)}{V_0} = \frac{V_0 - V(t,T,P)}{V_0}. \tag{4 - 23}$$

4.1.2. Experimental Verification: Case 1, Cement Slurry

The total weight (W), total volume (V) and moisture content (β) variation with aging (time) and curing environment (pressure and temperature) are the three measurements made in this study with solidifying cement-water mix. The total weight of sample at the initial and each stage is known while the solid weight ($W_S(t,T,P)$) and liquid weight ($W_L(t,T,P)$) are unknown any time t. Note that the weight and volume of the solid particles (W_{S_0}, V_{S_0}) and liquid (W_{L_0}, V_{L_0}) represents the initial stage. The total weight of the sample at time t includes liquid, gas and solid phases and represented as

$$W(t,T,P) = W_S(t,T,P) + W_L(t,T,P) + W_G(t,T,P). \quad \textbf{(4 - 24)}$$

Heating liquid and gas content the material to over 100°C for 24 hours will result in weight change caused by the loss in $W_L(t,T,P)$ and $W_G(t,T,P)$, hence the fluid content can be represented as the ratio between the liquid with gad and solid content. Therefore, using a total weight of sample W and change in weight ΔW, performing an experiment parameter $\beta(t,T,P)$ can be determined by

$$\beta(t,T,P) = \frac{W_L(t,T,P) + W_G(t,T,P)}{W_S(t,T,P)} \quad \textbf{(4 - 25)}$$

Hence, by measuring the total weight $W_2(t)$ and the fluid content, the weight of the solids $W_{s_2}(t)$, can be determined as

$$W_S(t,T,P) = \frac{W(t,T,P)}{1 + \beta(t,T,P)}. \quad \textbf{(4 - 26)}$$

Also the total fluid content can be determined as

$$W_L(t,T,P) + W_G(t,T,P) = \frac{\beta(t,T,P)}{1 + \beta(t,T,P)} W(t,T,P) \quad \textbf{(4 - 27)}$$

Table 4 - 1 shows the summery of the variables for three phase transition (Fig. 4 - 1).

Table 4 - 1: Three phase transition parameters

Variables	Variables (Case of Non-Reactive Gas)
$a(t,T,P)=\frac{W_S(t,T,P)}{W_{S_0}+m(t,T,P).W_{L_0}+\alpha(t,T,P).W_{G_0}}$	$a(t,T,P)=\frac{W_S(t,T,P)}{W_{S_0}+m(t,T,P).W_{L_0}}$
$b(t,T,P)=\frac{\eta(t,T,P).W_L(t,T,P)}{\eta(t,T,P).W_{S_0}+W_{L_0}+\xi(t,T,P).W_{G_0}}$	$b(t,T,P)=\frac{\eta(t,T,P).W_L(t,T,P)}{\eta(t,T,P).W_{S_0}+W_{L_0}}$
$c(t,T,P)=1-\frac{W_S(t,T,P)}{W_{S_0}+m(t,T,P).W_{L_0}+\alpha(t,T,P).W_{G_0}}-\frac{\eta(t,T,P).W_L(t,T,P)}{\eta(t,T,P).W_{S_0}+W_{L_0}+\xi(t,T,P).W_{G_0}}$	$c(t,T,P)=1-\frac{W_S(t,T,P)}{W_{S_0}+m(t,T,P).W_{L_0}}-\frac{\eta(t,T,P).W_L(t,T,P)}{\eta(t,T,P).W_{S_0}+W_{L_0}}$
$p(t,T,P)=\frac{m(t,T,P).W_S(t,T,P)}{W_{S_0}+m(t,T,P).W_{L_0}+\alpha(t,T,P).W_{G_0}}$	$p(t,T,P)=\frac{m(t,T,P).W_S(t,T,P)}{W_{S_0}+m(t,T,P).W_{L_0}}$
$q(t,T,P)=\frac{W_L(t,T,P)}{\eta(t,T,P).W_{S_0}+W_{L_0}+\xi(t,T,P).W_{G_0}}$	$q(t,T,P)=\frac{W_L(t,T,P)}{\eta(t,T,P).W_{S_0}+W_{L_0}}$
$r(t,T,P)=1-\frac{m(t,T,P).W_S(t,T,P)}{W_{S_0}+m(t,T,P).W_{L_0}+\alpha(t,T,P).W_{G_0}}-\frac{W_L(t,T,P)}{\eta(t,T,P).W_{S_0}+W_{L_0}+\xi(t,T,P).W_{G_0}}$	$r(t,T,P)=1-\frac{m(t,T,P).W_S(t,T,P)}{W_{S_0}+m(t,T,P).W_{L_0}}-\frac{W_L(t,T,P)}{\eta(t,T,P).W_{S_0}+W_{L_0}}$
$x(t,T,P)=\frac{\alpha(t,T,P).W_S(t,T,P)}{W_{S_0}+m(t,T,P).W_{L_0}+\alpha(t,T,P).W_{G_0}}$	$x(t,T,P)=\frac{\alpha(t,T,P).W_S(t,T,P)}{W_{S_0}+m(t,T,P).W_{L_0}}$
$y(t,T,P)=\frac{\xi(t,T,P).W_L(t,T,P)}{\eta(t,T,P).W_{S_0}+W_{L_0}+\xi(t,T,P).W_{G_0}}$	$y(t,T,P)=\frac{\xi(t,T,P).W_L(t,T,P)}{\eta(t,T,P).W_{S_0}+W_{L_0}}$
$z(t,T,P)=1-\frac{\alpha(t,T,P).W_S(t,T,P)}{W_{S_0}+m(t,T,P).W_{L_0}+\alpha(t,T,P).W_{G_0}}-\frac{\xi(t,T,P).W_L(t,T,P)}{\eta(t,T,P).W_{S_0}+W_{L_0}+\xi(t,T,P).W_{G_0}}$	$z(t,T,P)=1-\frac{\alpha(t,T,P).W_S(t,T,P)}{W_{S_0}+m(t,T,P).W_{L_0}}-\frac{\xi(t,T,P).W_L(t,T,P)}{\eta(t,T,P).W_{S_0}+W_{L_0}}$
$s(t,T,P)=\frac{V_0-V(t,T,P)}{V_0}$	$s(t,T,P)=\frac{V_0-V(t,T,P)}{V_0}$
$W_S(t,T,P)=\frac{W(t,T,P)}{1+\beta(t,T,P)}$	$W_S(t,T,P)=\frac{W(t,T,P)}{1+\beta(t,T,P)}$
$W_L(t,T,P)+W_G(t,T,P)=\frac{\beta(t,T,P)}{1+\beta(t,T,P)}W(t,T,P)$	$W_L(t,T,P)=\frac{\beta(t,T,P)}{1+\beta(t,T,P)}W(t,T,P)$

4.1.3. Measurements Results

The weight, volume and the moisture content was the three measurements done in this study in order to find the transition between the three phases. Cement with w/c = 0.4 was used and monitored during curing time and the properties were analyzed to track the transition between the phases. Fig. 4 - 2 shows the weight of the samples during the curing time of sample under room temperature and pressure which are constants. The changes are modeled by hyperbolic equation as a function of time based on second thermodynamic law. The weight decreased up to 6.5% during the curing of the cement. Fig. 4 - 3 captures the changes in volume versus time.

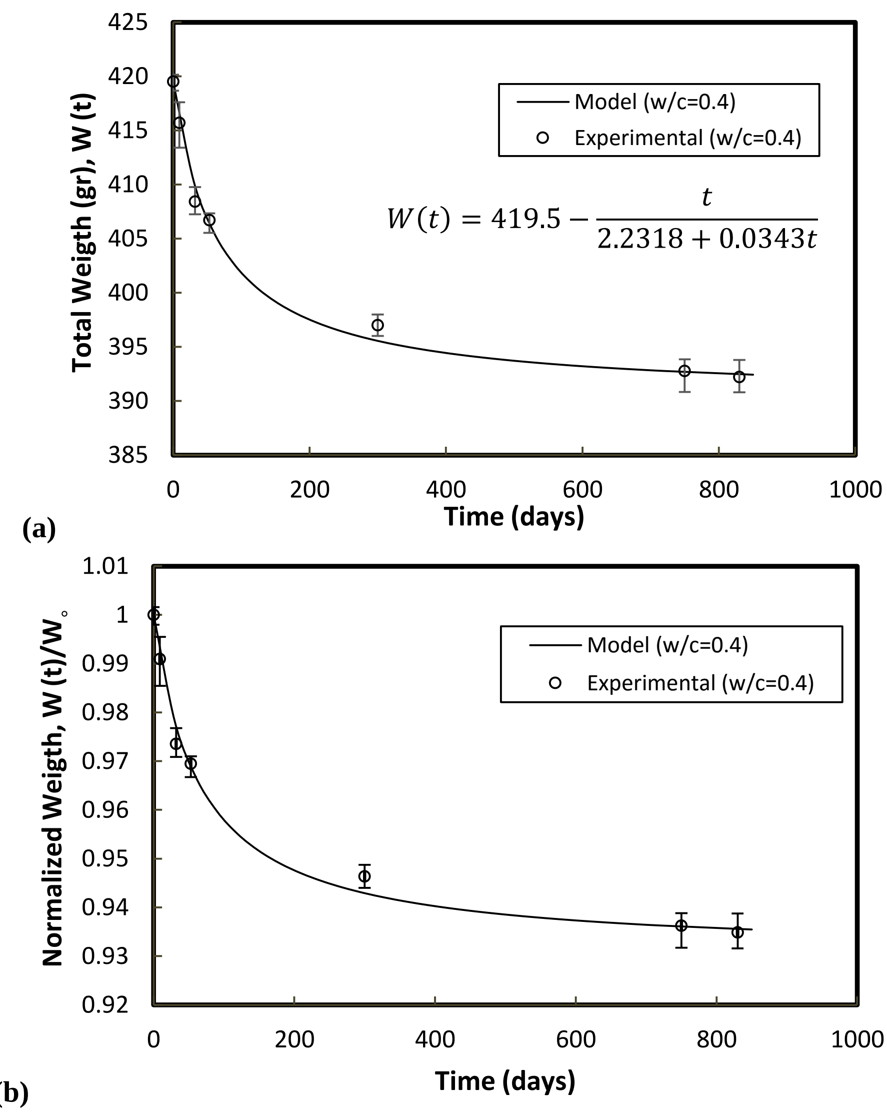

Fig. 4 - 2: Weight change during curing time of 830 days; (a) Total weight, (b) Normalized weight

The volume change is modeled by hyperbolic equation as shown in Fig. 4 - 3. The volume decreased about 16.6% during the curing time. therefore, the rate of the change of volume is more than the weight loss.

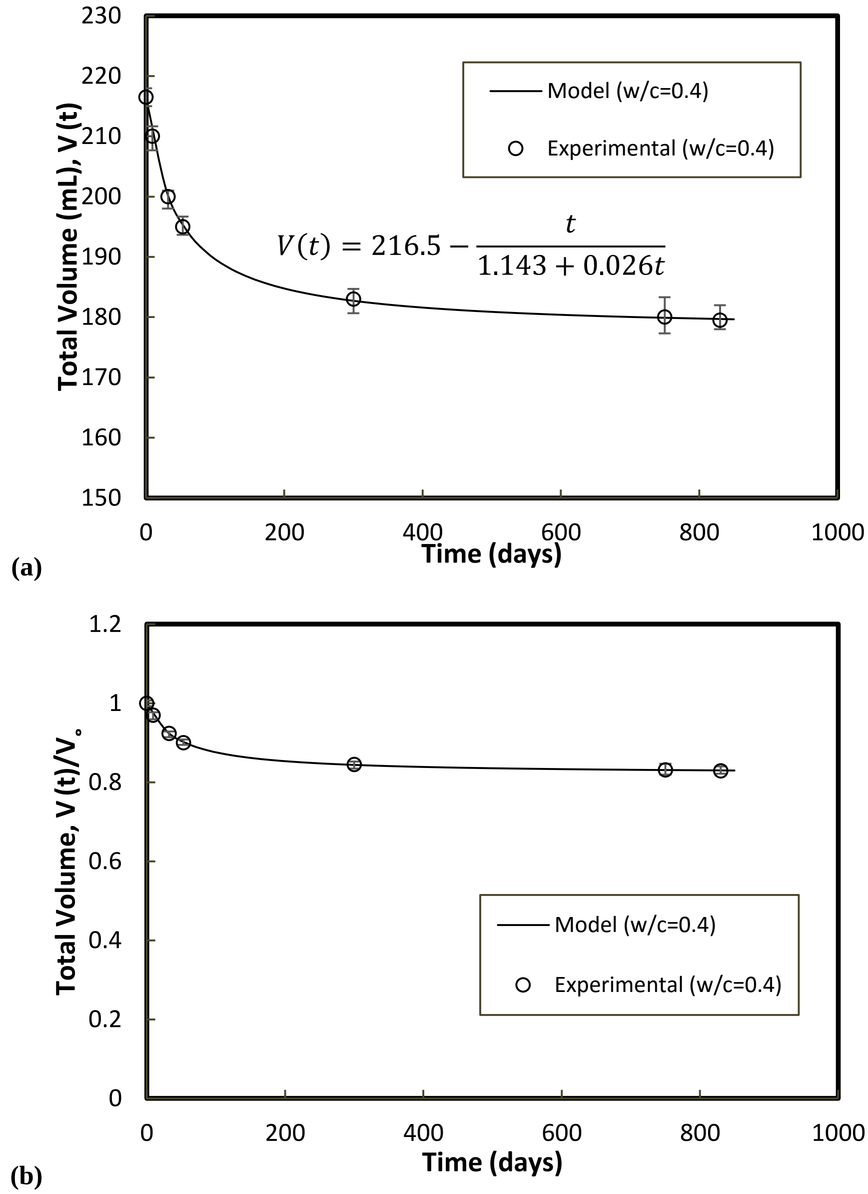

Fig. 4 - 3: Volume change during curing time of 830 days;
(a) Total volume, (b) Normalized volume

Fig. 4 - 4 shows the changes in moisture content of the cement (w/c=0.4). During the curing time, the moisture content decreased about 77.5 %.

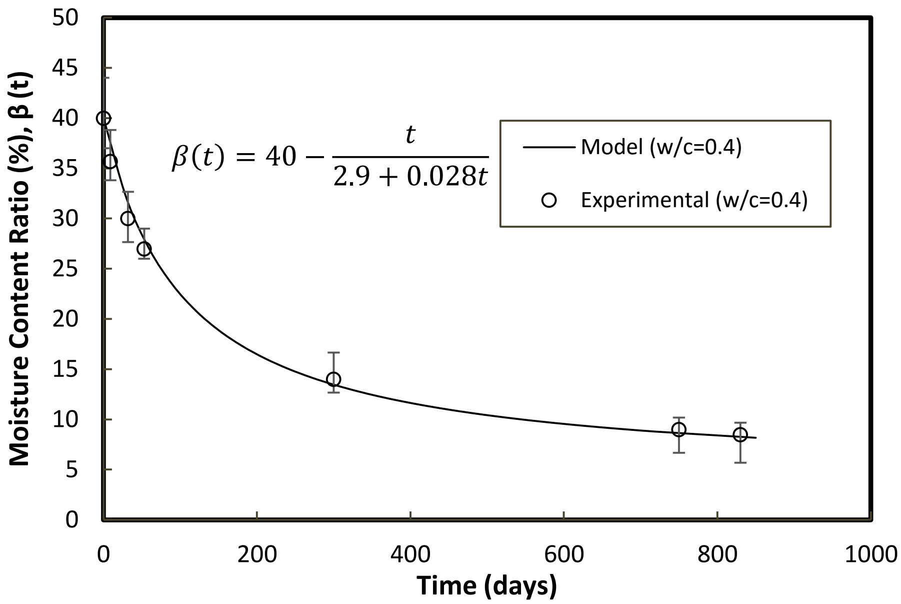

(a)

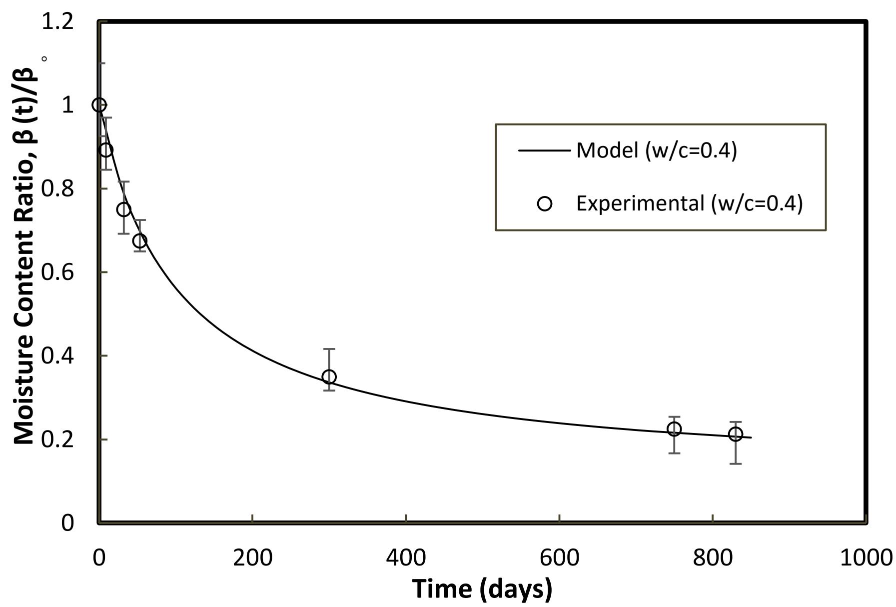

(b)

Fig. 4 - 4: Moisture content change during curing time of 830 days; (a) Total moisture content, (b) Normalized moisture content

According to Eq. (4 - 26), due to moisture content and weight of the cement the weight of solid particles is increasing during the curing time of the cement. The final solid phase increase about 20% (Fig. 4 - 5).

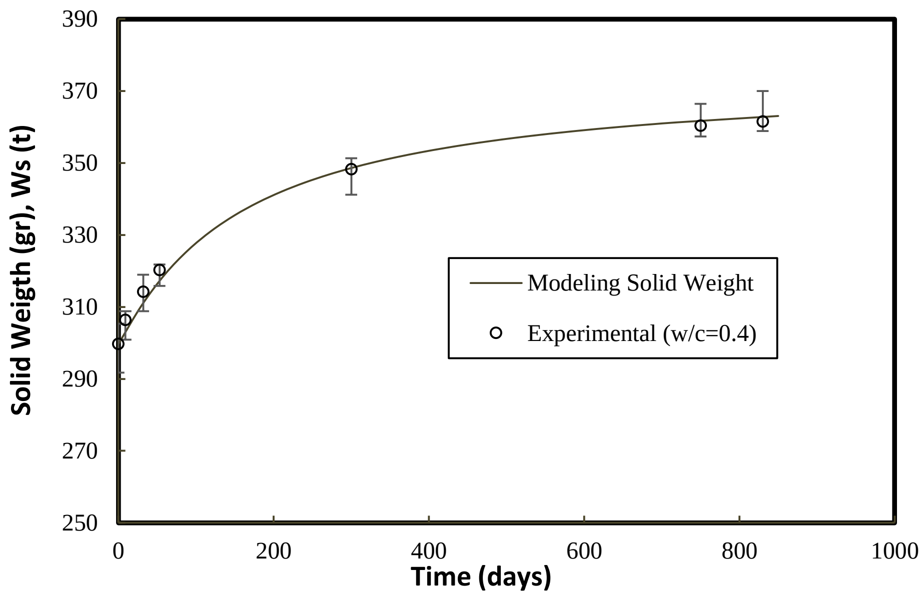

(a)

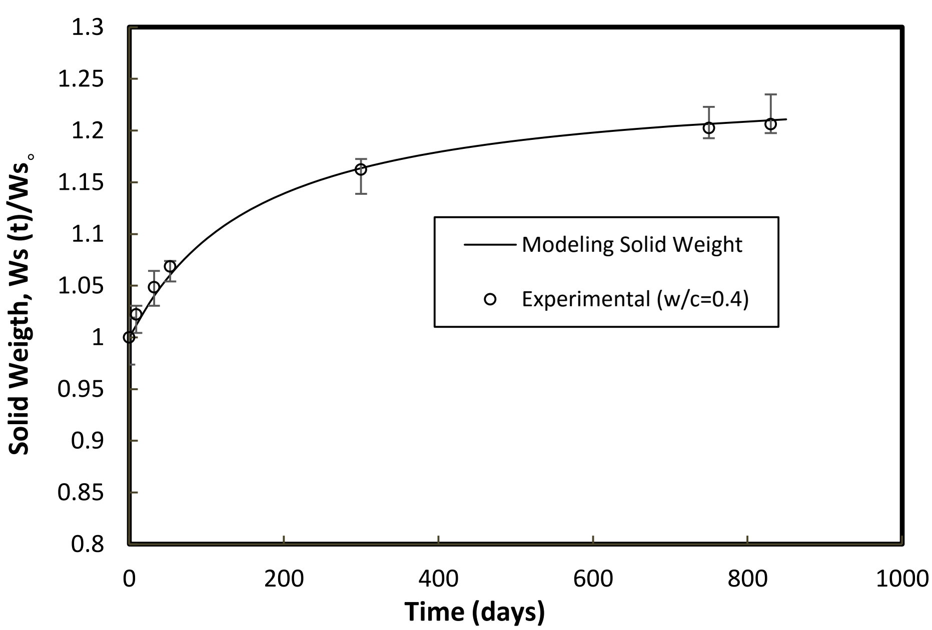

(b)

Fig. 4 - 5: Solid weight change during curing time of 830 days;
(a) Total solid weight, (b) Normalized solid weight

As shown in Eq. (4 - 27), the weight of liquid is decreasing during the curing time of the cement. The liquid weight decreased about 34% (Fig. 4 - 6).

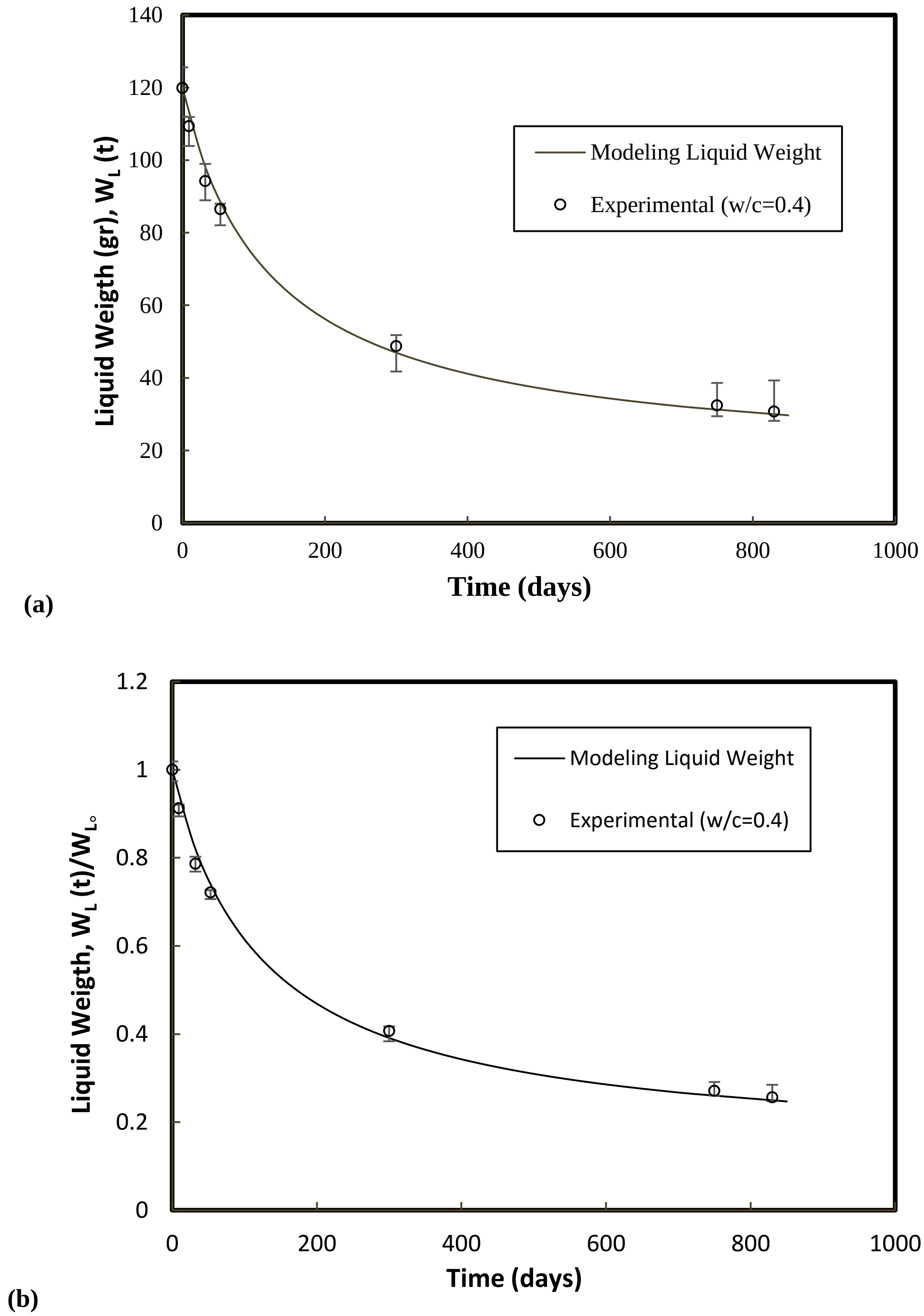

Fig. 4 - 6: Water weight change during curing time of 830 days; (a) Total liquid weight, (b) Normalized liquid weight

4.1.4. Chemical Reaction

(i) Parameter a(t) and p(t)

Now we are looking for the parameters "m(t)" and "η(t)". The reaction of the liquid inside solid particles "a(t)" which makes the solid gel "p(t)"is shown with parameter "m(t)". Parameter "a(t)" can be derived from Eq.(4 - 28). the solid particle weight initially and later "W_{S_0}" and "$W_S(t)$" are known as well as liquid weight "W_{L_0}" and by assigning numbers from 0 to 1 to "p(t)", the parameter "a(t)" can be calculated by

$$a(t) = \frac{W_S(t) - p(t).W_{L_0}}{W_{S_0}}. \qquad \textbf{(4 - 28)}$$

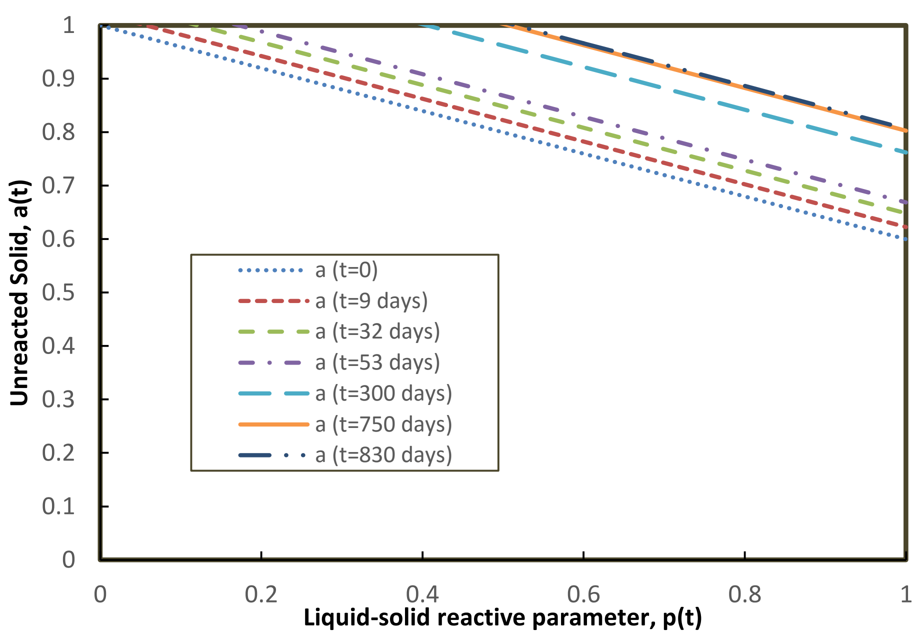

Fig. 4 - 7: Variation of parameter a(t) versus p(t)

Initially, $a_\circ$ will be equal to 1 and will decrease with time. Parameter "a(t)" can be estimated using the proposed equation as

$$a(t) = 1 - \frac{p(t)}{A + B.p(t)}. \qquad \textbf{(4 - 29)}$$

The constant values of A and B can be estimated by the limits of a(t) and p(t) which can only vary between 0 and 1. Based on the Eq. (4 - 29), the boundaries of A+B captures in the Fig. 4 - 8. Therefore, according to Eq. (4 - 28) and the solid particle weight "$W_{S_2}(t)$" which has the ascending order lead the parameter "a(t)" intersect with the line A+B > 1.

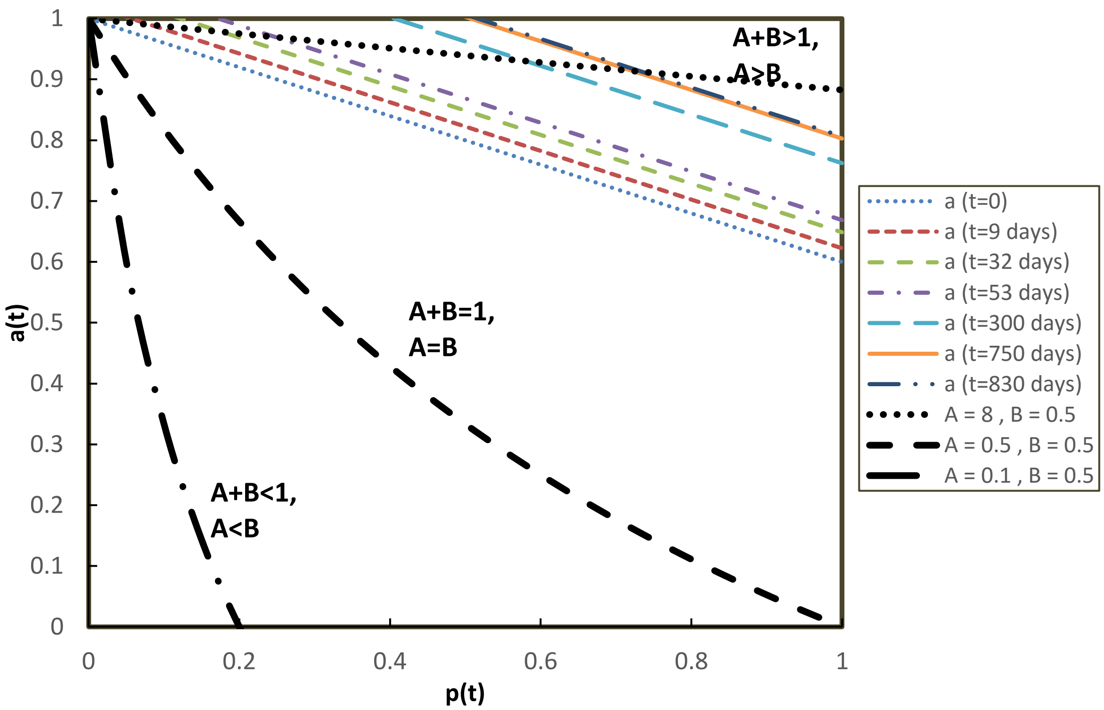

Fig. 4 - 8: Variation of parameter a(t) versus p(t) and capturing A and B constants

The A and B should be selected while a(t) from Eq. (4 - 29) intersect with all the lines at different time from the measurements. After finding the intersection, the p(t) values can be found at different time and by substituting "p(t)" values in Eq. (4 - 29), a(t) parameter can be found and using Eq. (4 - 6) the reaction "m(t)" can be calculated.

Table 4 - 2: Estimation of the reaction of the liquid into solid particles

Time (days)	p(t)	a(t)	m(t)
0	0	1	0
9	0.08	0.990	0.081
32	0.18	0.978	0.184
53	0.26	0.969	0.269
300	0.58	0.930	0.624
750	0.72	0.914	0.788
830	0.73	0.913	0.800

Therefore, "m(t)" the reaction of the liquid inside solid particles "a(t)" which produces the solid gel "p(t)" is estimated as

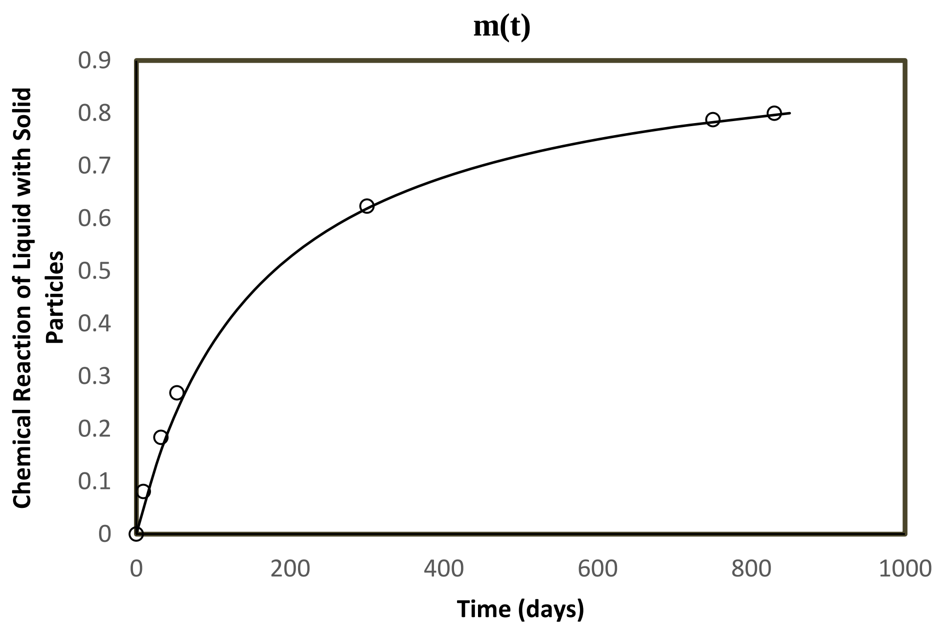

Fig. 4 - 9: Chemical reaction of the liquid inside solid particles

(ii) Parameter b(t) and q(t)

The other reaction called "η(t)" from the solid particles inside the liquid "q(t)" which makes liquid gel "b(t)". Parameter "q(t)" can be derived from Eq. (4 - 4). the solid particle weight initially and later "W_{S_0}" and "$W_L(t)$" are known as well as liquid weight "W_{L_0}" and by assigning numbers from 0 to 1 to "b(t)", the parameter "q(t)" can be found from

$$q(t) = \frac{W_L(t) - b(t).W_{S_0}}{W_{L_0}}. \tag{4 - 30}$$

The parameter "q(t)" can be estimated as

$$q(t) = 1 - \frac{b(t)}{C + D.b(t)}. \tag{4 - 31}$$

Where C and D are constants. The values of C and D can be estimated by the limits of b(t) and q(t) which can only vary between 0 and 1. Based on the Eq. (4 - 31), the boundaries of C+D captures in the Fig. 4 - 11. Therefore, according to Eq. (4 - 31) and the liquid weight "$W_L(t)$" which has the descending order lead the parameter "q(t)" intersect with the line C+D < 1.

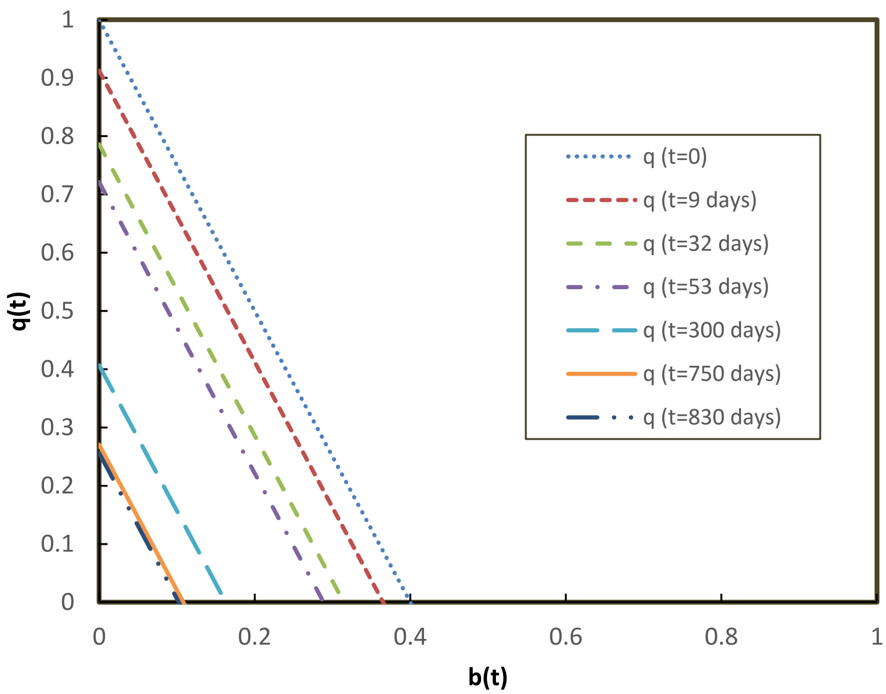

Fig. 4 - 10: Variation of parameter q(t) versus b(t)

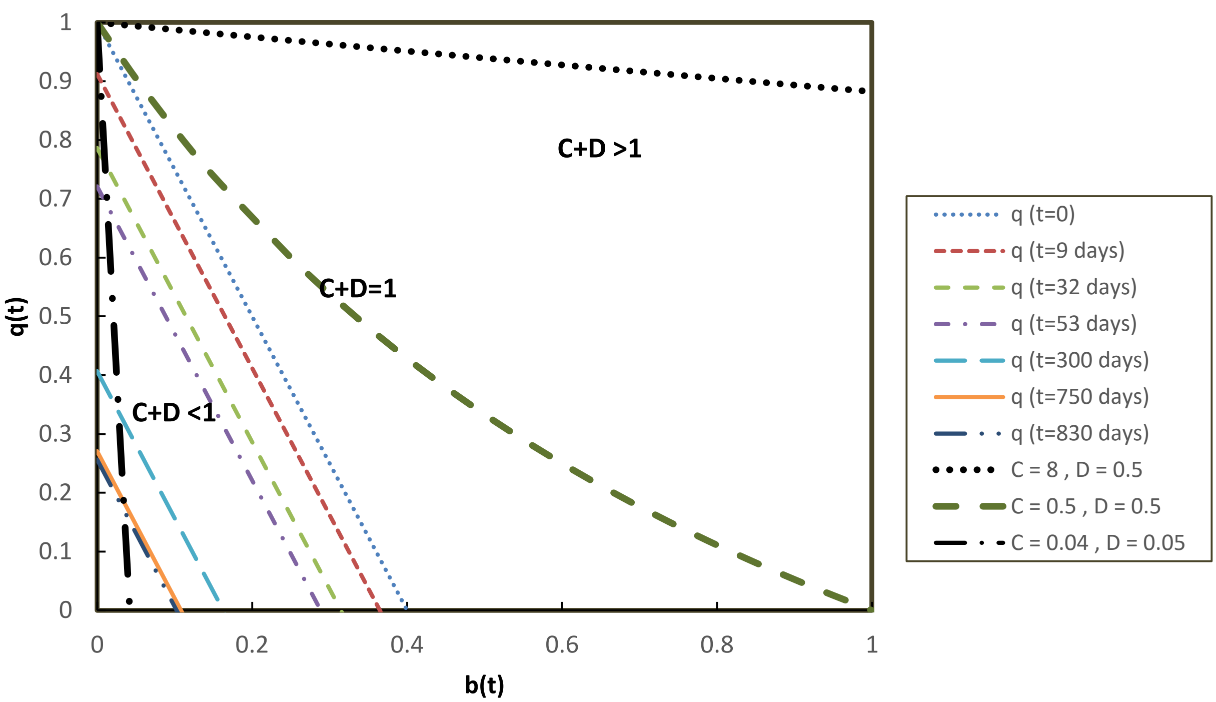

Fig. 4 - 11: Variation of parameter q(t) versus b(t) and capturing C and D constants

The C and D should be selected in such a way that "a(t)" from Eq. (4 - 31) intersect with all the lines at different time from the measurements. After finding the intersection, the b(t) values can be found at different time and by substituting b(t) values in Eq. (4 - 31), q(t) parameter can be found and using Eq. (4 - 7), the reaction "m(t)" can be calculated.

Table 4 - 3: Estimation of the reaction of the solid particles into liquid

Time (days)	b (t)	q (t)	η (t)
0	0	1	0
9	0.003	0.925	0.003
32	0.01	0.753	0.013
53	0.013	0.680	0.019
300	0.029	0.300	0.097
750	0.035	0.162	0.216
830	0.0352	0.157	0.224

Therefore, “η(t)” the reaction of the solid particles inside the liquid “q(t)” which produces the liquid gel “b(t)” is estimated as

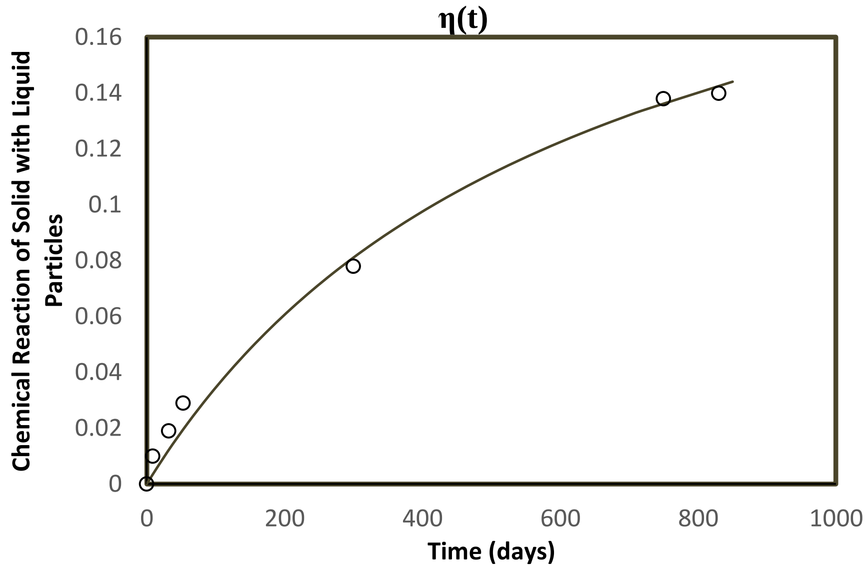

Fig. 4 - 12: Chemical reaction of solid particles with liquid

4.1.5. Reactive Parameter Analysis

The part of the liquid transfers to the solid particles “$p(t)$” of cement (w/c=0.4), called solid gel, in 830 days of curing increased by 70% (Fig. 4 - 13).

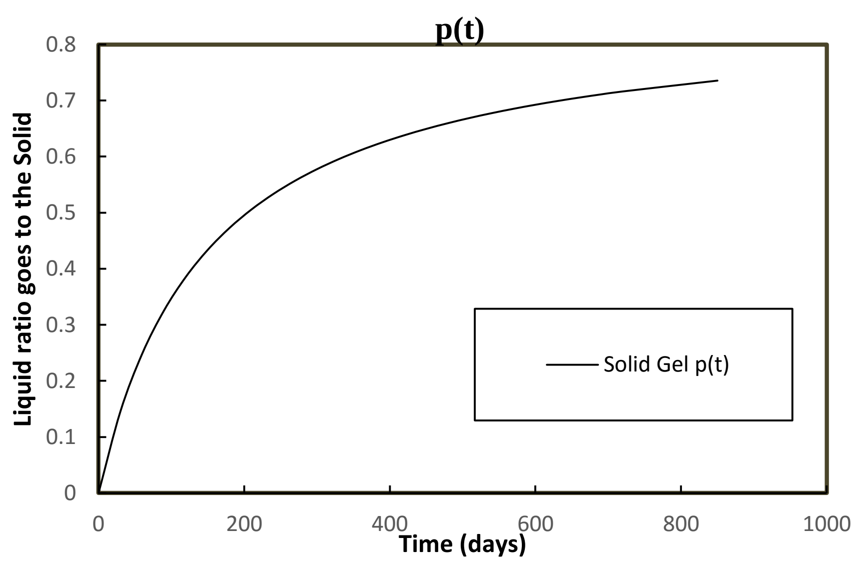

Fig. 4 - 13: Solid gel of cement (w/c=0.4), chemically in 830 days of curing

Fig. 4 - 14 shows the part of the liquid remains liquid in the cement "$q(t)$" decreased about 80%.

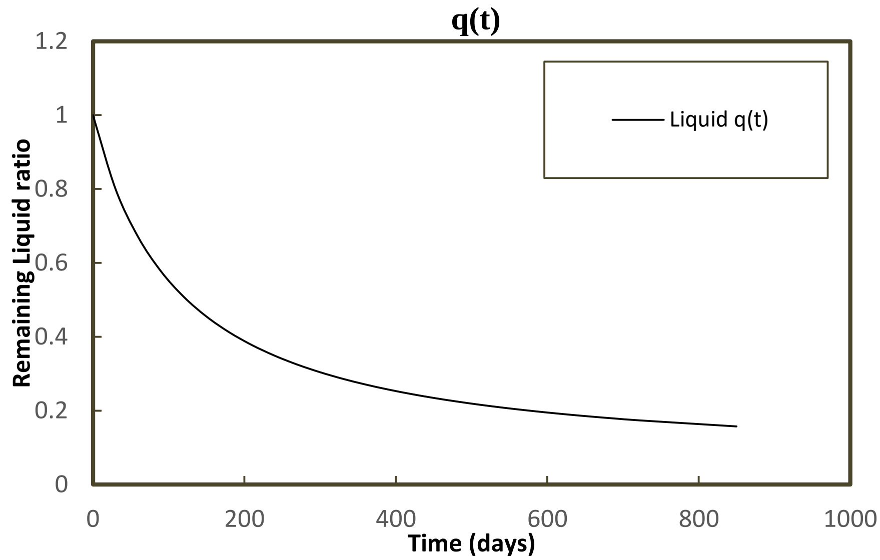

Fig. 4 - 14: Part of the liquid remains liquid in the cement (w/c=0.4) in 830 days of curing

The parameter "r(t)" which is the evaporation can be calculated from the model shown in Eq. (4 - 19). Evaporation was about 10% in the analysis (Fig. 4 - 15).

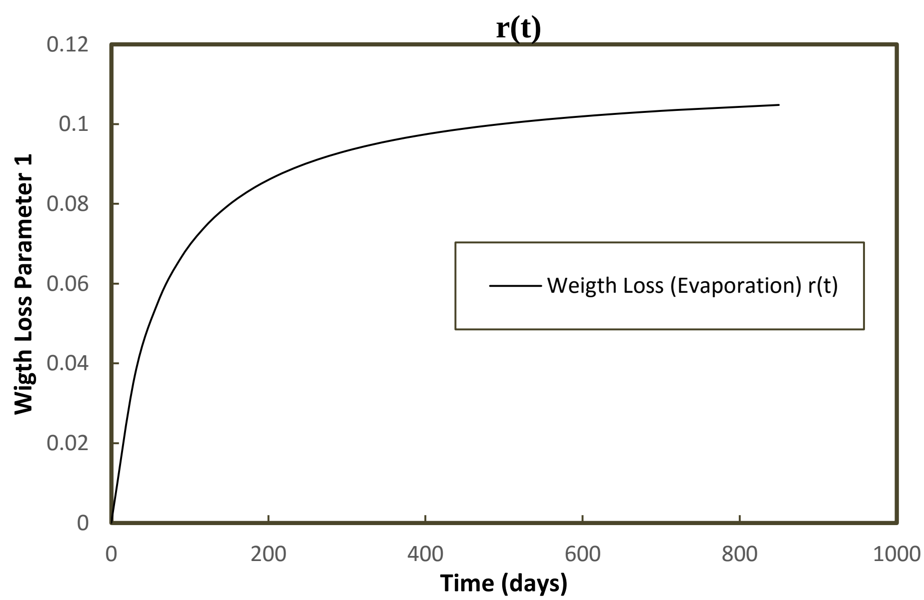

Fig. 4 - 15: Evaporation during 830 days of curing

Fig. 4 - 17 shows the part of the solid particle reacts with the liquid (solid gel) in the cement "$b(t)$" increased about 3.5% and the solid particle remains in the solid part "$a(t)$" of cement (w/c=0.4), chemically in 830 days of curing decreased by 8% (Fig. 4 - 16) in 830 days of curing.

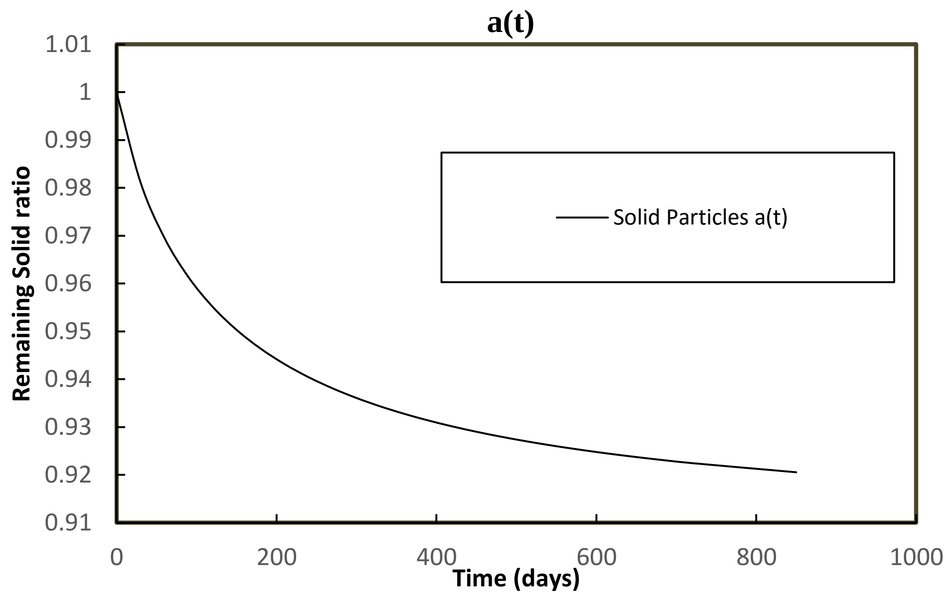

Fig. 4 - 16: Part of the solid particle remains in the solid part of cement (w/c=0.4) in 830 days of curing.

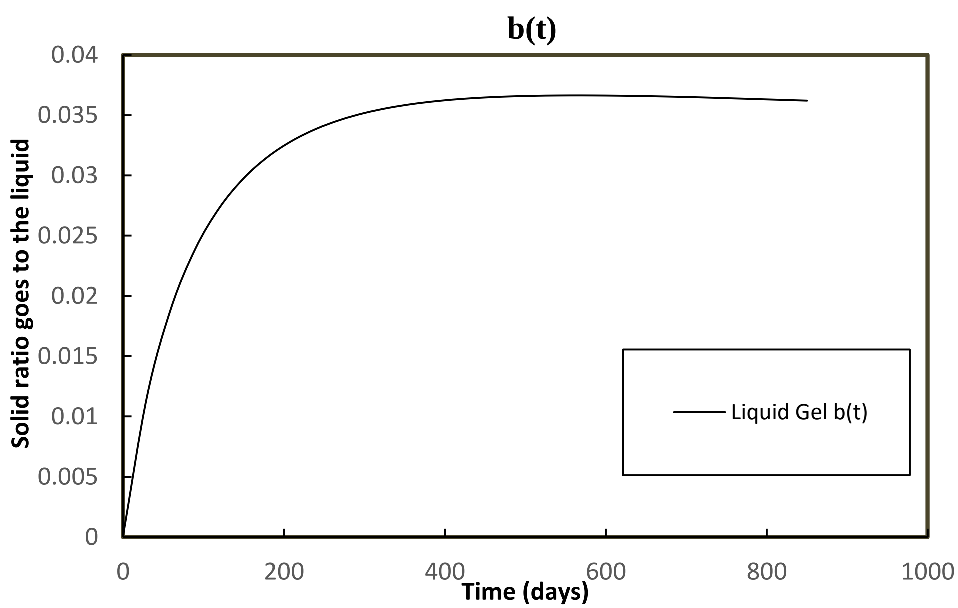

Fig. 4 - 17: Liquid gel in the cement (w/c=0.4) in 830 days of curing

The sublimation which is called weigh loss parameter 2, "c(t)" can be calculated from the model shown in Eq. (4 - 18). Sublimation from the model was about 4.5% in the analysis (Fig. 4 - 18).

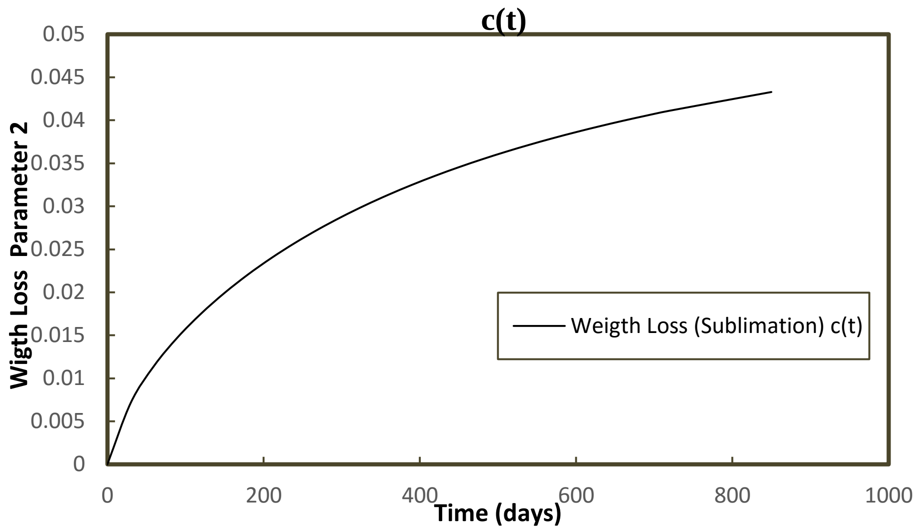

Fig. 4 - 18: Sublimation during 830 days of curing

Fig. 4 - 19 shows the volume shrinkage "$s(t)$" increased by 18% in 830 days of curing.

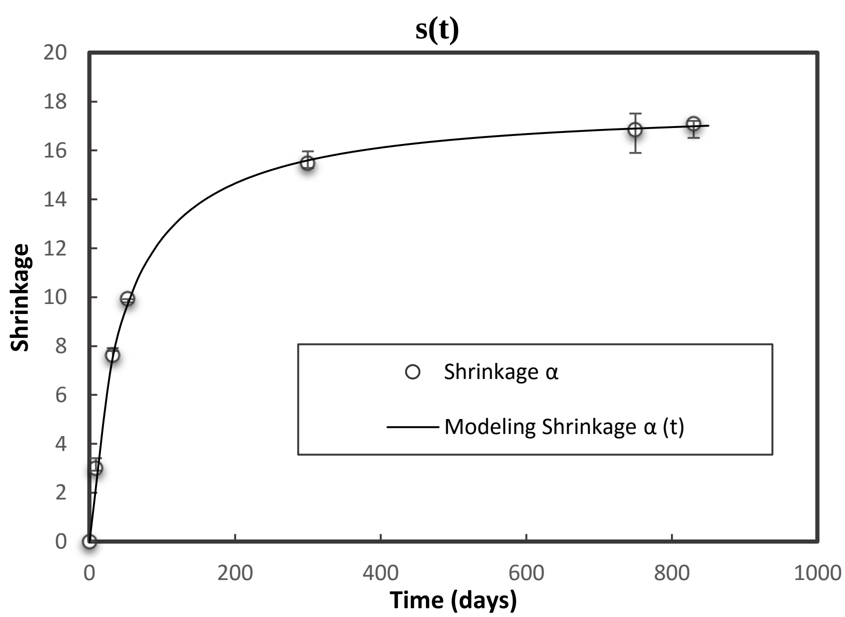

Fig. 4 - 19: Shrinkage of the cement (w/c=0.4) in 830 days of curing

4.1.6. Specific Weight and Porosity

There are two factors affecting specific weigh of the cement, shrinkage and weight loss. Shrinkage increases the specific weight while the weight loss decreases it. This study shows the specific weight of the cement increased during curing. Fig. 4 - 20, expresses the specific weight of cement (w/c=0.4) in 830 days of curing increased by 13%. According to total weight and volume of the sample, the specific weight during the time is

$$\gamma(t) = \frac{W(t)}{V(t)} = \frac{W_0 - r(t)W_{L_0} - c(t)W_{S_0}}{\big(1 - s(t)\big)V_0}. \tag{4 - 32}$$

The specific weight of the solid particles is defined as

$$\gamma_S(t) = \frac{W_S(t)}{V_S(t)} = \frac{a(t).W_{S_0} + p(t).W_{L_0}}{V_S(t)}. \tag{4 - 33}$$

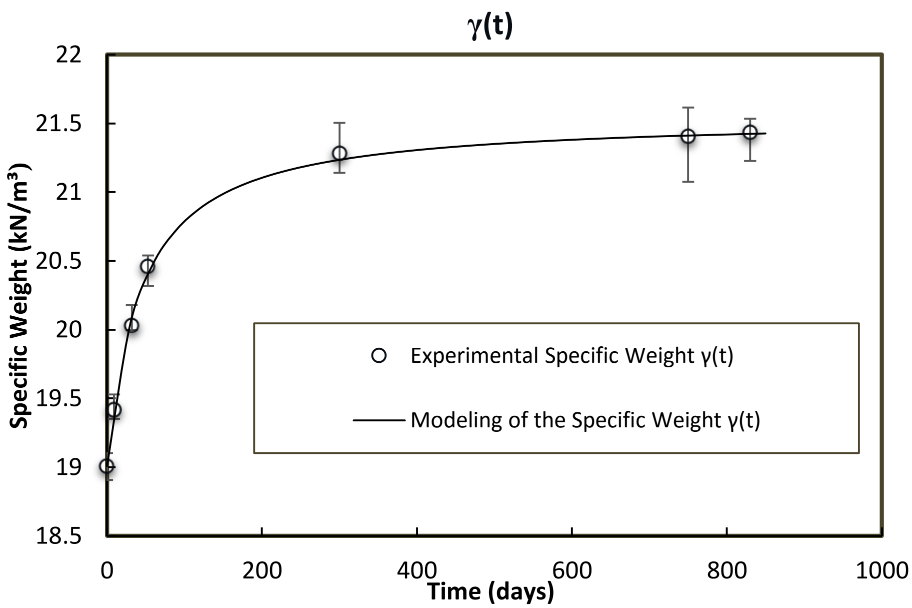

Fig. 4 - 20: Specific weight of the cement (w/c=0.4) in 830 days of curing

Therefore, by making an assumption for solid particles specific weight γ_S which has a limit values including the upper bound γ_{S_0} and lower bound of γ_w, the solid particle volume $V_S(t)$ can be found using Eq. (4 - 33). Four assumptions were made for solid particles specific weight γ_S, three of the assumptions are constant values (2, 2.5 and 3.1 gr/mL) The assumption with γ_S= 2 gr/mL is not acceptable because the calculated volume exceeded the total volume. The other assumption is $\gamma_S = \gamma_{S_0}$ = 3.1 gr/mL which is the upper bound. The last assumption is solid particles specific weight γ_{S_2}(t) which is a time dependent value which more close to the reality starting from γ_{S_0} = 3.1 gr/mL and ends up with 2.5 gr/mL (Fig. 4 - 22).

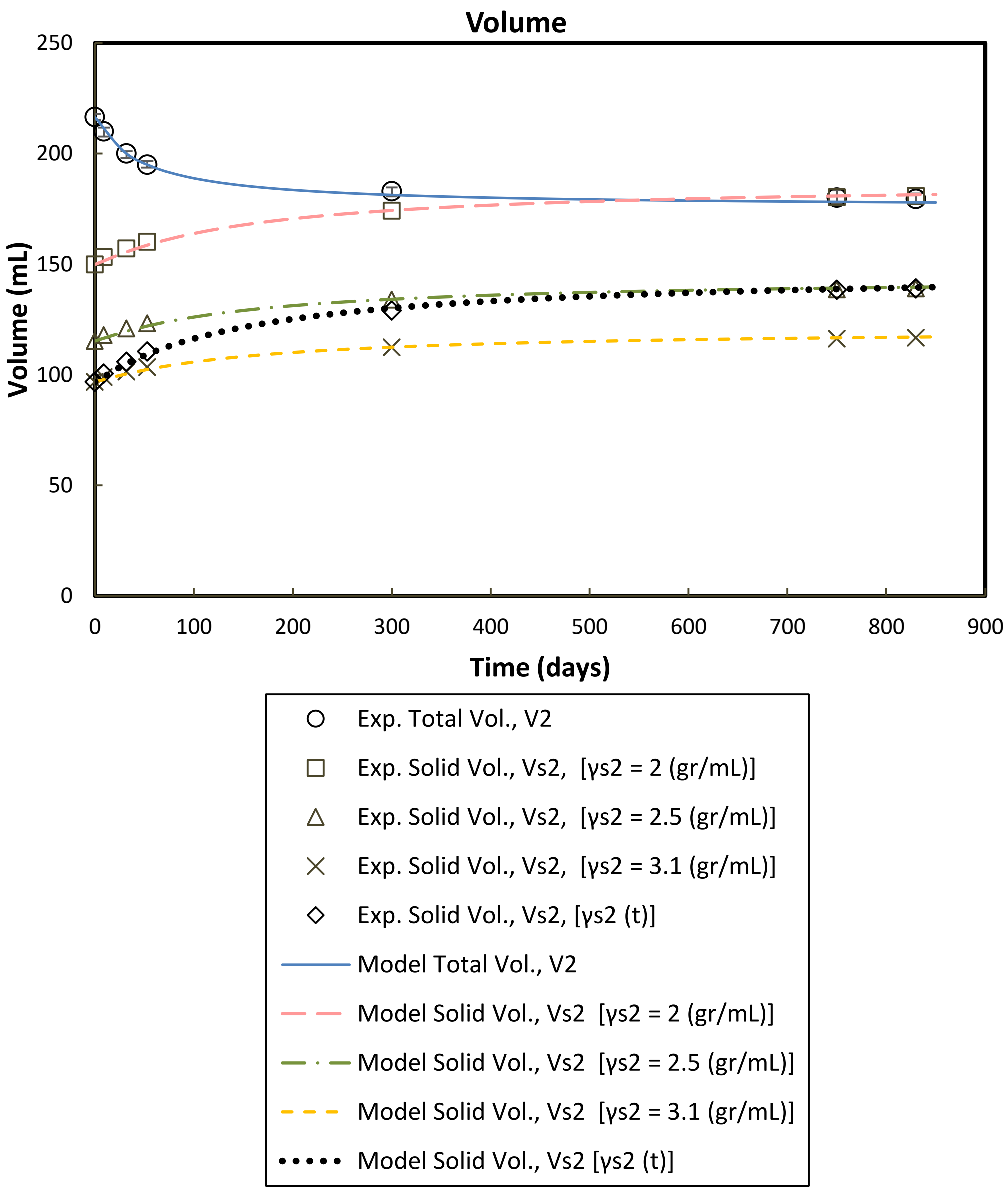

Fig. 4 - 21: Total volume and volume of the solid particles for cement (w/c=0.4) in 830 days of curing

After finding the solid particle volume $V_S(t)$, the porosity can be evaluated as

$$n(t) = 1 - \frac{V_S(t)}{V(t)}. \tag{4 - 34}$$

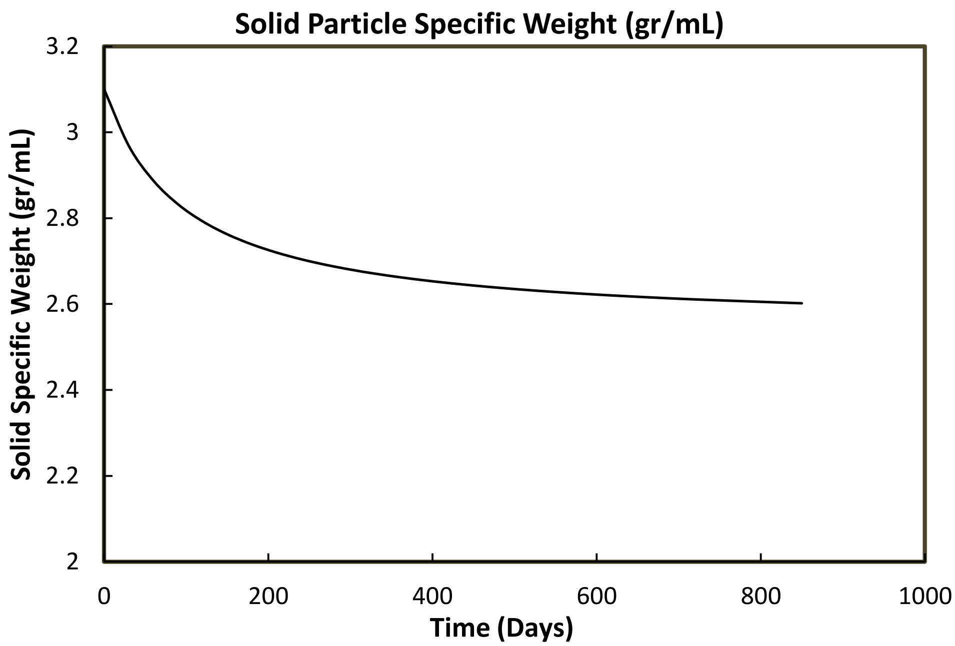

Fig. 4 - 22: Solid particle specific weight of the cement (w/c=0.4) in 830 days of curing

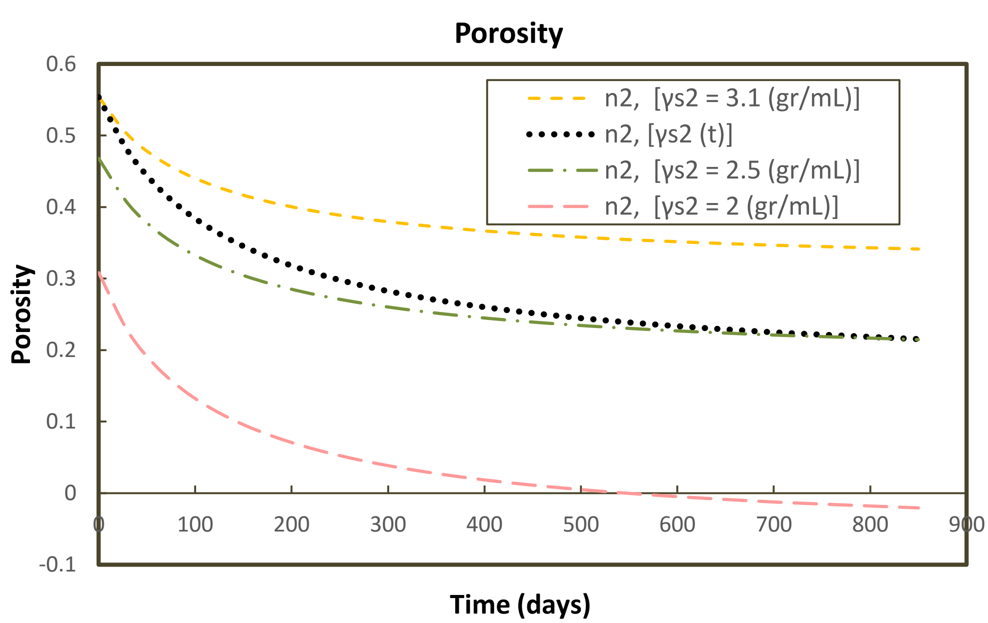

Fig. 4 - 23: Porosity of the cement (w/c=0.4) in 830 days of curing

The porosity of the cement is predicted based on the assumption made for solid particle specific weight. The porosity changed from 55% to 21% during 830 days of curing.

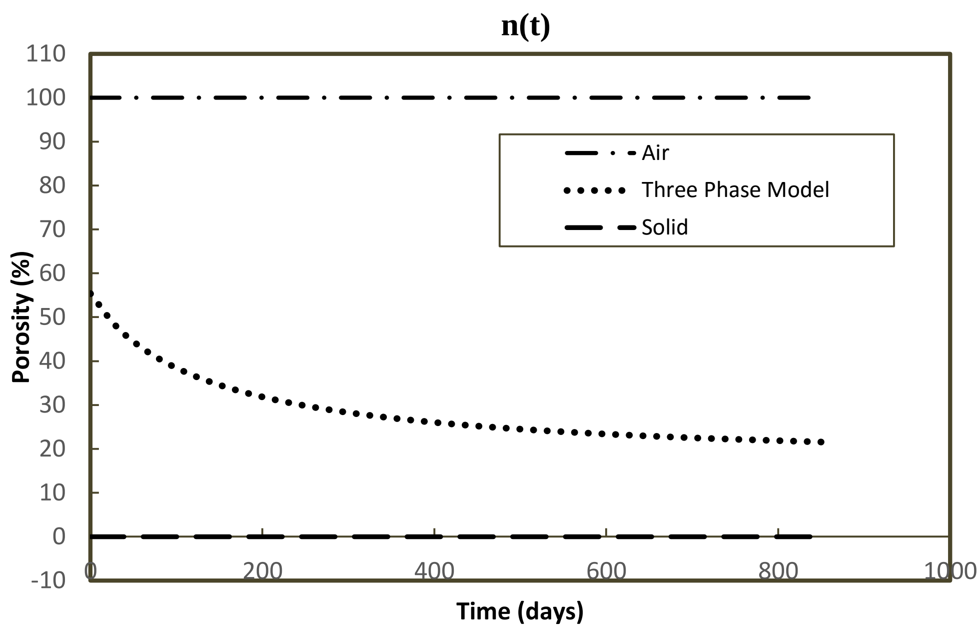

Fig. 4 - 24: Prediction of the porosity of the cement (w/c=0.4) in 830 days of curing

4.1.7. Resistivity Study

Smart cement is a new concept by Vipulanandan et al. with conductive fibers which has the high ability to sense of material characteristic changes and also piezoresistivity (Vipulanandan et al., 2015). The smart cement was used in this study in which the change in resistivity is correlated with the characteristics of the smart cement such as water content, porosity, specific weight, weight loss and shrinkage. Two kinds of the measurements were done.

The measurements were in two directions (Fig. 4 - 25), horizontally (wires 2 and 3) and vertically (wires 1 and 2).

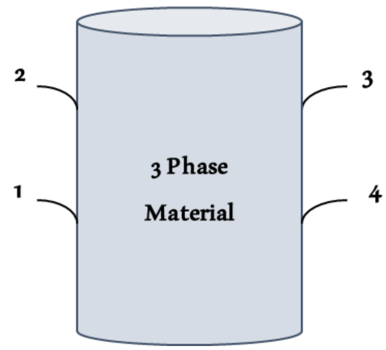

Fig. 4 - 25: Configuration of wires for resistivity study

The resistivity changes were measured along horizontal and vertical wires. As shown in Fig. 4 - 26 the resistivity changes versus moisture content of the material. The resistivity changes up to 1650% in 830 days curing of the cement. The hyperbolic models developed in order to predict the resistivity change versus moisture content (Fig. 4 - 26). With using these models, the resistivity measurements would predict the amount of the changes properties in the cement.

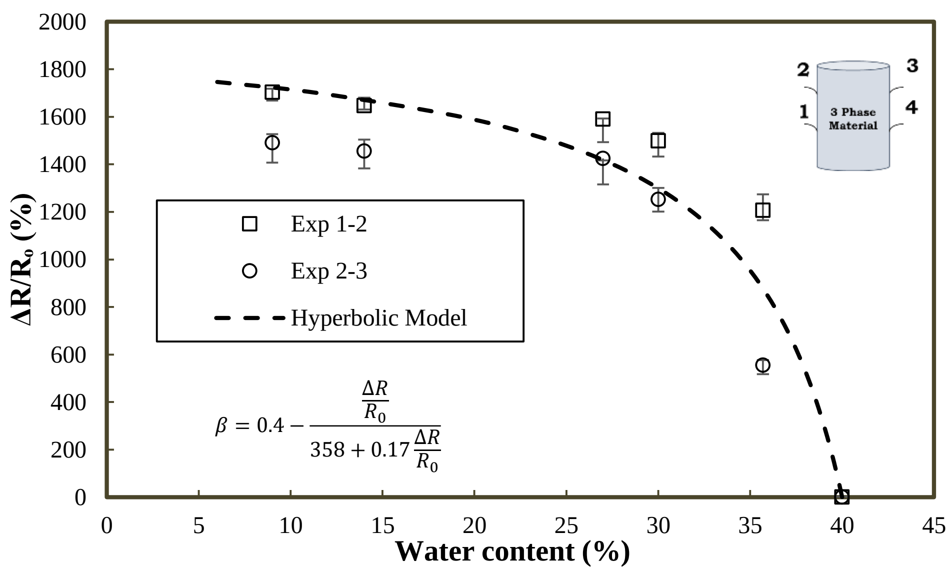

Fig. 4 - 26: Resistivity changes correlations with water content

The following analysis are the sensibility of the three phase parameters, Fig. 4 - 27 shows the changes of the resistivity versus the parameter changes. As shown the parameters "a(t), b(t) and c(t)" are more sensitive than other parameters.

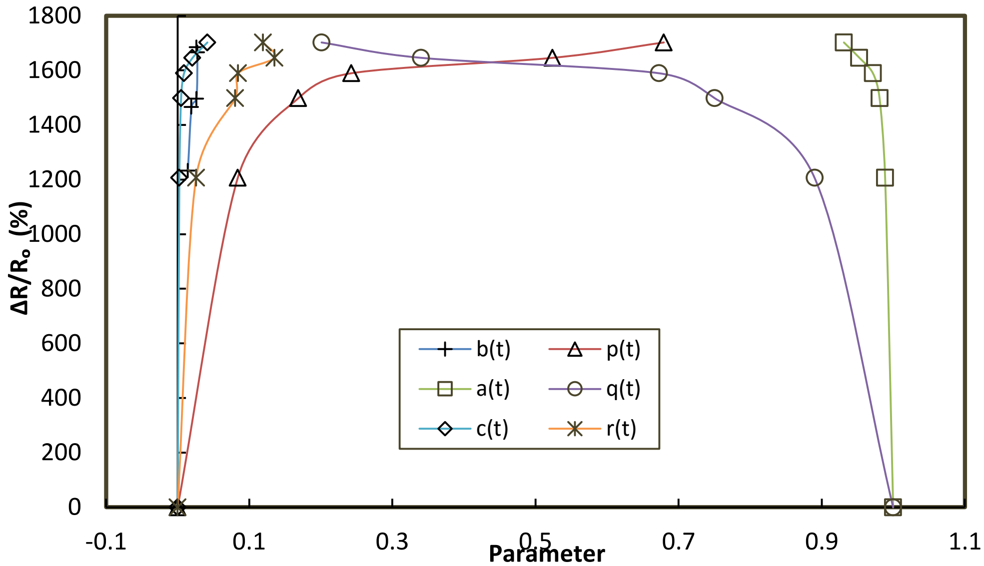

Fig. 4 - 27: Change of resistivity for parameters "a(t), b(t), c(t), r(t), q(t) and p(t)"

To have a better idea of more sensitive parameters, the change of the resistivity was normalized by the unit less parameters and compared during the time as shown in Fig. 4 - 28.

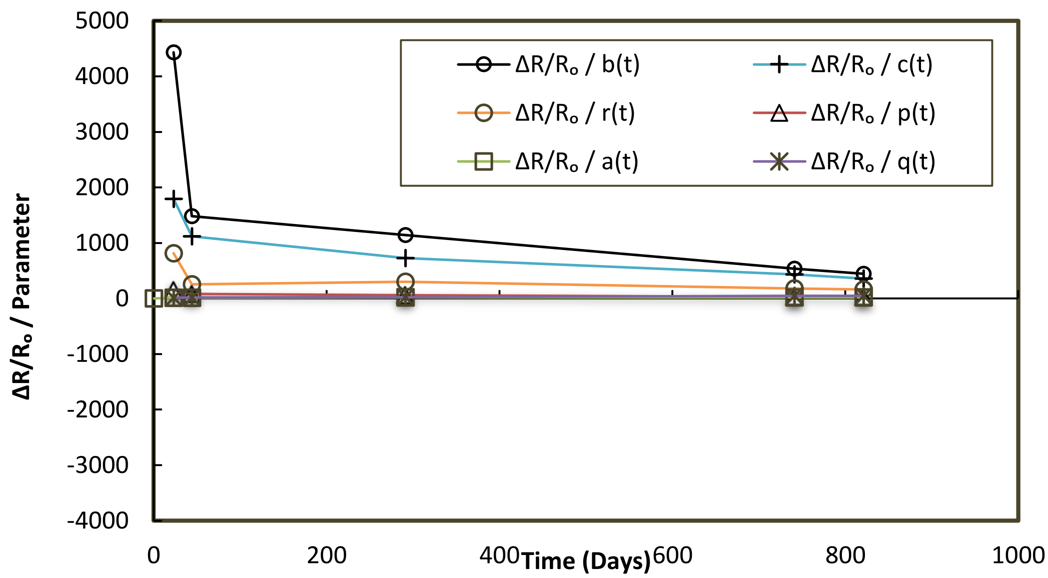

Fig. 4 - 28: Normalized change of resistivity by parameters during the time

As shown parameter "b(t)" which is the portion of the solid which reacts with water which is the gel water has the most sensitivity.

The other graph which is shown in Fig. 4 - 28 is the resistivity normalized by the parameters. Parameter a(t) is showing the most resistivity change. After parameter "b(t)" parameter "c(t)" has a high sensitivity. Among the chemical reactions the parameter "η(t)" has a higher sensitivity compared to "m(t)" as shown in Fig. 4 - 29.

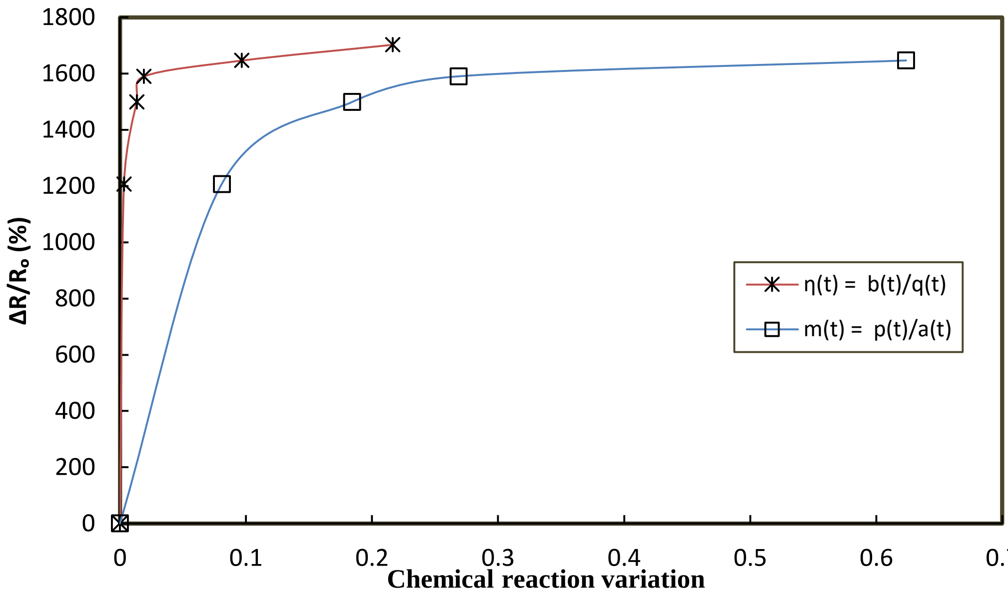

Fig. 4 - 29: Change of resistivity for parameter "m (t)" and "η (t)"

4.2. Fracture Analysis of the Smart Cement

A specimen of type H cement with a/d ratio of 0.3, depth of 3″ and notch length of 0.9″. The three bend flexural test was performed with 9″ distance between the supports. The cyclic load was applied on the specimen, as shown in the Fig. 4 - 30, the LCR meter was used to measure resistance while applying load.

4.2.1. Load vs CMOD

Variation of load (P) versus Crack Mouth Opening Displacement (CMOD) of class H oil well is shown in **Error! Reference source not found.**

Fig. 4 - 30: Typical load (P) versus crack mouth opening displacement relationship for notched beam

4.2.2. Load vs Resistance

The load versus resistance measurements is shown in Fig. 4 - 31. Therefore, the correlation between resistance and CMOD can be found.

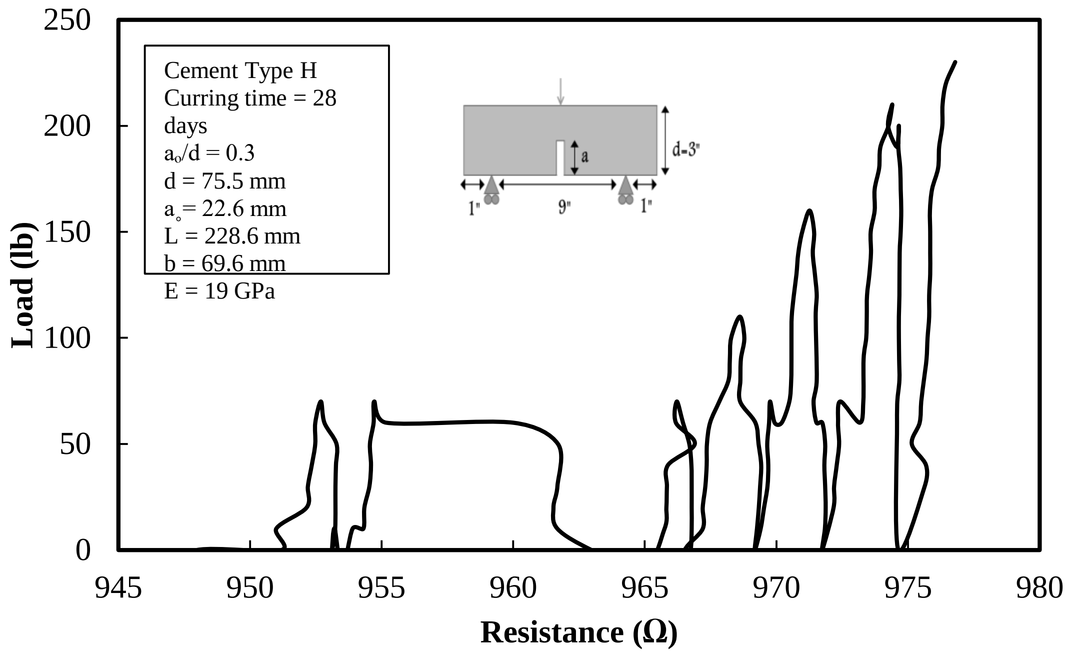

Fig. 4 - 31: Typical load (P) versus resistance relationship for notched beam

4.2.3. Stress and Fracture Toughness Analysis

There are two types of stresses: nominal and effective stress. First if the depth of the specimen is considered as a constant (full depth subtracted by initial crack depth, a_o) we will have the stress as a function of load only named nominal stress. If the depth calculated as full depth subtracted by crack depth a_e, the effective stress is defined as a function of load and crack depth.

The effective crack length also can be represented by variation of stress Fig. 4 - 32. The stress was analyzed and plotted versus effective crack growth, The p, q equation (Vipulanandan and Mebarkia, 1990) is used to model the behavior of some of the characteristics of the fracture study to capture the variations of the stress versus crack growth defined as

$$\frac{\sigma}{\sigma_{max}} = \frac{\frac{a-a_*}{a_c}}{q + (1-q-p)\frac{a-a_*}{a_c} + p(\frac{a-a_*}{a_c})^{\frac{p+q}{p}}}. \quad \textbf{(4 - 35)}$$

The data trend (Fig. 4 - 32) modeled with p, q equation and parameters are shown in Table 3 - 1.

Table 3 - 1: Stress as a function of effective length model parameters

Stress	a_*	a_c	σ_{max}	p	q
σ_e	22.63	13	330	0.04	0.3
$\sigma_\circ$	22.63	13	650	0.48	0.9

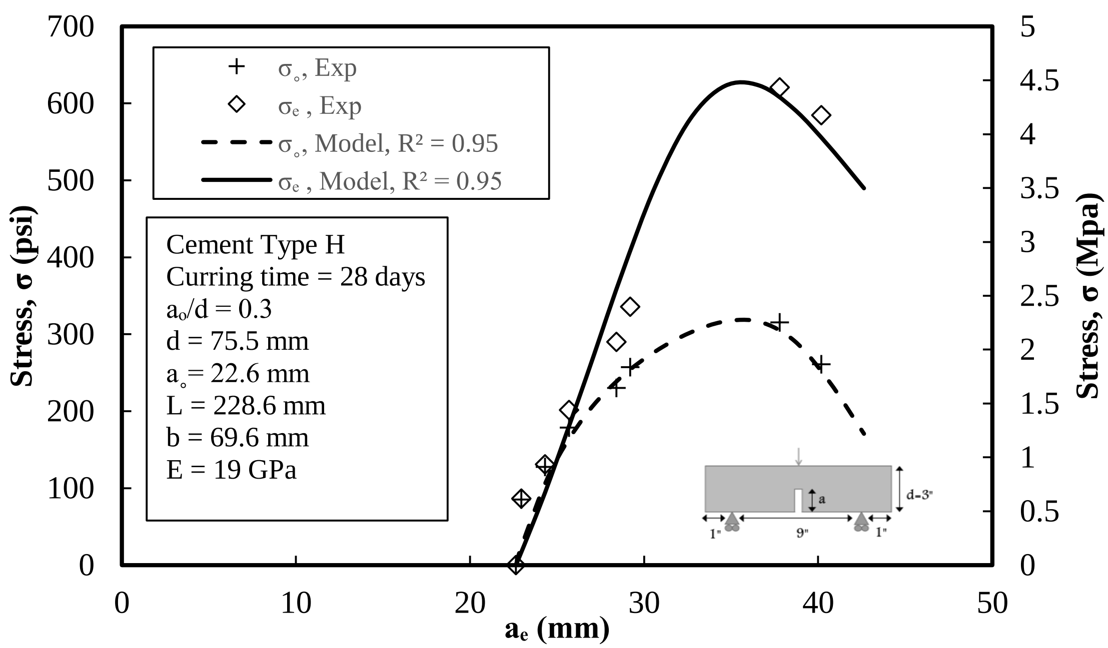

Fig. 4 - 32: Variation of effective crack length with stress

The effective stress intensity factor, ($K1c_e$), was calculated from the experimental results (Fig. 4 - 33).

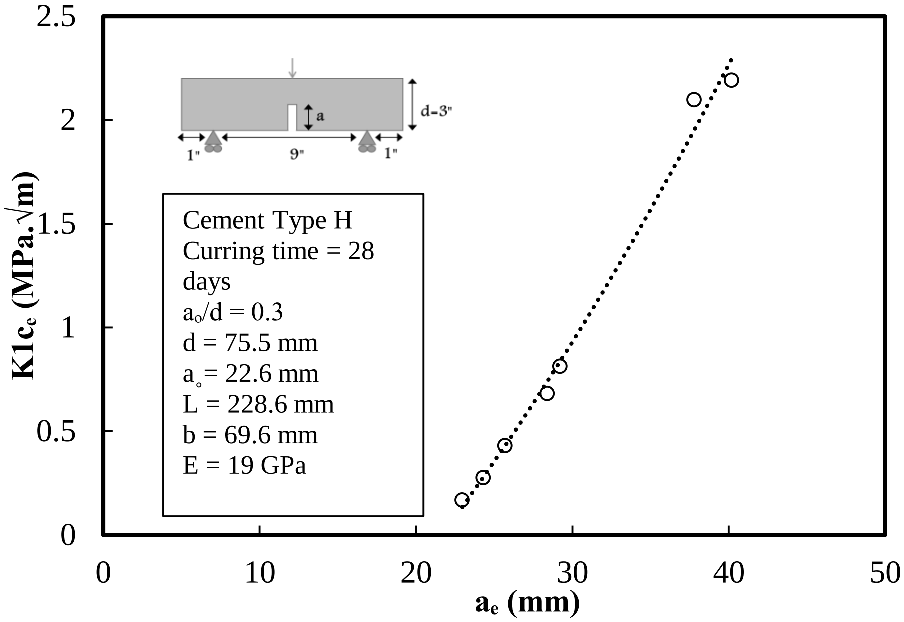

Fig. 4 - 33: Variation of $K1c_e$ stress versus effective crack length

4.2.4. Piezoresistive Method

The traditional method of the three-point bending test and determination of the fracture properties has been widely used by many researchers. In this study, the electrical measurements used to correlate the variation of load and CMOD. Simultaneous measurements of the resistivity changes were monitored while the crack was growing in the cement. Therefore, the changes in resistivity can be correlated with load variations and corresponding CMOD. In this study, the resistivity is a new tool in order to predict CMOD.

The resistivity of the specimen was measured while applying the load in fracture test by LCR meter. The load versus CMOD is shown in Fig. 4 - 34.

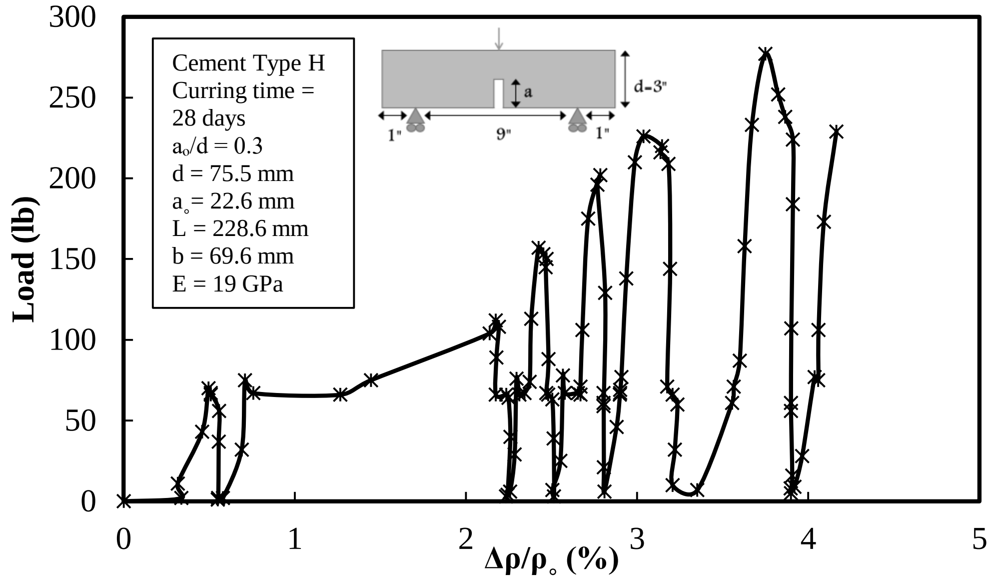

Fig. 4 - 34: Variation of load versus change of resistivity

As we mentioned before, the relation between CMOD and change of resistivity was analyzed. There are different CMODs including: total CMOD, initial elastic $CMOD_\circ^e$, elastic $CMOD^e$ and plastic $CMOD^p$. Fig. 4 - 35 shows the plastic $CMOD^p$ and total CMOD.

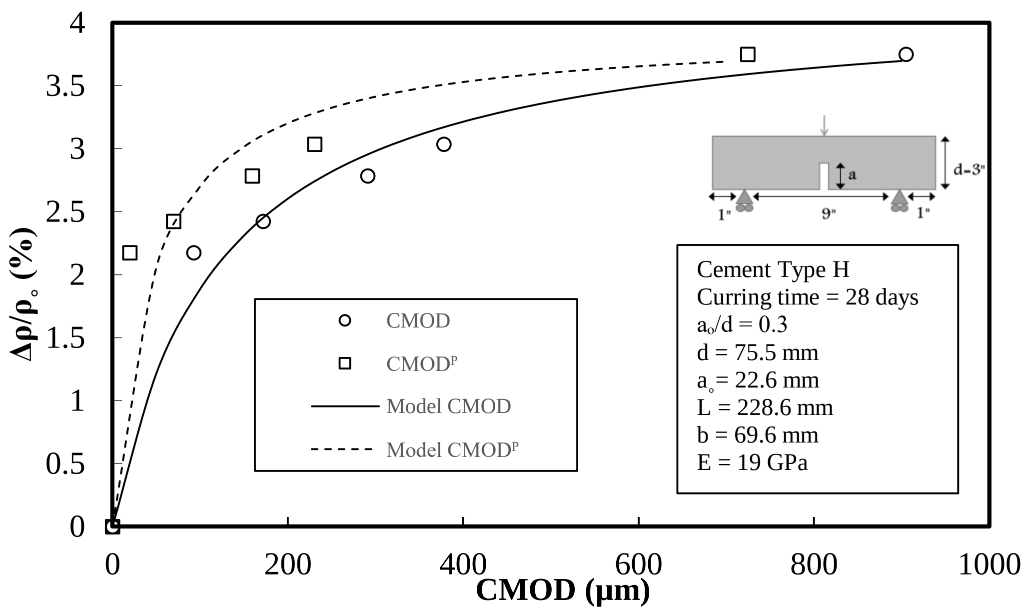

Fig. 4 - 35: Variation of CMOD versus change of resistivity

4.2.5. Crack Tip Opening Displacement (CTOD)

The Crack Tip Opening Displacement (CTOD) is a measure of fracture toughness of solid materials that undergo ductile-brittle transition and elastic-plastic or fully plastic behavior as in larges structures (Jeng et al., 1985; Vipulanandan et al., 1989). Elastic Crack Tip Opening Displacement (CTOD^e) is defined as

$$CTOD^e = CMOD^e Z(\alpha, \beta). \tag{4 - 36}$$

where $CMOD^e$ = [$4\sigma a V(\alpha)$]/E and $Z(\alpha, \beta)$ described as

$$Z(\alpha, \beta) = \left[(1-\beta)^2 + (1.081 - 1.149\alpha)(\beta - \beta^2)\right]^{\frac{1}{2}}. \tag{4 - 37}$$

where β is given as $\beta = a_0 / a_e$ and α was defined already. Fig. 4 - 36 shows the change of CTOD versus the crack propagation.

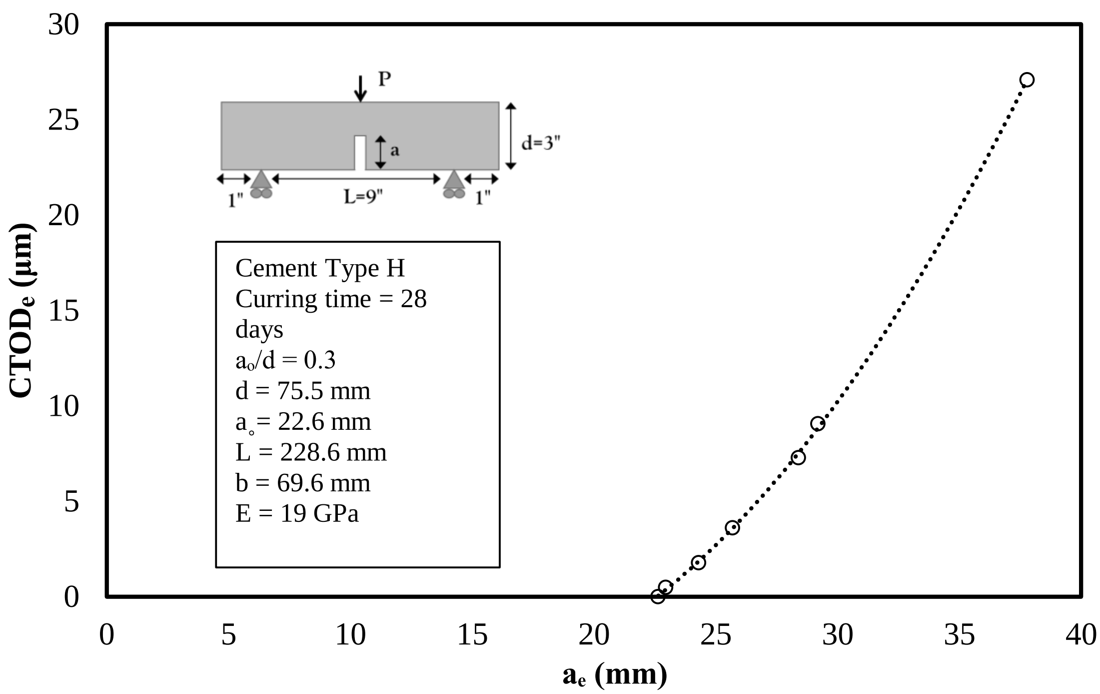

Fig. 4 - 36: Crack Tip Opening Displacement (CTOD) versus effective crack length

4.3. Equivalent Resistance in 3D Conductive Medium

Combining resistors based on principals of electricity leads to resistive network to a single resistance in such a way that an equivalent resistance is the resistance between network terminals and should exhibit the same current-voltage characteristics as the original network at the terminals. There are different techniques and methods in electricity to calculate the electrical resistance

4.3.1. Techniques and Methods

There are different techniques and methods to simplify a circuit in order to fin the equivalent resistance including (*http://highered.mcgraw-hill.com*).

- Series
- Parallel
- Delta to wye conversion
- Wye to delta conversion

In this study these techniques and method are described and used to derive the equivalent resistance for a 3D conductive medium.

(a) Series

When two resistors are connected in a circuit as Fig. 4 - 37, this situation is called as series. In the other word, two or more elements are in series if they share a single node and also carry the same current.

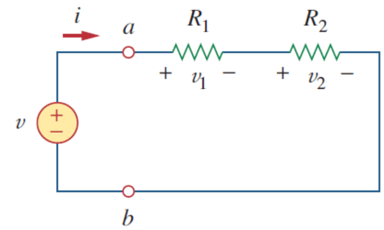

Fig. 4 - 37: A single-loop circuit with two resistors

The equivalent resistance of the series resistors is defined as

$$R_{eq} = R_1 + R_2. \tag{4 - 7}$$

(b) Parallel

When two resistors are connected in a circuit as figure below their position is named as parallel. In the other word, two or more elements are in parallel if they are connected to the same two nodes and consequently have the same voltage across them. The equivalent resistance of the parallel resistors is defined as following.

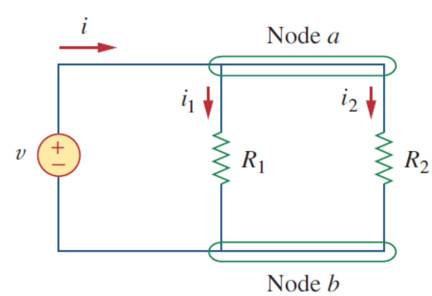

Fig. 3 - 10: A single-loop circuit with two resistors

The equivalent resistance of the parallel resistors is defined as

$$\frac{1}{R_{eq}} = \frac{1}{R_1} + \frac{1}{R_2}. \tag{4 - 8}$$

(c) Delta to wye conversion

Sometimes working with a wye network inside a circuit is much easier than a delta configuration. By superimposing a wye network on the existing delta network the equivalent resistances in the network will be found. The transformation of delta to wye network is defined as following

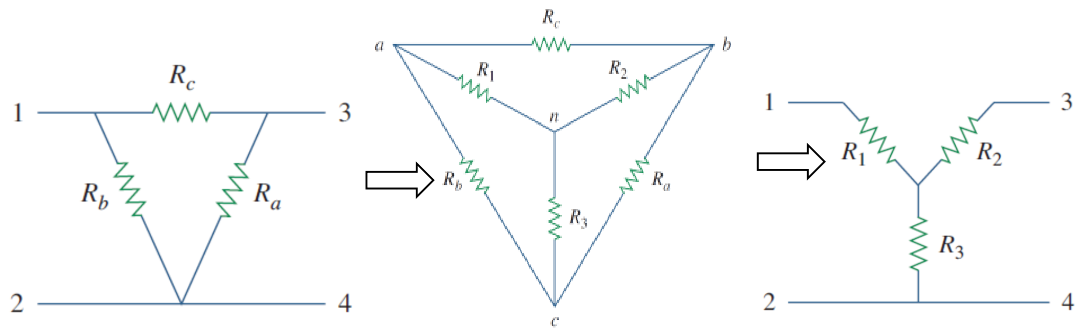

Fig. 4 - 38: Delta to wye conversion

R_a, R_b and R_c can be expressed as a combination of the R_1, R_2 and R_3, which are defined as following:

$$R_1 = \frac{R_b R_c}{R_a + R_b + R_c},$$

$$R_2 = \frac{R_c R_a}{R_a + R_b + R_c}, \qquad \textbf{(4 - 9)}$$

$$R_3 = \frac{R_b R_a}{R_a + R_b + R_c}.$$

(d) Wye to delta conversion

Sometimes working with a delta network in a circuit is much easier than a wye configuration. By superimposing a delta network on the existing wye network the equivalent resistances in the network will be found. The transformation of wye to delta network is defined as following.

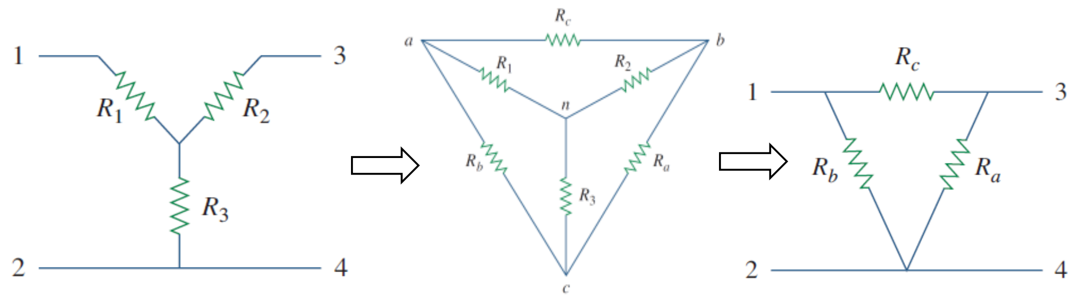

Fig. 4 - 39: Wye to delta conversion

R_a, R_b and R_c can be expressed as a combination of the R_1, R_2 and R_3, which are defined as following:

$$R_a = \frac{R_1R_2 + R_2R_3 + R_3R_1}{R_1},$$

$$R_b = \frac{R_1R_2 + R_2R_3 + R_3R_1}{R_2}, \qquad \textbf{(4 - 10)}$$

$$R_c = \frac{R_1R_2 + R_2R_3 + R_3R_1}{R_3}.$$

4.3.2. 3D Conductive Medium

Assume there is a resistor on each side of a 3-D cube. In several steps by using the methods and techniques of principals in electricity, the 3-D circuit will be simplified to 2-D problem and the equivalent resistance will be defined easily. The objective is finding equivalent resistance along O_1 and O_2

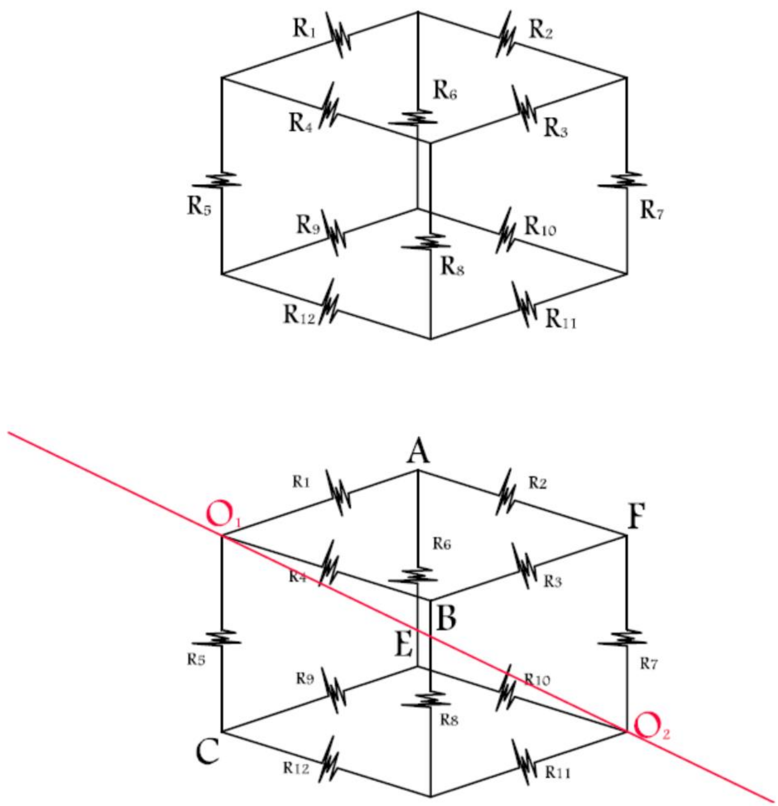

Fig. 4 - 40: 3D Conductive Medium

There are several steps to use the four techniques to simplify the 3D cubic form of the circuit to a 2D and finally 1D configuration between O_1 and O_2.

Step 1) Eliminate Node "F" in ABO_2 Plane

In this step the wye configuration of the ABO_2 which are attached through node F, is changes to delta configuration.

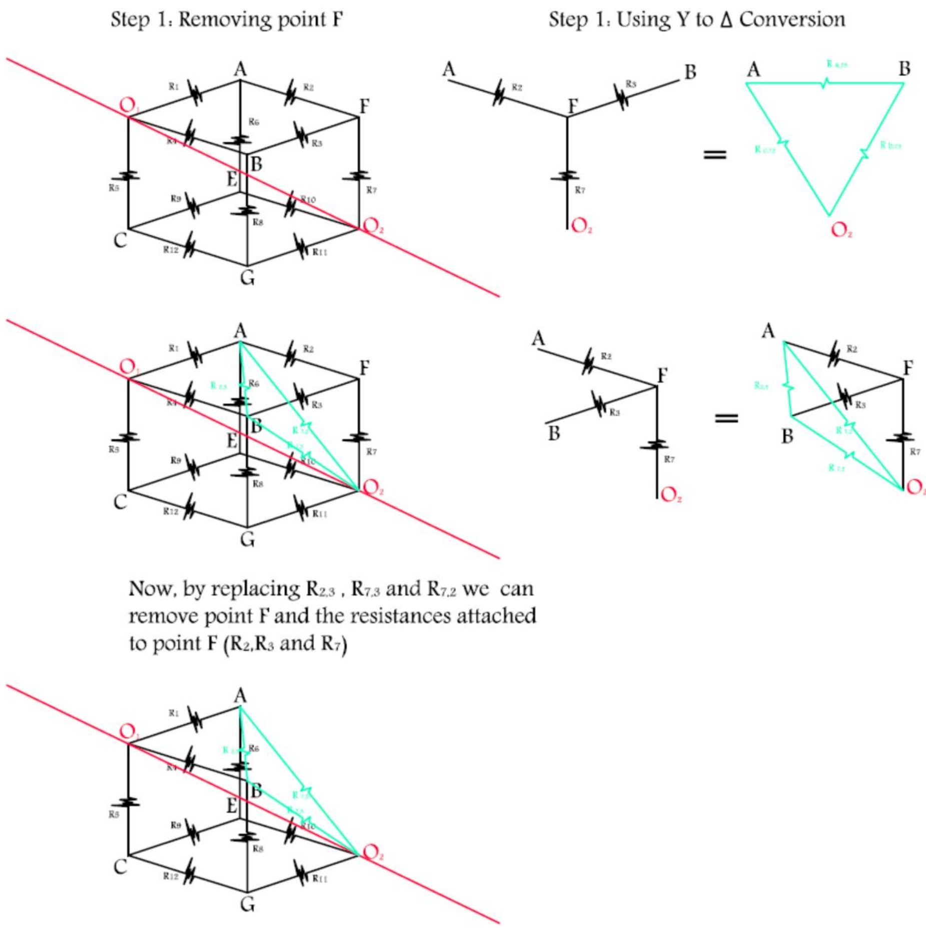

Fig. 4 - 41: Eliminate Node "F" in ABO_2 Plane

$R_{2.3}$, $R_{2.7}$ and $R_{3.7}$ are defined as following:

$$R_{2.3} = \frac{R_2R_7 + R_7R_3 + R_3R_2}{R_7},$$
$$R_{2.7} = \frac{R_2R_7 + R_7R_3 + R_3R_2}{R_3}, \qquad \textbf{(4 - 11)}$$
$$R_{3.7} = \frac{R_2R_7 + R_7R_3 + R_3R_2}{R_2}.$$

Step 2) Eliminate Node "G" in CBO_2 Plane

In this step the wye configuration of the CBO_2 which are attached through node G, is changes to delta configuration.

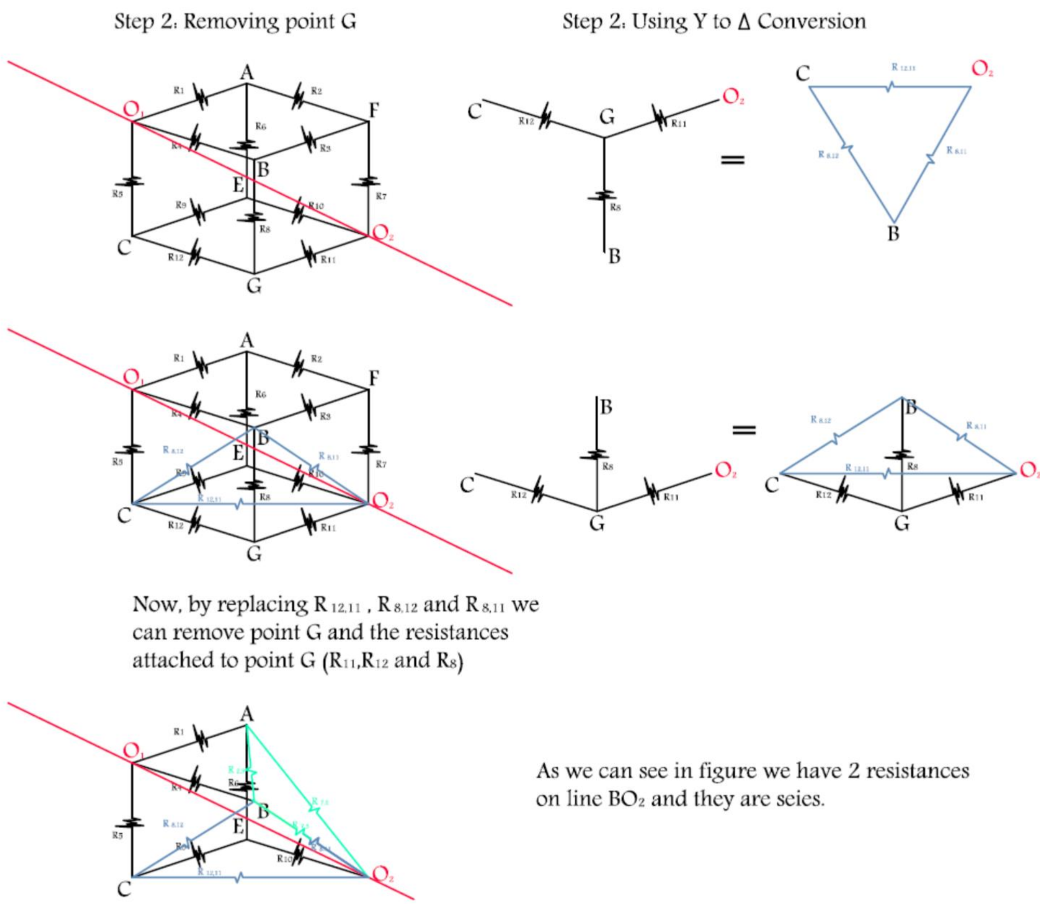

Fig. 4 - 42: Eliminate Node "G" in CBO_2 Plane

$R_{11.12}$, $R_{8.11}$ and $R_{8.12}$ are defined as following:

$$R_{11.12} = \frac{R_{12}R_{11} + R_{12}R_8 + R_{11}R_8}{R_8},$$

$$R_{8.11} = \frac{R_{12}R_{11} + R_{12}R_8 + R_{11}R_8}{R_{12}}, \qquad \textbf{(4 - 12)}$$

$$R_{8.12} = \frac{R_{12}R_{11} + R_{12}R_8 + R_{11}R_8}{R_{11}}.$$

Step 3) Eliminate Node “E” in ACO_2 Plane

In this step the wye configuration of the ACO_2 which are attached through node E, is changes to delta configuration.

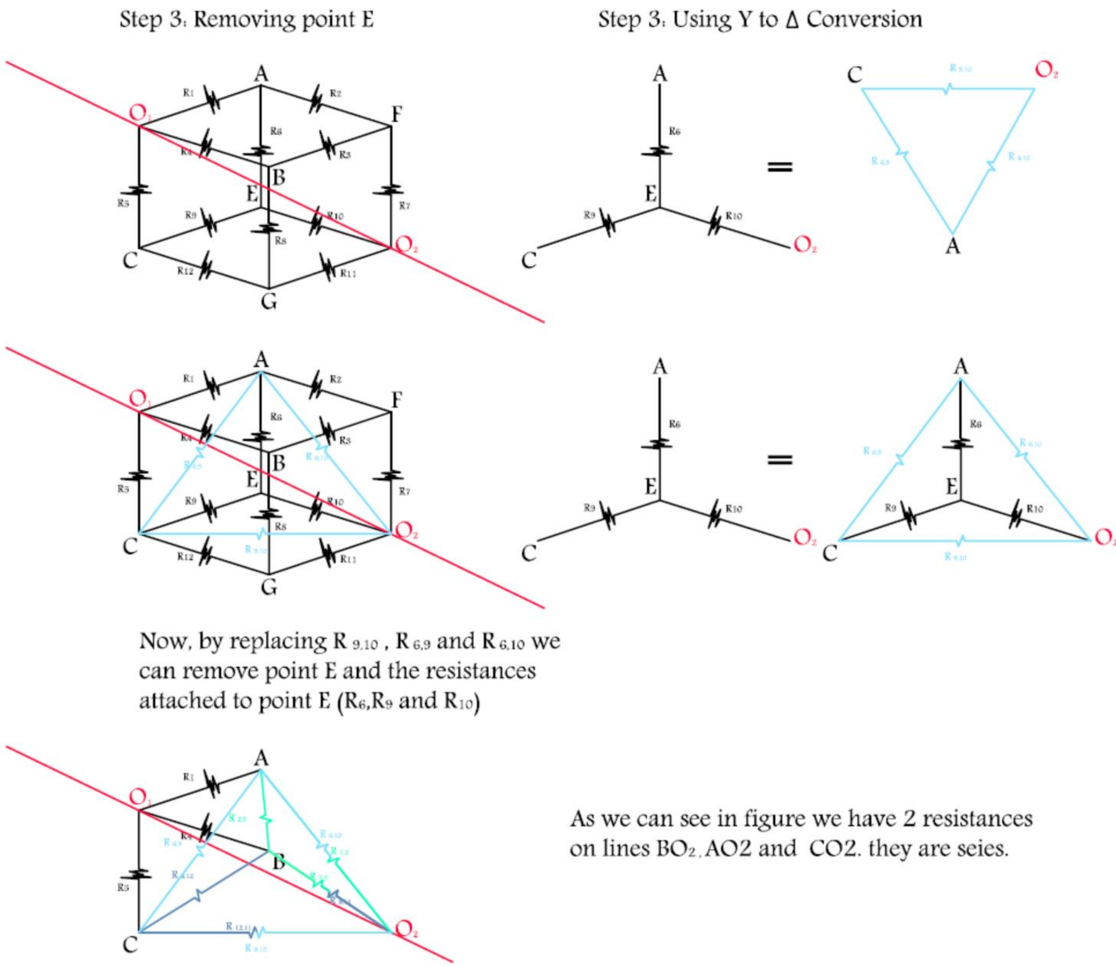

Fig. 4 - 43: Eliminate Node “E” in ACO_2 Plane

$R_{9.10}$, $R_{6.10}$and $R_{9.6}$are defined as following:

$$R_{9.10} = \frac{R_6R_9 + R_6R_{10} + R_{10}R_9}{R_6},$$

$$R_{6.10} = \frac{R_6R_9 + R_6R_{10} + R_{10}R_9}{R_9}, \tag{4 - 13}$$

$$R_{9.6} = \frac{R_6R_9 + R_6R_{10} + R_{10}R_9}{R_{10}}.$$

Between node A and O_2, there are two resistances from R 2.7 and R 6.10 from step 1 and 3. Which are parallel together. Hence, the R_{ao2} is

$$\frac{1}{R_{ao2}} = \frac{1}{R_{2.7}} + \frac{1}{R_{6.10}}. \tag{4 - 14}$$

Between node B and O_2, there are two resistances from R 7.3 and R 8.11 from step 1 and 2. Which are parallel together. Hence, the R_{bo2} is

$$\frac{1}{R_{bo2}} = \frac{1}{R_{7.3}} + \frac{1}{R_{8.11}}. \tag{4 - 15}$$

Between node C and O_2, there are two resistances from R 11.12 and R 9.10 from step 2 and 3. Which are parallel together. Hence, the R_{co2} is

$$\frac{1}{R_{co2}} = \frac{1}{R_{11.12}} + \frac{1}{R_{9.10}}. \tag{4 - 16}$$

Step 4) Create Node "D" in ABC Plane

In this step the delta configuration of the ABC is changes to wye configuration by creation of node D. the resistance between

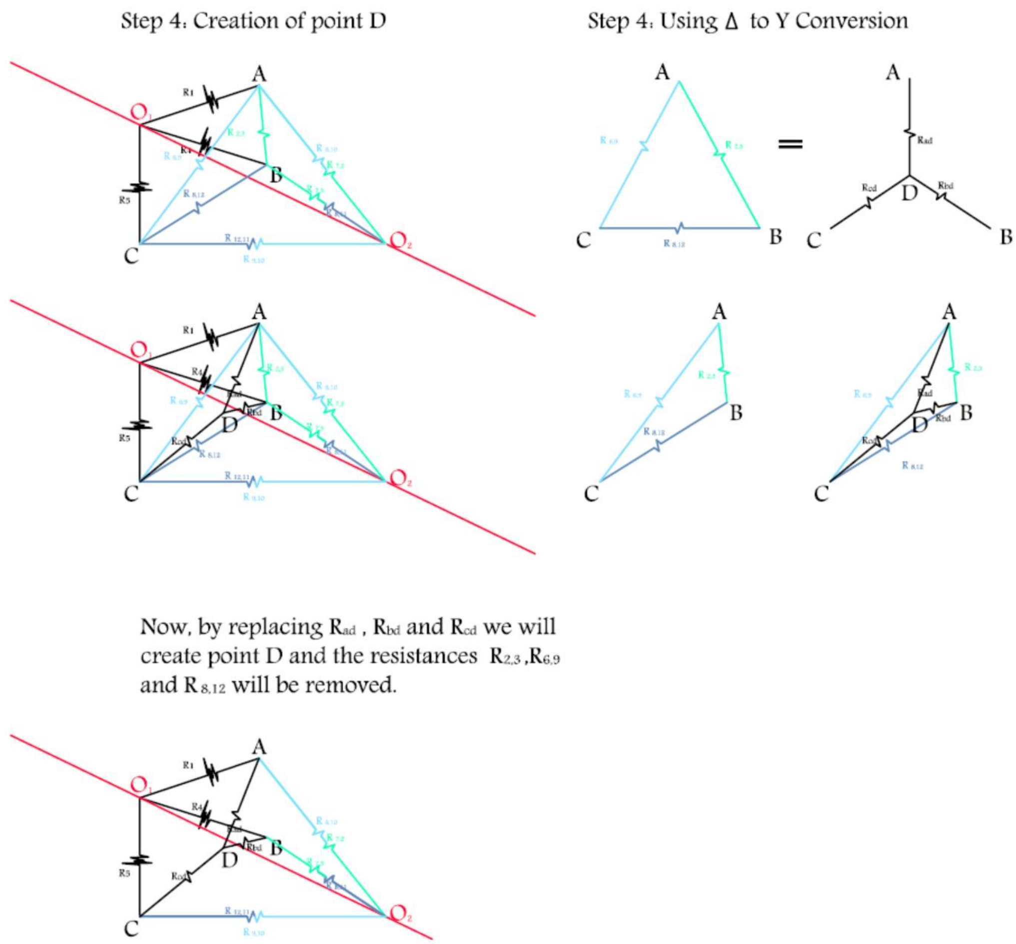

Fig. 4 - 44: Create Node "D" in ABC Plane

R_{ad}, R_{bd} and R_{cd} are defined as following:

$$R_{ad} = \frac{R_{2.3}R_{9.6}}{R_{2.3} + R_{8.12} + R_{9.6}},$$

$$R_{bd} = \frac{R_{2.3}R_{8.12}}{R_{2.3} + R_{8.12} + R_{9.6}}, \quad \textbf{(4 - 17)}$$

$$R_{cd} = \frac{R_{9.6}R_{8.12}}{R_{2.3} + R_{8.12} + R_{9.6}}.$$

Step 5) Eliminate Node "A" in $DO_1\ O_2$ Plane

In this step the wye configuration of the $DO_1\ O_2$ which are attached through node A, is changes to delta configuration.

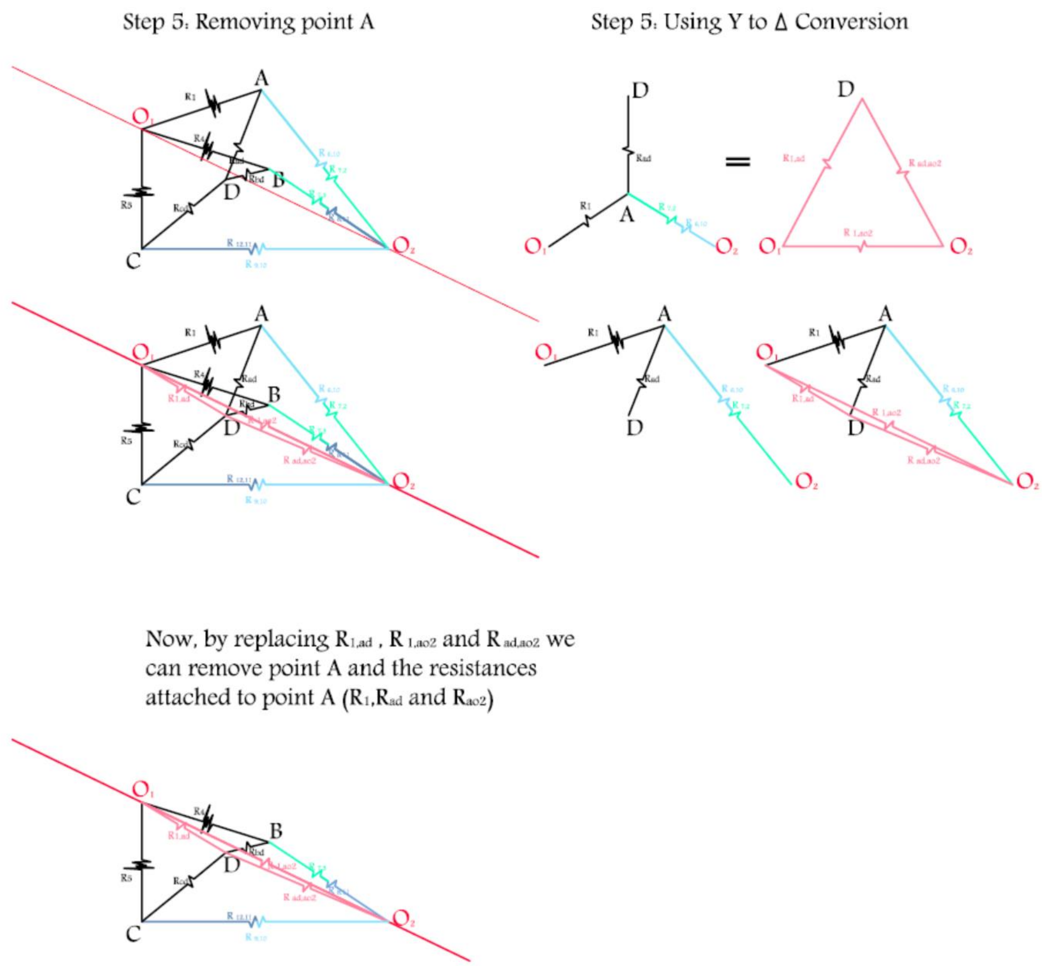

Fig. 4 - 45: Eliminate Node "A" in $DO_1\ O_2$ Plane

$R_{1,ao2}$, $R_{1,ad}$ and $R_{ad,ao2}$ are defined as following:

$$R_{1,ao2} = \frac{R_1 R_{ad} + R_1 R_{ao2} + R_{ad} R_{ao2}}{R_{ad}},$$

$$R_{1,ad} = \frac{R_1 R_{ad} + R_1 R_{ao2} + R_{ad} R_{ao2}}{R_{ao2}}, \tag{4 - 18}$$

$$R_{ad,ao2} = \frac{R_1 R_{ad} + R_1 R_{ao2} + R_{ad} R_{ao2}}{R_1}.$$

Step 6) Eliminate Node "B" in DO_1 O_2 Plane

In this step the wye configuration of the DO_1 O_2 which are attached through node B, is changes to delta configuration.

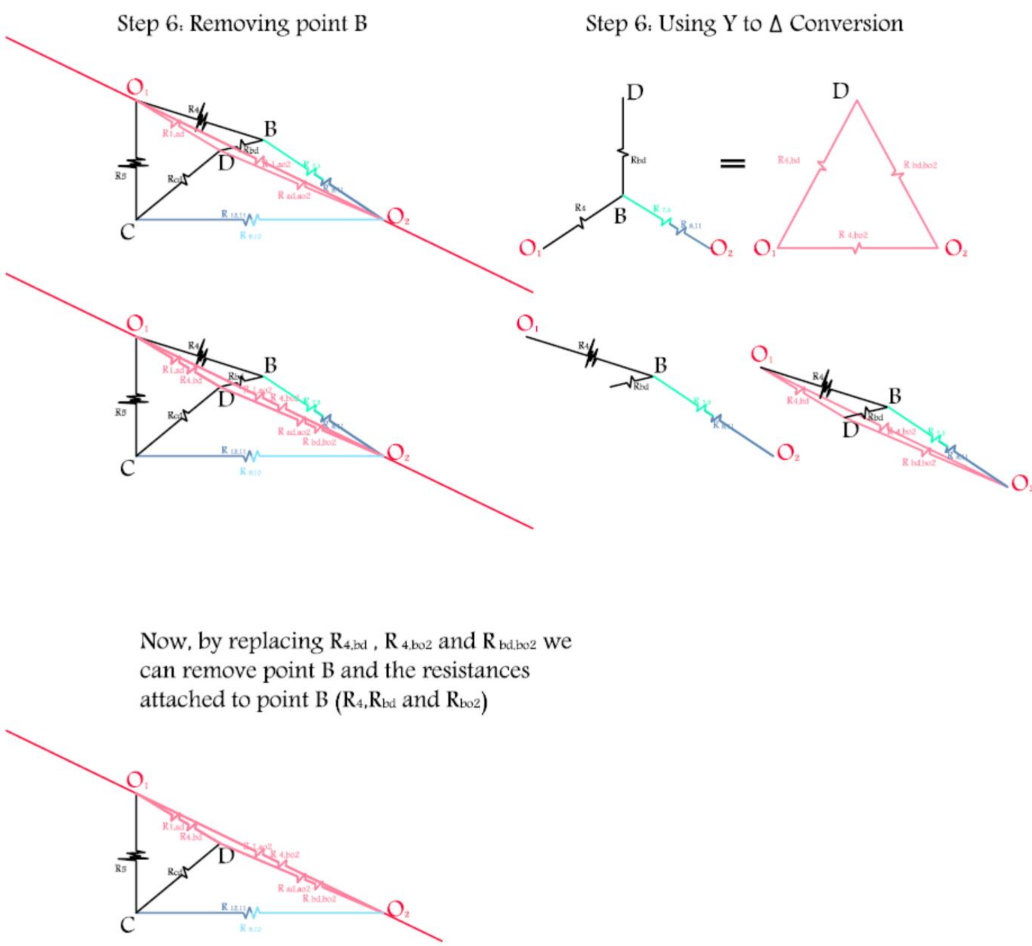

Fig. 4 - 46: Eliminate Node "B" in DO_1 O_2 Plane

$R_{4,bo2}$, $R_{bd,bo2}$ and $R_{4,bd}$ are defined as following:

$$R_{4,bo2} = \frac{R_4 R_{bd} + R_4 R_{bo2} + R_{bd} R_{bo2}}{R_{bd}},$$

$$R_{bd,bo2} = \frac{R_4 R_{bd} + R_4 R_{bo2} + R_{bd} R_{bo2}}{R_4}, \qquad \textbf{(4 - 19)}$$

$$R_{4,bd} = \frac{R_4 R_{bd} + R_4 R_{bo2} + R_{bd} R_{bo2}}{R_{bo2}}.$$

Step 7) Eliminate Node “C” in $DO_1\ O_2$ Plane

In this step the wye configuration of the $DO_1\ O_2$ which are attached through node C, is changes to delta configuration.

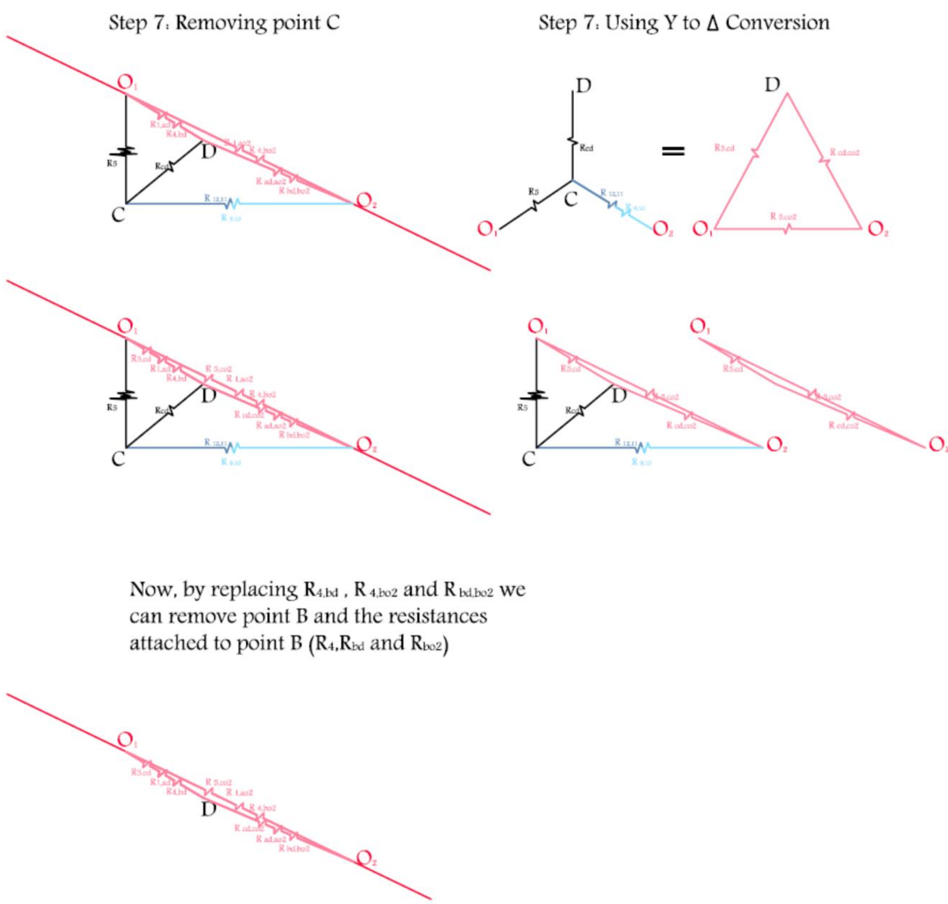

Fig. 4 - 47: Eliminate Node “C” in $DO_1\ O_2$ Plane

$R_{5,co2}$, $R_{cd,co2}$ and $R_{5,bd}$ are defined as following:

$$R_{5,co2} = \frac{R_5 R_{cd} + R_5 R_{co2} + R_{cd} R_{co2}}{R_{cd}},$$

$$R_{cd,co2} = \frac{R_5 R_{cd} + R_5 R_{co2} + R_{cd} R_{co2}}{R_5}, \qquad \textbf{(4 - 20)}$$

$$R_{5,bd} = \frac{R_5 R_{cd} + R_5 R_{co2} + R_{cd} R_{co2}}{R_{co2}}.$$

Step 8) 2D Plane DO$_1$ O$_2$

Resistance R1,ad, R5,cd and R4,bd are parallel along O$_1$ and D, while R5,co2, R1,ao2 and R4,bo2 are parallel along O$_1$ and O$_2$, also Rad,ao2, Rbd,bo2 and Rcd,co2 are parallel along O$_2$ and D. The equivalent form of each parallel group is calculated and it forms Rdo1 along O$_1$ and D, the equivalent along O$_1$ and O$_2$ is Ro1o2 and finally, Rco2 is the equivalent along D and O$_2$.

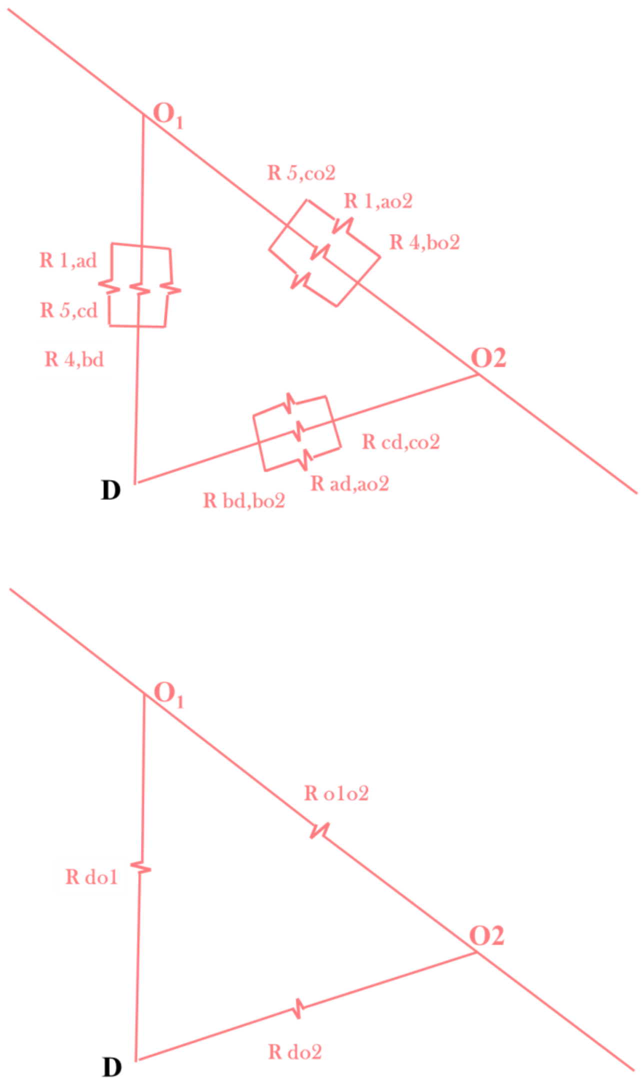

Fig. 4 - 48: 2D Plane DO$_1$ O$_2$

The equivalent resistance for the configuration of Fig. 4 - 48 is as following:

$$\frac{1}{R_{o1o2}} = \frac{1}{R_{1,ao2}} + \frac{1}{R_{4,bo2}} + \frac{1}{R_{5,co2}},$$

$$\frac{1}{R_{do2}} = \frac{1}{R_{ad,ao2}} + \frac{1}{R_{bd,bo2}} + \frac{1}{R_{cd,co2}}' \tag{3 - 21}$$

$$\frac{1}{R_{do1}} = \frac{1}{R_{1,ad}} + \frac{1}{R_{4,bd}} + \frac{1}{R_{5,cd}}.$$

Step 9) Equivalent Resistance along O_1 and O_2

Finally, the equivalent resistance O_1 and O_2 can be found by placing Rdo1 and Rdo2 series and the result is parallel with RO1O2. The equivalent resistant can be found as

$$R_{EQ} = \frac{R_{O1O2}R_{dO1} + R_{O1O2}R_{dO2}}{R_{O1O2} + R_{dO1} + R_{dO2}}. \tag{4 - 22}$$

The proposed method can be verified by Kirt Blattenberge method for solving a cube of resistors of 1Ω. He proved that the equivalent resistance of the cube with all resistors equal to 1 is 5/6 Ω.

4.4. Failure Criteria

In this study, a new failure criteria called Vipulanandan failure model has been developed represented by Hyperbolic equation. Different data from various rock type are represented (Hoek and Brown, 1980). The behavior of each rock and the failure model that predicted failure path is compared with the Drucker–Prager criterion. The new proposed criterion is defined as

$$\sqrt{J_2} = \frac{I_1}{A + B\, I_1} + C. \tag{4 - 38}$$

Where J_2 is second invariant of the deviatoric part of the Cauchy stress, I_1 is the first invariant of the Cauchy stress, C is the cohesion and A and B are the model parameters. By studying a wide range of data (Hoek and Brown, 1980) for different types of rock including: Dunham dolomite, Solenhofen limestone, Shirahama sandstone and Yuubari shale (Colmenares and Zoback, 2002) the proposed model is compared with the Drucker–Prager criterion as shown in Fig. 4 - 49.

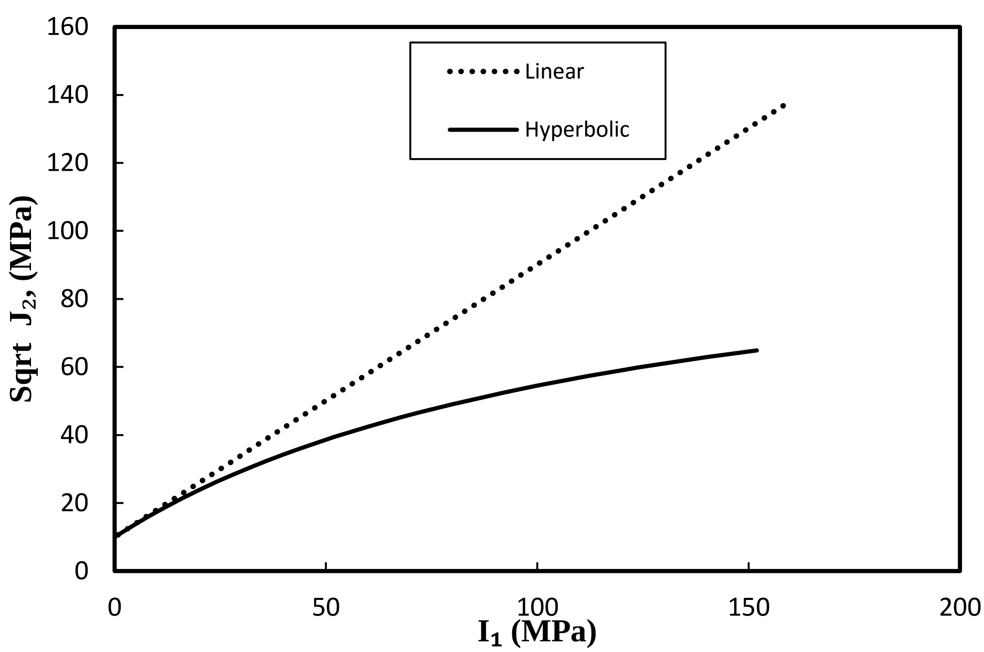

Fig. 4 - 49: Comparison of Drucker–Prager criterion and Vipulanandan (Hyperbolic) failure criterion

Fig. 4 - 50 and Fig. 4 - 51 are shown the triaxial test data by Hoek and Brown (1980) for dolomite and limestone, respectively.

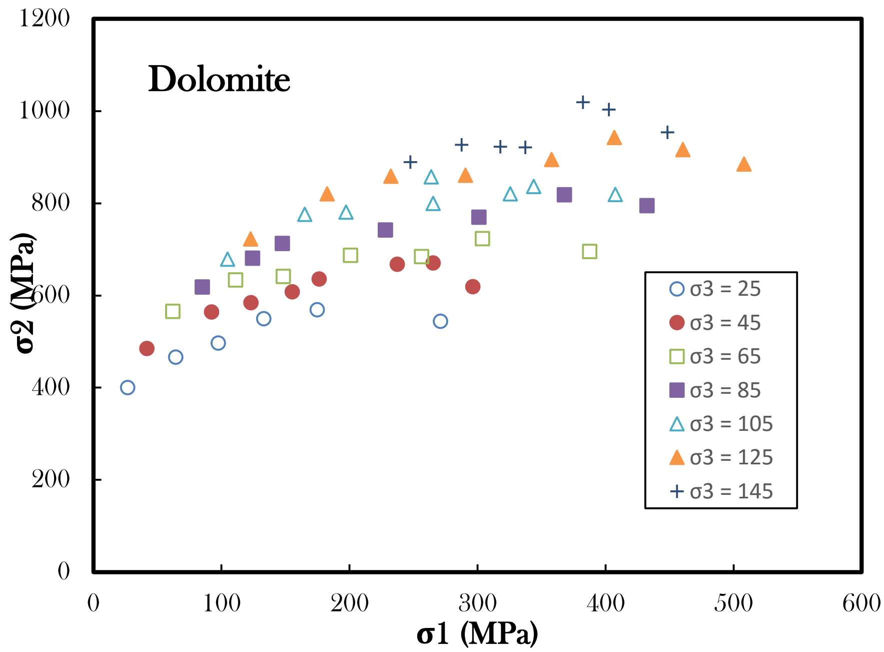

Fig. 4 - 50: Triaxle test data for Dunham dolomite (Hoek and Brown, 1980)

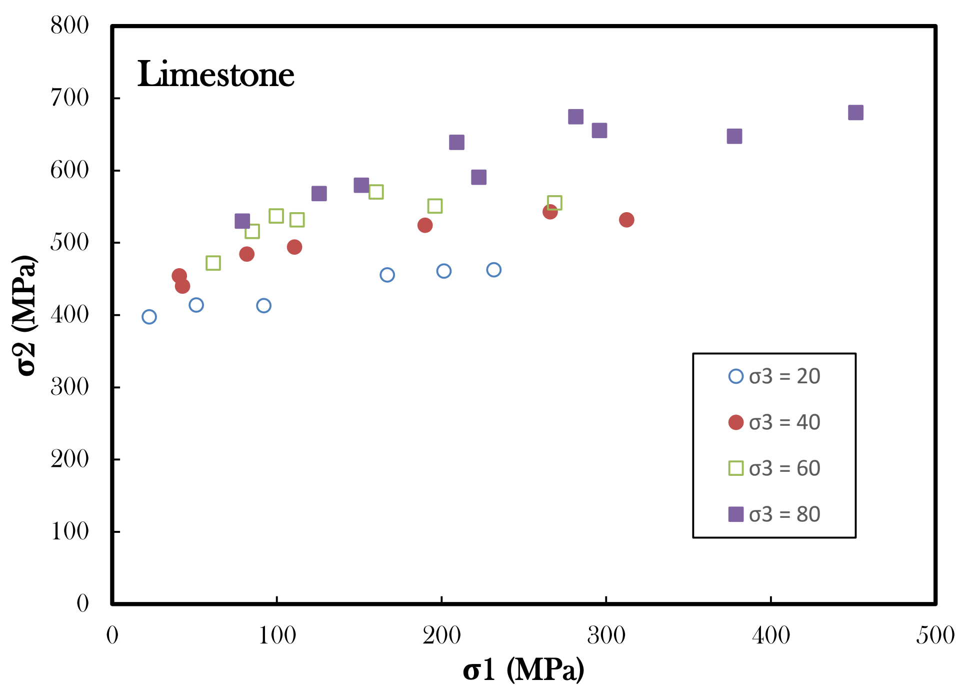

Fig. 4 - 51: Triaxle test data for Solenhofen limestone (Hoek and Brown, 1980)

Fig. 4 - 52 and Fig. 4 - 53 are shown the triaxial test data by Hoek and Brown (1980) for sandstone and shale, respectively.

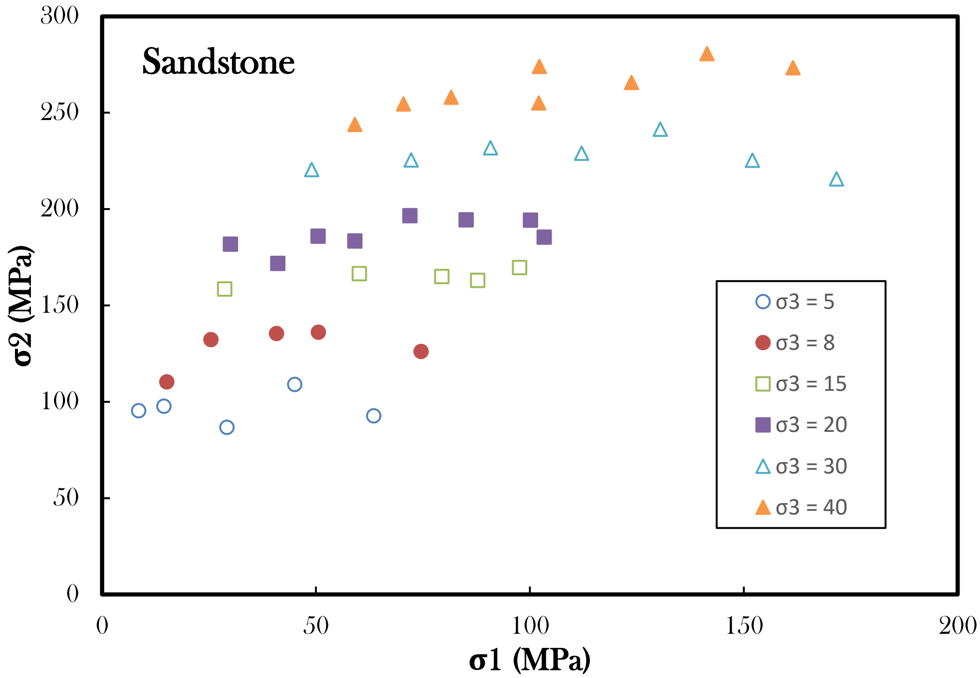

Fig. 4 - 52: Triaxle test data for Sandstone (Hoek and Brown, 1980)

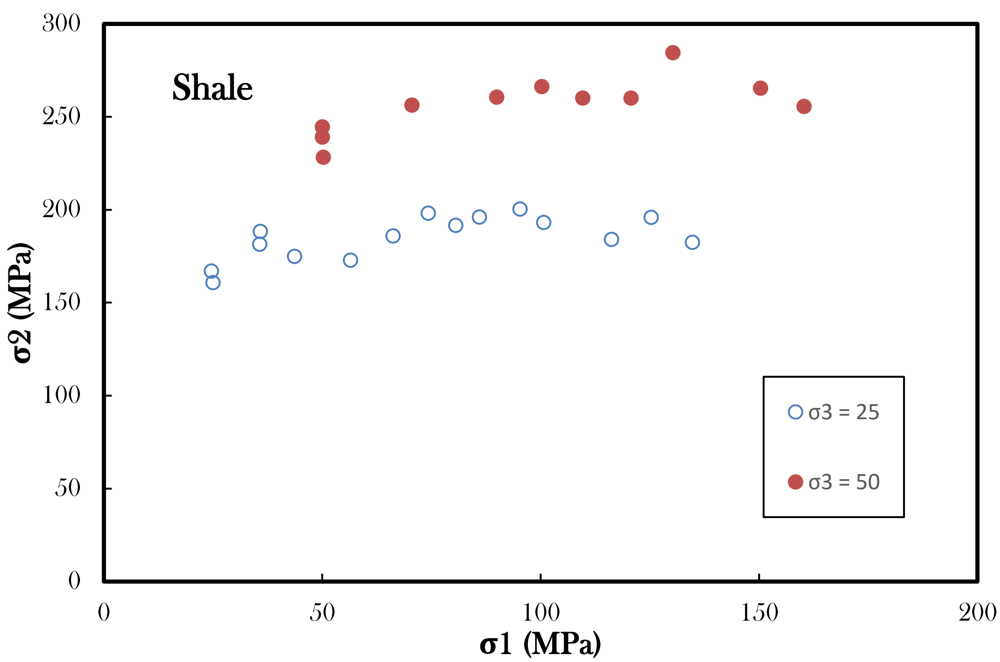

Fig. 4 - 53: Triaxle test data for Shale (Hoek and Brown, 1980)

The Fig. 4 - 54 shows the square root of the second invariant of the deviatoric part of the Cauchy stress versus first invariant of the Cauchy stress captured by Vipulanandan failure model and Drucker–Prager criterion for Dolomite.

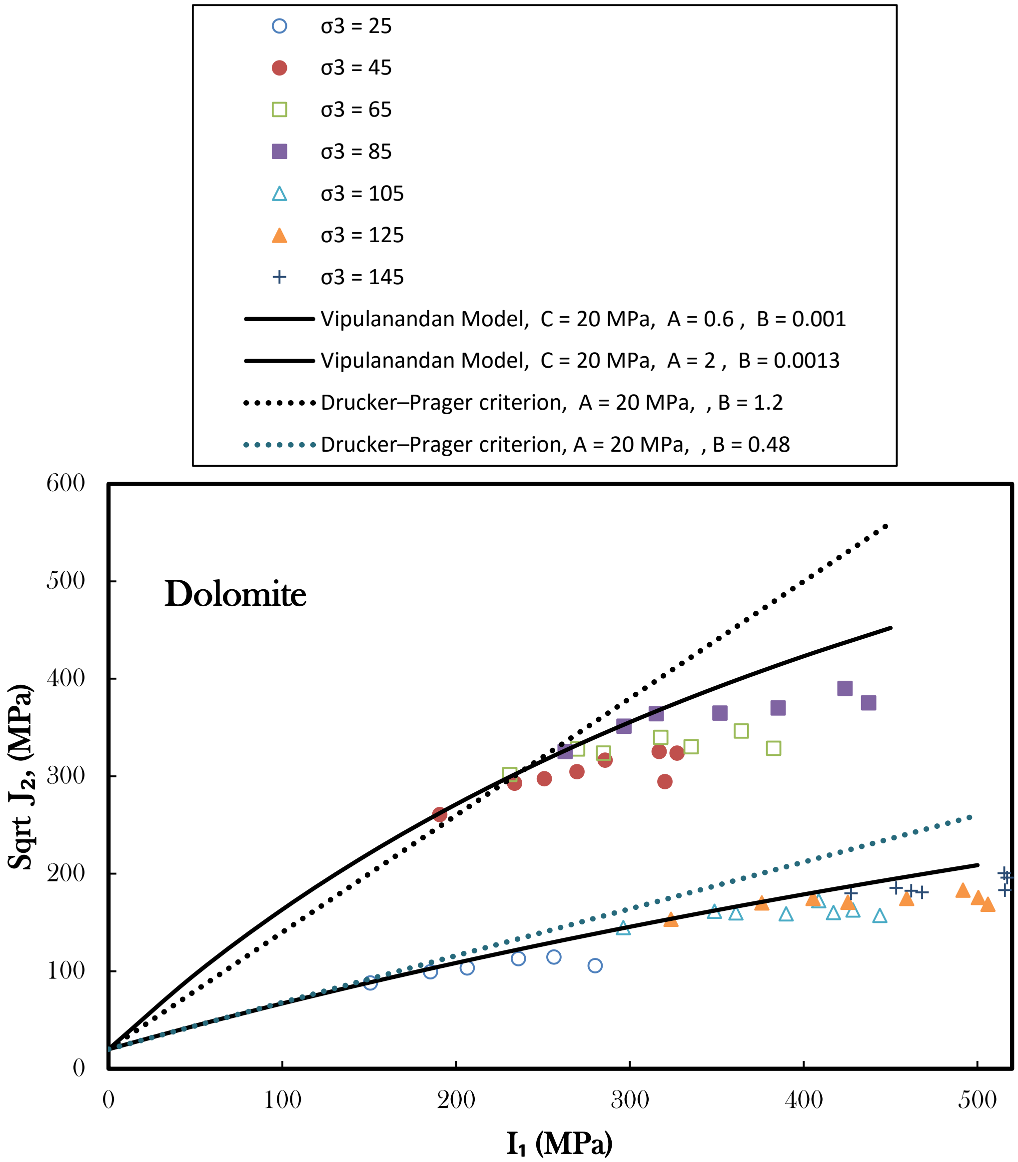

Fig. 4 - 54: Square root of the second invariant versus first invariant of the Cauchy stress captured by Vipulanandan failure model and Drucker–Prager criterion for Dolomite

The Fig. 4 - 55 expresses the square root of the second invariant of the deviatoric part of the Cauchy stress versus first invariant of the Cauchy stress captured by Vipulanandan failure model and Drucker–Prager criterion for Amphibolite.

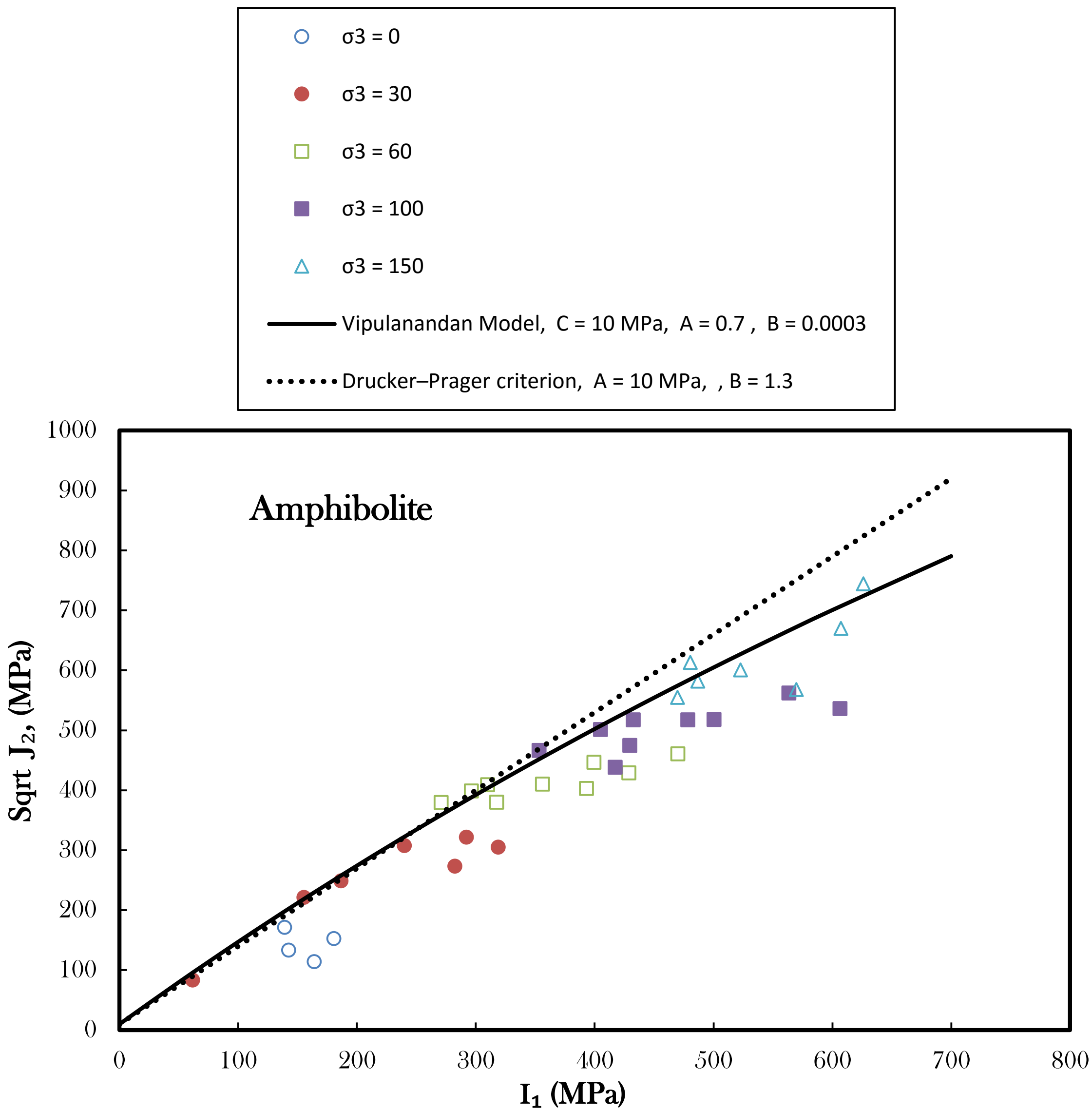

Fig. 4 - 55: Square root of the second invariant versus first invariant of the Cauchy stress captured by Vipulanandan failure model and Drucker–Prager criterion for Amphibolite

The Fig. 4 - 56 shows the square root of the second invariant of the deviatoric part of the Cauchy stress versus first invariant of the Cauchy stress captured by Vipulanandan failure model and Drucker–Prager criterion for Sandstone.

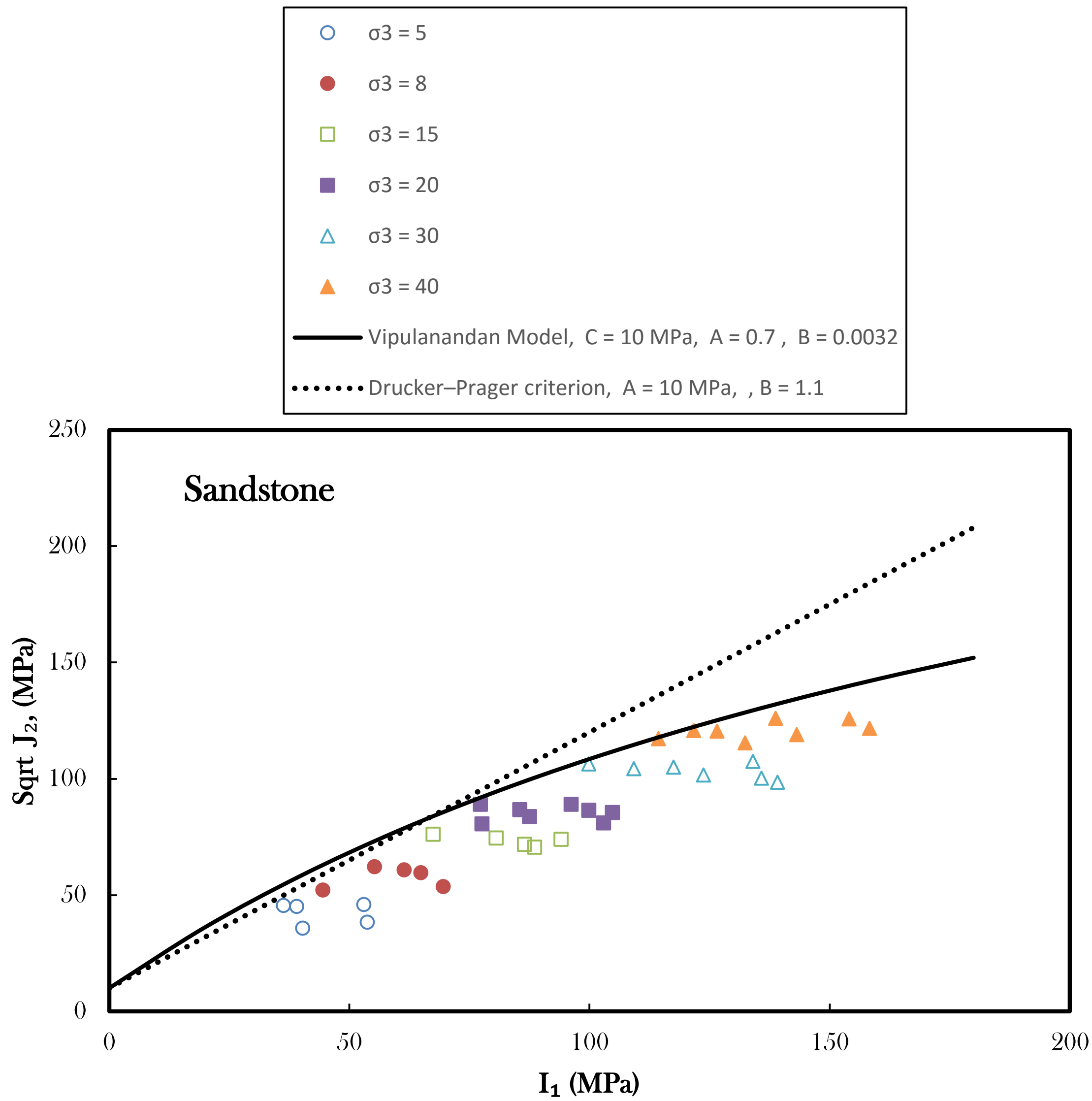

Fig. 4 - 56: Square root of the second invariant versus first invariant of the Cauchy stress captured by Vipulanandan failure model and Drucker–Prager criterion for Sandstone

The Fig. 4 - 57 shows the square root of the second invariant of the deviatoric part of the Cauchy stress versus first invariant of the Cauchy stress captured by Vipulanandan failure model and Drucker–Prager criterion for Shale.

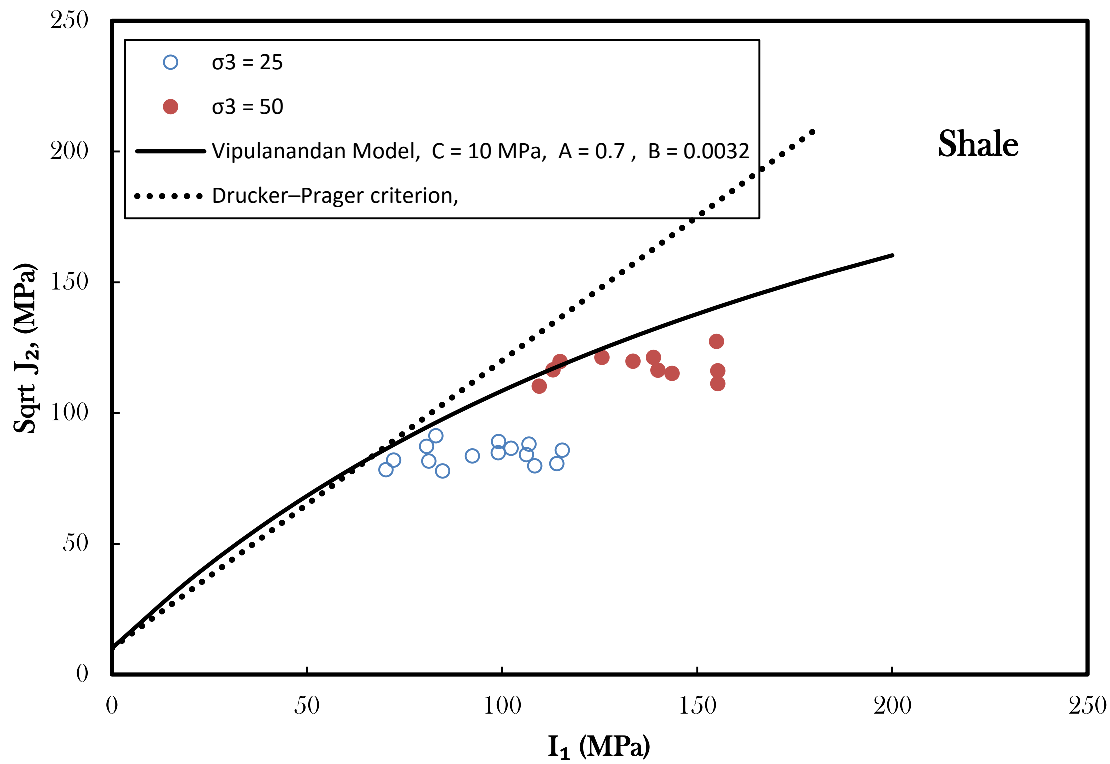

Fig. 4 - 57: Square root of the second invariant versus first invariant of the Cauchy stress captured by Vipulanandan failure model and Drucker–Prager criterion for Shale

As it is shown for different types of the rock, the new proposed failure model can predict the failure path much better than Drucker–Prager criterion.

4.5. Summary

The reaction between the three phases were quantified using six independent material parameters. There were three measurements, weight, volume and the moisture content with time and developing correlation between few selected parameters. The six independent material parameters were quantified. This model can be used for any material with three phases. In this study the cement with water – to – cement ratio (moisture content) of 0.4 were investigated for over 800 days cured under room condition. Influence of the six material parameters on the shrinkage, porosity and electrical resistivity of the solidified cement was quantified. The volume shrinkage was influenced by the liquid – solid reactive model parameter. The resistivity of the cement was influenced by the "b(t)" reactive model parameter.

1. The six parameter were quantified. The ratio of liquid remains in the sample is known as "$q(t)$" decreased by 80%, while the ratio of the liquid reacts with the solid particles "$p(t)$" were increased about 70%. The water loss parameter 1 "$r(t)$", which is the evaporation was reached to 10% during 830 days of curing. Volume shrinkage of the material "$\alpha(t)$" was measured about 10%. The part of the solid particle which did not react "$a(t)$" was decreased about 8%. The part of the solid particle reacted with water "$b(t)$" was increased by 3.5%. another parameter for weight loss, sublimation, "c(t)" increased about 4.5%.
2. Prediction of the porosity is a challenge in a porous material. Using this method with measuring weight, volume and moisture content of the material all the properties including porosity can be predicted. Along the porosity, the specific weight also increased with time. This study expresses the specific weight of cement (w/c=0.4) in 830 days of curing increased by 8%.
3. The resistivity measurement is a nondestructive measurement in order to predict the behavior of the material transition during curing time. For example, rather than measuring

moisture content through resistivity measurements expresses the moisture content changes and by using weigh and volume change all other properties are predictable. It this study the parameter “b(t)” found to be the most sensitive parameter among others when this parameter changes a bit the resistivity changes more rapidly.

4. The existence of micro cracks inside the cement in the oil well may cause gas migration the disasters might happen if the crack growth is not recognized in a right time and right place. Therefore, the knowledge of the cracks inside the cement is a vital task in oil well cement. Due to this important element (cemented casing), the fracture was investigated for the smart cement. The electrical measurement was evaluated beside the mechanical properties of the fracture, the piezoresistivity effects was monitored during the crack growth and crack mouth opening displacement. The relationship between the crack mouth displacement and the resistivity changes was developed.
5. The electrical measurement was evaluated beside the mechanical properties of the fracture, the piezoresistivity changed by 4.2 % during the fracture test.
6. Stress intensity factors for the considered classes of oil well cement varied from 0.3 to 2.2 MPa.√m. Elastic Crack Tip Opening Displacement ($CTOD^e$) varied up to 25 µm. The experimental result was validated with numerical analysis for stress intensity factor.
7. The equivalent resistance for a 3D conductive medium was studied using transformation of Wye to Delta methods.
8. The new failure criterion is introduced (Vipulanandan failure criterion), using Hyperbolic equation to capture the failure criterion of various types of rock in triaxial test and compared with the Drucker–Prager criterion.

CHAPTER 5. DRILLING AND WELL INSTALLATION

5.1. Borehole Drilling

By considering a cylinder rotating in a fluid at risk, the particles will be entrained through shear forces with the steady state situation, it is called irrotational flow in which there is no radial velocity and the tangential velocity is constant The flow around the rotating circular cylinder has a constant angular velocity, placed in a uniform stream (Stojkovic et al., 2002; Chattot and Hafez, 2015).

Flow past a circular cylinder is perhaps one of the popular candidate in theoretical, experimental and numerical studies of flows. The flow geometry is simple and two-dimensional but the flow actually involves vortices. Numerous investigations have been focused on the development and dynamics of the large-scale vortex street shed from the circular cylinder (Cantwell and Coles, 1983). This is because these vortices are largely responsible for physical processes associated with the flow, such as heat transfer, fluid mixing and noise generation (Lam, 2009).

Various studies have been performed on the effects of eccentricity of the drilled hole. Ajovalasit (1979) performed a theoretical study on the influence of eccentricity while the theoretical studies are mostly based on Kirsch's solution (1970). Kim et al. (2002) studied on the prediction of the error due to the eccentricity of hole in the uniaxial residual stress field using finite element and numerical analyses. In this study, the complex potential theory is used to investigate the effects of the eccentricity in vortex flow.

5.1.1. Continuity Equation

Consider the elementary rectangle of fluid of dx, dy as shown in Fig. 5 - 1. The velocities in the x and y directions are u and υ, respectively (Nakayama and Boucher, 1998). There is a thickness of b for this element, the flow rate can be written in x direction as

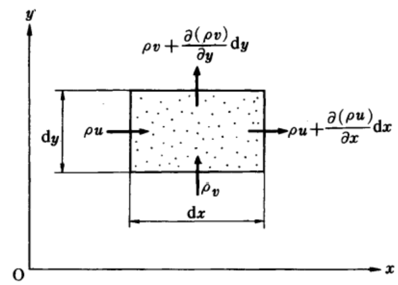

Fig. 5 - 1: Flow balance in a fluid element

$$\rho u\, b\, dy - \left[\rho u + \frac{\partial(\rho u)}{\partial x} dx\right] b\, dy = -\frac{\partial(\rho u)}{\partial x} b\, dx\, dy. \qquad \textbf{(5 - 1)}$$

The same for y direction is

$$\rho \upsilon\, b\, dx - \left[\rho \upsilon + \frac{\partial(\rho \upsilon)}{\partial y} dy\right] b\, dx = -\frac{\partial(\rho \upsilon)}{\partial y} b\, dx\, dy. \qquad \textbf{(5 - 2)}$$

Therefore, the continuity equation can be derived as Eq. (5 - 9)

$$-\frac{\partial(\rho u)}{\partial x} b\, dx\, dy - \frac{\partial(\rho \upsilon)}{\partial y} b\, dx\, dy = \frac{\partial(\rho\, b\, dxdy)}{\partial t},$$

$$\frac{\partial(\rho)}{\partial t} + \frac{\partial(\rho u)}{\partial x} + \frac{\partial(\rho \upsilon)}{\partial y} = 0. \qquad \textbf{(5 - 3)}$$

In the case of polar coordinate, the continuity equation is

$$\frac{\partial(\rho)}{\partial t} + \frac{1}{r}\frac{\partial(r\rho \upsilon_r)}{\partial r} + \frac{1}{r}\frac{\partial(\rho \upsilon_\theta)}{\partial \theta} = 0. \qquad \textbf{(5 - 4)}$$

Eq. (5 - 9) is applicable to the unsteady flow of a compressible fluid. In the case of steady flow, the first term becomes zero. For an incompressible fluid (applicable to both steady and unsteady flows), $\boldsymbol{\rho}$ is constant, so the following equation is obtained as

$$\frac{\partial u}{\partial x}+\frac{\partial v}{\partial y}=0. \tag{5 - 5}$$

For an incompressible fluid, in polar coordinate system, the continuity equation is

$$\frac{1}{r}\frac{\partial(rv_r)}{\partial r}+\frac{1}{r}\frac{\partial(v_\theta)}{\partial\theta}=0. \tag{5 - 6}$$

The continuity equation is independent of whether the fluid is viscous or not.

5.1.2. Velocity Potential

The relationship of the velocity potential Φ as a function of x and y is as following:

$$\boldsymbol{V}=[u,v]=\nabla\phi$$

$$u=\frac{\partial\phi}{\partial x}, \tag{5 - 7}$$

$$v=\frac{\partial\phi}{\partial y}.$$

Where **V** is the velocity vector. The derivative of the velocity in x direction with respect to y and the derivative of the velocity in y direction with respect to x is

$$\frac{\partial u}{\partial y}=\frac{\partial^2\phi}{\partial x\partial y},$$

$$\frac{\partial v}{\partial x}=\frac{\partial^2\phi}{\partial x\partial y}, \tag{5 - 8}$$

Therefore,

$$\frac{\partial u}{\partial y} = \frac{\partial \upsilon}{\partial x}. \tag{5 - 9}$$

This is the condition for irrotational motion. Conversely, if a flow is irrotational, function Φ as in the following equation must exist for u and υ as

$$d\phi = udx + \upsilon dy. \tag{5 - 10}$$

In the polar coordinate system, the velocity is defined as

$$\upsilon_r = \frac{\partial \phi}{\partial r},$$
$$\upsilon_\theta = \frac{\partial \phi}{r\partial \theta}. \tag{5 - 11}$$

For the potential flow of an incompressible fluid, substitute Eq. (5 - 7) into continuity equations (5 - 5) and the following relationship which is the Laplace's equation is obtained (Nakayama and Boucher, 1998) as

$$\frac{\partial^2 \phi}{\partial x^2} + \frac{\partial^2 \phi}{\partial y^2} = 0. \tag{5- 12}$$

5.1.3. Stream Function

If in the Eq. (5 - 10), u replaced with – υ and v replaced by u, the following equation can be defined as

$$d\psi = -\upsilon dx + udy. \tag{5 - 13}$$

and $d\psi$ can also be written as

$$d\psi = \frac{\partial \psi}{\partial x} dx + \frac{\partial \psi}{\partial y} dy. \tag{5 - 14}$$

u and υ are respectively expressed as

$$-\upsilon = \frac{\partial \psi}{\partial x},$$
$$u = \frac{\partial \psi}{\partial y}. \tag{5 - 15}$$

In the polar coordinate system, the velocity is

$$\upsilon_\theta = -\frac{\partial \psi}{\partial r},$$
$$\upsilon_r = \frac{\partial \psi}{r\partial \theta}. \tag{5 - 16}$$

5.1.4. Complex Potential

For a two-dimensional incompressible potential flow, since the velocity potential Φ and stream function ψ exist.

The following equations result from Eqs. (5 - 7) and (5 - 15) as

$$\frac{\partial \phi}{\partial y} = -\frac{\partial \psi}{\partial x},$$
$$\frac{\partial \phi}{\partial x} = \frac{\partial \psi}{\partial y}. \tag{5 - 17}$$

These equations are called the Cauchy-Riemann equations in the theory of complex variables. consider a complex function w(z) of complex variable z = x + iy by dividing it into real and imaginary parts (Nakayama and Boucher, 1998) and express it as following:

$$w(z) = \phi + i\psi$$

$$z = x + iy = r(cos\theta + i\,sin\theta) = re^{i\theta} \qquad \textbf{(5 - 18)}$$

$$\phi = \phi(x, y), \qquad \psi = \psi(x, y).$$

The complex function w(z) can be written as complex variable z = x + iy as

$$dw = \frac{\partial w}{\partial x}dx + \frac{\partial w}{\partial y}dy = \left(\frac{\partial \phi}{\partial x} + i\frac{\partial \psi}{\partial x}\right)dx + \left(\frac{\partial \phi}{\partial y} + i\frac{\partial \psi}{\partial y}\right)dy,$$

(5 - 19)

$$dw = (u - iv)dx + (v + iu)dy = (u - iv)(dx + idy) = (u - iv)dz.$$

And in the polar coordinate system, it can be expressed as

$$dw = \frac{\partial w}{\partial r}dr + \frac{1}{r}\frac{\partial w}{\partial \theta}d\theta = \left(\frac{\partial \phi}{\partial r} + i\frac{\partial \psi}{\partial r}\right)dr + \frac{1}{r}\left(\frac{\partial \phi}{\partial \theta} + i\frac{\partial \psi}{\partial \theta}\right)d\theta,$$

(5 - 20)

$$dw = (v_r - iv_\theta)dr + \frac{1}{r}(rv_\theta + irv_r)d\theta.$$

(a) Free Vortex

If fluid rotates around the origin with tangential velocity v_θ at any given radius r (Fig. 5 - 2) (Nakayama and Boucher, 1998)**.**

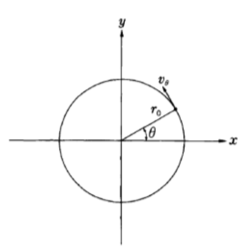

Fig. 5 - 2: Vortex

There is no velocity in r direction $v_\theta = 0$. Eq. (5 - 11) can be written as

$$v_\theta = \frac{\partial\phi}{r\partial\theta} = \frac{k}{r},$$
$$v_r = \frac{\partial\phi}{\partial r} = 0. \tag{5 - 21}$$

Therefore, the potential function Φ can be a function of θ but it cannot be a function of r due to Eq. (5 - 21). Which is defined as

$$\phi = k\theta. \tag{5 - 22}$$

Where k is called circulation. Eq. (5 - 16) can be expressed as

$$v_\theta = -\frac{\partial\psi}{\partial r} = \frac{k}{r},$$
$$v_r = \frac{\partial\psi}{r\partial\theta} = 0 \tag{5 - 23}$$

The stream function ψ can be integrated from Eq. (5 - 23) and expressed as

$$\psi = -k\ln(r). \tag{5 - 24}$$

Therefore, the complex form of the potential and stream function is

$$w(z) = \phi + i\psi = k\theta - ki\ln(r) = -ki\,[i\theta + \ln(r)] = -ki\,ln(z). \tag{5 - 25}$$

For the vortex it was proved that the complex potential function is

$$w(z) = -ki\ln(z),$$
$$w(r,\theta) = -ki\ln\left(re^{i\theta}\right). \tag{5 - 26}$$

(b) Free vortex with eccentricity

With the with the eccentricity of z_0 (at radius r_0 and at the θ_0), it can be subtracted from the function z as following:

$$w(z) = -ki\, ln(z - z_0),$$
$$w(r,\theta) = -ki\, ln\left(re^{i\theta} - r_0 e^{i\theta_0}\right). \quad \textbf{(5 - 27)}$$

According to Eq. (5 - 20), by taking the derivative of the complex potential function (Eq. (5 - 27)). The derivative can be written as

$$\frac{\partial w}{\partial r} = \frac{-ki\left(ie^{i\theta}\right)}{re^{i\theta} - r_0 e^{i\theta_0}} = \frac{-ki(cos\theta + i\, sin\theta)}{(r.cos\theta + i\, r.sin\theta) - (r_0.cos\theta_0 + i\, r_0.sin\theta_0)}. \quad \textbf{(5 - 28)}$$

By simplifying Eq. (5 - 28), $\frac{\partial w}{\partial r}$ is defined as

$$\frac{\partial w}{\partial r} = \frac{-ki(cos\theta + i\, sin\theta)}{(r.cos\theta - r_0.cos\theta_0) + i(r.sin\theta - r_0.sin\theta_0)},$$
$$\frac{\partial w}{\partial r} = \frac{-ki(cos\theta + i\, sin\theta)}{X + iY}. \quad \textbf{(5 - 29)}$$

Where $X = r.cos\theta - r_0.cos\theta_0$ and $Y = r.sin\theta - r_0.sin\theta_0$ and by more simplification, it can be expressed as

$$\frac{\partial w}{\partial r} = \frac{-ki(cos\theta + i\, sin\theta)}{X + iY} \times \frac{X - iY}{X - iY} = \frac{-ki(cos\theta + i\, sin\theta)(X - iY)}{X^2 - i^2 Y^2},$$
$$\frac{\partial w}{\partial r} = \frac{k(X.sin\theta - Y.cos\theta)}{X^2 + Y^2} - i\frac{k(Y.sin\theta + X.cos\theta)}{X^2 + Y^2}. \quad \textbf{(5 - 30)}$$

And according to Eq. (5 - 20), the derivatives can be written as

$$\frac{\partial w}{\partial r} = \frac{\partial \phi}{\partial r} + i\frac{\partial \psi}{\partial r} = \frac{k(X.sin\theta - Y.cos\theta)}{X^2 + Y^2} - i\frac{k(Y.sin\theta + X.cos\theta)}{X^2 + Y^2},$$

$$\frac{\partial \phi}{\partial r} = \frac{k(X.sin\theta - Y.cos\theta)}{X^2 + Y^2}, \tag{5 - 31}$$

$$\frac{\partial \psi}{\partial r} = \frac{-k(Y.sin\theta + X.cos\theta)}{X^2 + Y^2}.$$

And $\frac{\partial \phi}{\partial r} + i\frac{\partial \psi}{\partial r} = v_r - iv_\theta$, therefore, velocity can be expressed as

$$v_r = \frac{\partial \phi}{\partial r} = \frac{k(X.sin\theta - Y.cos\theta)}{X^2 + Y^2},$$

(5 - 32)

$$v_\theta = \frac{\partial \psi}{\partial r} = \frac{k(Y.sin\theta + X.cos\theta)}{X^2 + Y^2}.$$

And by substituting X and Y, the velocities for an eccentric flow expressed as following:

$$v_r = \frac{\partial \phi}{\partial r} = k\frac{(r.cos\theta - r_0.cos\theta_0).sin\theta - (r.sin\theta - r_0.sin\theta_0).cos\theta}{(r.cos\theta - r_0.cos\theta_0)^2 + (r.sin\theta - r_0.sin\theta_0)^2},$$

(5 - 33)

$$v_\theta = \frac{\partial \psi}{\partial r} = k\frac{(r.sin\theta - r_0.sin\theta_0).sin\theta + (r.cos\theta - r_0.cos\theta_0).cos\theta}{(r.cos\theta - r_0.cos\theta_0)^2 + (r.sin\theta - r_0.sin\theta_0)^2}.$$

In a special case, if we assume θ and θ_0 to be zero, the radial and tangential velocities will be

$$v_r = 0,$$

(5 - 34)

$$v_\theta = \frac{k}{(r - r_0)}.$$

Fig. 5 - 3 (a) shows the concentric vortex flow when there is no eccentricity, Fig. 5 - 3 (b), (c) and (d) are related to the eccentricity of 0.25, 0.35 and 0.5, respectively.

expresses the velocity related to these four cases and compared the tangential velocity when the circulation is assumed to be 1.

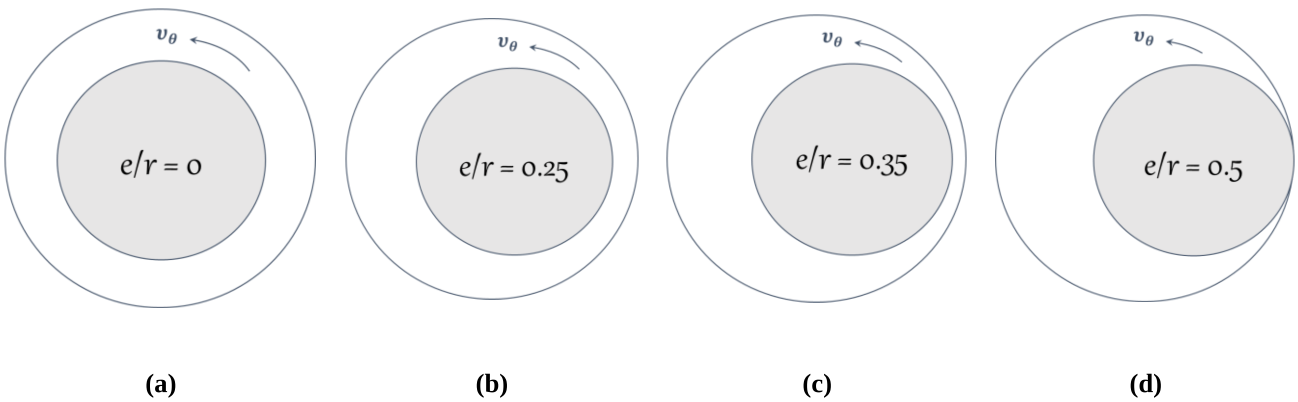

Fig. 5 - 3: Four different case of free vortex flow; (a) Concentric flow, (b) Eccentric, e/r = 0.25, (c) Eccentric, e/r = 0.35, (d) Eccentric, e/r = 0. 5

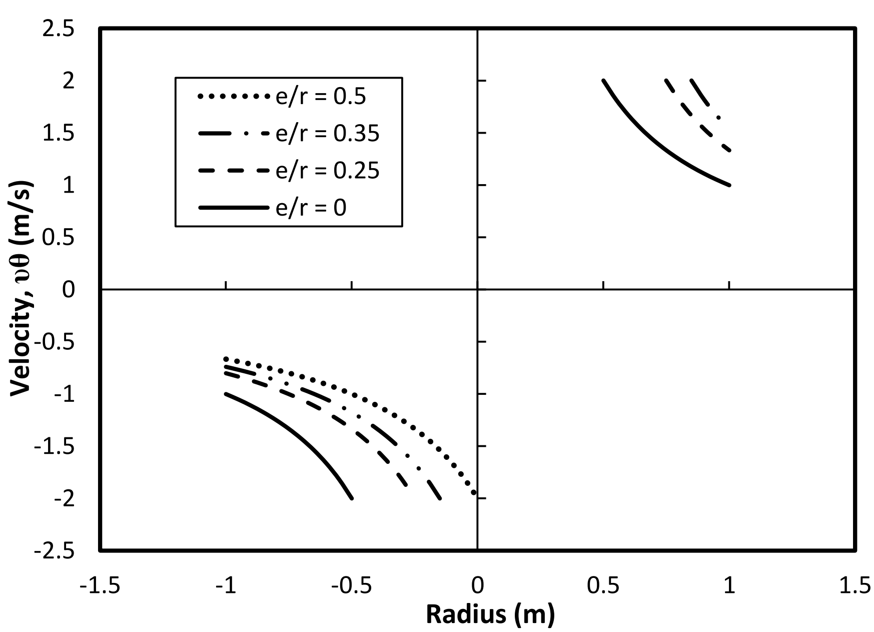

Fig. 5 - 4: Comparison of velocity in concentric and eccentric vortex flow

5.2. Well Installation (Axial Flow)

The drilling mud and also cement slurry showed non-linear shear thinning behavior with a yield stress. The Bingham plastic model and the Power law model are widely used in the industry as rheological models for drilling mud and cement slurries (Guillot, 1990). Azar and Samuel (2007) proposed the analytical model for determination of the velocity generated by Newtonian, Power law and Bingham model for the fluid flow. In this study a new shear thinning rheological model called Hyperbolic model (Vipulanandan and Mohammad, 2014) is proposed to evaluate the flow pattern of the drilling fluid in the borehole. In the Newtonian, Power law and Bingham model, when the strain rate reaches infinity, the shear rate also reaches to infinity, which is not in the reality, since there is limit to the shear stress carried by any material including the drilling mud. The hyperbolic model eliminates this problem and the trend is much close to the reality. In this study, the analytical modeling of the axial fluid flow is investigated for the drilling mud. The Newtonian model analytical solution is shown and the Hyperbolic model is proposed (Vipulanandan and Mohammed, 2014) which does not have the limitation of the Newtonian model.

The hyperbolic model flow pattern was verified with numerical model using the COMSOL Multiphysics. Also, the hyperbolic model used to simulate the effect of the eccentricity numerically in axial flow.

Following conditions have to be satisfied for the shear thinning model to represent the observed behavior, defined as

$$\begin{gathered}\frac{\partial \tau}{\partial \dot{\gamma}} > 0, \\ \frac{\partial^2 \tau}{\partial \dot{\gamma}^2} > 0, \\ \dot{\gamma} = 0 \implies \tau = \tau_0, \\ \dot{\gamma} \to \infty \implies \tau = \tau^*. \end{gathered} \tag{5 - 35}$$

Hyperbolic model which is called Vipu Model in this study (Vipulanandan and Mohammed, 2014(Vipulanandan and Mohammed, 2014), is defined as

$$\tau = \tau_0 + \frac{\dot{\gamma}}{A + B\dot{\gamma}}. \qquad \textbf{(5 - 36)}$$

Where τ_0 is the yield stress (Pa), $\dot{\gamma}$ is the shear strain rate (s^{-1}), A $(Pa.s)^{-1}$ and B $(Pa)^{-1}$ are model parameters. Hyperbolic model (Vipu Model) is a shear thinning model which has to satisfy the following conditions, which are expressed as

$$\begin{gathered}
\frac{\partial \tau}{\partial \dot{\gamma}} = \frac{A}{(A + B\dot{\gamma})^2} > 0 \implies A > 0, \\
\frac{\partial^2 \tau}{\partial \dot{\gamma}^2} = \frac{-2AB}{(A + B\dot{\gamma})^3} < 0 \implies B > 0, \\
\dot{\gamma} = 0 \implies \tau = \tau_0, \\
\dot{\gamma} \to \infty \implies \tau_{max} = \frac{1}{B}\tau_{02}.
\end{gathered} \qquad \textbf{(5 - 37)}$$

The linear (Newtonian) and shear thinning (Hyperbolic) model of the fluid is shown as

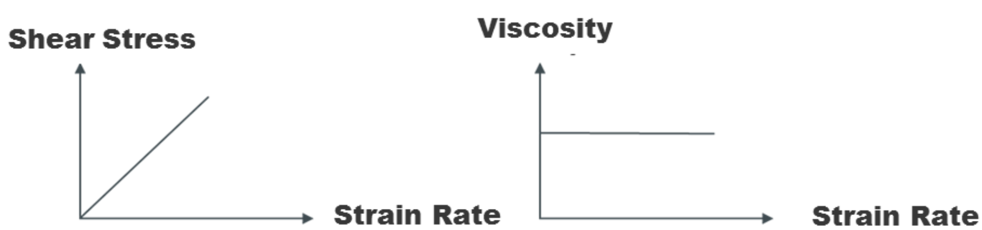

Fig. 5 - 5: Linear behavior (Newtonian fluid behavior)

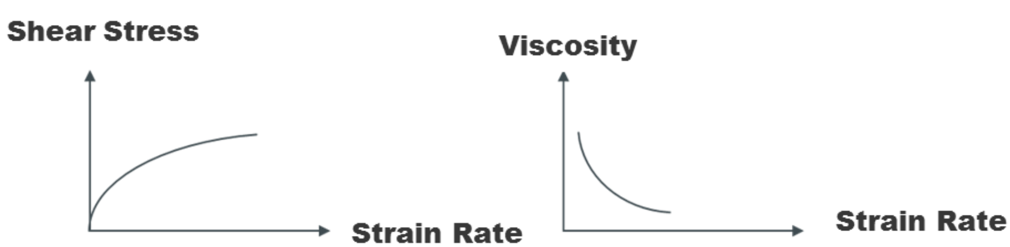

Fig. 5 - 6: The shear thinning behavior, Hyperbolic Model, (Vipulanadan and Mohammad, 2014))

5.2.1. Equilibrium in Cylindrical Coordinate System

The velocity at some arbitrary point is defined as

$$\mathbf{V} = \nu_r \mathbf{e_r} + \nu_\theta \mathbf{e_\theta} + \nu_z \mathbf{e_z}. \tag{5 - 38}$$

Where ν_r, ν_θ and ν_z are the velocity of the flow in r, ɵ and z directions.

The relationship between the velocity and the strain rate in a cylindrical coordinate system is defined as

$$\begin{aligned}
\dot{\varepsilon_r} &= \frac{\partial v_r}{\partial r}, \\
\dot{\varepsilon_\theta} &= \frac{v_r}{r} + \frac{1}{r} . \frac{\partial v_\theta}{\partial \theta}, \\
\dot{\varepsilon_z} &= \frac{\partial v_z}{\partial z}, \\
\dot{\gamma}_{r\theta} &= \frac{1}{2}\left(\frac{\partial v_\theta}{\partial r} + \frac{1}{r} . \frac{\partial v_r}{\partial \theta}\right), \\
\dot{\gamma}_{z\theta} &= \frac{1}{2}\left(\frac{1}{r} . \frac{\partial v_z}{\partial \theta} + \frac{\partial v_\theta}{\partial z}\right), \\
\dot{\gamma}_{zr} &= \frac{1}{2}\left(\frac{\partial v_r}{\partial z} + \frac{\partial v_z}{\partial r}\right).
\end{aligned} \tag{5 - 39}$$

In the axisymmetric condition the velocity in circumferential direction and the derivative of this direction is zero $v_\theta = 0, \frac{\partial}{\partial \theta} = 0$. Therefore, the strain rates will be simplified as

$$\begin{aligned}
\dot{\varepsilon_r} &= \frac{\partial v_r}{\partial r}, \\
\dot{\varepsilon_\theta} &= \frac{v_r}{r}, \\
\dot{\varepsilon_z} &= \frac{\partial v_z}{\partial z}, \\
\dot{\gamma}_{zr} &= \frac{1}{2}\left(\frac{\partial v_r}{\partial z} + \frac{\partial v_z}{\partial r}\right).
\end{aligned} \tag{5 - 40}$$

The assumptions are made as following:

- Axisymmetric condition and no swirl, $v_\theta = 0, \frac{\partial}{\partial\theta} = 0$
- Flow is laminar and parallel to the wall, $v_r = 0$
- Steady Flow, $\frac{\partial}{\partial t} = 0$
- Fully-developed Flow, $\frac{\partial}{\partial z} = 0$

Therefore,

$$\dot{\varepsilon_r} = \dot{\varepsilon_\theta} = \dot{\varepsilon_z} = 0,$$

$$\dot{\gamma}_{r\theta} = \dot{\gamma}_{z\theta} = 0, \tag{5 - 41}$$

$$\dot{\gamma}_{zr} = \frac{1}{2}\left(\frac{dv_z}{dr}\right).$$

The equilibrium equation in cylindrical coordinate system was studied for the drilling mud with axial flow for an element shown in Fig. 5 - 7.

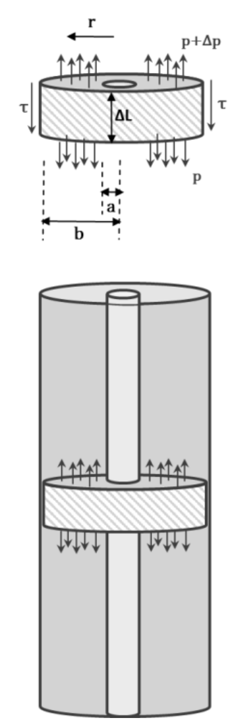

Fig. 5 - 7: Drilling mud axial flow scheme

The shear stress in outer side and inner side of the element is calculated as Fs. The force due to piezo head and due to gravity is Fp and Fg, respectively defined as

$$F_S = [(\tau + \Delta\tau).2\pi(r + \Delta r) - \tau.2\pi(r)].\Delta l = (\tau.\Delta r + \Delta\tau.r).2\pi\Delta l,$$

$$F_p = [(p + \Delta p).2\pi(r + \Delta r) - \tau.2\pi(r)].\Delta l = 2\pi\,\Delta p\,\Delta r, \quad \textbf{(5 - 42)}$$

$$F_g = \rho g.2\pi r.\Delta r\Delta l,$$

By substituting the Eqs. (5 - 42) into $F_p + F_s = F_g$, it can be written as

$$2\pi\,\Delta p\,\Delta r + (\tau.\Delta r + \Delta\tau.r).2\pi\Delta l = \rho g.2\pi r.\Delta r\,\Delta l. \quad \textbf{(5 - 43)}$$

Therefore,

$$\frac{\tau}{r} + \frac{\Delta\tau}{\Delta r} = \left(\frac{\Delta p}{\Delta z} - \rho g\right). \quad \textbf{(5 - 44)}$$

Eq. (5 - 44) is a first order differential equation which can be solved as Eq. - 45)

$$\tau = \frac{r}{2}.\left(\frac{\Delta p}{\Delta z} - \rho g\right) + \frac{C_1}{\mathrm{r}}. \quad \textbf{(5 - 45)}$$

(a) Newtonian Fluid Flow

For a Newtonian fluid flow, the constitutive model is a linear relationship between the shear stress and strain rate defined as

$$\tau_{zr} = \mu\dot{\gamma}_{zr}. \quad \textbf{(5 - 46)}$$

by substituting Eq. (5 - 41) and - 45) in Eq. (5 - 46). It can be written as

$$\dot{\gamma}_{zr} = \frac{1}{\mu}\left(\frac{r}{2}.\left(\frac{\Delta p}{\Delta z} - \rho g\right) + \frac{C_1}{\mathrm{r}}\right). \qquad \textbf{(5 - 47)}$$

and by taking the integration as

$$\int dv_z = \frac{2}{\mu}\int \left(\frac{r}{2}.\left(\frac{\Delta p}{\Delta z} - \rho g\right) + \frac{C_1}{\mathrm{r}}\right)\, dr. \qquad \textbf{(5 - 48)}$$

The velocity will is

$$v_z = 2\left(\frac{r^2}{4\mu}.\left(\frac{\Delta p}{\Delta z} - \rho g\right) + \frac{C_1}{\mu}\ln(r) + C_2\right). \qquad \textbf{(5 - 49)}$$

Now by applying the boundary conditions: at r = a and r = b the velocity will be zero. The two constant from Eq. (5 - 49) will be derived as

$$C_1 = -\frac{(b^2 - a^2)\left(\frac{\Delta p}{\Delta z} - \rho g\right)}{4\ln\left(\frac{b}{a}\right)},$$

$$C_2 = \frac{-a^2}{4\mu}\left(\frac{\Delta p}{\Delta z} - \rho g\right) + \frac{(b^2 - a^2)\left(\frac{\Delta p}{\Delta z} - \rho g\right)}{4\mu ln\left(\frac{b}{a}\right)} l\,n(a). \qquad \textbf{(5 - 50)}$$

Where D = (Δp/Δz - ρg) is the piezo head difference which is assumed to be 2 N/m³. If a borehole (a = 0.5 m) with the casing (b = 1 m) and the fluid with a specific weight of γ = 10000 N/m³ and a constant viscosity of 0.02 Pa.s. By applying the boundary conditions, the constant C_1 and C_2 can be derived as 0.54 and 25, respectively.

The constitutive model (shear stress and strain rate relationship) for the Newtonian fluid is a linear relationship, shown in Fig. 5 - 8.

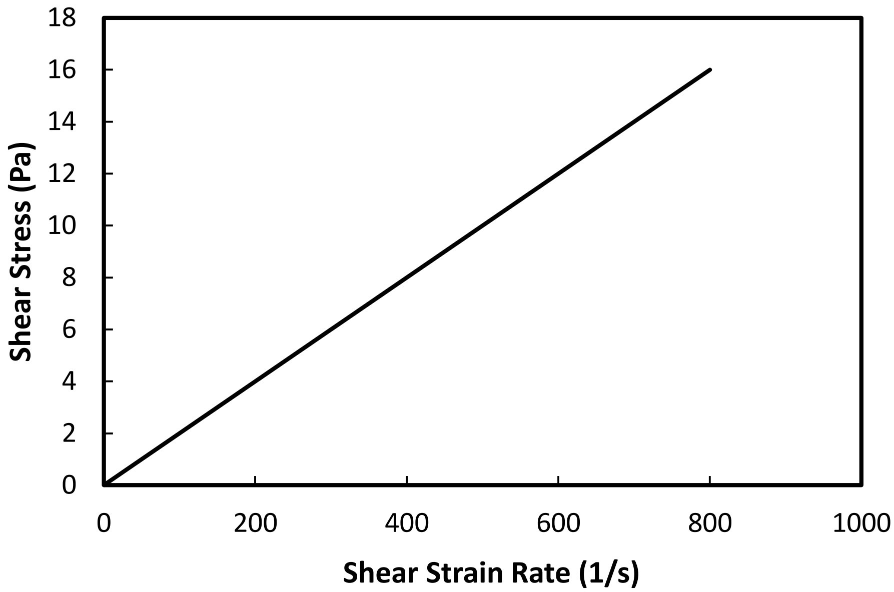

Fig. 5 - 8: Shear stress – strain rate relationship for Newtonian Fluid

The velocity and strain rate are shown along the radius in Fig. 5 - 9 and Fig. 5 - 10, respectively.

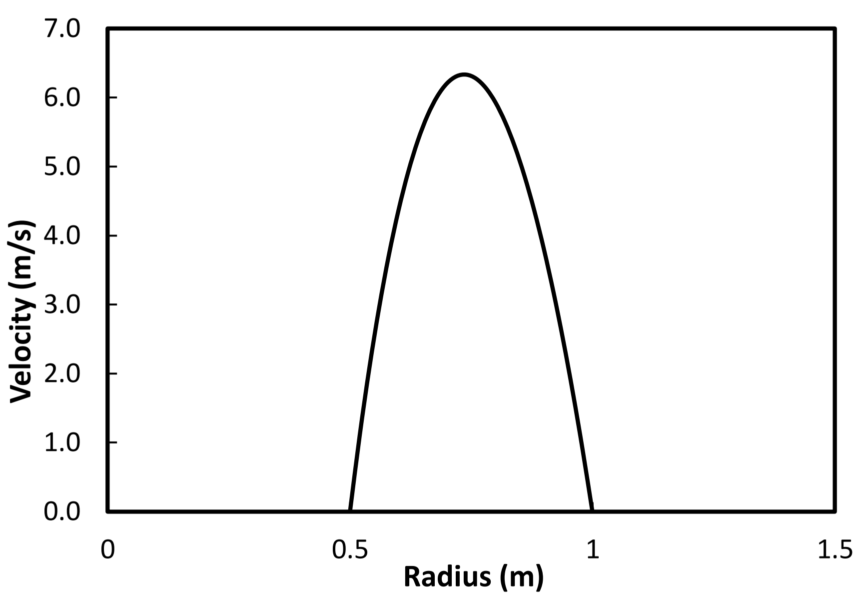

Fig. 5 - 9: Velocity along the radius for Newtonian fluid flow (a = 0.5 m, b = 1 m)

For the Newtonian fluid flow, the shear strain rate is shown as

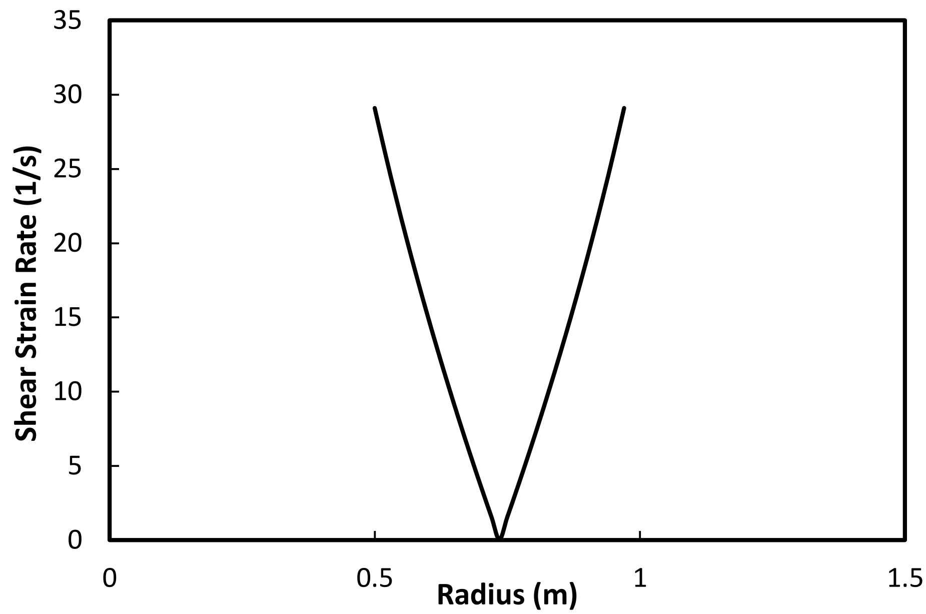

Fig. 5 - 10: Strain rate along the radius for Newtonian fluid flow (a = 0.5 m, b = 1 m)

Fig. 5 - 11 shows the shear stress versus radius while the viscosity is constant

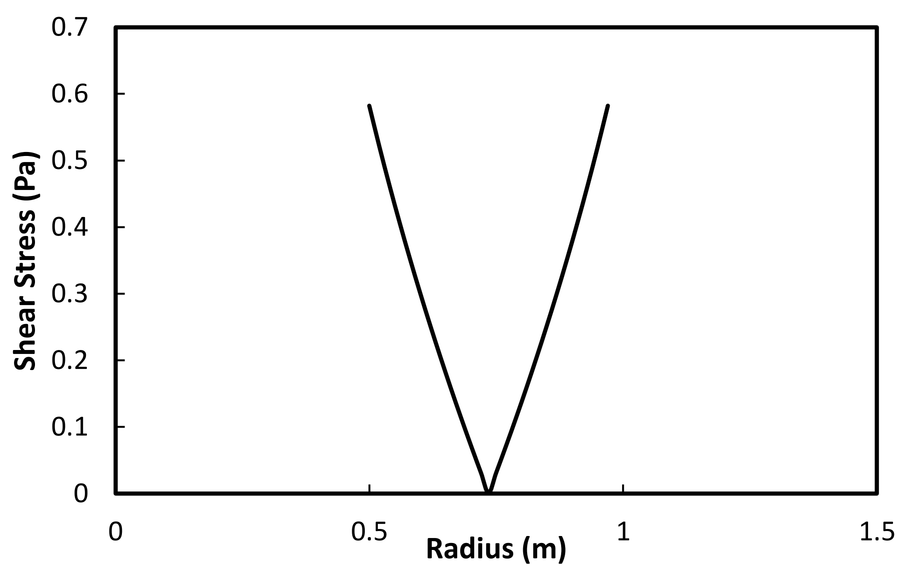

Fig. 5 - 11: Shear stress along the radius for Newtonian fluid flow (a = 0.5 m, b = 1 m)

(a) Hyperbolic Fluid Flow

Now, for a Hyperbolic fluid flow the rheology model is shown as

$$\tau = \tau_0 + \frac{\dot{\gamma}}{A + B\dot{\gamma}}. \qquad \textbf{(5 - 51)}$$

which is the rate of the change of shear rate. The derivative of the shear stress can be derived as

$$\mu = \frac{\partial \tau}{\partial \dot{\gamma}} = \frac{A}{(A + B\dot{\gamma})^2}. \qquad \textbf{(5 - 52)}$$

Where A and B are the hyperbolic model constants. Velocity can be derived by substituting Eq. and - 45) in Eq. (5 - 51**)**, shown as

$$\dot{\gamma} = \frac{\frac{rA}{2}\left(\frac{\Delta p}{\Delta z} - \rho g\right) + \frac{C_1 A}{r} - A\tau_0}{1 - \frac{rB}{2}\left(\frac{\Delta p}{\Delta z} - \rho g\right) - \frac{C_1 B}{r} + B\tau_0}. \qquad \textbf{(5 - 53)}$$

And by taking the integration as

$$\int dv_z = 2\int \left(\frac{\frac{rA}{2}\left(\frac{\Delta p}{\Delta z} - \rho g\right) + \frac{C_1 A}{r} - A\tau_0}{1 - \frac{rB}{2}\left(\frac{\Delta p}{\Delta z} - \rho g\right) - \frac{C_1 B}{r} + B\tau_0} \right) dr. \qquad \textbf{(5 - 54)}$$

The velocity for Hyperbolic fluid flow is shown as

$$v_z = 2\left[-\frac{A}{B}r - \frac{A}{B^2 D} ln(-2r + 2BC_1 + BDr^2 - 2B\tau_0 r) - \frac{4A}{B^2 D\sqrt{8B^2 C_1 D - 4B^2\tau_0^2 - 8B\tau_0 - 4}} . \left(atan\left(\frac{2BDr - 2}{\sqrt{8B^2 C_1 D - 4B^2\tau_0^2 - 8B\tau_0 - 4}} \right) \right) + C_2 \right]. \qquad \textbf{(5 - 55)}$$

The general shear stress and strain rate relationship for the Hyperbolic model is a linear relationship shown in Fig. 5 - 12.

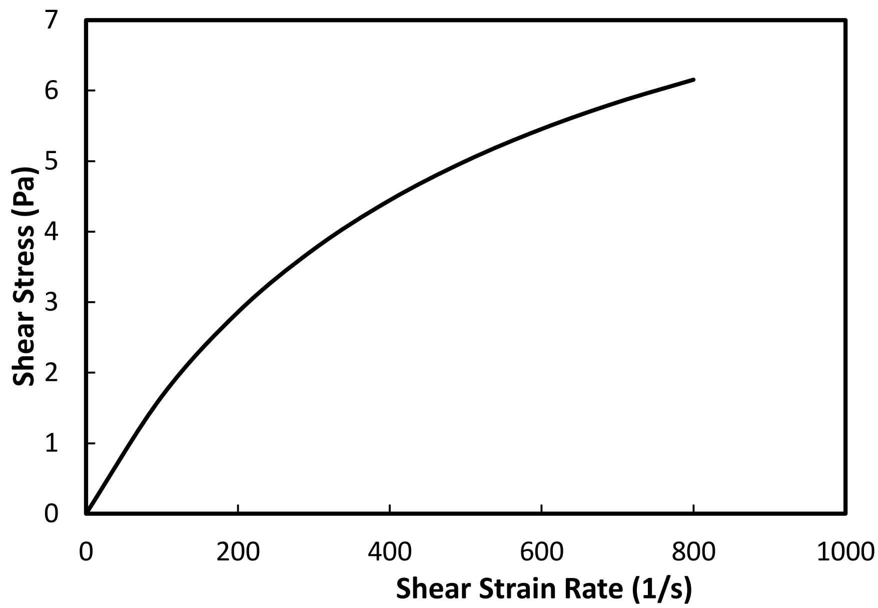

Fig. 5 - 12: Shear stress – strain rate relationship for Hyperbolic Model

In Eq. (5 - 55), D = (Δp/Δz - ρg) is the piezo head difference. Now by applying the boundary conditions: at r = a and r = b the velocity will be zero and using numerical solution for solving two equations and two unknowns Eqs.(5 - 56).

$$
\begin{aligned}
&Equation\ I: \quad -\frac{A}{B}(a)-\frac{A}{B^2D}\ln(-2a+2BC_1+BDa^2)\\
&\qquad -\frac{4A}{B^2D\sqrt{8B^2C_1D-4}}.\left(atan\left(\frac{2BDa-2}{\sqrt{8B^2C_1D-4}}\right)\right)+C_2=0,\\
&Equation\ II: \quad -\frac{A}{B}(b)-\frac{A}{B^2D}\ln(-2b+2BC_1+BDb^2)\\
&\qquad -\frac{4A}{B^2D\sqrt{8B^2C_1D-4}}.\left(atan\left(\frac{2BDb-2}{\sqrt{8B^2C_1D-4}}\right)\right)+C_2=0.
\end{aligned}
\tag{5 - 56}
$$

If the piezo head of D = (Δp/Δz - ρg) is 2 N/m³ with the dimension of borehole, a =0.5 m and the casing b = 1 m with the fluid with a specific weight of γ = 10000 N/m³ and the Hyperbolic model constants A = 50 m²/N.s and B = 0.1 m²/N also the τ_0 is assumed to be zero. By applying the boundary conditions, the constant C_1 and C_2 can be derived as 48.415 and 5590.365, respectively, byThe velocity is shown along the radius in Fig. 5 - 13. Compared with Newtonian flow the velocity is lower in hyperbolic model.

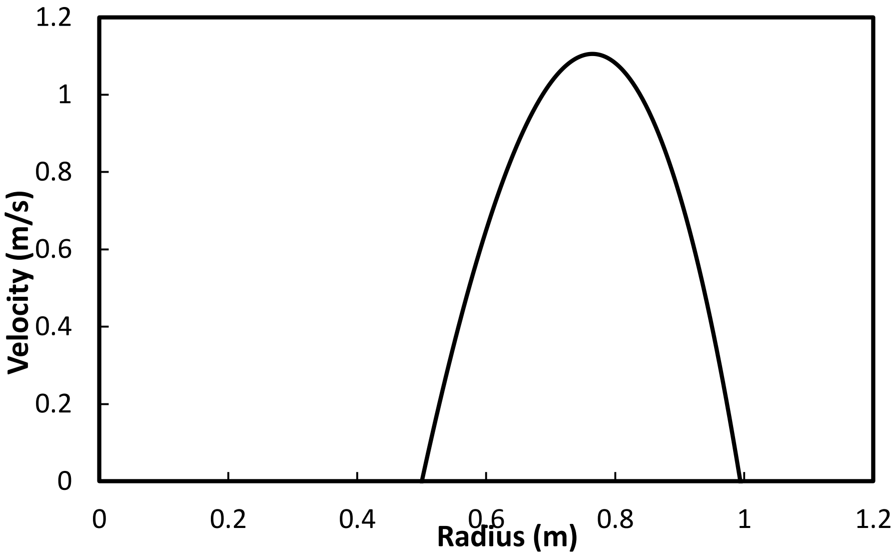

Fig. 5 - 13: Velocity along the radius for Hyperbolic fluid flow (a = 0.5 m, b = 1 m)

Fig. 5 - 14 and Fig. 5 - 15 show the strain rate and shear stress along the radius. The rate of changes in velocity is zero in the middle and higher near the wellbore wall, therefore the strain rate decreased and increased in those zones, respectively.

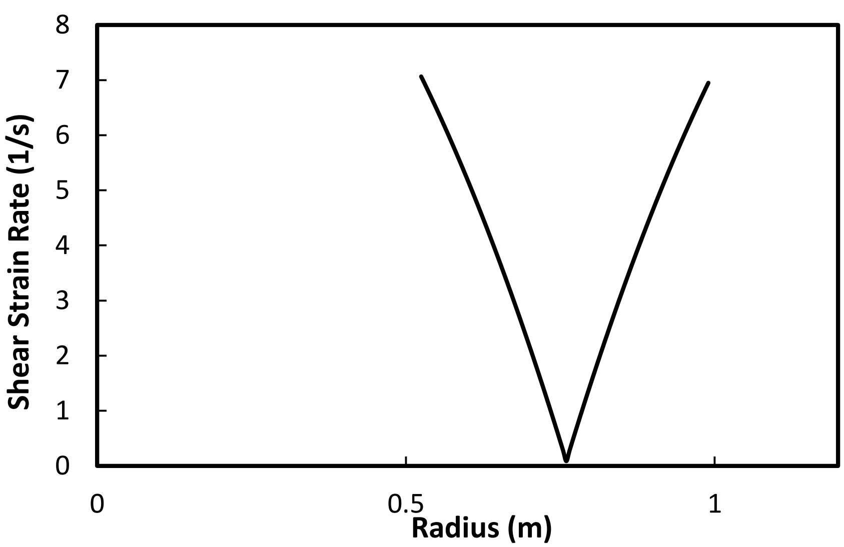

Fig. 5 - 14: Strain rate along the radius for Hyperbolic fluid flow (a = 0.5 m, b = 1 m)

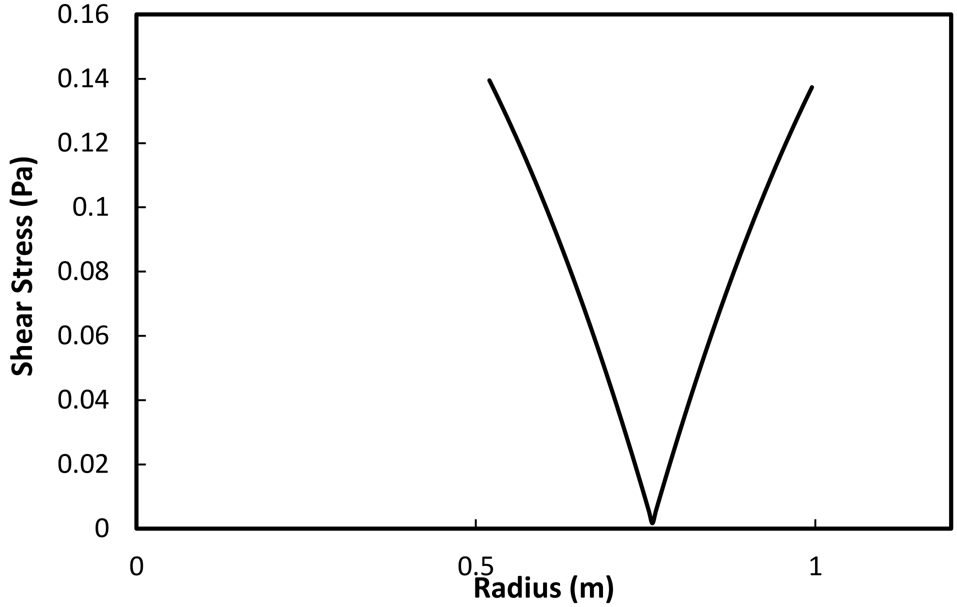

Fig. 5 - 15: Shear stress along the radius for Hyperbolic fluid flow (a = 0.5 m, b = 1 m)

(b) Comparison of the Newtonian Model and Hyperbolic Model

The rheological models including Newtonian and Hyperbolic model is compared in this section. According to the assumptions made which is the piezo head, D = ($\Delta p/\Delta z$-ρg) = 2 N/m³ and the borehole radius of, a = 1 m and the casing radius of b = 0.5 m. The dynamic viscosity in the Newtonian fluid is assumed to be μ = 0.02 Pa.s and Hyperbolic model parameters are found as A = 0.52 m²/N.s and B = 2 Pa.s (Vipulanandan, et al., in 2014) while in this study these constants are assumed to be A = 50 m²/N.s and B = 0.1 m²/N.

Fig. 5 - 16 shows the stress strain rate relationship (rheological model) for the fluid. The rate of the change of the shear versus strain rate is less for the hyperbolic model. For Hyperbolic model, the stress reaches a specific number (1/B) at infinity strain rate, while the stress reaches infinity for the Newtonian fluid. In the reality at high shear strain rate the shear stress does not exceed a number represents the Hyperbolic model.

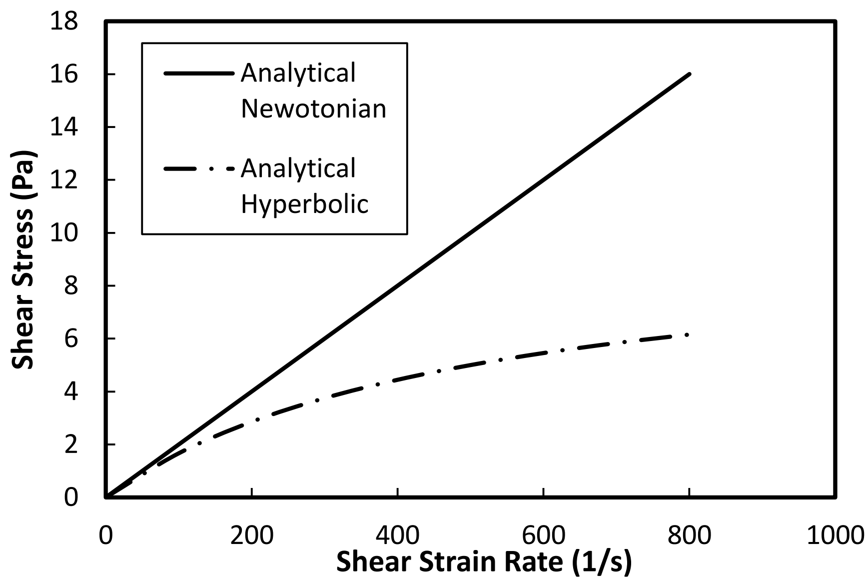

Fig. 5 - 16: Shear stress versus strain rate for Newtonian and Hyperbolic model

The main difference between the Hyperbolic and Newtonian model is the viscosity. The viscosity for the Hyperbolic is a time dependent variable while in the Newtonian fluid it is a constant value. Therefore, the viscosity changes along the radius for Hyperbolic model while it is constant in the Newtonian fluid (Fig. 5 - 17). The viscosity decreases while the strain rate increases.

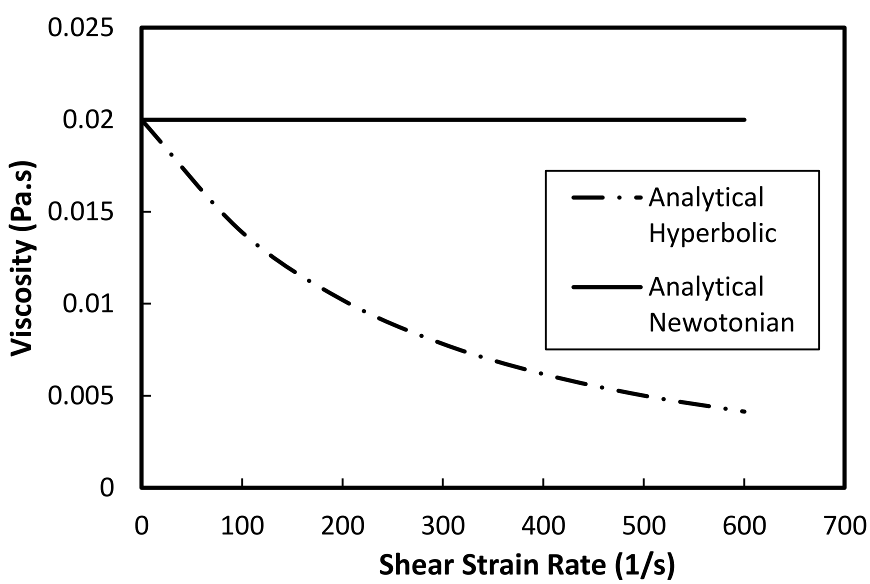

Fig. 5 - 17: Viscosity versus strain rate for Newtonian and Hyperbolic model

Fig. 5 - 18 shows the velocity along the radius. The velocity for Hyperbolic model is about 82% less than Newtonian fluid.

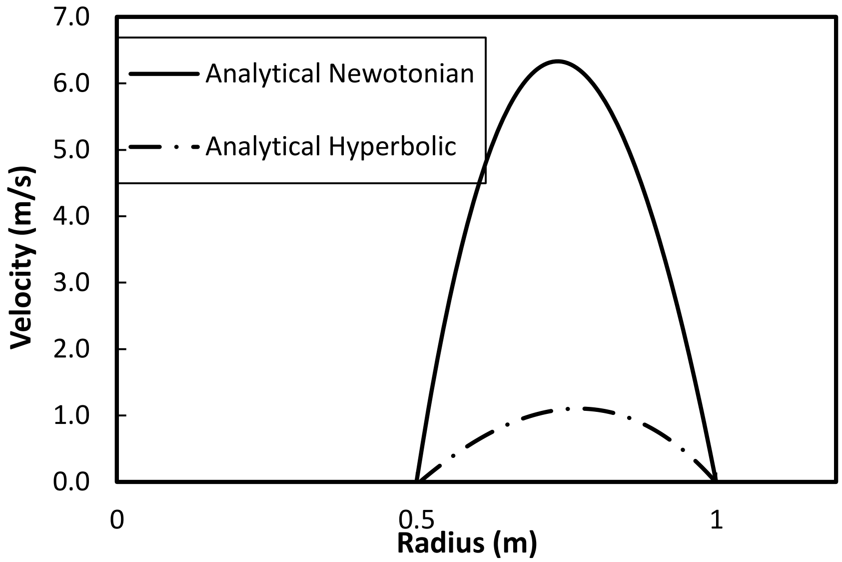

Fig. 5 - 18: Velocity along the radius for Newtonian and Hyperbolic model

The strain rate along the radius is compared for the two models in Fig. 5 - 19.

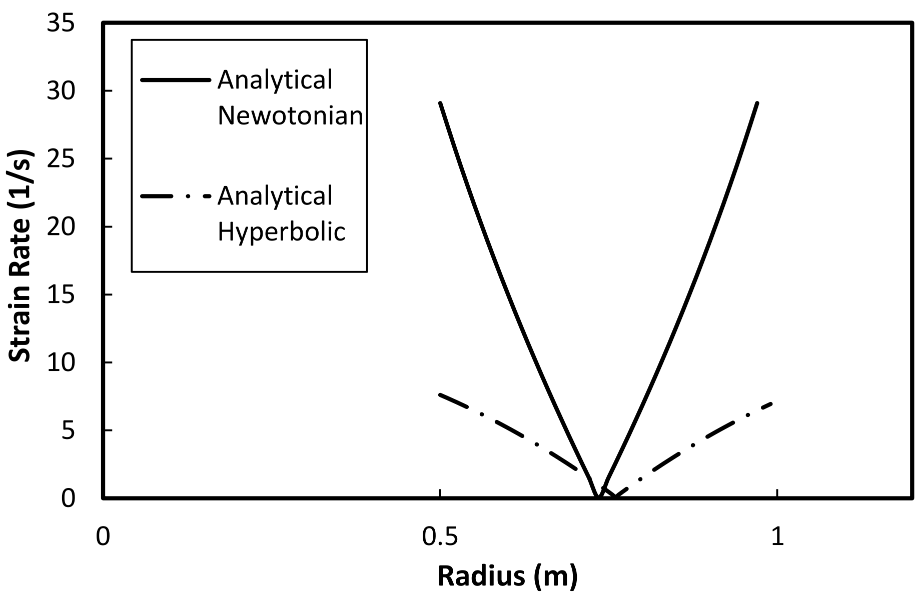

Fig. 5 - 19: Strain rate along the radius for Newtonian and Hyperbolic model

The shear stress in the Hyperbolic model is 74% less than respect to Newtonian model (Fig. 5 - 20).

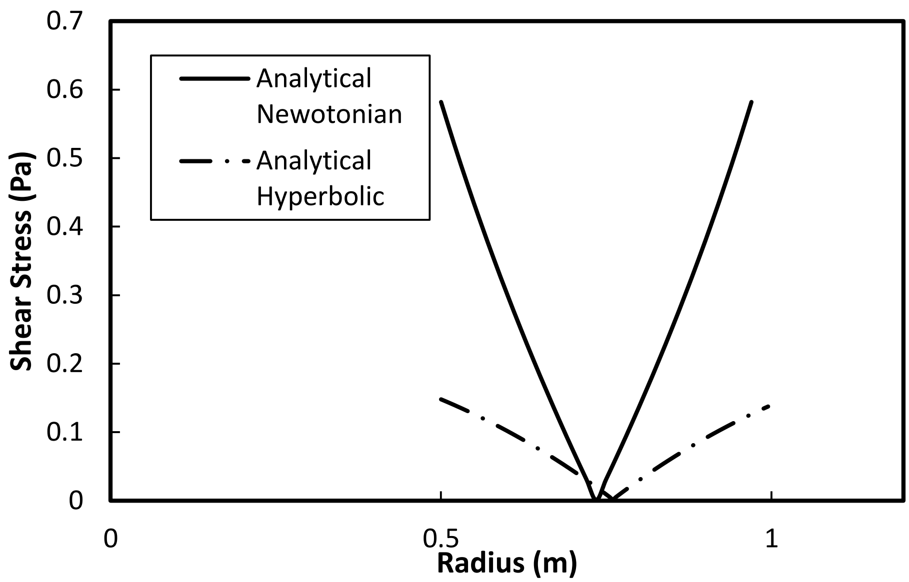

Fig. 5 - 20: Shear stress along the radius for Newtonian and Hyperbolic model

5.3. Numerical Modelling of Axial Drilling Flow

The numerical model is performed with the COMSOL Multiphysics. A drilling fluid model was modeled with CFD Module, the flow was selected to be laminar and stationary. Two cases were modeled the Newtonian and Hyperbolic model.

The borehole radius of, a = 1 m and the casing radius of b = 0.5 m while the length of the fluid is 40 m. The gravity body load was applied as (γ = 10000 N/m^3). the velocity along the walls (inner wall and outer wall) was selected to be zero as the boundary conditions. The piezo head, $D = (\Delta p/\Delta z - \rho g) = 2$ N/m^3. Therefore, by assigning 1 atm pressure or 101,325 Pa at the outlet the inlet pressure should be 493,405 Pa to provide D= 2 N/m^3 pressure along 40-meter length of the fluid.

5.3.1. Mesh Generation

The mesh generation was swept along the model and the six node prismatic element (Fig. 5 - 21) was used to build the mesh for both models, Newtonian fluid and Hyperbolic model. The number of the element was 268000 elements with the maximum size of 10 cm. Fig. 5 - 22 shows the mesh generation along the model.

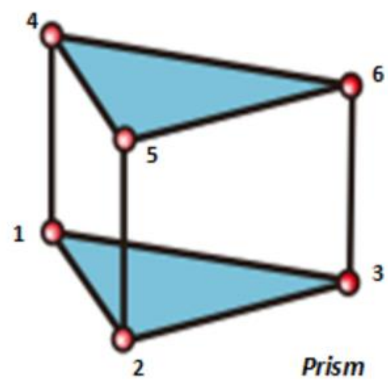

Fig. 5 - 21: Element type: six nodes Prismatic element

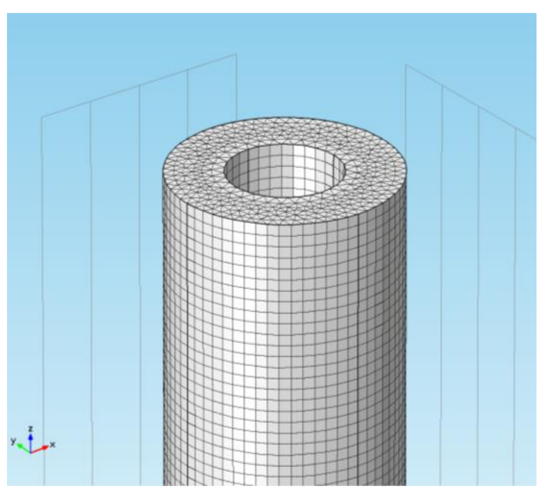

Fig. 5 - 22: Mesh generation along the wellbore

(a) Newtonian flow

The dynamic viscosity in the Newtonian fluid was selected as μ = 0.02 Pa.s and the analytical model result is compared with the numerical analysis results. The velocity of the analytical and numerical model is compared and verified (Fig. 5 - 23) as well as the strain rate values (Fig. 5 - 24).

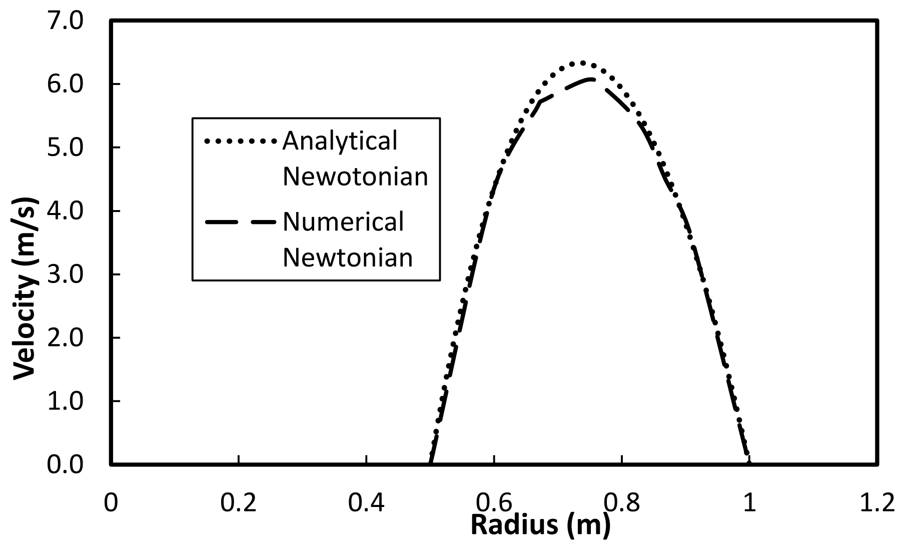

Fig. 5 - 23: Velocity from numerical and analytical modeling along the radius for Newtonian fluid

The shear rate from numerical and analytical models are compared as following.

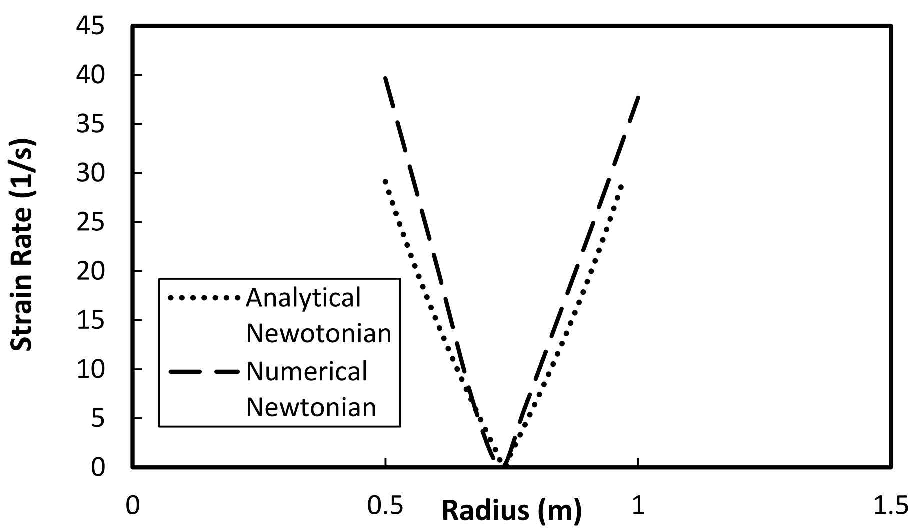

Fig. 5 - 24: Strain rate from numerical and analytical modeling along the radius for Newtonian fluid

The shear stress values are compared in Fig. 5 - 25.

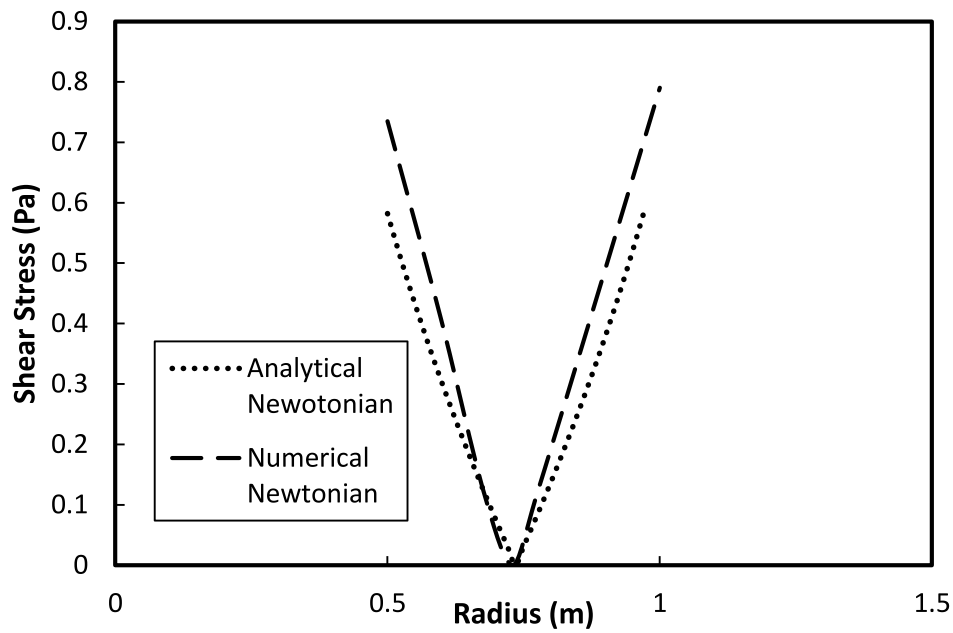

Fig. 5 - 25: Shear stress from numerical and analytical modeling along the radius for Newtonian fluid

(b) Hyperbolic flow

The fluid model in COMSOL Multiphysics is Bingham, Power law and Newtonian model. Hence, the hyperbolic model is selected as new constitutive model which has to be implemented into the software. There are three ways to implement a new function into the software, including: Analytic, Piecewise and Interpolation functions. In this model under the material part the viscosity is selected as a function of strain rate and the viscosity function is defined as an Analytic function for the software. The Eq. (5 - 52) was implemented into the Analytic function using the two parameters (A and B) defined in the software. Where these parameters in the Hyperbolic model constants are assumed to be A = 50 m^2/ N. s and B = 0.1 m^2/N.

The viscosity as a function of strain rate is captured in Fig. 5 - 26 for analytical and numerical analysis of hyperbolic fluid model. The velocity is compared and verified in Fig. 5 - 27.

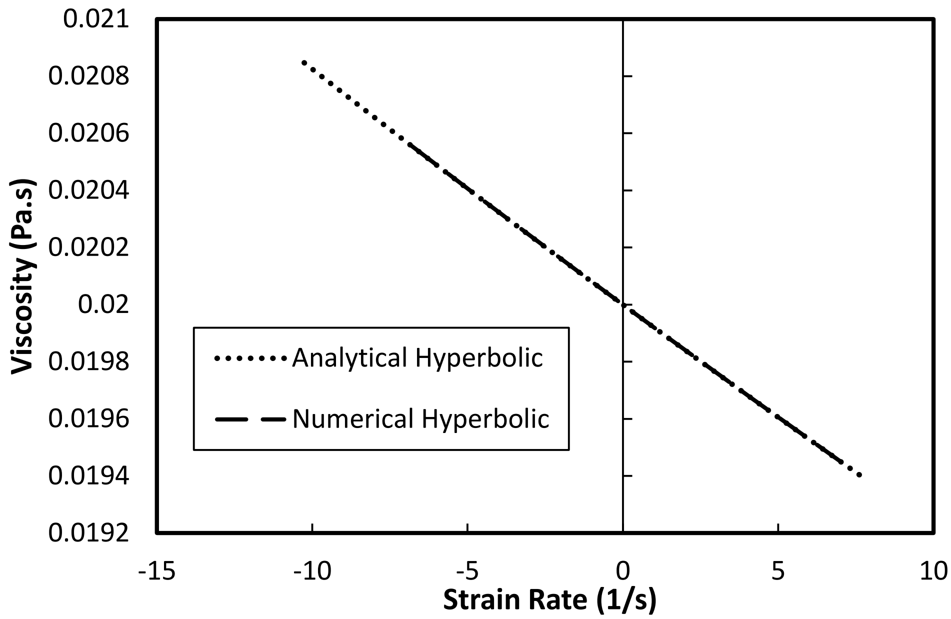

Fig. 5 - 26: Viscosity versus strain rate from numerical and analytical modeling along the radius for Hyperbolic model

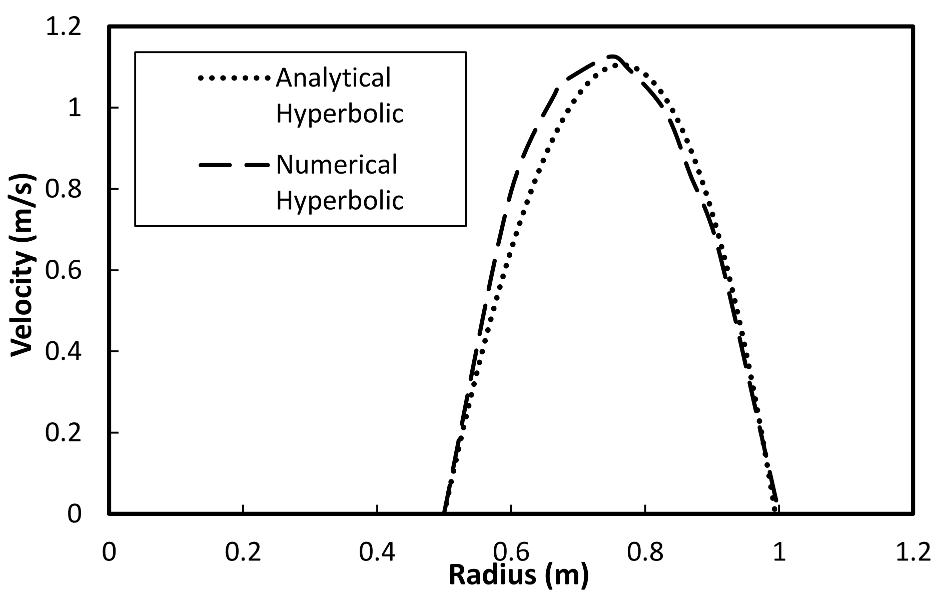

Fig. 5 - 27: Velocity from numerical and analytical modeling along the radius for Hyperbolic model

The strain rate and the shear rate are also compared and shown from numerical and analytical modeling along the radius in Fig. 5 - 28 and Fig. 5 - 29, respectively.

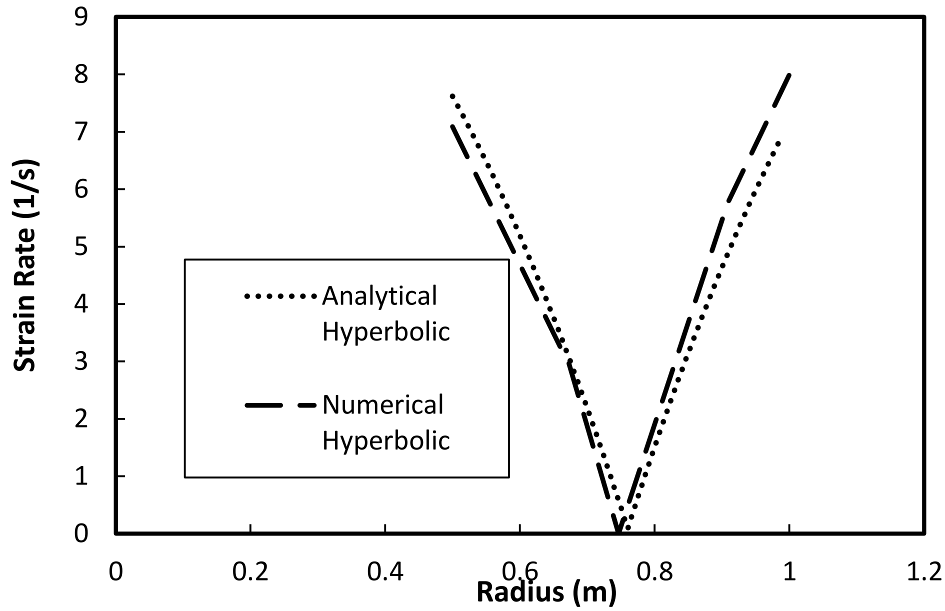

Fig. 5 - 28: Strain rate from numerical and analytical modeling along the radius for Hyperbolic model

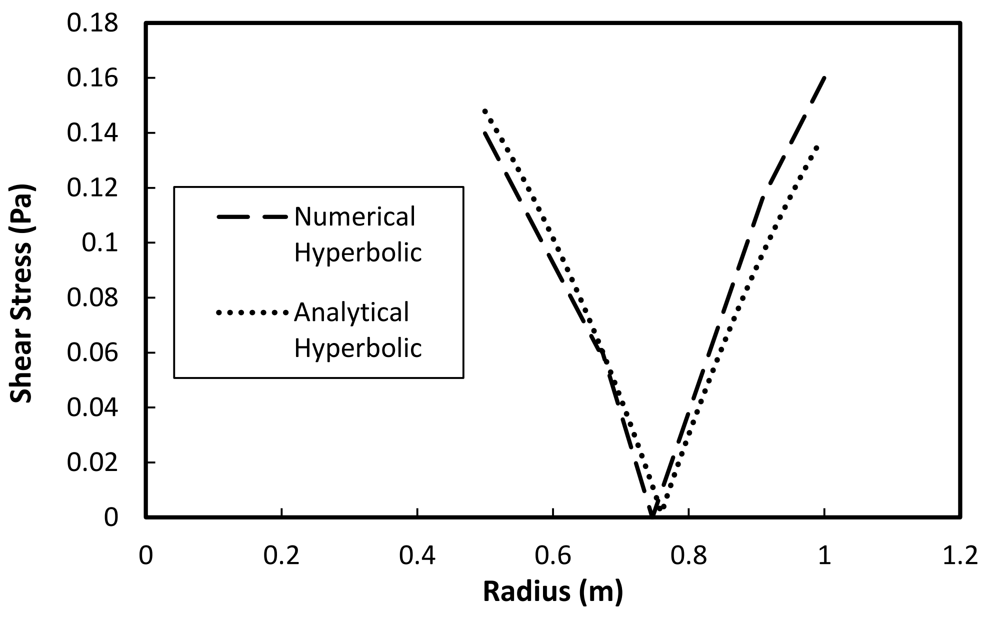

Fig. 5 - 29: Shear stress from numerical and analytical modeling along the radius for Hyperbolic model

The velocity contour plots of the numerical analysis from Newtonian and Hyperbolic analysis, are shown in Fig. 5 - 30. As it was shown the velocity along the walls is zero as the boundary conditions were forced and the maximum velocity happens in the middle of the inner and outer walls.

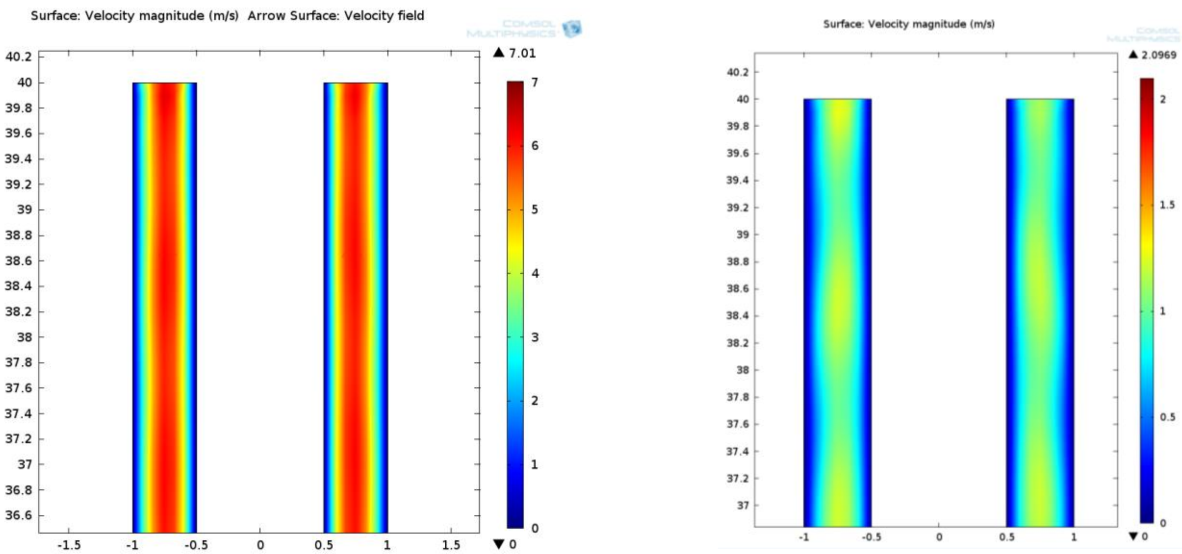

Velocity (m/s) of Newtonian Fluid **Velocity(m/s) of Hyperbolic Fluid**

Fig. 5 - 30: Velocity of the numerical analysis for (a) Newtonian fluid, (b) Hyperbolic Fluid

According to Eq. (5 - 55), due to the existence of the square root, there is a limitation for D which is related to the piezo head. Based on the made assumptions and inputs the parameter D can be in the range of 0.6 to 11.4 N/m³. The velocity of the Newtonian fluid has a linear relationship and it has the range of 1.9 m/s to 36 m/s when D varies from of 0.6 to 11.4 N/m³ (Fig. 5 - 31).

The shear stress varies linearly with respect to D as Fig. 5 - 32 while the Hyperbolic model reaches to a specific value.

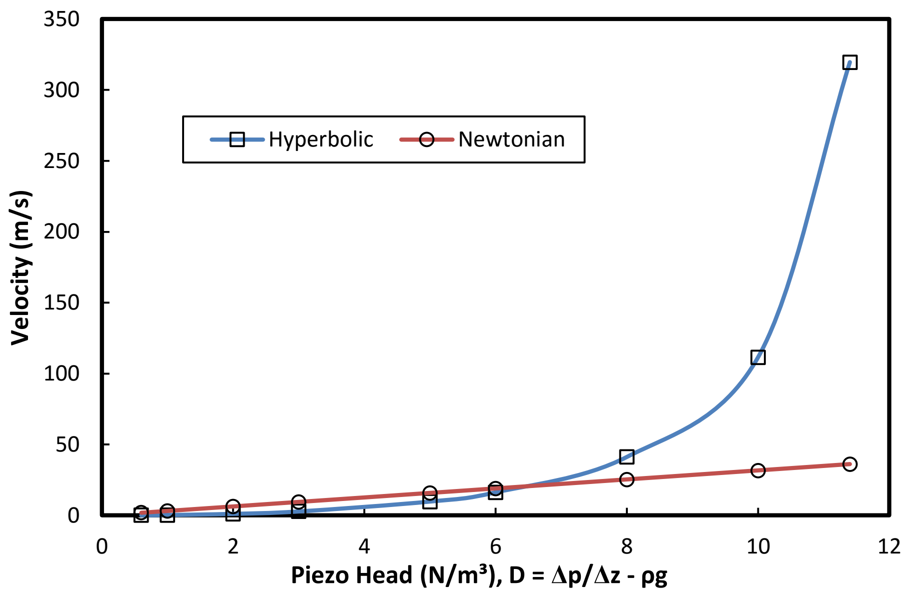

Fig. 5 - 31: Velocity versus piezo head

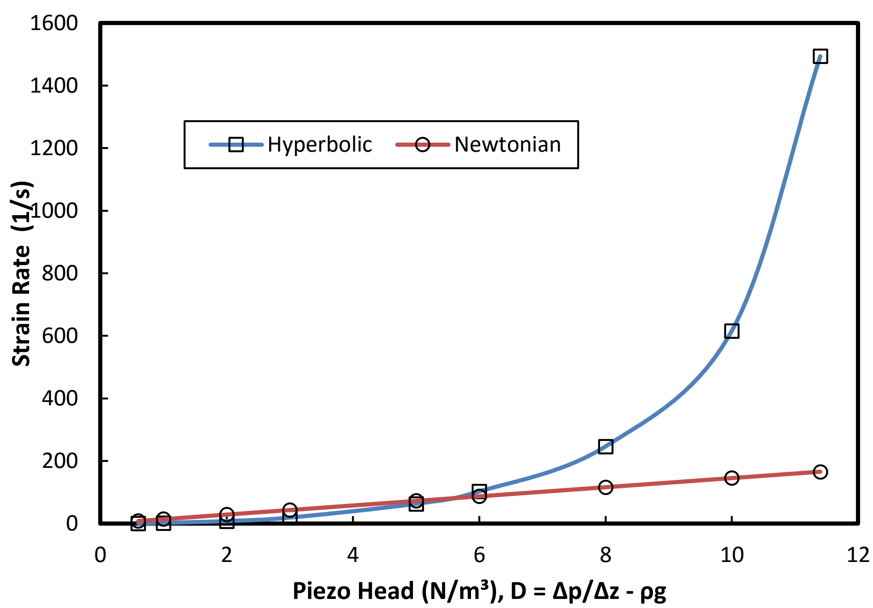

Fig. 5 - 32: Strain rate versus piezo head

The strain rate as a function of D is changing as Fig. 5 - 33. If we calculate pressure with the assumption of the outer pressure is 1 atm, the shear stress versus pressure is shown in Fig. 5 - 34

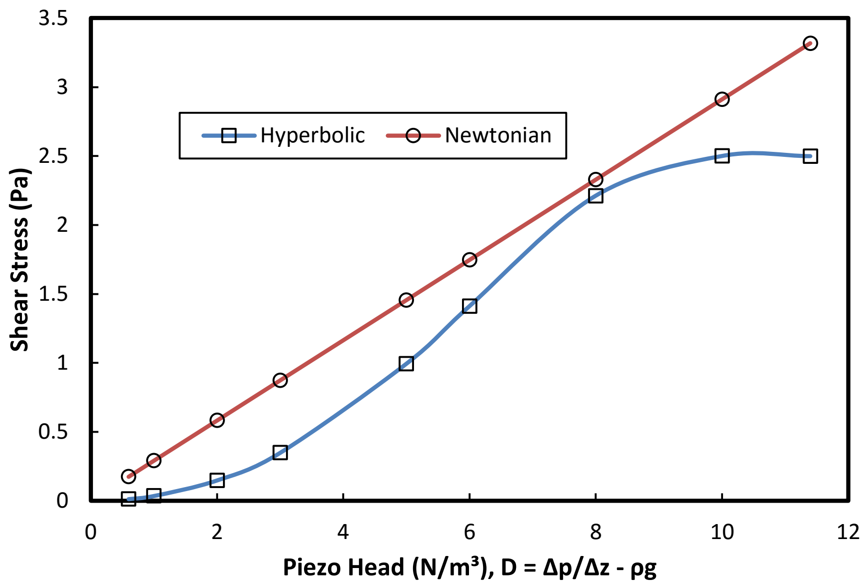

Fig. 5 - 33: Shear stress versus piezo head

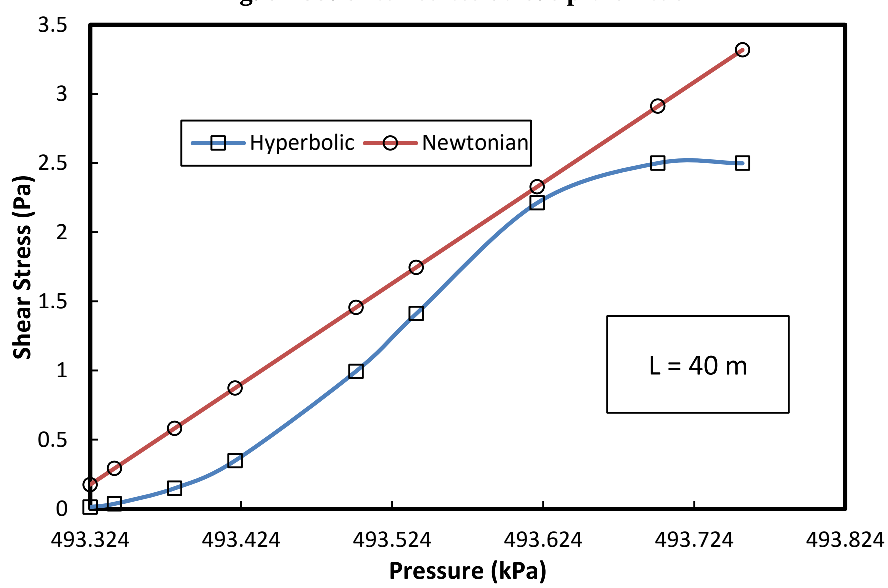

Fig. 5 - 34: Shear stress versus applied pressure

5.3.2. Eccentricity of Axial Drilling Flow

In the axial flow, the eccentricity was investigated numerically, four cases were considered. Fig. 5 - 35 (a) shows the concentric case when there is no eccentricity, other three cases are related to the eccentricities of e/r = 0.25, 0.35 and 0.5.

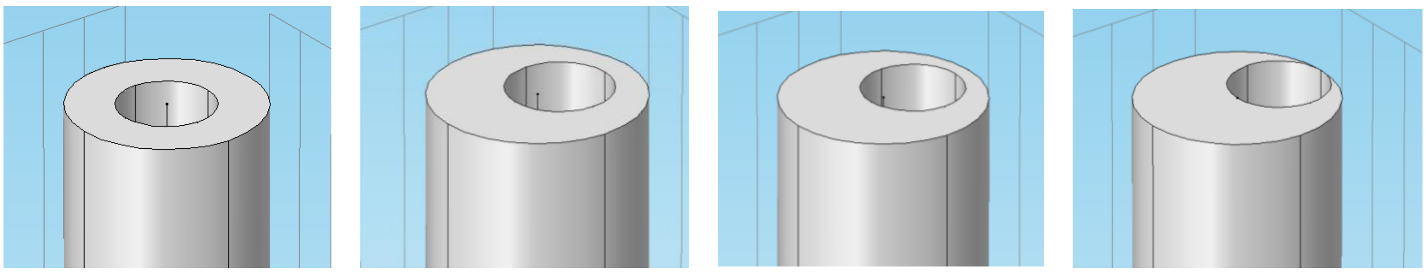

(a) (b) (c) (d)

Fig. 5 - 35: Four different case of free vortex flow; (a) Concentric flow, (b) Eccentric, e/r = 0.25, (c) Eccentric, e/r = 0.35, (d) Eccentric, e/r = 0. 5

In the case of Newtonian fluid flow these four cases were analyzed (Fig. 5 - 36).

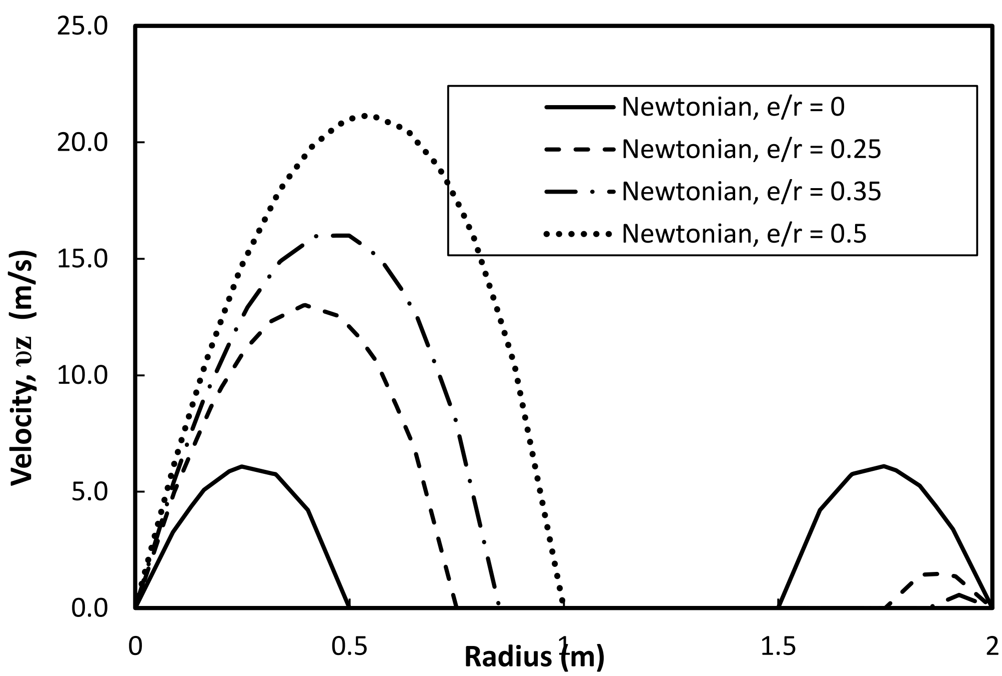

Fig. 5 - 36: Comparison of velocity in concentric and eccentric axial Newtonian flow

Fig. 5 - 37 shows the four cases mentioned before for Hyperbolic model. The velocity from Newtonian model is almost 5 times of the Hyperbolic model. The maximum velocity is compared in different cases for both Hyperbolic and Newtonian flow (Fig. 5 - 38).

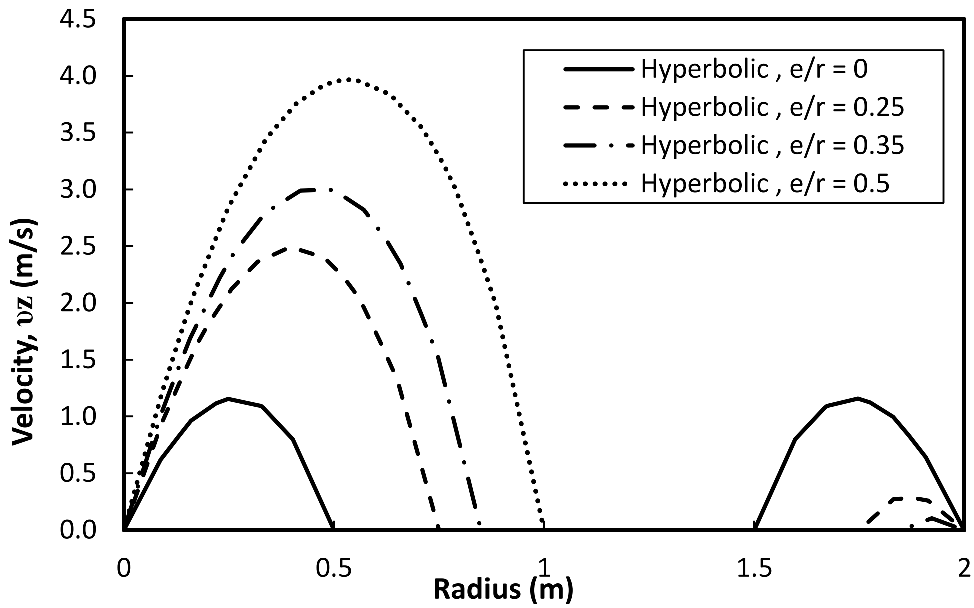

Fig. 5 - 37: Comparison of velocity in concentric and eccentric axial Hyperbolic flow

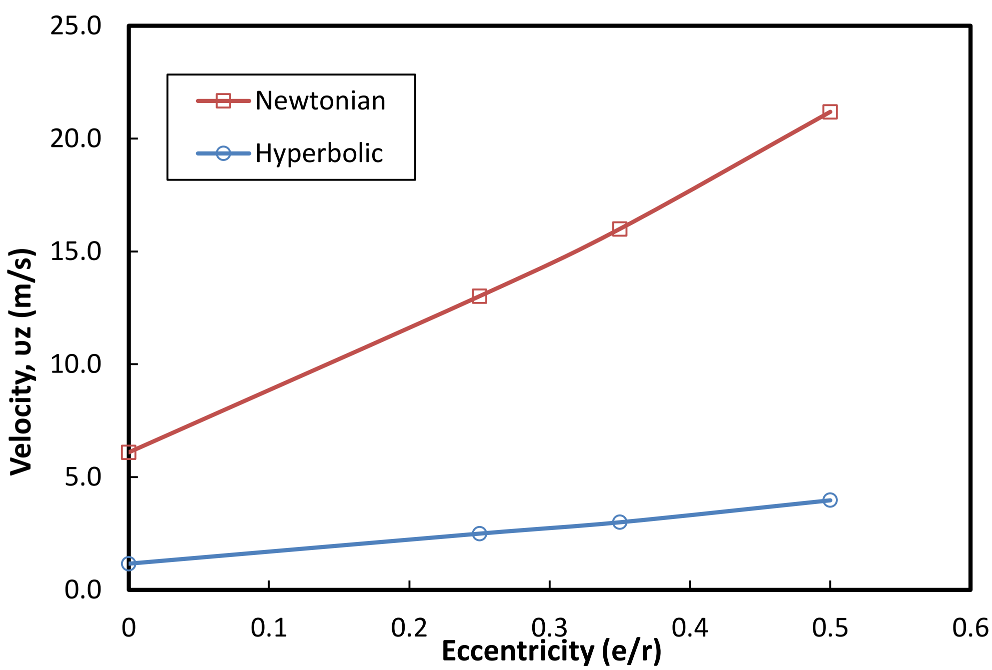

Fig. 5 - 38: Comparison of maximum velocity versus eccentricity for axial Hyperbolic and Newtonian flow

The maximum velocity is normalized for both Hyperbolic and Newtonian fluid versus eccentricity as following. The shear stress also was investigated for Newtonian fluid for concentric and eccentric cases as shown in Fig. 5 - 40.

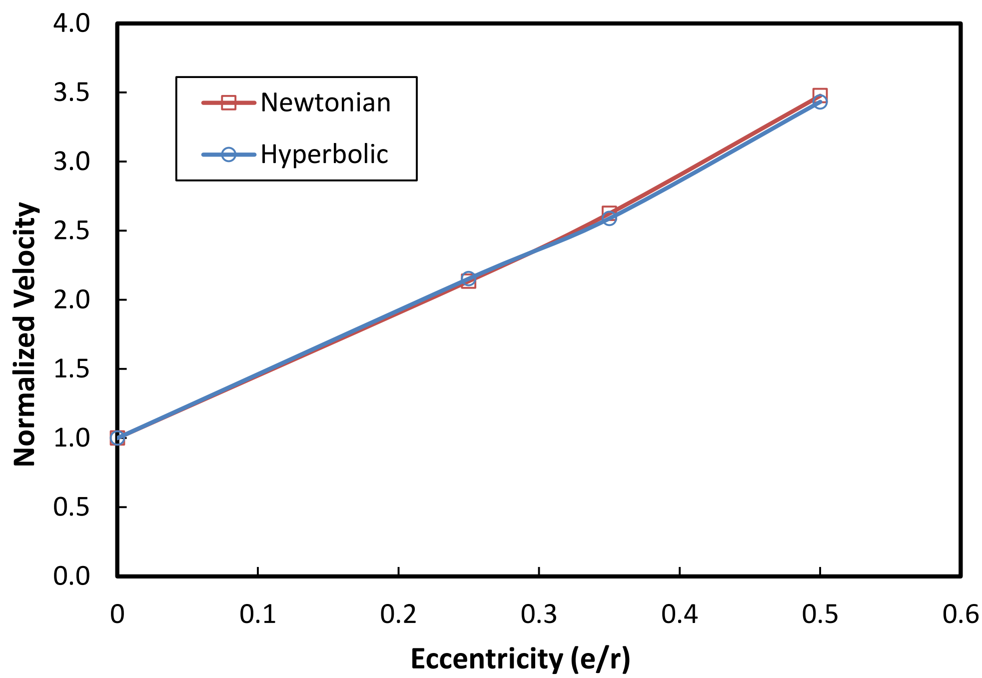

Fig. 5 - 39: Comparison of normalized maximum velocity versus eccentricity for axial Hyperbolic and Newtonian flow

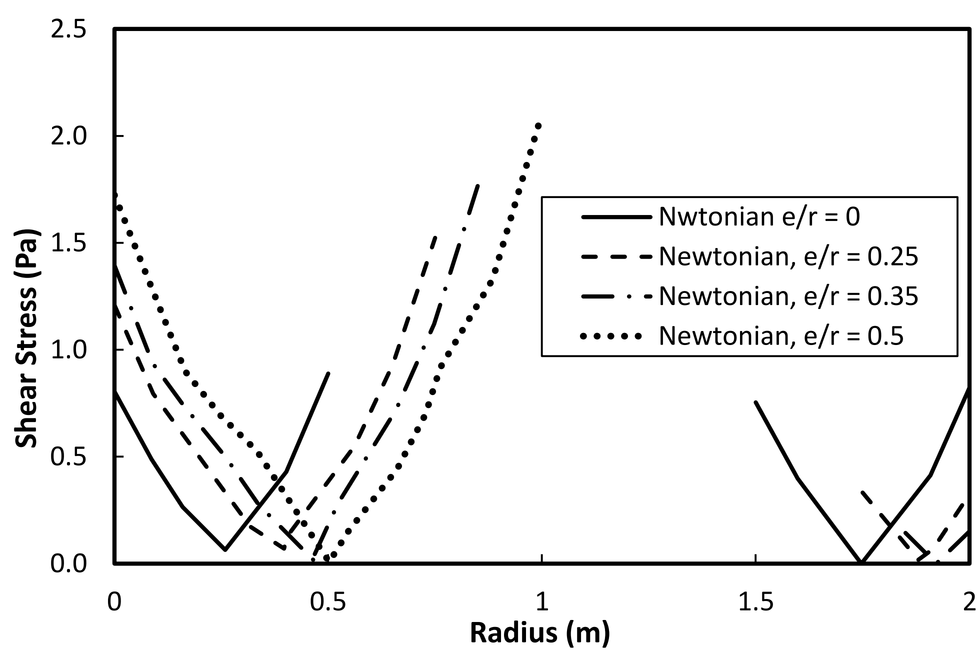

Fig. 5 - 40: Comparison of shear stress in concentric and eccentric axial Newtonian flow

For the case of Hyperbolic flow, the concentric and eccentric were analyzed as shown in Fig. 5 - 41. The maximum shear stress for both Newtonian and Hyperbolic model is compared in Fig. 5 - 42.

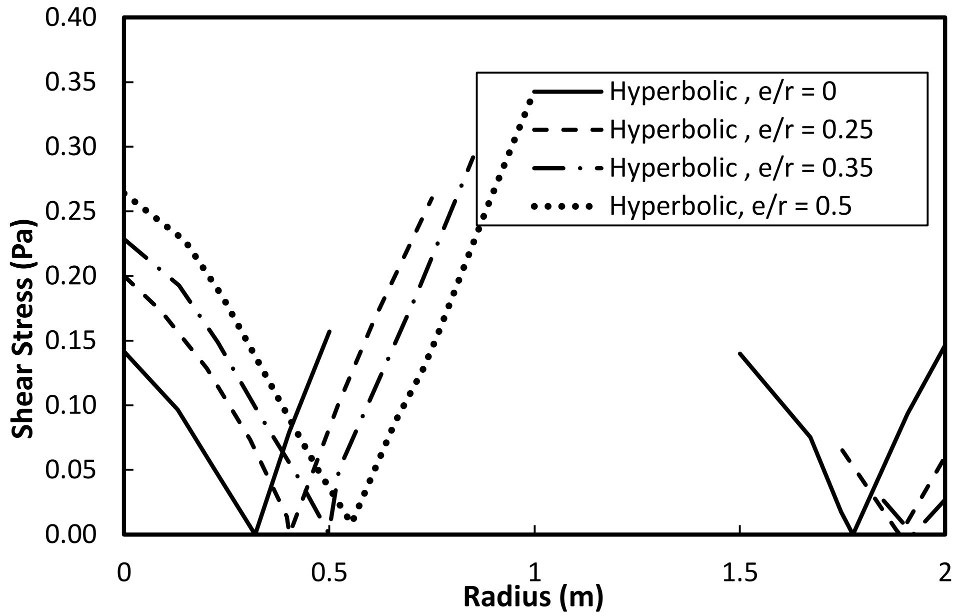

Fig. 5 - 41: Comparison of shear stress in concentric and eccentric axial Hyperbolic flow

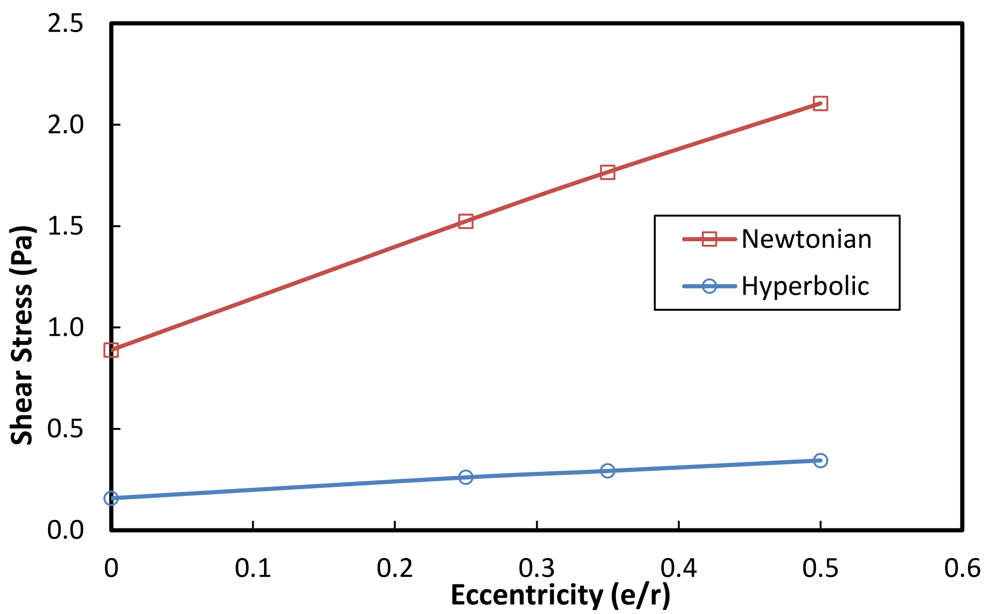

Fig. 5 - 42: Comparison of maximum shear stress versus eccentricity for axial Hyperbolic and Newtonian flow

The normalized comparison of maximum shear stress versus eccentricity for axial Hyperbolic and Newtonian flow is as following.

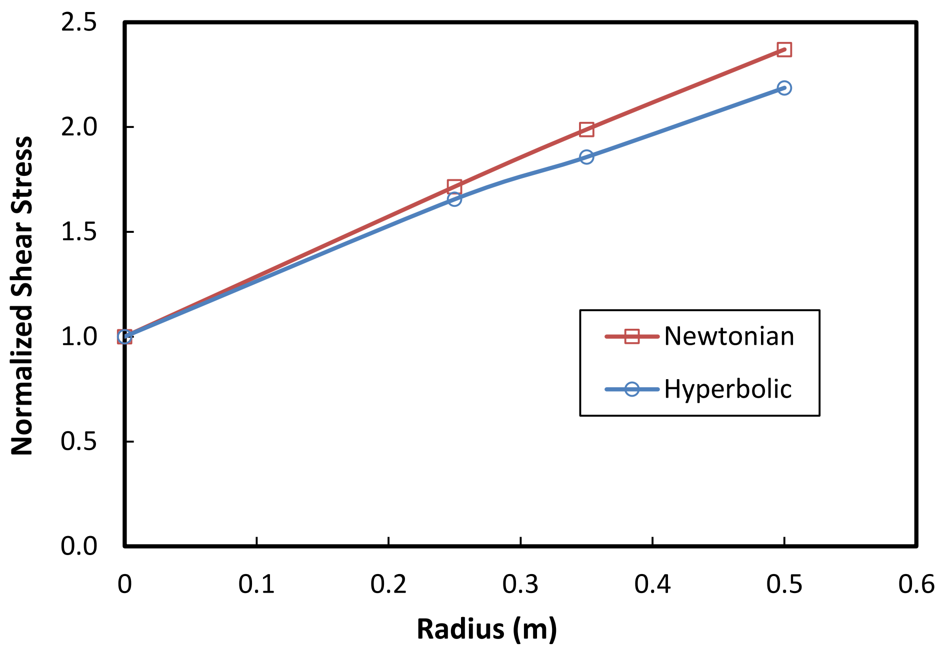

Fig. 5 - 43: Comparison of normalized maximum shear stress versus eccentricity for axial Hyperbolic and Newtonian flow

The rate of the changes in shear stress for eccentricity shown in Fig. 5 - 43 is more for Newtonian respect to Hyperbolic model.

5.4. Characterize the Filter Cake

A new kinetic model has been developed assuming that the permeability and solid content during the filter cake is changing with time, temperature and pressure. The new kinetic model was verified with results from various fluid loss studies reported in the literature and experiments performed on bentonite based drilling muds during this study. Hence the new kinetic model can be used to better model the filter cake formation and filter loss real time with the changes in permeability and solid content in the filter cake.

5.4.1. API Model

The classical method to evaluate the infiltration through filter cake is given by the following equations (Andrea et al., 2012). In which, the flow of mud filtrate is described by Darcy's law. Thus, the rate of filtration is given by

$$\frac{dV_f}{dt} = \frac{kA\Delta p}{\mu h_{mc}}. \tag{5 - 57}$$

At any time during filtration process, the volume of solids in the mud that has been filtrated is equal to the volume of solids deposited in the filter cake as

$$f_{sm}V_m = f_{sc}h_{mc}A \tag{5 - 58}$$

where

f_{sm} = volume fraction of solids in the mud

f_{sc}= volume fraction of solids in the cake.

Eq. (5 - 58) can be defined as

$$f_{sm}\left(h_{mc}A + V_f\right) = f_{sc}h_{mc}A. \tag{5 - 59}$$

Therefore,

$$h_{mc} = \frac{f_{sm}V_f}{A(f_{sc} - f_{sm})} = \frac{V_f}{A\left(\frac{f_{sc}}{f_{sm}} - 1\right)}. \quad \textbf{(5 - 60)}$$

Substitute Eq. (5 - 60) in (5 - 57) as following:

$$\int_0^{V_f} V_f dV_f = \int_0^t \frac{kA\Delta p}{\mu} A\left(\frac{f_{sc}}{f_{sm}} - 1\right) dt,$$

(5 - 61)

$$V_f = \sqrt{2k\Delta p\left(\frac{f_{sc}}{f_{cm}} - 1\right)} \; A\frac{\sqrt{t}}{\sqrt{\mu}}.$$

Equation 5 can be re-written as

$$V_f = N * \sqrt{t}. \quad \textbf{(5 - 62)}$$

Where:

V_f = volume of fluid loss (cm³)

k = drilling mud permeability (Darcy)

k_o = initial permeability of drilling mud (Darcy)

Δp = applied pressure (atm)

f_{sc} = volume fraction of solid in cake

f_{sm} = volume fraction in mud

A = filter area (cm²)

t = time(min)

μ = mud viscosity (cp)

h_{mc}= the thickness of the filter (mud) cake (cm)

And $N = \sqrt{\frac{2k\Delta p\left(\frac{f_{sc}}{f_{cm}} - 1\right)}{\mu}} A$

5.4.2. Hyperbolic Model

This model has the following features:

- The permeability is a function of time as

$$k = \frac{2A * k_o}{(A + Bt)^2}. \tag{5 - 63}$$

- The ratio of the solid content in the cake to the solid content in the mud as a volume fraction is a function of time as

$$\left(\frac{f_{sc}}{f_{sm}} - 1\right) = \frac{\alpha_o t}{A + Bt}. \tag{5 - 64}$$

- The final form of the filtration versus time is taking the form of hyperbolic function as

$$V_f = \sqrt{\frac{2 * k_o * \alpha_o * \Delta p}{\mu}} * A_r * \frac{t}{A + Bt}. \tag{5 - 65}$$

Where:

$A =$ arbitrary constant, B=arbitrary constant (1⁄min),
$\alpha_o =$ arbitrary constant (1⁄min), A_r =filter area (cm^2).

In this model the filter loss can be written as

$$V_f = m * \frac{t}{A + Bt}. \tag{5 - 66}$$

From the volume fraction of solid in cake, fsc, the porosity can be defined as

$$n(t) = 1 - f_{sc}(t). \tag{5 - 67}$$

5.4.3. Results and Analysis

The material used for this test was water with 4% bentonite and 0.57% xanthan gum. The standard filter loss test (Fig. 5 - 44) was performed and the results is shown in Fig. 5 - 45. The API model and Hyperbolic model compared to capture the tests results. As shown in Fig. 5 - 46, the Hyperbolic model (A is 1.6e-07 and B is 3.17e-08). can capture the results of the filter loss in a better way

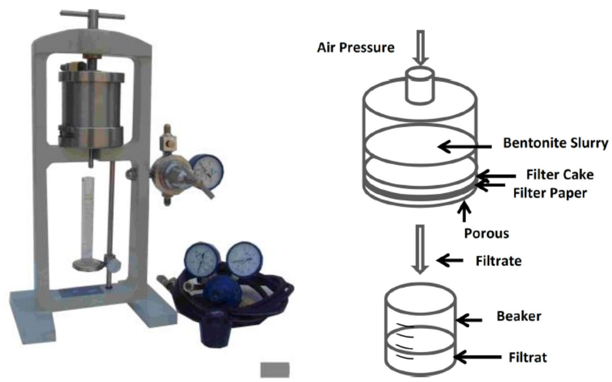

Fig. 5 - 44: Schematic filter loss test

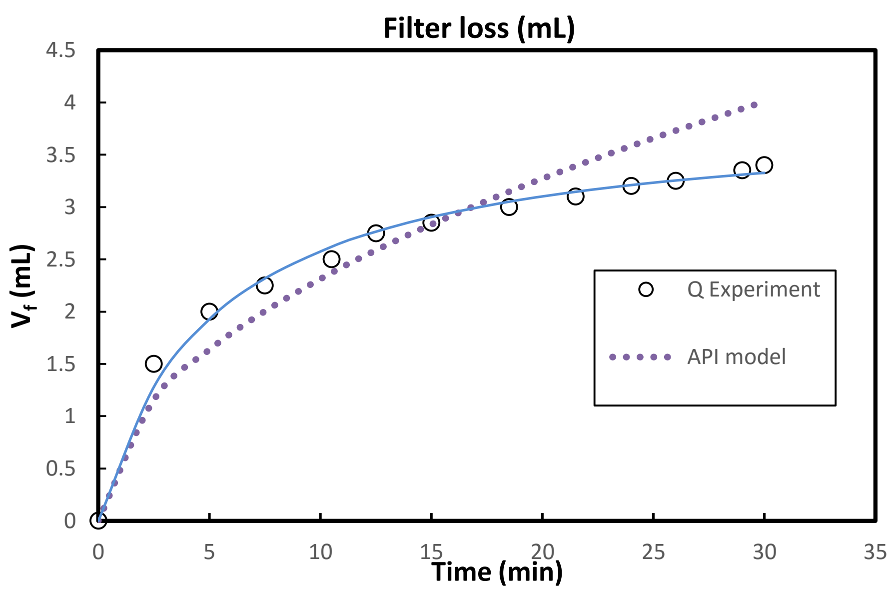

Fig. 5 - 45. Filter loss versus time for Hyperbolic and API model

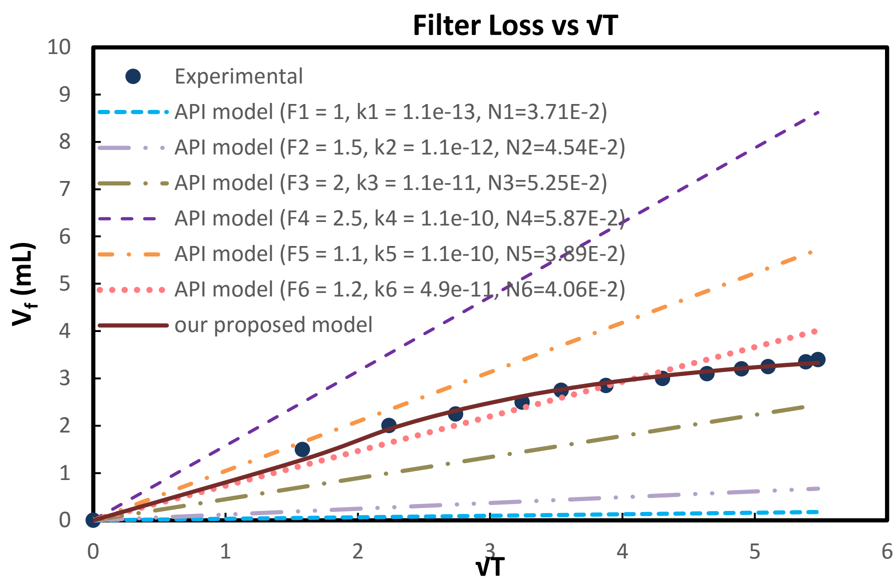

Fig. 5 - 46: Filter loss versus square root of time for Hyperbolic and API model

In the Eq. (5 - 64), the term of $\left(\frac{f_{sc}}{f_{sm}} - 1\right)$ is called f(t) which can be shown as Fig. 5 - 47 as a function of time while it is a constant in API model.

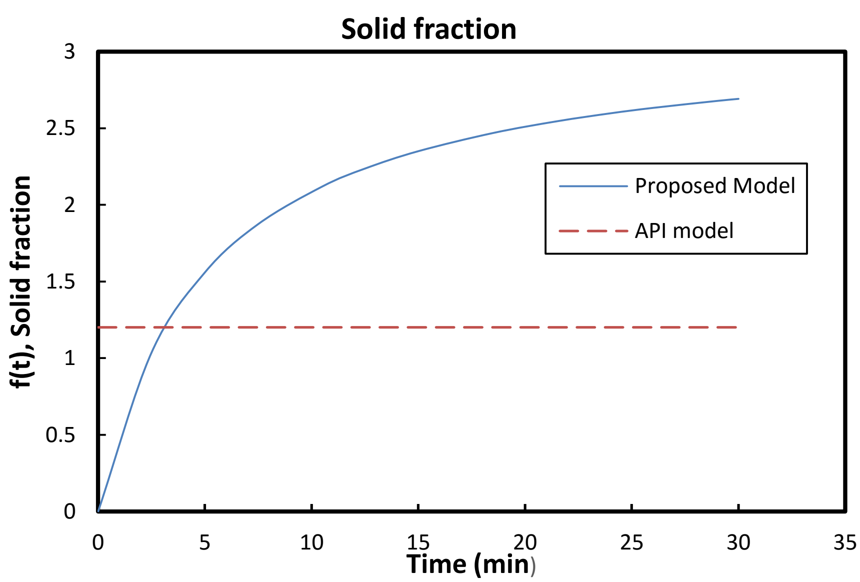

Fig. 5 - 47: Solid fraction versus time for Hyperbolic and API model

The permeability in Eq. (5 - 63) shown and compared with API model in Fig. 5 - 48.

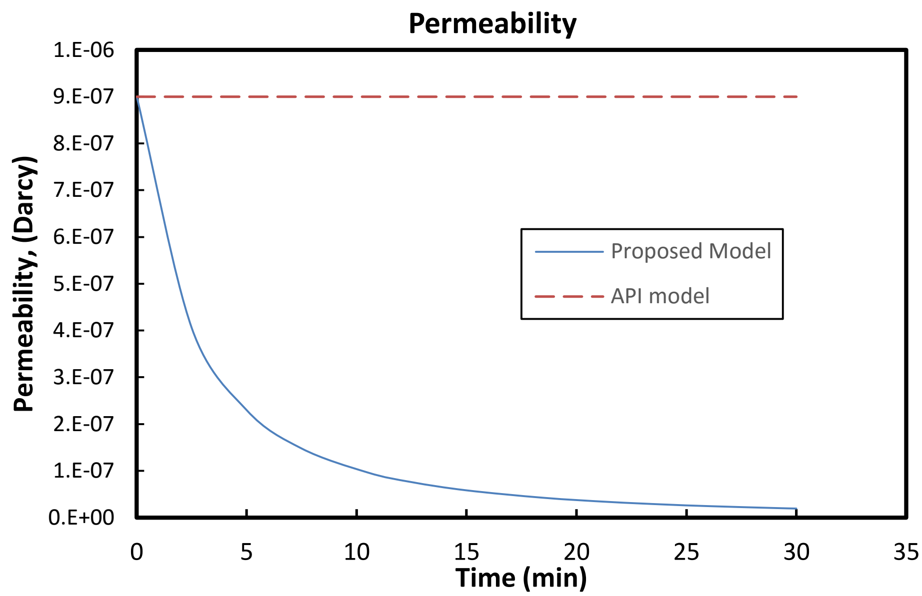

Fig. 5 - 48: Permeability versus time for Hyperbolic and API model

The porosity from Eq. (5 - 67) for Hyperbolic model and API model is compared in Fig. 5 - 49.

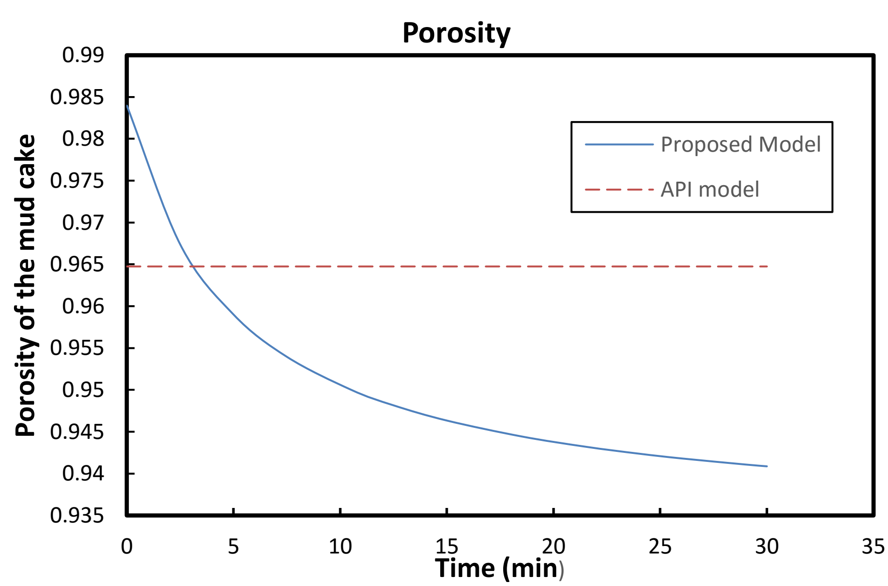

Fig. 5 - 49: Permeability versus time for Hyperbolic and API model

5.5. Summary

In this study the axial flow of the drilling was investigated analytically. A new rheological model called Hyperbolic model was introduced which eliminated the Newtonian, Bingham and Power law models' limitation in expression of the shear stress versus strain rate which reach infinity when the shear strain reaches high numbers. The proposed analytical model compared with Newtonian model. The results of the analytical solution verified with numerical solution with COMSOL Multiphysics software for both Hyperbolic and Newtonian Model.

The eccentricity effect is investigated for the axial flow analytically for both case of the Newtonian and Hyperbolic model. And also the eccentricity effect is analyzed analytically for vortex flow using the theory of complex variables.

Later on, a new kinetic model has been developed assuming that the permeability and solid content during the filter cake is changing with time, temperature and pressure using Hyperbolic Model. The new kinetic model was verified with results from of fluid loss and compared with the API model.

1. The new rheological model called Hyperbolic model (Vipu Model) eliminated the Newtonian model's limitations. The velocity results from the Newtonian model is almost 5 times the Hyperbolic model. The viscosity in the Hyperbolic model is a function of strain rate while the viscosity in the Newtonian model is a constant.
2. The new kinetic model can be compared with API model and it expressed the filter cake permeability, solid content in the filter cake a time dependent function while in the API model these parameters are constant.

CHAPTER 6. WELL CEMENED CASING

6.1. Physical Model Test

Three physical tests are covered in this part including small model, large model and field test. The casing was placed in the middle of the instrumentations and the smart cement was casted around the casing. In all these tests the resistance was monitored to track the changes of smart cement. The models were built to demonstrate the concept of real time monitoring of the smart cement by means of two probe method. The LCR meter device (Inductance, Capacitance and Resistance).

6.1.1. Small Model

The sensitivity of the smart cement while the pressure was applying in the casing was monitored in the small model (Fig. 6 - 1). Different pressures were applied in the casing and the resistivity changes monitored in different levels.

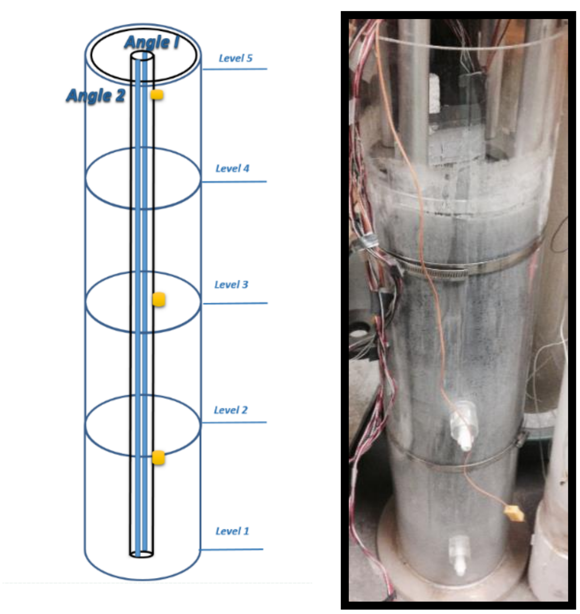

Fig. 6 - 1: Small Model Test

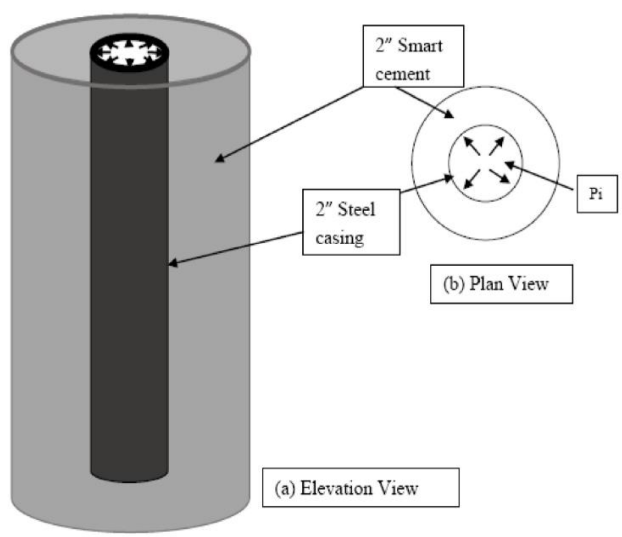

Fig. 6 - 2: Pressure test in small model

Initially there is no pressure and resistance was measured (Fig. 6 - 3) initially (R_o) and later the pressure applied as 60 psi, 100 psi and 140 psi and the resistance changes monitored while the pressure was increasing (Fig. 6 - 4).

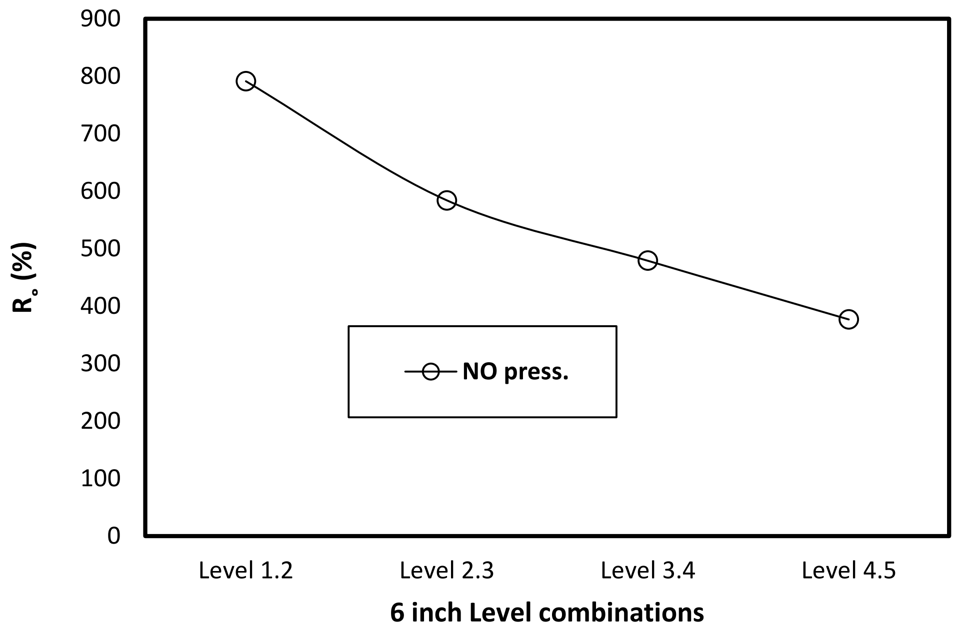

Fig. 6 - 3: Initial resistance (no pressure inside casing) after 100 days of curing

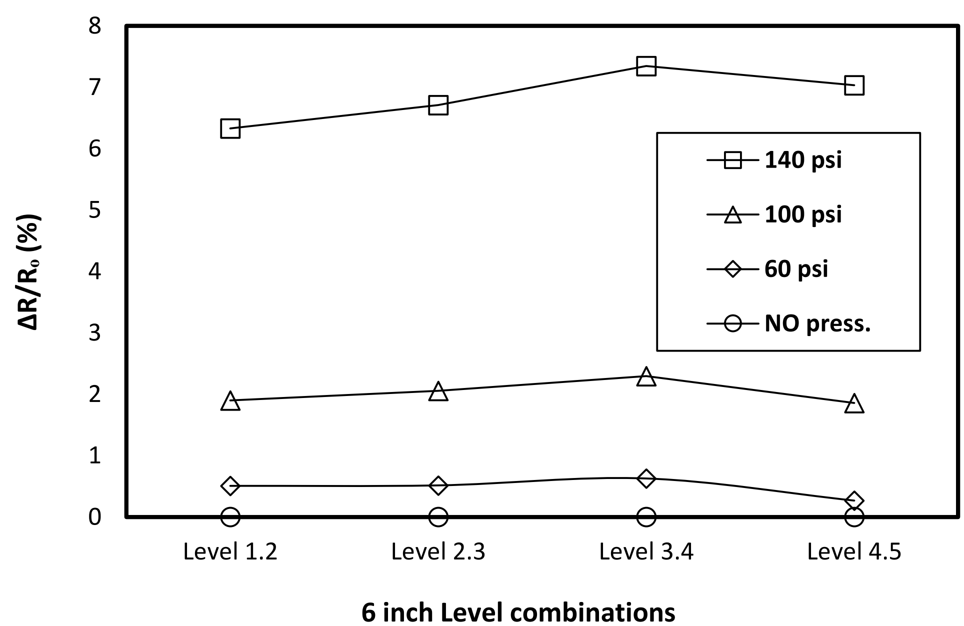

Fig. 6 - 4: Resistance changes in different levels at various pressures after 100 days of curing

Fig. 6 - 5 shows the relation between the resistivity changes modeled using p, q model (Vipulanandan and Mebarkia, 1990),

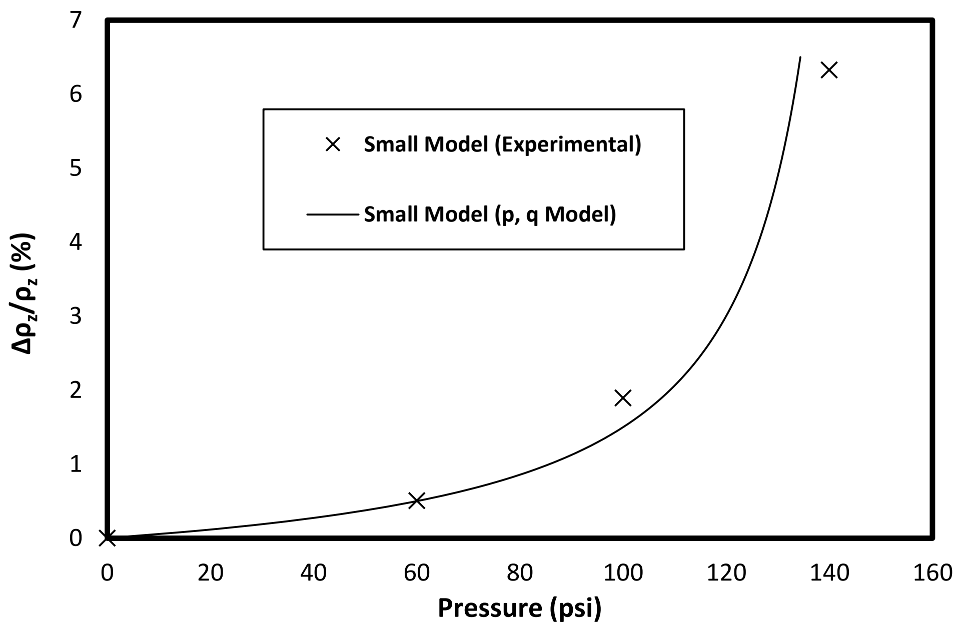

Fig. 6 - 5: Model prediction of changes in resistivity with applied pressure for smart cement after 100 days of curing

The p, q model is defined as Eq.(6 - 1) proposed by Vipulanandan and Mebarkia in 1990.

$$p_i = \frac{\left(\frac{\Delta\rho_z}{\rho_z}(\%)\right)}{q + (1 - q - p)\frac{\Delta\rho_z}{\rho_z}(\%) + p\left(\frac{\Delta\rho_z}{\rho_z}(\%)\right)^{\frac{p+q}{p}}} \qquad \textbf{(6 - 1)}$$

where p and q are 0.75 and 0.001, respectively.

6.1.2. Large Model

The large model test (Fig. 6 - 6) was built in order to simulate the more realistic condition of the cementing and monitoring of the resistance.

The pressure applied inside the casing as well as small model test but in lower pressures (10 psi, 20 psi and 40 psi) it showed higher resistivity changes and the changes were modeled by p, q model, (Vipulanandan and Mebarkia 1990), where p and q were 0.823 and 0.192, respectively (Eq.(6 - 2)). The experimental and the model is shown in Fig. 6 - 7 for 150 days of curing of the cement.

$$p_i = \frac{\left(\frac{\Delta\rho_z}{\rho_z}\right)}{q + (1-p-q)\left(\frac{\Delta\rho_z}{\rho_z}\right) + p\left(\frac{\Delta\rho_z}{\rho_z}\right)^{\frac{1-p-q}{p}}} \qquad \textbf{(6 - 2)}$$

Fig. 6 - 6: Large Model Test

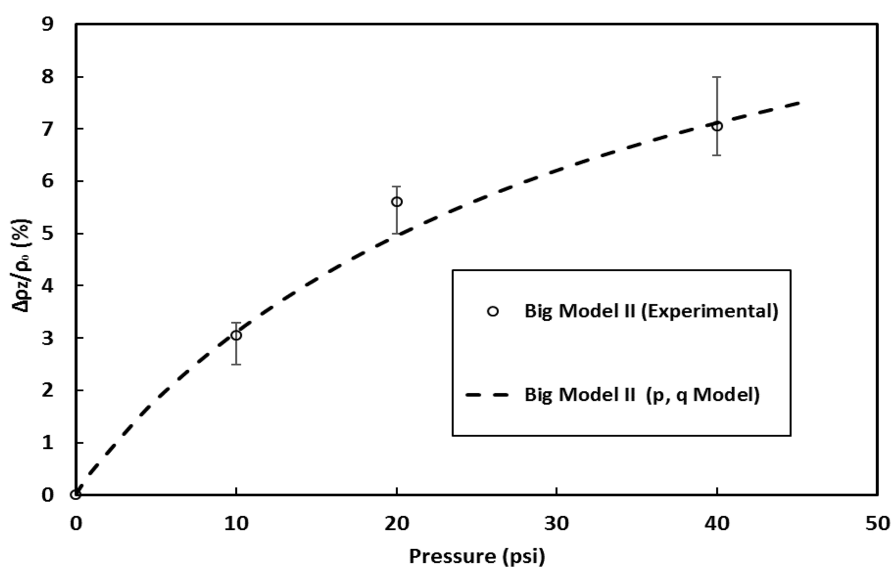

Fig. 6 - 7: Model prediction of changes in resistivity with applied pressure for smart cement, 150 days of curing

6.1.3. Field Model

For the first time, the real smart cemented wellbore (Fig. 6 - 7) was built in the Energy Research Park (ERP) in University of Houston. The depth of the wellbore is about 37 feet while the water table was located 25 feet below the ground level. The change in the cement resistance was monitored with four angles (AB, CD, EF and GH) in 15 levels. The field model test was performed using the smart cement where the soil, underground water is in contact with the cement.

Fig. 6 - 8: Field Model Test

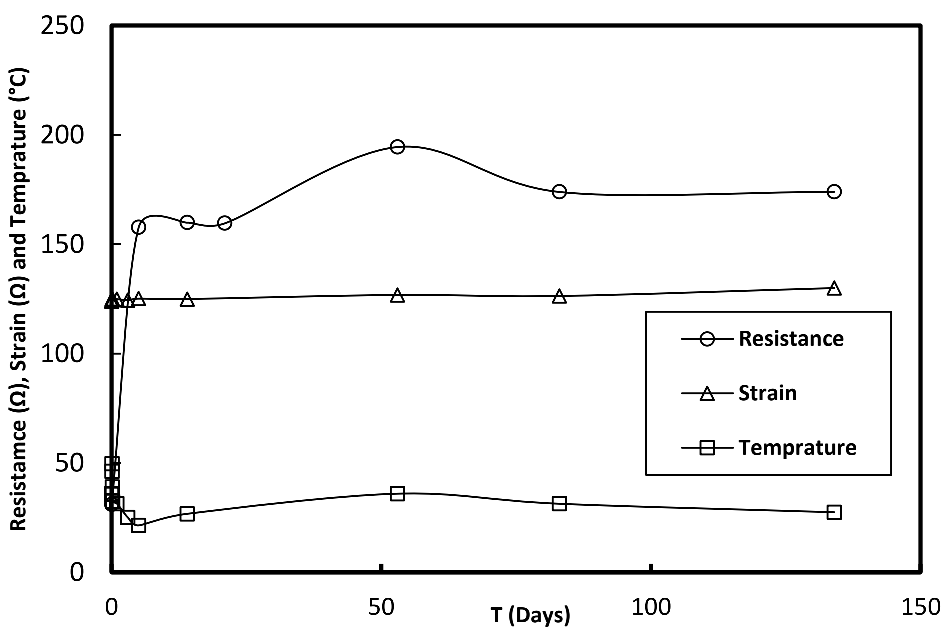

Fig. 6 - 9: Monitoring Resistance, Strain and Temperature in curing time of the cement

The instrumentation was performed with using wires for monitoring resistance, thermocouples and strain gages in order to monitor the changes as shown while temperature increased in summer the resistance could capture in precisely The instrumentation of the angles in the downhole for the field test is shown as following.

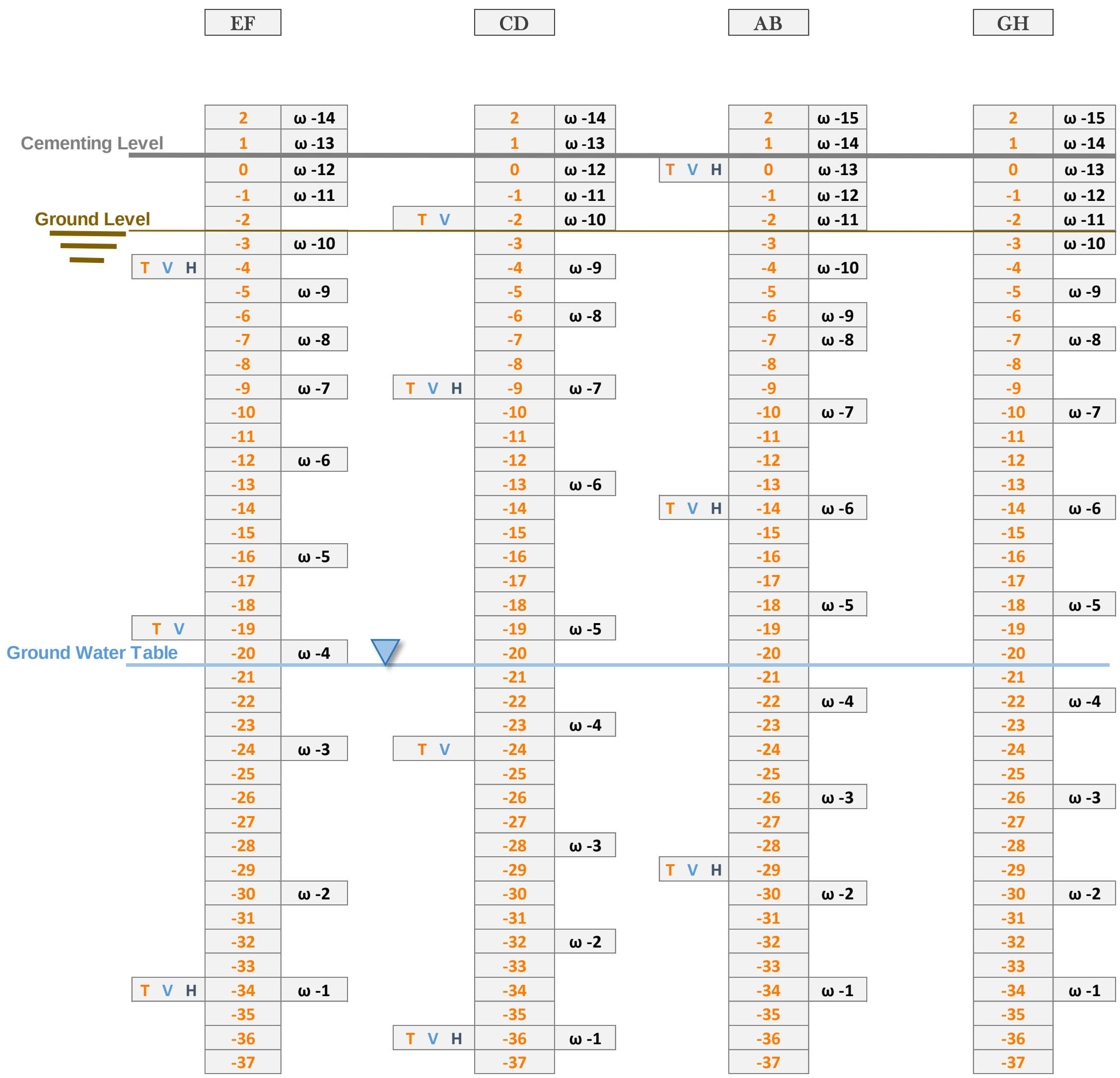

Fig. 6 - 10: Field instrumentation plan

(a) Applying pressure in the borehole

The pressure applied in the pressurizing tube and the resistivity changes measured and monitored through the depth of the borehole Fig. 6 - 11, using the

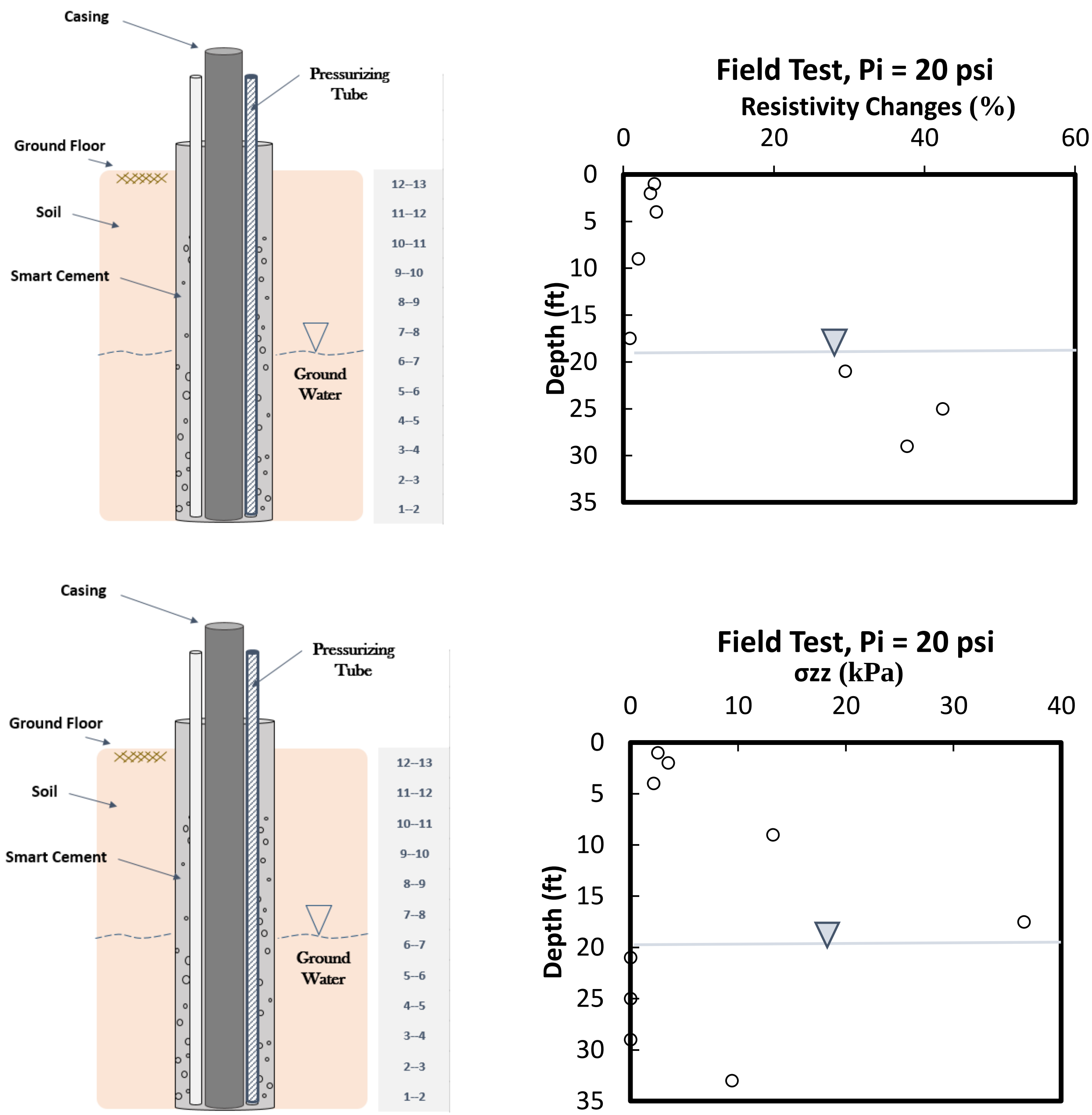

Fig. 6 - 11: Applying pressure through the borehole and monitoring the change of resistivity

The relationship of the resistivity changes with the applied pressure is shown and model with p, q model (Vipulanandan and Mebarkia 1990).

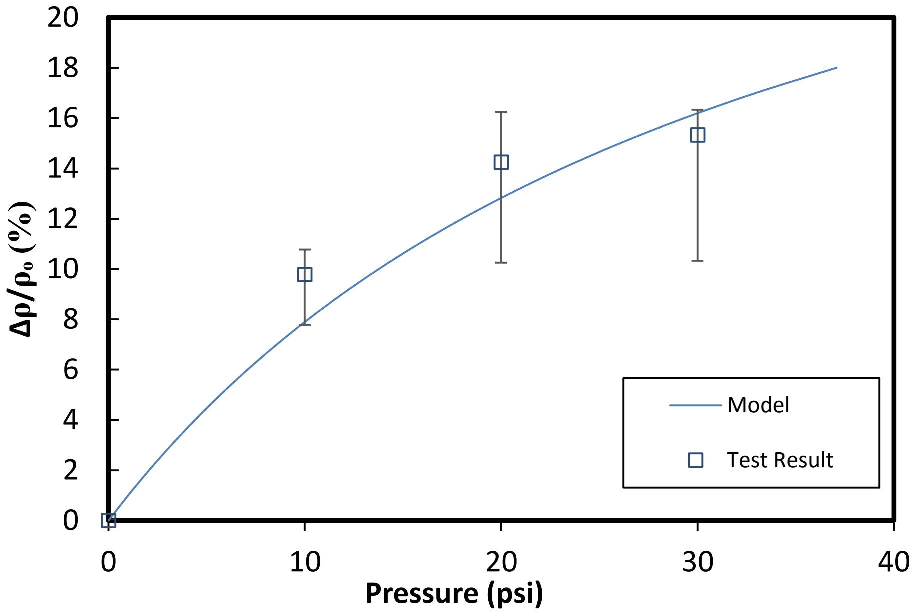

Fig. 6 - 12: The resistivity changes versus pressure inside the wellbore

The p, q model which shows the relationship between the pressure and resistivity changes is

$$p_i(t) = \frac{\frac{\Delta\rho_z}{\rho_z}(\%)}{q + (1 - p - q)\left(\frac{\Delta\rho_z}{\rho_z}(\%)\right) + p\left(\frac{\Delta\rho_z}{\rho_z}(\%)\right)^{\frac{p}{q-p}}}. \qquad \textbf{(6 - 3)}$$

Parameter p and q were selected to be 0.823 and q 0.192, respectively.

(b) Stress in Downhole

According to three phase interaction for cement with w/c= 0.38, specific weight is increasing with time (Fig. 6 - 13) and void ratio decreasing with time (Fig. 6 - 14). By using the hyperbolic model, we can predict the specific weight and void ratio for 1, 7 and 28 days of curing. In the field we have the water table in 25 ft from ground level. Therefore, we need to know the saturated specific weight of the cement. Using Fig. 6 - 13, Fig. 6 - 14 and Eq.(6 - 4), the saturated and effective specific weight were calculated. We already have specific weight and void ratio of cement with w/c = 0.4 from three phase interaction analysis. Using the following equation, we can find the saturated specific weight accordingly. Therefore, the effective specific weight can be derived.

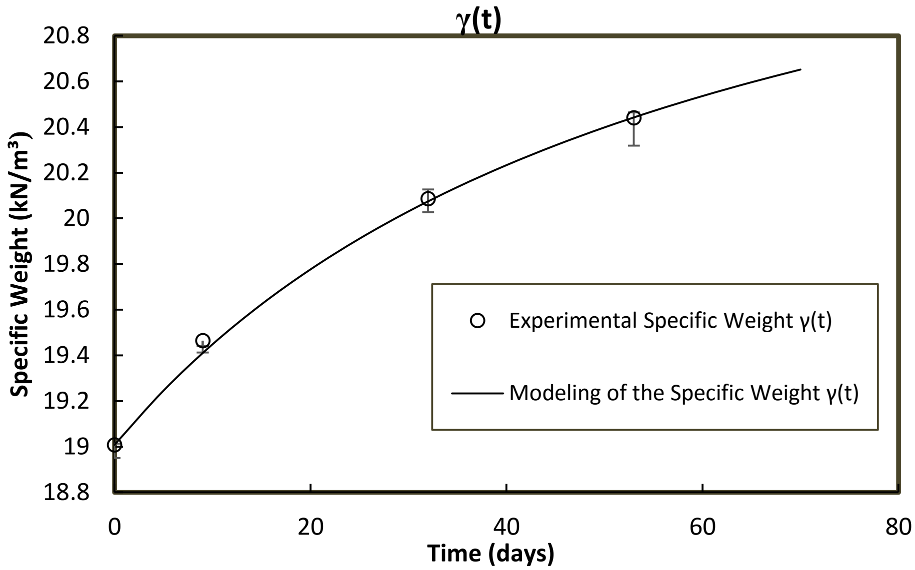

Fig. 6 - 13: Specific weight variation versus time

The saturated specific weight can be calculated using Eq. (6 - 4) using the three phase model can be evaluated as

$$\gamma_{sat} = \frac{(G_s + e)\,\gamma_w}{1 + e}. \qquad \textbf{(6 - 4)}$$

The calculated saturated specific weight and effective specific weight is shown in Table 6 - 1

Table 6 - 1: Cement properties predictions

Time	γ (kN/m³)	e	Gs	γw (kN/m³)	γsat (kN/m³)	γ' (kN/m³)
1 Day	**19**	**1.27**	**3.15**	**9.81**	**19.10141**	**9.2914**
7 Day	**19.3**	**1.18**	**3.15**	**9.81**	**19.485**	**9.675**
28 Day	**20**	**0.95**	**3.15**	**9.81**	**20.63**	**10.81**

The void ratio (Fig. 6 - 14) from three phase modeling can be shown as

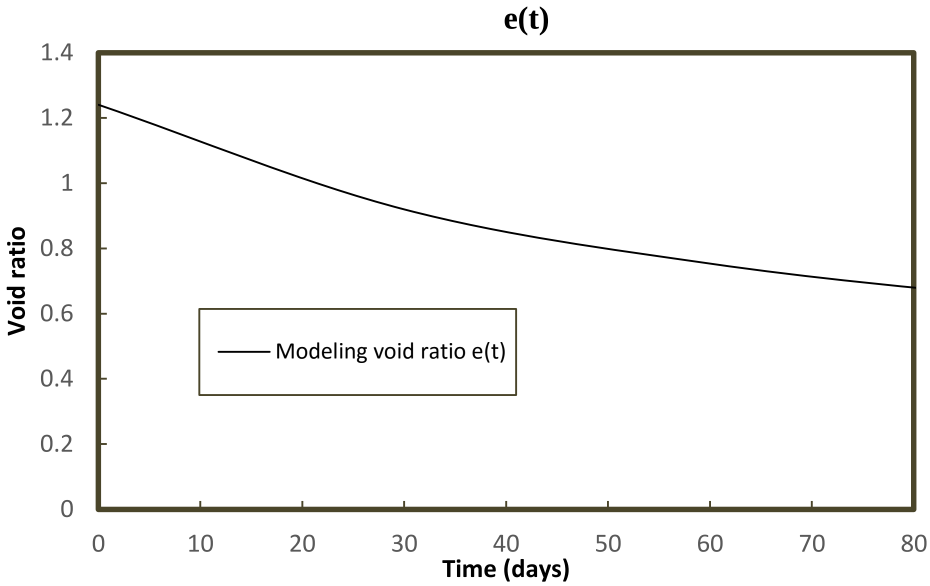

Fig. 6 - 14: Void ratio variation versus time

(b) Stress Above and Below Water Table

Vertical stress is calculated using Table 6 - 1 and plotted versus depth at different curing time according to the specific weight of the cement for below and above water level, respectively (Fig. 6 - 15).

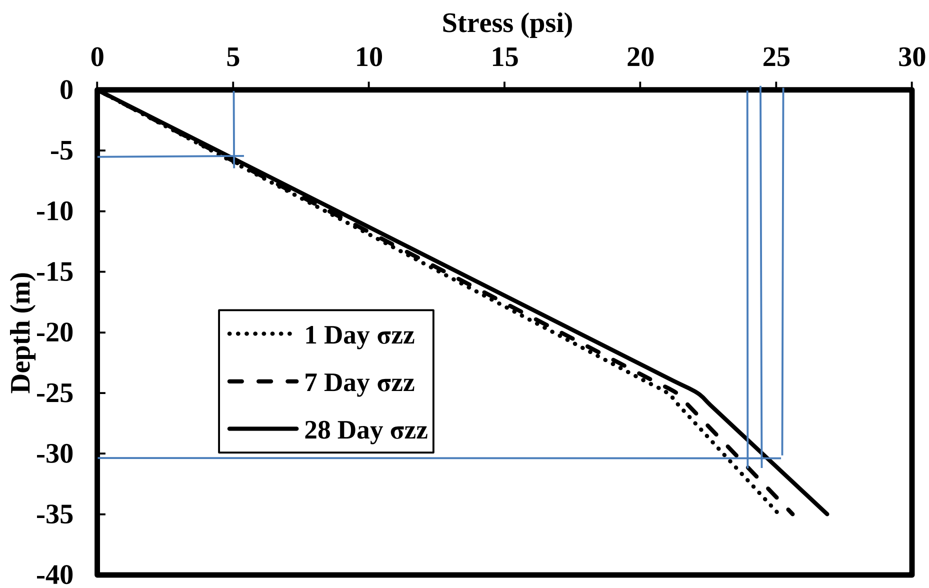

Fig. 6 - 15: Vertical stress versus depth

Two specific level were selected the first one is (Level 1.2 in the measuring scale) above water table at 32 ft below ground level and the second one is (level 7.8) below water table at 5 ft below ground level. The Stresses for different curing time at below and above water level are shown in Fig. 6 - 3.

Table 6 - 2: Stresses for different curing time at different levels

Curing Time	**Below Water Level 1.2 D = 32 ft**	**Above Water Level 7.8 D = 5 ft**
Time (Day)	**σ (psi)**	**σ (psi)**
1 DAY	**23.8**	**5**
7 DAY	**24.3**	**5**
28 DAY	**25.5**	**5**

(c) Resistivity Due to Stress

Fig. 6 - 16 shows the piezoresistivity of the smart cement (Vipulanandan and Amani 2015). The resistivity changes due to weight of the cement or vertical stresses can be found from Fig. 6 - 15 and locate in Fig. 6 - 16 to find resistivity changes.

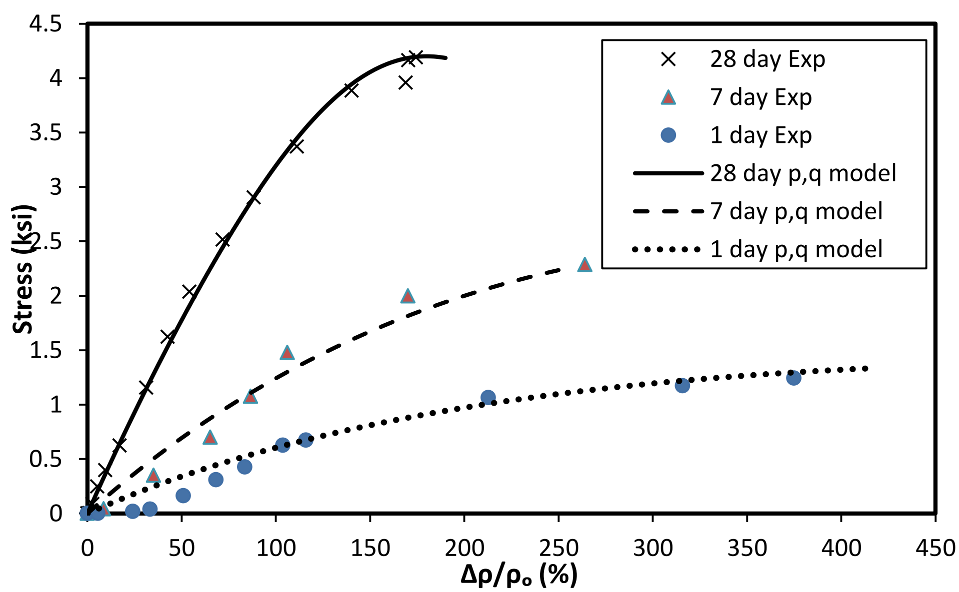

Fig. 6 - 16: Piezoresistivity of smart cement for different cuing time (Vipulanandan and Amani 2015)

The Stresses for different curing time at below and above water level were found. Furthermore, according to the measured resistance result, the rest of resistivity changes can be calculated and will be considered as resistivity changes due to curing and shrinkage. The stresses found in Table 6 - 2 below water level are marked on Fig. 6 - 17 and the resistivity changes are reported in Table 6 - 3

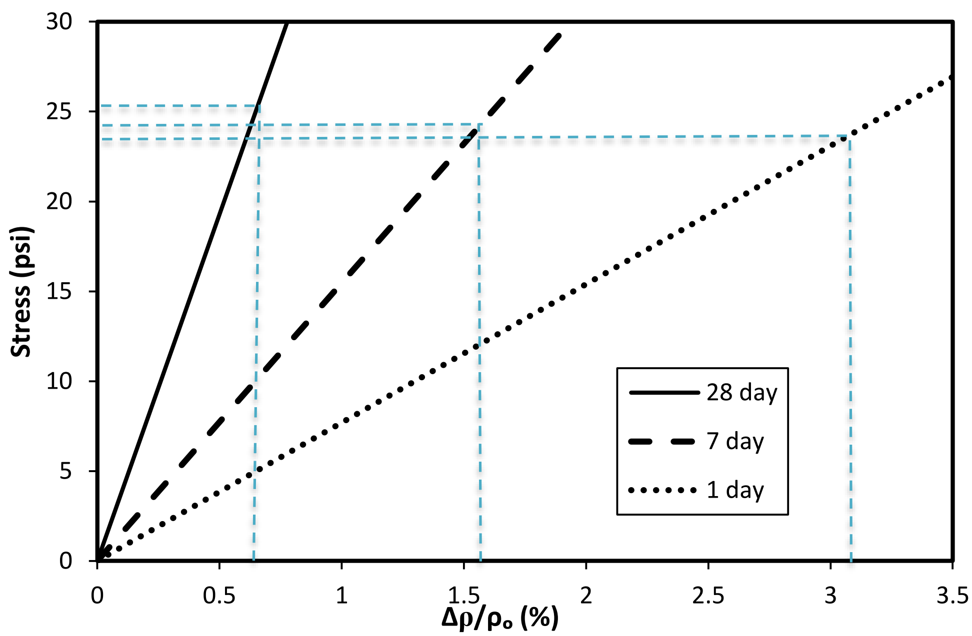

Fig. 6 - 17: Piezoresistivity of smart cement for different cuing time (Vipulanandan and Amani, 2015), Stress at level 1 (D = 32 ft) below water table

Table 6 - 3: Resistivity changes due to stress below water level for different curing time

Curing Time	**Below Water Level 1.2 D = 32 ft**	**Resistivity changes due to stress**
T (Day)	**σ (psi)**	**$\Delta\rho/\rho_o$ (%)**
1 DAY	**23.8**	**3.1**
7 DAY	**24.3**	**1.6**
28 DAY	**25.5**	**0.625**

The stresses found in below water level are marked on Fig. 6 - 18 and the resistivity changes are reported in Table 6 - 4.

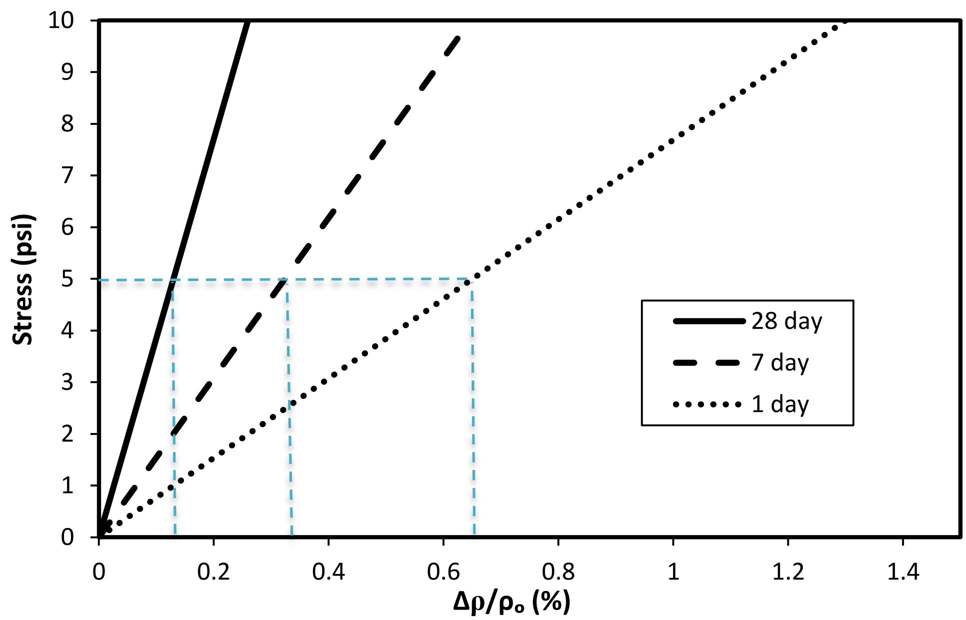

Fig. 6 - 18: Piezoresistivity of smart cement for different cuing time (Vipulanandan and Amani 2015), Stress at level 7.8 (D = 5 ft) above water table

Table 6 - 4: Resistivity changes due to stress above water level for different curing time

Curing Time	**Above Water Level 7.8 D = 5 ft**	**Resistivity changes due to stress**
Time (Day)	**σ (psi)**	**$\Delta\rho/\rho_o$ (%)**
1 DAY	**5**	**0.65**
7 DAY	**5**	**0.33**
28 DAY	**5**	**0.12**

(d) Resistivity Due to Shrinkage and Curing

Fig. 6 - 19 shows the results of field measurements. The resistance monitored during the time of curing are plotted for different levels.

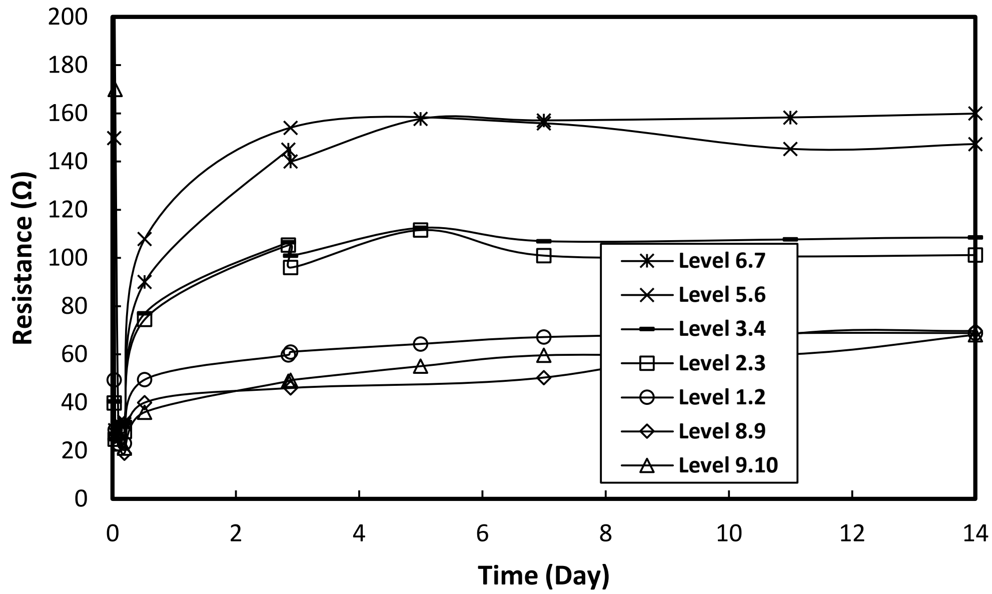

Fig. 6 - 19: Resistance monitoring during 14 days of time curing

Eq. (6 - 5) shows the resistivity changes during time of the curing which is called $\left(\frac{\Delta\rho}{\rho_0}\right)_{Exp}$ in Eq. (6 - 5).

Table 6 - 5: Measured resistivity change

Curing Time	**Below Water Level 1.2**	**Above Water Level 7.8**
Time (Day)	**$\Delta\rho/\rho_o$ (%)**	**$\Delta\rho/\rho_o$ (%)**
1 DAY	**11.3**	**67.9**
7 DAY	**35.9**	**164.2**
28 DAY	**41.7**	**168.6**

The measured resistivity change is due to piezoresistivity effects, shrinkage and curing effect. Therefore, it is separated to three parts according to

$$\left(\frac{\Delta\rho}{\rho_0}\right)_{Exp} = \left(\frac{\Delta\rho}{\rho_0}\right)_{\sigma} + \left(\frac{\Delta\rho}{\rho_0}\right)_{\varepsilon} + \left(\frac{\Delta\rho}{\rho_0}\right)_{curing}. \quad \textbf{(6 - 5)}$$

The resistivity changes due to curing and shrinkage is calculated according to Eq. (6 - 5) for different curing time and for above and below water table levels are shown in Table 6 - 6 and Table 6 - 7, respectively.

Table 6 - 6: The resistivity changes due to curing and shrinkage (above water table)

Above Water Level	$\left(\frac{\Delta\rho}{\rho_0}\right)_{\sigma}$	$\left(\frac{\Delta\rho}{\rho_0}\right)_{\varepsilon} + \left(\frac{\Delta\rho}{\rho_0}\right)_{curing}$	$\left(\frac{\Delta\rho}{\rho_0}\right)_{Total}$
1 Day	**0.65**	**67.25%**	**67.9**
7 Day	**0.33**	**163.87%**	**164.2**
28 Day	**0.12**	**168.48**	**168.6**

Table 6 - 7: The resistivity changes due to curing and shrinkage (below water table)

Below Water Level	$\left(\frac{\Delta\rho}{\rho_0}\right)_{\sigma}$	$\left(\frac{\Delta\rho}{\rho_0}\right)_{\varepsilon} + \left(\frac{\Delta\rho}{\rho_0}\right)_{curing}$	$\left(\frac{\Delta\rho}{\rho_0}\right)_{Total}$
1 Day	**3.1**	**8.2%**	**11.3**
7 Day	**1.6**	**34.3%**	**35.9**
28 Day	**0.625**	**41.075**	**41.7**

6.2. Numerical Analysis for Cemented Casing

The numerical analysis was performed using the COMSOL Multiphysics software. The stage 3 of performing a well called cemented casing is simulated. The borehole with the inner radius of 1 meter and outer radius of 2 meter, with the height of 10 meter. The 2D axisymmetric model used to model the borehole.

The material used in this study was the cement properties, elasticity modulus of E = 19 GPa, specific weight of 19 kN/m³ and the poison's ratio of 0.2. The surcharge is assumed to be zero. The internal pressure of 100 psi was applied inside the borehole. The external wall of the cement is assumed to be fixed as well as bottom of the cement.

6.2.1. Mesh generation

Linear quadrilateral elements used to model the 2D axisymmetric model, the maximum size of the element was 0.08 m, including 1625 elements.

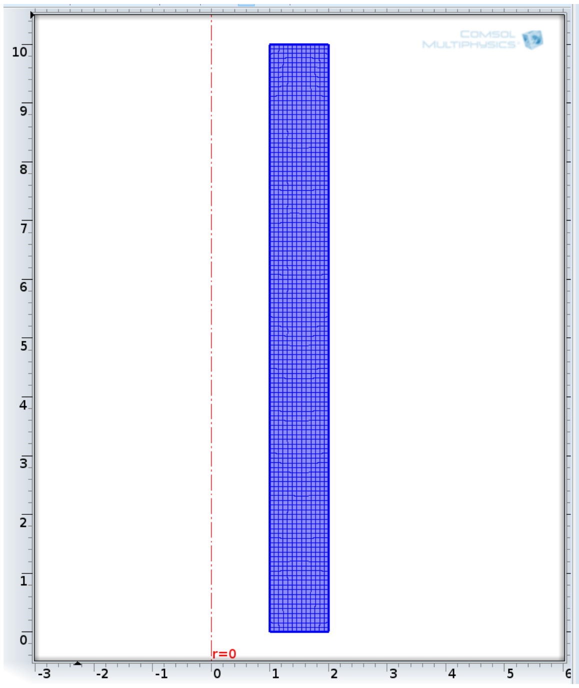

Fig. 6 - 20: Simulation of the 2D axisymmetric borehole

6.2.2. Results and Analysis

The radial, tangential stress and vertical stress contours are shown in Fig. 6 - 21, Fig. 6 - 22 and Fig. 6 - 23, respectively.

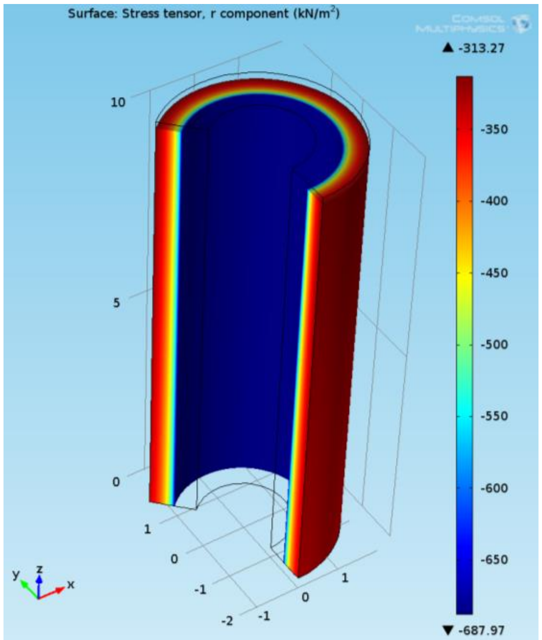

Fig. 6 - 21: Radial stress contour

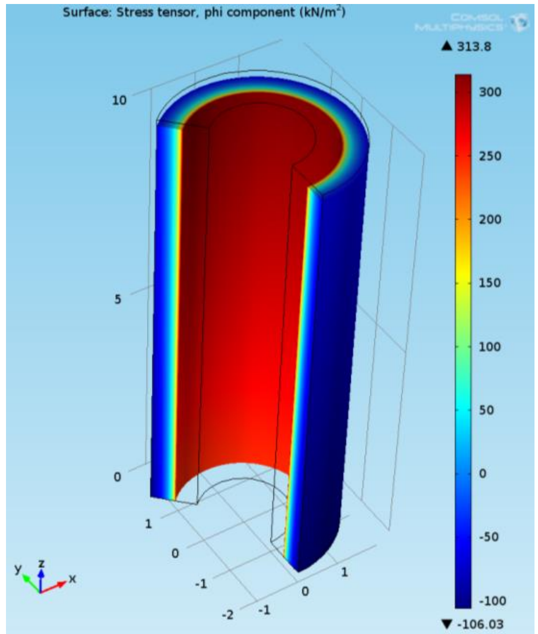

Fig. 6 - 22: Tangentional stress contour

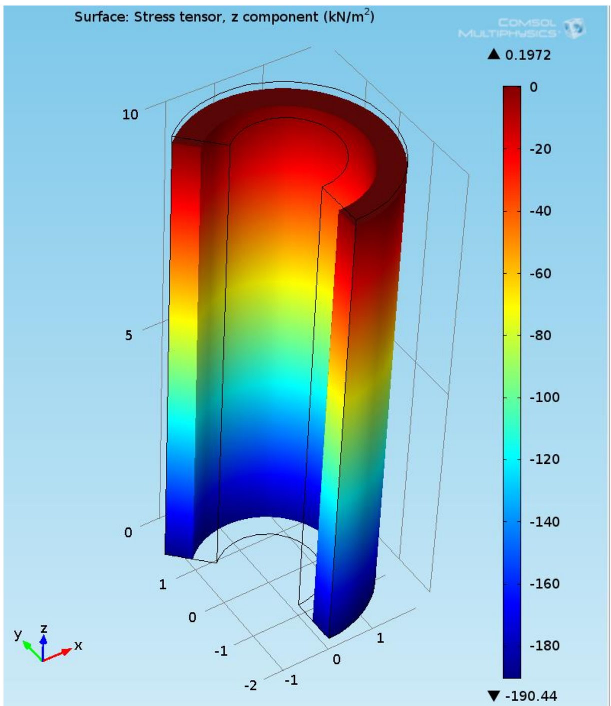

Fig. 6 - 23: Vertical stress contour

The displacement in radial and vertical displacement are shown in Fig. 6 - 24 and Fig. 6 - 25 and total displacement contour is as following.

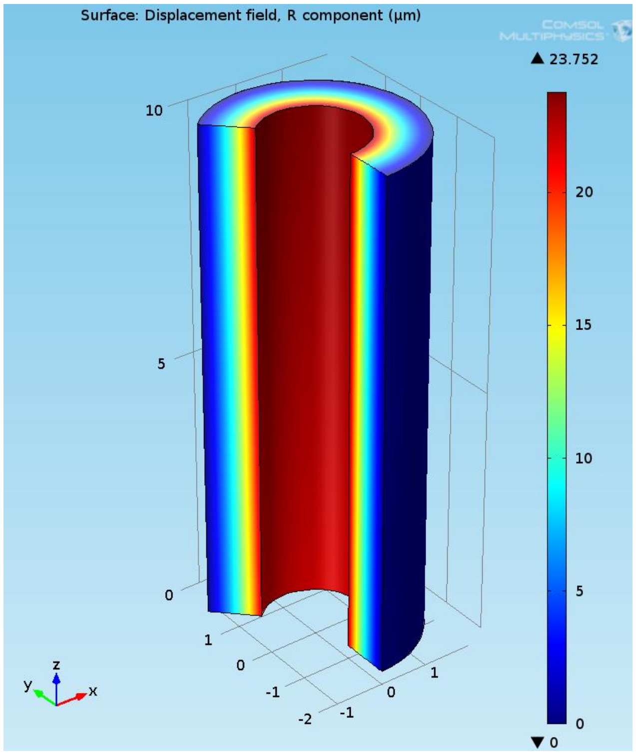

Fig. 6 - 24: Radial displacement contour

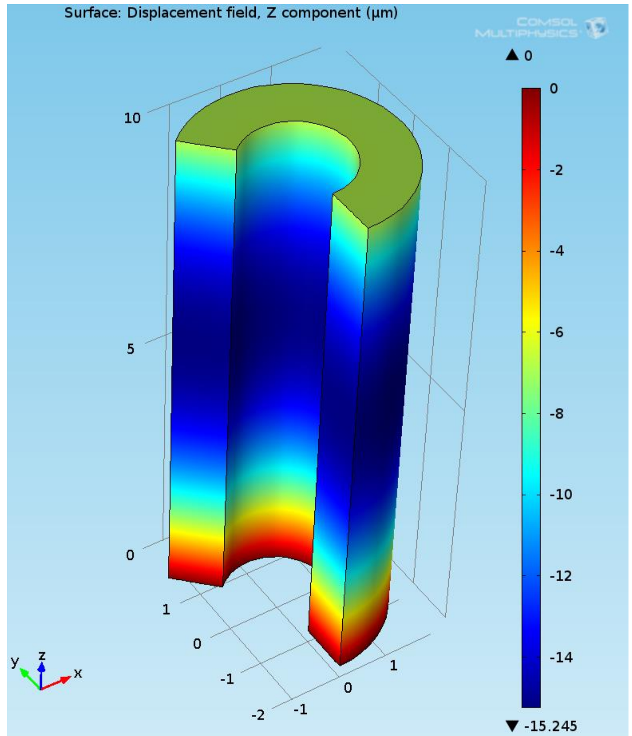

Fig. 6 - 25: Vertical displacement contour

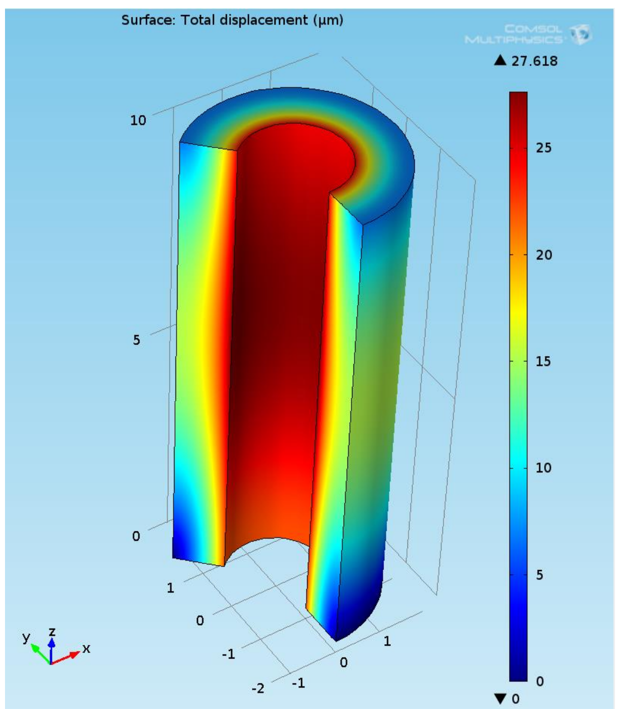

Fig. 6 - 26: Total displacement contour

The mesh refinement was performed to optimize the number of the mesh and it was found the mesh element size between 0.06 m and 0.04 m and the mesh number of 5000 is the optimum.

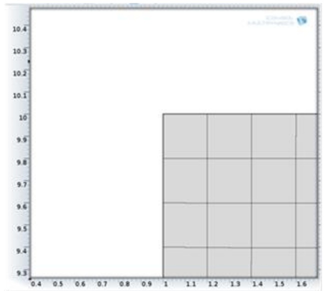

Mesh Element Size: 0.2 m
Mesh Element Number: 250

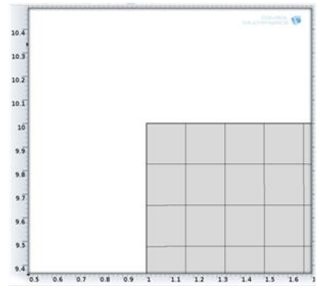

Mesh Element Size: 0.175 m
Mesh Element Number: 342

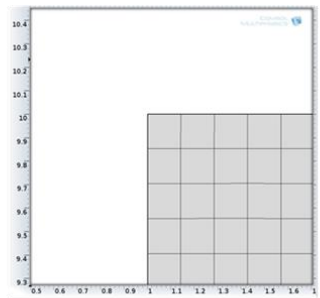

Mesh Element Size: 0.15 m
Mesh Element Number: 469

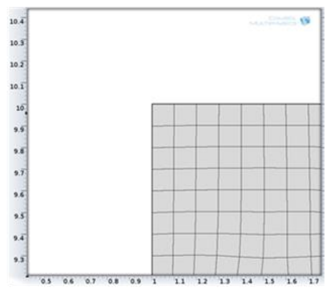

Mesh Element Size: 0.1 m
Mesh Element Number: 1158

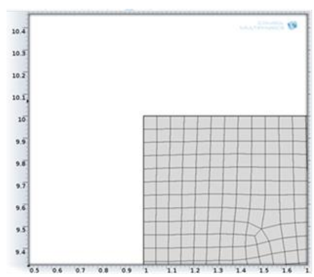

Mesh Element Size: 0.06 m
Mesh Element Number: 3135

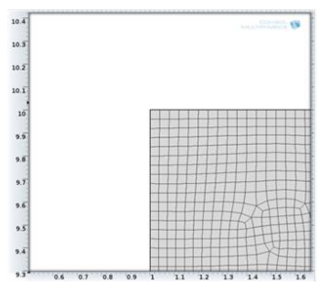

Mesh Element Size: 0.04 m
Mesh Element Number: 6841

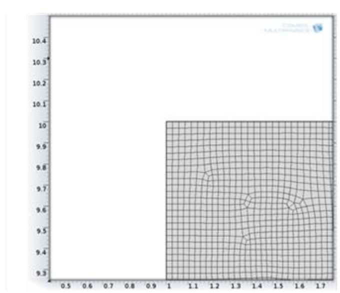

Mesh Element Size: 0.03 m
Mesh Element Number: 12241

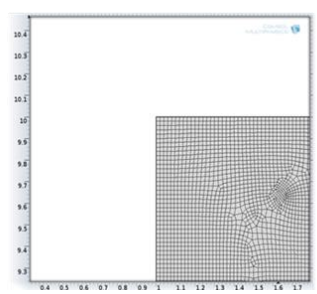

Mesh Element Size: 0.02 m
Mesh Element Number: 27483

Fig. 6 - 27: Mesh refinements of the axisymmetric model for cemented casing

The radial stress from the numerical solution the radius is captured as following. The mesh refinement for the minimum radial stress at the external side of the cement was done and the optimum number of the element is estimated around 5000.

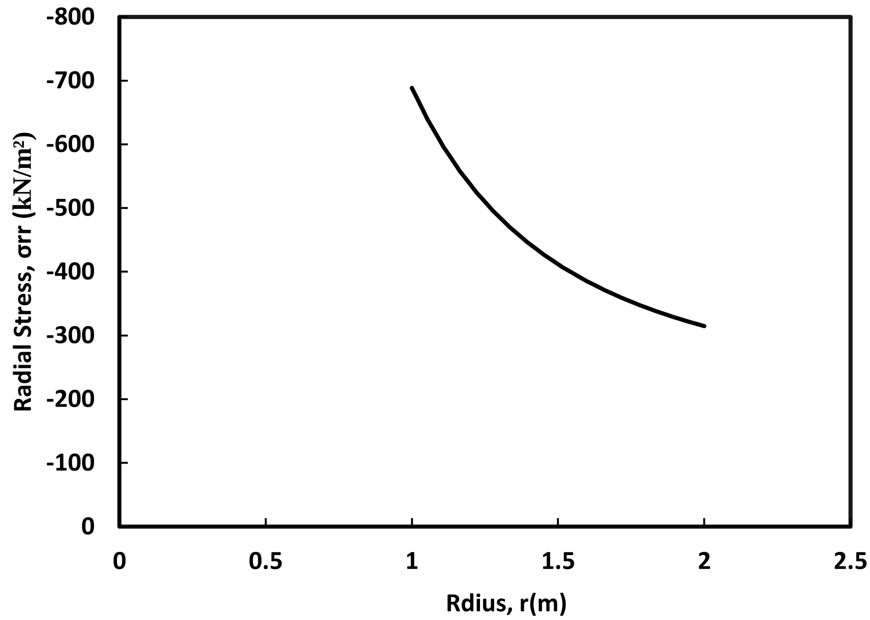

Fig. 6 - 28: Numerical analysis for radial stress along the radius

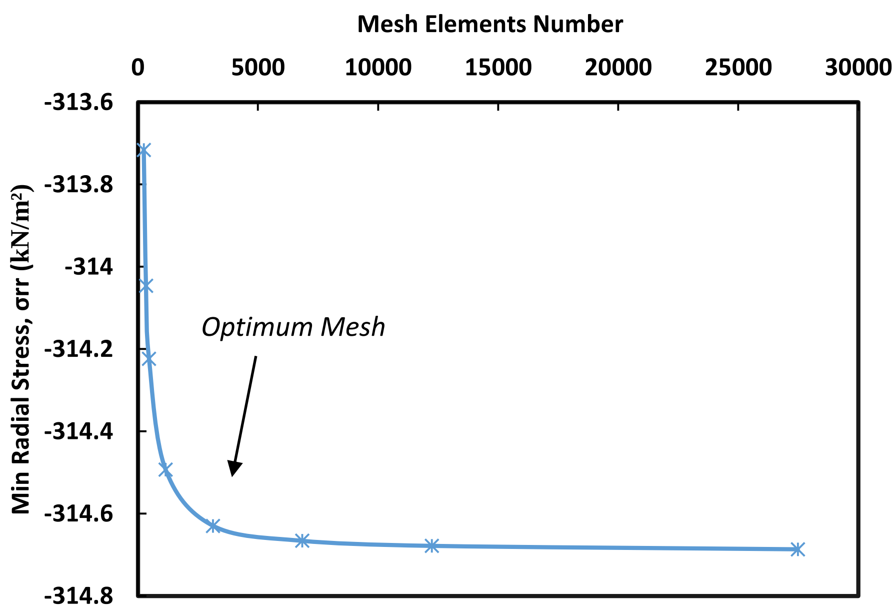

Fig. 6 - 29: Min radial stress optimization

The hoop stress from the numerical solution along the radius is shown and the mesh refinement for the maximum shows the optimum mesh number is about 5000 elements. The maximum hoop stress happens near the wellbore wall as tension and at external part of cemented casing it becomes compression.

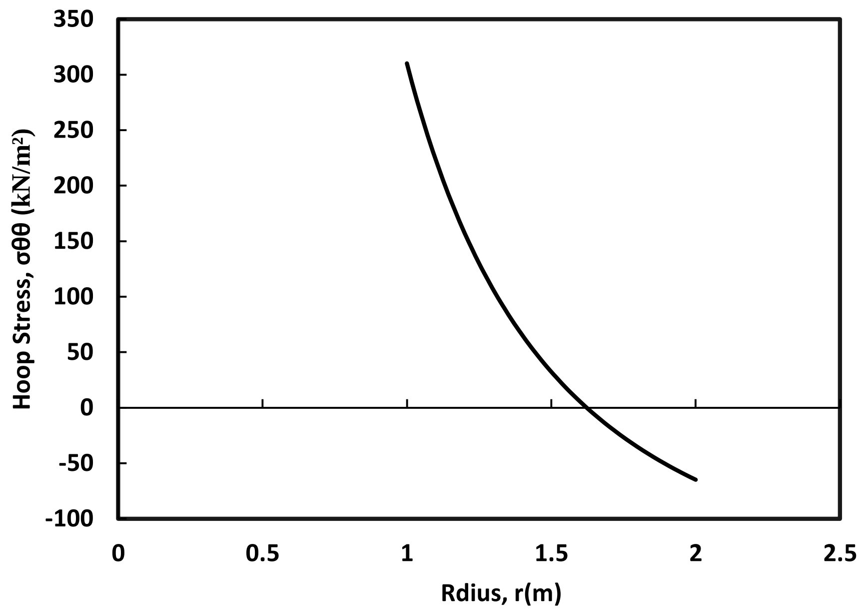

Fig. 6 - 30: Numerical analysis for hoop stress along the radius

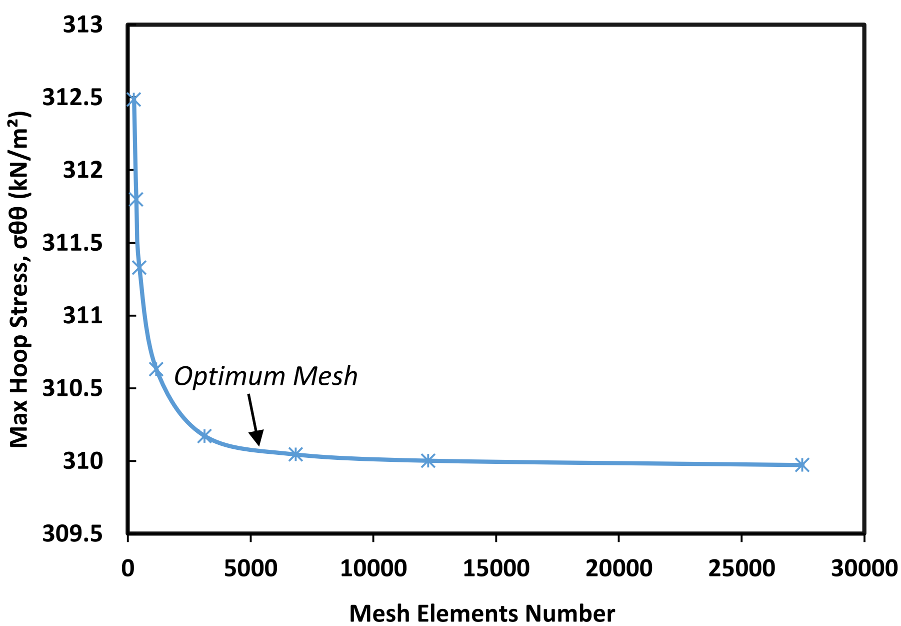

Fig. 6 - 31: Max hoop stress optimization

The vertical stress through the depth is analyzed and shown in Fig. 6 - 32. The mesh refinement also was done and shown in Fig. 6 - 33 which express the 5000 mesh element is the optimum number.

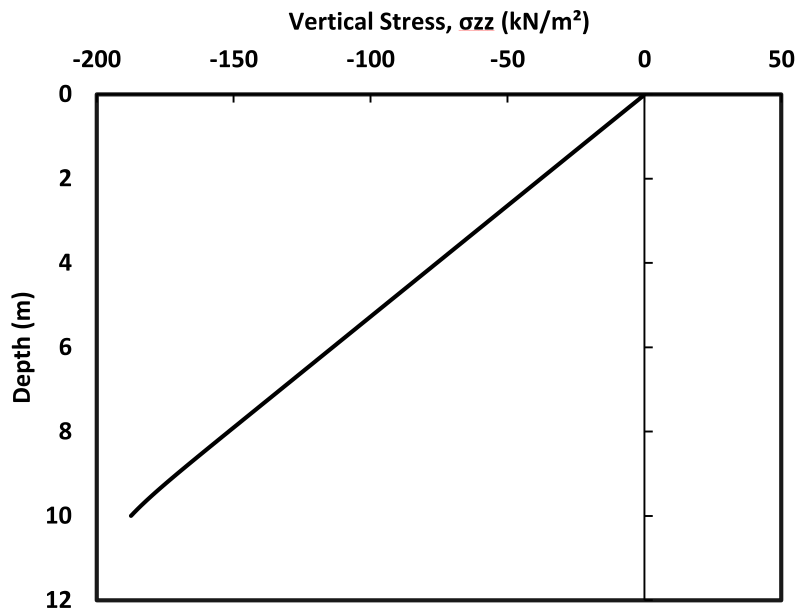

Fig. 6 - 32: Numerical analysis for vertical stress through the depth

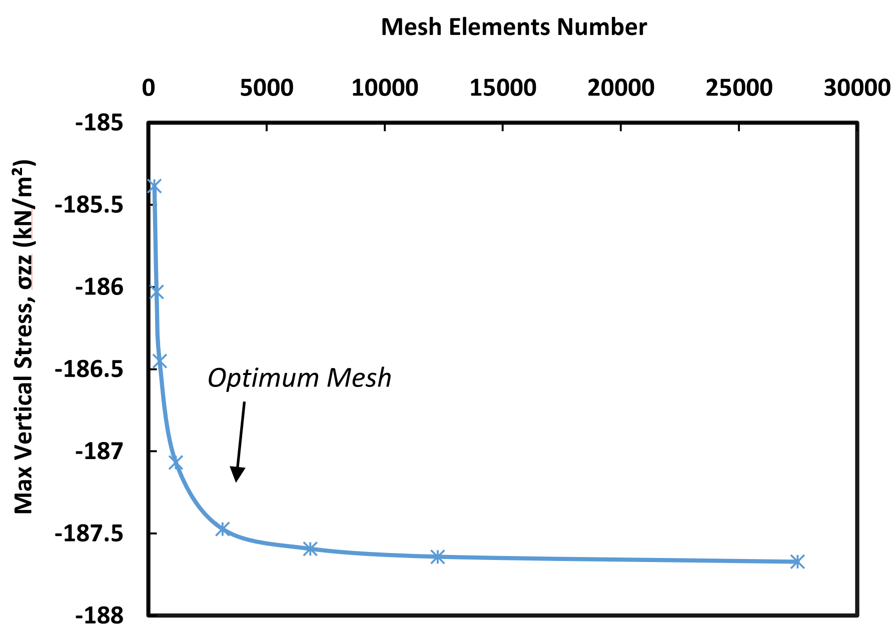

Fig. 6 - 33: Max vertical stress optimization

The displacement versus radius is analyzed and shown in following figure while the mesh refinement shows the optimum number of the element is around 5000 elements.

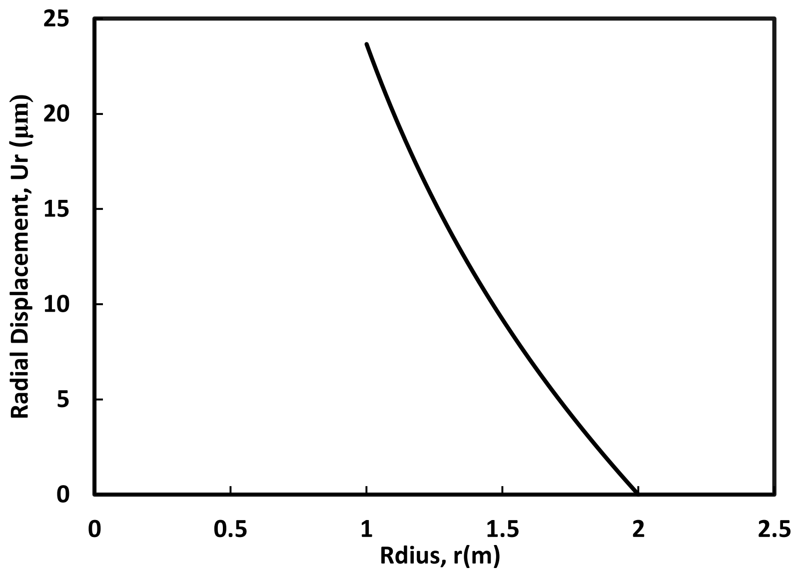

Fig. 6 - 34: Numerical analysis for radial displacement along the radius

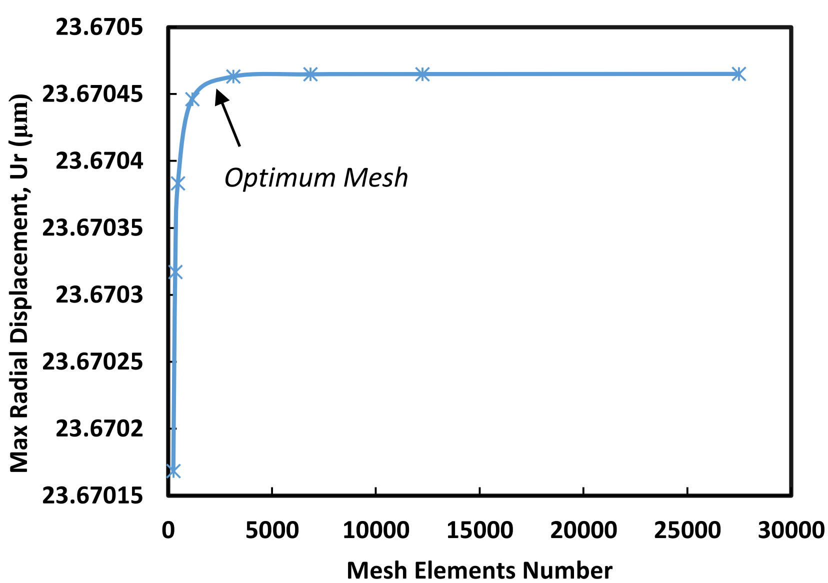

Fig. 6 - 35: Max radial displacement optimization

The field test cemented casing is considered with r = 0.122 m and the internal pressure of 20 psi. The vertical stress calculated from the relationship between resistivity changes and stresses was predicted in Fig. 6 - 11. The vertical stress using the COMSOL Multiphysics is compared with the field test results and it is shown in Fig. 6 - 36.

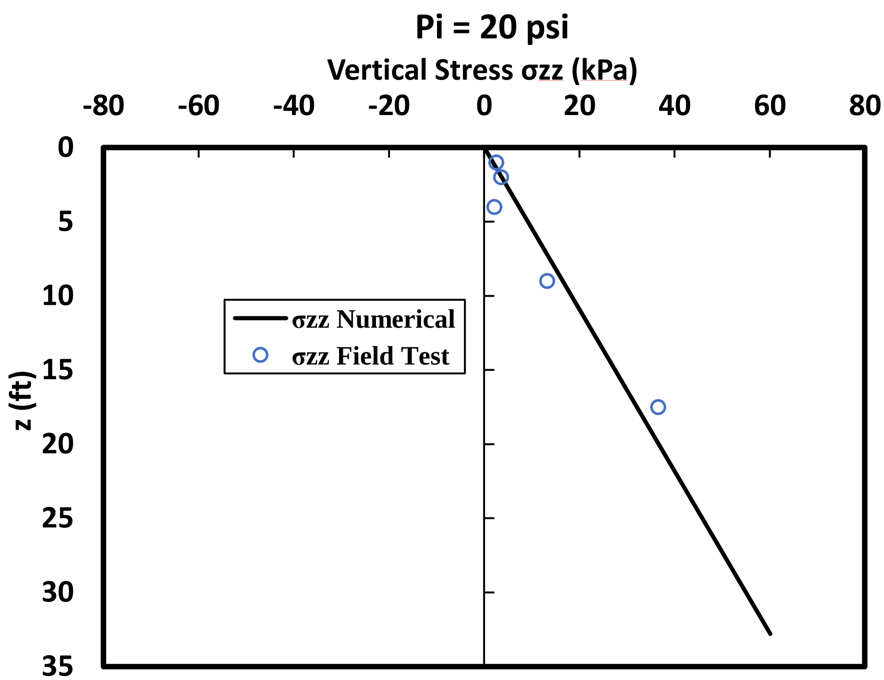

Fig. 6 - 36: The numerical and field test results for vertical stress

The preliminary study of the analytical solution for cemented casing was done which is explained in the appendix.

6.3. Summary

Three physical models have been investigated here including small model, large model and field model tests. The pressure applied inside the casing in small and large model test and the change of resistivity in smart cement was capture through p, q model. In the field model we have plan to apply the pressure. The resistivity changes monitored in the field tests and from piezoresstivitiy effects the resistivity changes due to stress was separated from curing and shrinkage resistivity changes below and above water table.

The numerical solution using the COMSOL Multiphysics for the stage 3 of the performance of the oil well which is the cemented casing. In the physical model related to the field well results, due to the piezoresistivity effects, the vertical stress predicted from the resistivity changes measurements. The vertical stress analyzed from numerical analysis compared with the stress predicted from the resistivity changes and the results was verified.

1. Three physical models made to find the relationship between the pressure inside the casing and the changes in the resistivity.
2. The stress results from numerical model was performed. The results of the radial stress, hoop stress and vertical stress was captured with the radial displacement effect along the radius. The mesh refinement was studied to optimize the proper amount of the mesh element number and mesh element size. The numerical results compared with the stresses predicted from resistivity changes due to the piezoresistive model proposed in this study.

CONCLUSION AND FUTURE WORK

The reaction between the three phases were quantified using six independent material parameters. These parameters are functions of time, temperature and pressure. In this study, at room temperature and pressure the cement with water to cement ratio of 0.4 cured and monitored over 800 days. There were three measurements, weight, volume and the moisture content with time and developing correlation between few selected parameters. The six independent material parameters were quantified. This model can be used for any material with three phases in any field due to consideration of the physical and chemical reactions. Influence of the six material parameters on the shrinkage, porosity and electrical resistivity of the solidified cement was quantified. The volume shrinkage was influenced by the liquid – solid reactive model parameter. Later on a new model proposed for the failure criterion called Vipulananadan model (Hyperbolic model). Which can be utilized in the failure of any material.

The first stage of the performance of the oil well is drilling with vortex flow. In this study, the complex potential of the vortex flow used to implement the eccentricity effects in the first stage of the performance of the oil well. For the second stage, which is installing of the casing, the axial flow of the drilling mud and cementing is considered. The new rheological model called Hyperbolic model used to develop the fluid characteristics such as velocity, shear stress and strain rate. the proposed model was implemented in COMSOL Multiphysics as analytic base function and the results compared with the Newtonian fluid as well and also the eccentricity of the axial fluid flow was analyzed using numerical method. Later on, a new kinetic for model has been developed assuming that the permeability and solid content during is changing with time while the cake is built up. The new kinetic model can model the fluid loss tests and compared with the API model that has the limitation of the constant permeability and solid fraction in the filter cake. The proposed model captures a realistic behavior of the filter cake characteristics.

Self-sensing smart cement was used in this study with adding less than 1% of conduct filler which makes the sensing properties much higher than normal cement. Two cases of the circuit, one with the resistance only bulk material and the other the combination of the resistance and capacitance are compared. By comparison of the impedance as a function of frequency which show in first case, the resistance only bulk material has impedance residue at high frequencies (300 kHz) while in the second case with the combination of resistance-capacitance material, the impedance reaches to zero. Monitoring impedance of the smart cement's impedance proved this material's behavior is matching with resistance only bulk material. Which justifies the measurement of the resistance and resistivity changes in this study. Also with the impedance monitoring of the smart cement, it was proved that the two probe measurements work perfectly at high frequency (300 kHz) and due to elimination of the contact capacitance effects.

The existence of micro cracks inside the cement in the oil well may cause gas migration the disasters might happen if the crack growth is not recognized in a right time and right place. Therefore, the knowledge of the cracks inside the cement is a vital task in oil well cement. Due to this important element (cemented casing), the fracture was investigated for the smart cement. The electrical measurement was evaluated beside the mechanical properties of the fracture, the piezoresistivity effects was monitored during the crack growth and crack mouth opening displacement. Using this real time monitoring of cement resistivity changes is leading us to locate the crack. The stress intensity factor was calculated from the three-point bending test. Finally, the stress intensity factor values were compared with the numerical methods.

Three physical models including in small model test, large model test and field well (built in Energy Research Park) have been investigated in this study. In each physical test, four angles were built and used to install the thermocouples and wires at different levels at four sides. The angles were calibrated and after setting the cement the pressure applied inside the casing in small and large model test and the change of resistivity in smart cement was captured through p, q model through piezoresistivity effects. In the field model, there were water table at a specific height under ground level. The resistivity changes monitored in the field tests below and above water level and from piezoresstivitiy effects the resistivity changes due to stress was separated from the curing and shrinkage resistivity changes below and above water table.

The numerical solution using the COMSOL Multiphysics for the stage 3 of the performance of the oil well which is the cemented casing. The results of the radial stress, hoop stress and vertical stress was captured with the radial displacement effect along the radius. The mesh refinement was studied to optimize the proper amount of the mesh element number and mesh element size. In the physical model related to the field well results, due to the piezoresistivity effects, the vertical stress predicted from the resistivity changes measurements and it was compared with the numerical analysis.

This study can be continued in future as following

1. The effect of the temperature can be added to the models. The thermal effect was studied on the field and this study can be continued adding the thermal effects either in the physical models and also in the three phase reactive materials.
2. The eccentricity is a big challenge in the oil well cementing. The eccentricity effects can be evaluated according to the real situation in the wellbore while there is not only one casing in the installation process.
3. The boundary conditions around the wellbore is not a realistic case used in the numerical analysis. One can continue the solution using more realistic boundary conditions.
4. In the numerical analysis, the cement is not a linear elastic material in reality. This study can be continued with nonlinear behavior of the cementitious material as well as anisotropy effect of the cement.

REFERENCES

Abbas, R., Cunningham, E., Munk, T., Bjelland, B., Chukwueke, V., Ferri, A., Moussa, O. (2002). “Solutions for Long-Term Zonal Isolation.” *Oilfield Review - Schlumberger*, 1(1), 16–29.

Ajovalasit, A., (1979), “Measurement of Residual Stresses by the Hole-drilling Method: Influence of Hole Eccentricity,” *Journal of Strain Analysis*, Vol. 14, No. 4, pp. 171--178.

API Recommended Practice 10B (1997), Recommended Practice for Testing Well Cements Exploration and Production Department, 22nd Edition.

API Recommended Practice 10B (1997). “Recommended practice for testing well cements.” Exploration and Production Department, 22nd Edition.

API recommended Practice 65 (2002) Cementing Shallow Water Flow Zones in Deepwater Wells.

API recommended Practice 65 (2002). “Cementing shallow water flow zones in deepwater wells.”

Atkinson, B.K., ed., (1987), “Fracture Mechanics of Rock,” Academic Press, London, 534 p.

Avci, A., Arikan, H. and Akdemir, A., (2004), “Fracture behavior of glass fiber reinforced polymer composite.” *Cem Concr Res* 2004; 34:429–34

Azar, J. J. and Samuel, G. Robello, (2007), “Drilling Engineering,” ebrary, Inc. Publisher: PennWell Corp.

Azhari, F. and Banthia, N., (2012). “Cement-based sensors with carbon fibers and carbon nanotubes for piezoresistive sensing,” *Cement Concrete Compos*. 34,866–873.

Brameshuber, W., and Raupach, M. (2003). “Nondestructive Determination of the Water Content in the Concrete Cover using the Multiring Electrode” Part I Aspects of Concrete Technology. *International Symposium (NDT-CE)*, 6–11.

Brouwers, H. J. H. (2004a). “The work of Powers and Brownyard revisited: Part 1.” *Cement and Concrete Research*, *34*(9), 1697–1716. http://doi.org/10.1016/j.cemconres.2004.05.031

Brouwers, H. J. H. (2004b). “The work of Powers and Brownyard revisited: Part 2.” *Cement and Concrete Research*, *34*(9), 1697–1716. http://doi.org/10.1016/j.cemconres.2004.05.031

Brouwers, H. J. H., (2012). “Paste models for hydrating calcium sulfates, using the approach by Powers and Brownyard.” *Construction and Building Materials*, *36*, 1044–1047. http://doi.org/10.1016/j.conbuildmat.2012.06.019.

Budynas, R. G., (1999), “*Advanced Strength and Applied Stress Analysis* (Second Edi).” McGraw-Hill Book Company.

Bundar, B. (2015). “Ferron Bio mineralized Cement Based Materials: Impact of Inoculating Bacteria on Hydration and Strength.” *Cement and Concrete Research*.

Cantwell, B. and Coles, D., (1983). “An experimental study of entrainment and transport in the turbulent near wake of a circular cylinder.” *Journal of Fluid Mechanics* 136, 321–374.

Carter, K. M. and Van Oort, E. and Barendrecht, A., (2014), "Improved Regulatory Oversight Using Real- Time Data Monitoring Technologies in the Wake of Macondo," *SPE 170323*, pp. 1–51.

Chattot, J. J. and Hafez, M.M. (2015) “*Theoretical and Applied Aerodynamics*,” DOI 10.1007/978-94-017-9825-9_2

Chung, D. D. L (1995), "Strain Sensors Based on Electrical Resistance Change,” *Smart Materials Structures*, No. 4, pp. 59-61.

Chung, D.D.L (2001), “Functional Properties of Cement-Matrix Composites,” *Journal of Material Science*, Vol. 36, pp. 1315-1324.

Civan, F., (1996), "A Multi-Purpose Formation Damage Model," paper SPE 31101 presented at the 1996 SPE *International Symposium on Formation Damage Control*, Lafayette, Louisiana, 14–15 February.

Colmenares L. B. and Zoback M. D. (2002), "A statistical evaluation of intact rock failure criteria constrained by polyaxial test data for five different rocks" *International Journal of Rock Mechanics & Mining Sciences*, 39: 695–729.

Darbe, R., Gordon, C. and Morgan, R. (2008). "Slurry Design Considerations for Mechanically Enhanced Cement Systems." *AADE.*

Delale, F. (1984), "Stress analysis of multilayered plates around circular holes." *International Journal of Engineering Science*, 22(1):57–75.

Fan, L., Fujie, K., Long, T., and Tang, W. (1987), "Bioreactor with Immobilized Living Cells for Phenol Degradation." *Biotechnology and Bioengineering*, 498–504.

Fathi-Najafi, M. and Theliander, H., (1995), "Determination of Local Filtration Properties at Constant Pressure." *Separations Technology* **5** (3): 165-178.

Garboczi, E. J. (2000), "Conductivity of the Interfacial Transition Zone in Cement Mortars Introduction." *Journal of the American Ceramic Society*, *38*(5), 1137–1144.

Goodwin, K. J., and Co, M. T., (1997), "Oilwell / Gaswell Cement-Sheath Evaluation." *Society of Petroleum Engineers*, (December).

Griffith, J. and Faul, R. (1997). "Mud Management Special Slurries Improve Deepwater Cementing Operations," *Oil and Gas Journal*, Vol. 95, No. 42, pp. 49-51.

Guillot, D. (1990). "Rheology of well cement slurries." In: E.B. Nelson and Guillot, D. (Eds.), *Well Cementing*, *Schlumberger*, Texas, pp. 93-142.

Handin, J., (1965), “Strength of Oil Well Cements at Downhole Pressure- Temperature Conditions” *Society of Petroleum Engineers*.

Hansen, T. C., (1986). “Physical structure of hardened cement paste. A classical approach.” *Materials and Structures, 19*(6), 423–436. http://doi.org/10.1007/BF02472146

Harness, P.E. and Sabins, F.L. (1992). “New Technique Provides Better Low Density Cement Evaluation.” *Society of Petroleum Engineers*

Herschel, W. H. and Bulkley, R., (1926), “Konsistenzmessungen von Gummi-Benzollösungen.” Kolloid Z. 39, 291–300.

Hill, A. D. (1990). “Cement-Quality Logging. Production Logging—Theoretical and Interpretative Elements”, Vol. 14, 123-140. Richardson, Texas: Monograph Series, SPE.

Hoek, E. and Brown, E. (1980), “Empirical strength criterion for rock masses.” *J Geotech Eng Div*;106(GT9):1013–35.

Izon, D., Mayes, M. (2007). “Absence of fatalities in blowouts encouraging in MMS study of OCS incidents 1992-2006.” *Well Control*, pp. 86-90.

Jalali. “ Sulphuric acid resistance of plain polymer modified concrete.” *Construction and Building Materials.*

Jaeger JC, N. G. W. COOK. (1979), “*Fundamentals of rock mechanics*.”3rd ed. London: Chapman & Hall.

Jamiolkowski, M. B., Lancellotta, R. and Lo Presti, D., (1999), “*Presti failure Deformation Characteristics of Geomaterials,*” Volume 1, Torino/Italy1q

Jenq. Y. S and Shah. P, (1985). “A Fracture toughness Criterion for Concrete” *Engineering Fracture Mechanics*, Vol 21, No 5, pp. 1055-1069.

Jensen, O. M. and Hansen, P. F. (2000). “Water-entrained cement-based materials I . Principle and theoretical background,” *31*(October), 1–13.

Jiao, D., and Sharma, M. M., (1994), “Mechanism of cake buildup in crossflow filtration of colloidal suspensions.” *Journal of Colloid and Interface Science*, 162(2), 454-462. DOI: 10.1006/jcis.1994.1060

Jiegiong. (2013). “Antibacterial and Physical Properties of EGCG Containing Glass Ionomer Cements.” *Journal of dentistry*.

John, B. (1992). “Class G and H Basic Oil Well Cements,” World Cement.

Khatib, Z., I., (1994), “Prediction of Formation Damage Due to Suspended Solids: Modeling Approach of Filter Cake Buildup in Injectors.” Paper *SPE 28488* presented at the Annual Technical Conference and Exhibition, New Orleans, Louisiana, 25-28 September.

Al-Buraik, Khalid A., Al-Abdulqader, Khalid A. and Bsaibes, R., (1998), “Prevention of Shallow Gas Migration Through Cement.” *SPE 47775*.

Khandka, R. kumar. (2007), “*Leakage Behind Casing*.” Norway, Well R-3H (chapter 5).

Kim, C., Seok, C.S. and Yang, W. H., 2000, “Influence of the Hole Eccentricity in Residual Stresses Measurement by the Hole-drilling Method,” *Transactions of the KSME*, Vol. 24, No. 8, pp. 2059~2064(in Korean).

Kim, Ch. and Yang, W. (2002), “Prediction of Error due to Eccentricity of Hole in Hole-Drilling Method Using Neural Network”, *KSME International Journal*, Vol. 16No. 11, pp. 1359~1366.

Kim, J. and Vipulanandan, C. (2006)"Removal of Lead from Contaminated Water and Clay Soil Using a Biosurfactant," *Journal of Environmental Engineering*, Vol. 132, No. 7, pp.857-865.

Kim, J. and Vipulanandan, C. (2003) "Effect of pH, Sulfate and Sodium on the EDTA titration of Calcium," *Cement and Concrete Research*, Vol. 33(5), pp. 621-627.

King, G.E. (2012). “Cement Evaluation Methods to Prove Isolation of Barriers in Oil and Gas Wells: Should a Cement Bond Log (CBL) Be Run or Required in Every Well?” *Apache Corporation.*

Kirsch G.Die “*Theorie der Elastizität und die Bedürfnisseder Festigkeitslehre. Zeitschrift des Vereines deutscher Ingenieure*”;42(28):797–807.

Kopko, V. M. (2002). “Heat network pipe heat insulation: Study Guide.” Minsk, M: Tehnoprint.

Kyle, M. and Eric, O. (2014). “Improved regulatory oversight using real- time data monitoring technologies in the Wake of Mocondo.” *SPE 170323*, pp. 1-51.

Labibzadeh, M., Zhhabizadeh, B. and Khajehdezfuly, A., (2010) "Early Age Compressive Strength Assessment of Oil Well Class G Cement Due to Borehole Pressure and Temperature Changes, *Journal of American Science*, Vol. 6, No.7, pp.38-47.

Lam, K. M., (2009) “Vortex shedding flow behind a slowly rotating circular cylinder.” *J. Fluids. Struct.*, 25(2), pp. 245-262.

Li and Wei. (2003), “The Electrical Resistivity of Cement Paste Incorporated with Retarder “LI Zong-jin WEI Xiao-sheng. *Journal of Wuhan University of Technology - Mater. SCi. Ed.*, *18*, 2–4.

Liang, Y., Wang H. and Ren X., (2008), “Analytical solution for spatially axisymmetric problem of thick-walled cylinder subjected to different linearly varying pressures along the axis and uniform pressures at two ends,” *Science in China Series G: Physics, Mechanics & Astronomy*, Vol. 51, pp:98-104.

Liao, Y. and Wei, X. (2014). "Relationship between chemical shrinkage and electrical resistivity for cement pastes at early age." Journal of Materials in Civil Engineering, Vol. 26, pp. 384–387.

Mairoser, Th., Mundy, J. A. Melville, A., Hodash, D., Cueva, P., Held, R., Glavic, A., Schubert, J., Muller, D.A., Schlom, D.G. and Schmehl, A., (2015), "High-Quality EuO Thin Films the Easy Way via Topotactic Transformation," *Nature Communications* 6, 7716.

McDaniel, J., (2014), "Cement Sheath Durability: Increasing Cement Sheath Integrity to Reduce Gas Migration in the Marcellus Shale Play." *SPE 168650 Hydraulic Fracturing Technology Conference*. http://doi.org/10.2118/168650-MS

Mebarkia, S. and Vipulanandan, C. (1992). "Compressive behavior of glass-fiber-reinforced polymer concrete." *Journal of Materials in Civil Engineering*, Vol. 4, pp. 91–105.

Mellas, M., Mezghiche, B., and Ash, J. E. (2003). "Estimation of the Porosity of Portland Cement Pastes Using Backscattered Electron Image," 47–51.

Mohammed, A. and Vipulanandan, C. (2013). "Compressive and tensile behavior of polymer treated sulfate contaminated CL soil." *Journal of Geotechnical and Geological Engineering*, Vol. 32, pp. 71-83.

Naik, T.R., Kumar, R., and Ramme, B.W., (2010). "Effect of High Carbon Fly Ash on the Electrical Resistivity of Fly Ash Concrete Containing Carbon Fibers." *Sustainable Construction Materials and Technologies.*

Nakayama, Y. and Boucher R., (1998), "*Introduction to Fluid Mechanics."* Oxford: Butterworth-Heinemann.

Ochoa, M., (2006), “Analysis of Drilling Fluid Rheology and Tool Joint Effect to Reduce Errors in Hydraulics Calculations” (Petroleum Engineering Doctor of Philosophy). Texas A&M University, pp.1–191.

Osisanya, S. O. and Griffith, J. (1997), “Evaluation of Cement Slurry Quality Using Filter Cake Permeability and Thickness”, Paper PETSOC-97-136 presented Annual Technical Meeting, June 8 - 11, Calgary, Alberta.

Paulini, P. (1994), “A through solution model for volume changes of cement hydration.” *Cement and Concrete Research*, *24*(3), 488–496. http://doi.org/10.1016/0008-8846(94)90137-6

Pallardy, R. (2010). “Deepwater Horizon oil spill of 2010, Oil Spill, Gulf of Mexico.” Encyclopedia Britannica.

Park, J, Vipulanandan, C., Kim, J. and Oh, M. H. (2006) "Effect of Surfactants and Electrolyte Solutions on the Properties of Soils," *Journal of Environmental Geology*, Vol. 49, pp.977-989.

Philippa, L. M., and Henryk, G. P., (2012). “Validation of Methods to Determine CTOD from SENT specimens.” *Isope*, *4*, 1–8.

Powers, T. C., (1958), “Structure and Physical properties of Hardened Portland Cement Paste.” *American Ceramic Society. Structure*, 41(1), 1–6.

Powers, T.C., (1947), “A discussion of cement hydration in relation to the curing of concrete, Bull.” 25, Res. Lab. of Portland Cement Association, Skokie, IL, U.S., reprinted from Proc. Highway Res. Board, Vol. 27 (1947), p. 178-188.

Powers, T.C. and Brownyard, T.L. (1948), “Studies of the physical properties of hardened Portland cement paste, Bull.” 22, Res. Lab. of Portland Cement Association, Skokie, IL, U.S, reprinted from *J. Am. Concrete Inst.* (Proc.), Vol. 43 (1947), p. 101-132, p. 249-336, p. 469-505, p. 549-602, p. 669-712, p. 845-880, p. 933-992.

Powers, T. C., (1960), "Physical properties of cement paste," Bull. 154, Res. Lab. of Portland Cement Association, Skokie, IL, U.S. reprinted from Proc. 4th ISCC, vol. 2, pp. 577–609.

Ravi, K., Bosma, M. and Gastebled, O. (2002), "Improve the Economics of Oil and Gas Wells by Reducing the Risk of Cement Failure." *Proceedings of IADC/SPE Drilling Conference*. http://doi.org/10.2118/74497-MS

Reddy, B.R. and Riley, W.D., (2004), "High temperature viscosifying and fluid loss controlling additives for well cements, well cement compositions and methods." US Patent 6 770 604, Assigned to Halliburton Energy Services, Inc. (Duncan, OK).

Saada, A. S. (2009). "*Elasticity: Theory and Applications*." J. Ross Publishing, Inc.

Sadd, M. H., (2005) "*Elasticity: Theory, Applications, and Numerics,*" Elsevier Inc.

Salim, P. and Amani, M. "Special Considerations in Cementing HPHT Wells." *International Journal of Engineering and Applied Science.*

Samsuri, A., Junin, R., Osman, A.M. (2001). "The utilization of Malaysian local bentonite as an extender and free water controller in oil-well cement technology," *Society of Petroleum Engineers.*

Sarap, G.D., Sivanandan, M., Patil, S., and Deshpande, A.P. (2009), "The use of high performance spacers for zonal isolation in high temperature High-pressure wells" SPE/IADC 124275.

Savin, GN., (1961), "*Stress concentrations around holes*." NewYork: Pergamon.

Selvadurai, A. P. S. (2000). "*Partial Differential Equations in Mechanics* 2." Springer.

Shah, S. P., (1991), “Toughening mechanisms in quasi-brittle materials.” *Kluwer Academic Publisher*, Dordrecht.

Shah, S. P. and Subramaniam, K. V., (2000), “Use of nondestructive ultrasonic techniques for material assessment and in-service monitoring of concrete structures,” *NDTnet*, vol. 5, no. 02.

Shahrouzi, J., Hesaraki, S., and Zamanian, A. (2012), “The Effect of Paste Concentration on Mechanical and Setting Properties of Calcium Phosphate Bone Cements,” *1*(1), 1–7.

Soutas-Little, Robert W., (1999) “*Elasticity*” Dover, NY, ISBN: 0486406903.

Swayze, M. A., (1954)., “Effects of High Pressures and Temperatures on Strength of Oil-well Cements.” *American Petroleum Institute*.

Takagi, S., and Chow, L. C. (2001), “Formation of macro pores in calcium phosphate cement implants.” *Journal of Materials Science: Materials in Medicine*, *12*, 135–139. http://doi.org/10.1023/A:1008917910468

Talabani, S., (1997), “Gas Migration Eliminated Through Correct Cement Design Including Elastomers.” *SPE-39279-MS*.

Tang, J., Ge, G., and Brus, L. E. (2002), “Gas-liquid-solid phase transition model for two-dimensional nanocrystal self-assembly on graphite.” *Journal of Physical Chemistry B*, *106*(22), 5653–5658. http://doi.org/10.1021/jp014559c

Thaemlitz, J. and Patel, A.D., (1999), "New environmentally safe high-temperature water-based drilling-fluid system." *SPE Drilling & Completion* Vol. 14(3), 185-189.

Tien, C., Bai, R. and Ramarao, B. V., (1997), “Analysis of cake growth in cake filtration. The case of fine particle retention.” AIChE J., 43, 1, 33-44.

Timoshenko, S. and Goodier, J.N., (1951), “*Theory of Elasticity*,” New York-Toronto-London: McGraw-Hill book Co.

Tirasat, S. and Chai, J., (2007), “Evaluation of Sulphate Resistance of Concrete Containing Palm Oil Fuel Ash.” *Construction and Building Materials*.

Tsivillis. (2012). “Sulfate Resistance of Limestone Cement Concrete Exposed to Combined Chloride Attack.” *Cement and Concrete Composites*.

Usluogullari, O. and Vipulanandan, C. (2011). “Stress-strain behavior and California Bearing Ratio of artificially cemented sand" *Journal of Testing and Evaluation*, Vol. 39, pp. 1-9.

Vadim, Yudina. (2013). “Research of Sulfate Resistance of Cement Containing Composition.” *Procedia Engineering*.

Vipulanandan, C., (2014a), "Development and Characterization of Smart Cement for Real Time Monitoring of Ultra-Deepwater Oil Well Cementing Applications," *OTC-25099-MS.*

Vipulanandan, C. and Amani, N., (2015), “Behavior of Nano Calcium Carbonate Modified Smart Cement Contaminated with Oil Based Drilling Mud.” *Offshore Technology Conference, OTC* 1–20.

Vipulanandan, C. and Dharmarajan., N., (1989). “Critical Crack Tip Opening Displacement for Polymer Composites.” *Engineering Fracture Mechanics* 33(3):409–19.

Vipulanandan, C. and Garas, V. (2008). “Electrical resistivity, pulse velocity and compressive properties of carbon fiber reinforced cement mortar.” *Journal of Materials in Civil Engineering*, Vol. 20, pp. 93-101.

Vipulanandan, C. and Mohammed, A. (2014). “Hyperbolic rheological model with shear stress limit for acrylamide polymer modified bentonite drilling muds.” *Journal of Petroleum Science and Engineering*, Vol. 122, pp. 38–47.

Vipulanandan, C. and Mohammed, A. (2015a). “Smart cement modified with iron oxide nanoparticles to enhance the piezoresistive behavior and compressive strength for oil well applications.” *Smart Mater. Struct.* 24 (2015) 125020 (11pp).

Vipulanandan, C., and Mohammed, A., (2015b) "Smart cement rheological and piezoresistive behavior for oil well applications." *Journal of Petroleum Science and Engineering,* V-135, 2015, pp. 50–58.

Vipulanandan, C. and Prashanth, P. (2013). “Impedance spectroscopy characterization of a piezoresistive structural polymer composite bulk sensor.” *Journal of Testing and Evaluation*, Vol. 41, pp. 898-904.

Vipulanandan, C. Ahossin, Y.J. and Bilgin, O. (2007). “Geotechnical properties of marine and deltaic soft clays.” GSP 173 *Advances in Measurement and Modelling of Soil Behaviour*, pp. 1-13.

Vipulanandan, C., Ali, M., Basirat, B., Reddy, A., Amani, N., Mohammed, A., Dighe, S., and Farzam, H., (2016), "Field Test for Real Time Monitoring of Piezoresistive Smart Cement to Verify the Cementing Operations", *27060-MS OTC Conference*.

Vipulanandan, C. and Garas, V. (2006), "Piezoresistivity of Carbon Fiber Reinforced Cement Mortar", *Proceedings, Engineering, Construction and Operations in Challenging Environments, Earth & Space*, Proceedings ASCE Aerospace Division, League City, TX, CD-ROM.

Vipulanandan, C. and Liu, J. (2005) "Polyuretane Based Grouts for Deep Off-Shore Pipe-in-Pipe Application", *Proceedings, Pipelines*, ASCE, Houston, TX, pp. 216-227.

Vipulanandan, C. and Sett, K. (2004) "Development and Characterization of Piezoresistive Smart Structural Materials", *Proceedings, Engineering, Construction and Operations in Challenging Environments, Earth & Space*, ASCE Aerospace Division, League City, TX, pp. 656-663.

Vipulanandan, C., Heidari, M., Qu, Q., Farzam, H.and Pappas, J. M. (2014). "Behavior of piezoresistive smart cement contaminate with Oil Based." In *Offshore Technology Conferences*.

Vipulanandan, C. and Mebarkia, S., (1990), "Effect of Strain Rate and Temperature on the Performance of Epoxy Mortar." *Polymer engineering and science* 30:734–40.

Vipulanandan, C. and Prashanth, P. (2013). "Impedance Spectroscopy Characterization of a Piezoresistive Structural Polymer Composite Bulk Sensor." *Journal of Testing and Evaluation*.

Vipulanandan, C., Raheem, A., Basirat, B. and Mohammed, A., S., (2014), "New Kinetic Model to Characterize the Filter Cake Formation and Fluid Loss in HPHT Process." *Offshore Technology Conference, OTC-25100-MS.*

Vipulanandan, C., Ramanathan, P., Ali, M., Basirat, B. and Pappas, J. (2015) "Real Time Monitoring of Oil Based Mud, Spacer Fluid and Piezoresistive Smart Cement to Verify the Oil Well Drilling and Cementing Operation Using Model Tests," *Offshore Technology Conference (OTC)* 2015, OTC-25851-MS, pp. 1&-18.

Wang, S. Y. and Vipulanandan, C. (1996) "Leachability of Lead from Solidified Cement-Fly Ash Binders," *Cement and Concrete Research*, Vol. 26, No. 6, pp. 895-905.

Wecharatna, M. and Shah, S. P., 1982, "Slow Crack Growth in Cement Composites", *J. Structural Division*, ASCE 108, pp. 1400-1413.

Wei, X., Lianzhen, X. and Li, Z. (2008). "Electrical measurement to assess hydration process and the porosity formation." *Journal of Wuhan University of Technology-Material Science. Ed.*, Vol. 23, pp. 761-766.

White, F.M. (2009), "*Fluid Mechanics*," 7th edn. McGraw Hill, New York

Wittmann, F. H., and Metzener-Gheorghita, I., (1985), "Fracture toughness of concrete determined on large specimens." *Materials and Structures*, *18*, 93–95

Wong, H. S. and Buenfeld, N. R. (2009). "Cement and Concrete Research Determining the water – cement ratio , cement content , water content and degree of hydration of hardened cement paste : Method development and validation on paste samples." *Cement and Concrete Research*, 39(10), 957–965. http://doi.org/10.1016/j.cemconres.2009.06.013

Yoshiyuki Yamamoto and Kazuo A., (1976), "Stress Intensity Factors for Cracks in Notch Bend Specimens for Three Point Bending." *Int Journ of Fracture* 12 (1976), 122(4), 495–498.

Zerbst, U., Klinger, C. and Clegg, R., (2015), "Fracture mechanics as a tool in failure analysis – prospects and limitations." *Engineering Failure Analysis*, 55, 376–410. http://doi.org/10.1016/j.engfailanal.2015.07.001

Zhang, J., Weissinger, E.A., Peethamparan S. and Scherer G.W. (2010). "Early hydration and setting of oil well cement," *Cement and Concrete research*, Vol. 40, 1023-1033.

Zhang, M., Sisomphon, K., Ng, T.S, and Sun, D.J, (2010). "Effect of superplasticizers on workability retention and initial setting time of cement pastes," *Construction and Building Materials* 24, 1700–1707.

Zhang, J., Weissinger, E.A., Peethamparan, S. and Scherer, G.W. (2010). "Early hydration and setting of oil well cement." *Journal of Cement and Concrete Research*, Vol. 40, pp. 1023-1033.

Zhu, Y. and Xu, S. L., (1990), "Fracture properties of cement paste and mortar : an experimental investigation." *Department of Civil Engineering, Dalian University of Technology*.

Ziegeldorf, S., Muller, H. S., and Hilsdorf, H. K., 1987, "A Model Law for the Notch Sensitivity of Brittle Materials," *Cem. Concr. Res*., **10**, pp. 589–599.

Zielke, L., Hutzenlaub, T. Wheeler, D. R., Chao, Ch. W, Manke, I., Hilger, A., Paust, N., Zengerle, R. and Thiele, S. (2014), "Three-Phase Multiscale Modeling of a LiCoO2 Cathode: Combining the Advantages of FIB–SEM Imaging and X-Ray Tomography" *Journal of Advanced Energy Materials*, 5(5), http://doi.org/10.1002/aenm.201401612.

Zuo, Y., Zi, J. and Wei, X. (2014). "Hydration of cement with retarder characterized via electrical resistivity measurements and computer simulation." J*ournal of Construction and Building Materials*, Vol. 53, pp. 411–418.

APPENDIX

The preliminary study was done on the analytical solution for finding the stress and the displacements around the well bore:

Navier's Equation

The equilibrium equation is defined in Eq. (6) where F is the body force, described as

$$\frac{\partial \sigma_{ij}}{\partial x_j} + F_i = 0. \tag{6}$$

The stress strain relationship for isotropic homogenous material is

$$\sigma_{ij} = 2G\varepsilon_{ij} + \lambda \delta_{ij} \varepsilon_{kk}. \tag{7}$$

The strain displacement relationship can be expressed as

$$\varepsilon_{ij} = \frac{1}{2}\left(\frac{\partial u_i}{\partial x_j} + \frac{\partial u_j}{\partial x_i}\right). \tag{8}$$

Substituting Eq. (7) and (8) in equilibrium Eq. (6), leads to Navier's equations of elasticity as

$$G\nabla^2 u_i + (\lambda + G)\frac{\partial \varepsilon_{kk}}{\partial x_i} + F_i = 0. \tag{9}$$

Vector form of the Navier's equation is

$$G\nabla^2 \boldsymbol{u} + (\lambda + G)\, \nabla(\nabla \cdot \boldsymbol{u}) + \boldsymbol{F} = 0. \tag{10}$$

Vector form of the homogenous Navier's equation is as follows

$$G\nabla^2 \boldsymbol{u} + (\lambda + G)\, \nabla(\nabla \cdot \boldsymbol{u}) = 0. \tag{11}$$

Helmholtz's theorem expresses the vector field displacement u in terms of the scalar and potential vectors $\phi(x_1, x_2, x_3)$ and $\psi(x_1, x_2, x_3)$, shown by

$$\boldsymbol{u} = grad\ \phi + curl\ \boldsymbol{\psi} = \nabla\phi + \nabla \times \boldsymbol{\psi}. \tag{12}$$

Now we are looking for a solution for Navier's equation

Galerkin Vector

A general solution for Navier's equation proposed by Galerkin which is shown by vector V (Saada, 2009; Selvadurai, 2000), expressed as

$$2G\boldsymbol{u} = 2(1-\nu)\nabla^2\boldsymbol{V} - \nabla(\nabla \cdot \boldsymbol{V}). \tag{13}$$

Consider a particular case which Galerkin vector V has only the third component. In this case the Galerkin vector is called Love's strain function (Saada, 2009). Love (1863-1940) proposed a strain function approach for the solution of axisymmetric problems in elasticity. A generalization of Love's approach can be regarded as problems in cylindrical polar coordinate system (r, θ, z) and the Galerkin vector can be defined as

$$\boldsymbol{V} = V_z i_z. \tag{14}$$

By substituting Eq. (13) into Navier's Eq. (10) (Soutas-Little, 1999), it is shown

$$\widetilde{\nabla}^2\widetilde{\nabla}^2 V_z = -\frac{F_z}{1-\upsilon} \tag{15}$$

Where $\widetilde{\nabla}^2$ is Laplace's operator referred to generalized cylindrical coordinate system as

$$\widetilde{\nabla}^2 = \frac{\partial}{\partial r^2} + \frac{1}{r}\frac{\partial}{\partial r} + \frac{1}{r^2}\frac{\partial^2}{\partial \theta^2} + \frac{\partial^2}{\partial z^2} \tag{16}$$

The displacement in cylindrical coordinate system $u = u_r i_r + u_\theta i_\theta + u_z i_z$ can be presented as strain potential function V_z defined as following

$$2Gu_r = -\frac{\partial^2 V_z}{\partial r \partial z},$$

$$2Gu_\theta = -\frac{1}{r}\frac{\partial^2 V_z}{\partial \theta \partial z}, \qquad \textbf{(17)}$$

$$2Gu_z = 2(1-\nu)\widetilde{\nabla}^2 V_z - \frac{\partial^2 V_z}{\partial z^2}.$$

The stress in cylindrical coordinate system expressed as

$$\sigma = \begin{bmatrix} \sigma_{rr} & \sigma_{r\theta} & \sigma_{rz} \\ \sigma_{r\theta} & \sigma_{\theta\theta} & \sigma_{\theta z} \\ \sigma_{rz} & \sigma_{\theta z} & \sigma_{zz} \end{bmatrix}. \qquad \textbf{(18)}$$

The stress components in terms of V_z function are expressed in Eq. (19).

$$\sigma_{rr} = \frac{\partial}{\partial z}\left[\nu\widetilde{\nabla}^2 V_z - \frac{\partial^2 V_z}{\partial r^2}\right]$$

$$\sigma_{\theta\theta} = \frac{\partial}{\partial z}\left[\nu\widetilde{\nabla}^2 V_z - \frac{1}{r}\frac{\partial V_z}{\partial r} - \frac{1}{r^2}\frac{\partial^2 V_z}{\partial \theta^2}\right]$$

$$\sigma_{zz} = \frac{\partial}{\partial z}\left[(2-\nu)\widetilde{\nabla}^2 V_z - \frac{\partial^2 V_z}{\partial z^2}\right]$$

$$\sigma_{r\theta} = -\frac{\partial^3}{\partial r \partial \theta \partial z}\left[\frac{V_z}{r}\right] \qquad \textbf{(19)}$$

$$\sigma_{\theta z} = \frac{1}{r}\frac{\partial}{\partial \theta}\left[(1-\nu)\widetilde{\nabla}^2 V_z - \frac{\partial^2 V_z}{\partial z^2}\right]$$

$$\sigma_{rz} = \frac{\partial}{\partial r}\left[(1-\nu)\widetilde{\nabla}^2 V_z - \frac{\partial^2 V_z}{\partial z^2}\right]$$

Axisymmetric Cylindrical Coordinate System

The stress and displacement in three dimensional related to an axisymmetric cylindrical coordinate system using Love's strain function are described as

$$2Gu_r = -\frac{\partial^2 V_z}{\partial r \partial z},$$
$$2Gu_z = 2(1-\nu)\hat{\nabla}^2 V_z - \frac{\partial^2 V_z}{\partial z^2}, \tag{20}$$

$$\sigma_{rr} = \frac{\partial}{\partial z}\left[\nu\hat{\nabla}^2 V_z - \frac{\partial^2 V_z}{\partial r^2}\right],$$
$$\sigma_{\theta\theta} = \frac{\partial}{\partial z}\left[\nu\hat{\nabla}^2 V_z - \frac{1}{r}\frac{\partial V_z}{\partial r}\right],$$
$$\sigma_{zz} = \frac{\partial}{\partial z}\left[(2-\nu)\hat{\nabla}^2 V_z - \frac{\partial^2 V_z}{\partial z^2}\right], \tag{21}$$
$$\sigma_{rz} = \frac{\partial}{\partial r}\left[(1-\nu)\hat{\nabla}^2 V_z - \frac{\partial^2 V_z}{\partial z^2}\right].$$

Proposed Solution

In this study, for this axisymmetric problem in cylindrical polar coordinate system the following Love's strain function is used to simulate the cemented casing. Knowing the fact that for a three dimensional axisymmetric problem, the number of boundary condition is 8, the Love's strain function in 5 terms and 5 constants can be expressed by

$$V_z(r,z) = Azr^2 + Bz\,ln(r) + Cz^4 + Dr^4 + Ez^3. \tag{22}$$

Some of the derivatives are as following

$$\frac{\partial^2 V_z}{\partial r^2} = 2Az - B\frac{z}{r^2} + 12Dr^2,$$

$$\frac{1}{r}\frac{\partial V_z}{\partial r} = 2Az + B\frac{z}{r^2} + 4Dr^2, \quad \textbf{(23)}$$

$$\frac{\partial^2 V_z}{\partial z^2} = 12Cz^2 + 6Ez,$$

$$\widehat{\nabla}^2 V_z = 4Az + 16Dr^2 + 12Cz^2 + 6Ez,$$

$$\widehat{\nabla}^4 V_z = 64D + 24C. \quad \textbf{(24)}$$

The reason that I considered the term Dr^4, was to have σ_{rz} non-zero. In the $\sigma_{rz} = \frac{\partial}{\partial r}\left[(1-\nu)\widehat{\nabla}^2 V_z - \frac{\partial^2 V_z}{\partial z^2}\right]$, the derivative of the $\widehat{\nabla}^2 V_z$ and $\frac{\partial^2 V_z}{\partial z^2}$ with respect to "r" should exists. One way is $\frac{\partial^3 V_z}{\partial r \partial z^2}$ to be non-zero, but if I have selected $z^2 r$, the term $\frac{\partial^2 V_z}{\partial r \partial z}$ in u_r became a function of z. therefore when I wanted to apply the boundary condition of $u_r(r = b) = 0$, the variable z has to be specified and it was a restriction for this boundary condition while I wanted to specify $u_r(r = b) = 0$ all over the depth without specify any special depth. The other way is to have $\widehat{\nabla}^2 V_z$ as a function of r. Therefore, by having the term Dr^4, it makes σ_{rz} non-zero and does not interfere with $u_r(r = b) = 0$. For example, the reason for considering Cz^4 is having $\sigma_{zz} = \frac{\partial}{\partial z}\left[(2-\nu)\widehat{\nabla}^2 V_z - \frac{\partial^2 V_z}{\partial z^2}\right]$ as a function of depth (z). The similar philosophies were considered for all 5 terms.

Parameters

Using Eq. (15), with considering the weight of the cement, the volume body force is the specific weight of the cement, $F_z = \gamma$.

$$\widehat{\nabla}^4 V_z(r,z)v = 64D + 24C = -\frac{\gamma}{1-v} \quad \textbf{(25)}$$

Eqs. (26) express the boundary conditions around the borehole and Fig. 1 shows the schematic of borehole the pressures p_i applied on the inner side of the wellbore, while on the top surface, the surcharge ω is applied. The outer side has zero displacement as well as the bottom side of the wellbore.

$$\begin{gathered}\sigma_{rr}(r=a) = p_i \\ \sigma_{zz}(z=0) = \omega \\ u_r(r=b) = 0 \\ u_z(z=H) = 0\end{gathered} \quad \textbf{(26)}$$

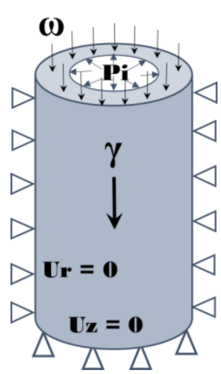

Fig. 1: Schematic of borehole pressures

By substituting $V_z(r,z)$ from Eq. (22) in Eq. (20) the displacement can be written as

$$2Gu_r = -\frac{\partial^2 V_z}{\partial r \partial z} = -2Ar - \frac{B}{r} \tag{27}$$

Using $u_r(r=b) = 0$, the relationship between A and B can be found

$$B = -2Ab^2 \tag{28}$$

Applying $\sigma_{zz}(z=0) = \omega$, the relationship of A and E can be found

$$\sigma_{zz} = \frac{\partial}{\partial z}\left[(2-\nu)\hat{\nabla}^2 V_z - \frac{\partial^2 V_z}{\partial z^2}\right] = (2-\upsilon)4A + (1-\upsilon)6E + (1-\upsilon)24Cz$$

$$(2-\upsilon)4A + (1-\upsilon)6E = \omega \tag{29}$$

Using $\sigma_{rr}(r=a) = p_i$, the relationship between A, E and B can be found

$$\sigma_{rr} = \frac{\partial}{\partial z}\left[\nu\hat{\nabla}^2 V_z - \frac{\partial^2 V_z}{\partial r^2}\right] = (2\upsilon - 1)2A + 6E\upsilon + (24C)\upsilon z + \frac{B}{r^2}$$

$$(2\upsilon - 1)2A + 6E\upsilon + \frac{B}{a^2} = p_i \tag{30}$$

Now we have three unknowns (A, B and E) and also three equations (28), (29) and (30). Therefore, A, B and E can be found.

$$A = \frac{\omega - \frac{(1-\upsilon)}{\upsilon}p_i}{4(2-\upsilon) - 2\frac{(1-\upsilon)}{\upsilon}\left((2\upsilon - 1) - \frac{b^2}{a^2}\right)}$$

$$B = -b^2 \frac{\omega - \frac{(1-\upsilon)}{\upsilon}p_i}{2(2-\upsilon) - \frac{(1-\upsilon)}{\upsilon}\left((2\upsilon - 1) - \frac{b^2}{a^2}\right)} \tag{31}$$

$$E = \frac{1}{6\upsilon}\left[p_i - \left((2\upsilon - 1) - \frac{b^2}{a^2}\right)\frac{\omega - \frac{(1-\upsilon)}{\upsilon}p_i}{2(2-\upsilon) - \frac{(1-\upsilon)}{\upsilon}\left((2\upsilon - 1) - \frac{b^2}{a^2}\right)}\right]$$

The last boundary condition is $u_z(z = H) = 0$. Now we have to find D from the following equation

$$2Gu_z = 2(1-\nu)\hat{\nabla}^2 V_z - \frac{\partial^2 V_z}{\partial z^2}$$

$$= 2(1-\upsilon)(4Az + 16Dr^2) + (1-2\upsilon)(12Cz^2 + 6Ez) \quad \textbf{(32)}$$

$$2(1-\upsilon)(4AH + 16Db^2) + (1-2\upsilon)(12CzH^2 + 6EH) = 0$$

The parameter D can be found by substituting known parameters A, B and E

$$D = \frac{-\gamma}{64(1-\upsilon)} - \frac{3}{8}\left[\frac{(1-2\upsilon)3EH + (1-\upsilon)4AH - \frac{\gamma b^2}{4}}{b^2(1-\upsilon) - H^2(1-2\upsilon)}\right] \quad \textbf{(33)}$$

By considering Eq. (25), parameter C also can be calculated

$$C = \frac{(1-2\upsilon)3EH + (1-\upsilon)4AH - \frac{\gamma b^2}{4}}{6b^2(1-\upsilon) - 6H^2(1-2\upsilon)} \quad \textbf{(34)}$$

Stress and Displacement Analysis

substituting the constants, A, B, C, D and E in the displacement and stresses can be derived as shown

$$u_r = -\frac{\omega - \frac{(1-\upsilon)}{\upsilon} p_i}{4(2-\upsilon)G - 2\frac{(1-\upsilon)}{\upsilon} G\left((2\upsilon - 1) - \frac{b^2}{a^2}\right)}\left[r - \frac{b^2}{r}\right]$$

$$u_z = \frac{1}{G}\left[\left((1-2\upsilon)3Ez + (1-\upsilon)4Az - \frac{\gamma r^2}{4}\right) - \frac{(1-2\upsilon)z^2 + (1-\upsilon)r^2}{(1-2\upsilon)H^2 + (1-\upsilon)b^2}\left((1-2\upsilon)3EH + (1-\upsilon)4AH - \frac{\gamma b^2}{4}\right)\right] \tag{35}$$

$$\sigma_{rr} = p_i + \left(\frac{(1-2\upsilon)3EH + (1-\upsilon)4AH - \frac{\gamma b^2}{4}}{4b^2(1-\upsilon) - 4H^2(1-2\upsilon)}\right)\upsilon z - \left(\frac{\omega - \frac{(1-\upsilon)}{\upsilon} p_i}{2(2-\upsilon) - \frac{(1-\upsilon)}{\upsilon}\left((2\upsilon - 1) - \frac{b^2}{a^2}\right)}\right)\left[\frac{b^2}{a^2} - \frac{b^2}{r^2}\right]$$

$$\sigma_{\theta\theta} = p_i + \left(\frac{(1-2\upsilon)3EH + (1-\upsilon)4AH - \frac{\gamma b^2}{4}}{4b^2(1-\upsilon) - 4H^2(1-2\upsilon)}\right)\upsilon z + \left(\frac{\omega - \frac{(1-\upsilon)}{\upsilon} p_i}{2(2-\upsilon) - \frac{(1-\upsilon)}{\upsilon}\left((2\upsilon - 1) - \frac{b^2}{a^2}\right)}\right)\left[\frac{b^2}{a^2} + \frac{b^2}{r^2}\right] \tag{36}$$

$$\sigma_{zz} = \omega + 4(1-\upsilon)\left(\frac{(1-2\upsilon)3EH + (1-\upsilon)4AH - \frac{\gamma b^2}{4}}{b^2(1-\upsilon) - H^2(1-2\upsilon)}\right)(z)$$

$$\sigma_{rz} = (1-\upsilon)\left(\frac{-\gamma}{2(1-\upsilon)} - 12\left[\frac{(1-2\upsilon)3EH + (1-\upsilon)4AH - \frac{\gamma b^2}{4}}{b^2(1-\upsilon) - H^2(1-2\upsilon)}\right]\right)(r)$$

Internal Pressure as a Function of Resistivity changes

The following p, q model (Eq. (37)) is selected to correlate the resistivity changes with pressure for analytical solutions proposed

$$p_i\left(\frac{\Delta\rho}{\rho_0}\right) = \frac{\left(\frac{\Delta\rho}{\rho_0}\right)}{q + (1-p-q)\left(\frac{\Delta\rho}{\rho_0}\right) + p\left(\frac{\Delta\rho}{\rho_0}\right)^{\frac{p}{q-p}}}. \tag{37}$$

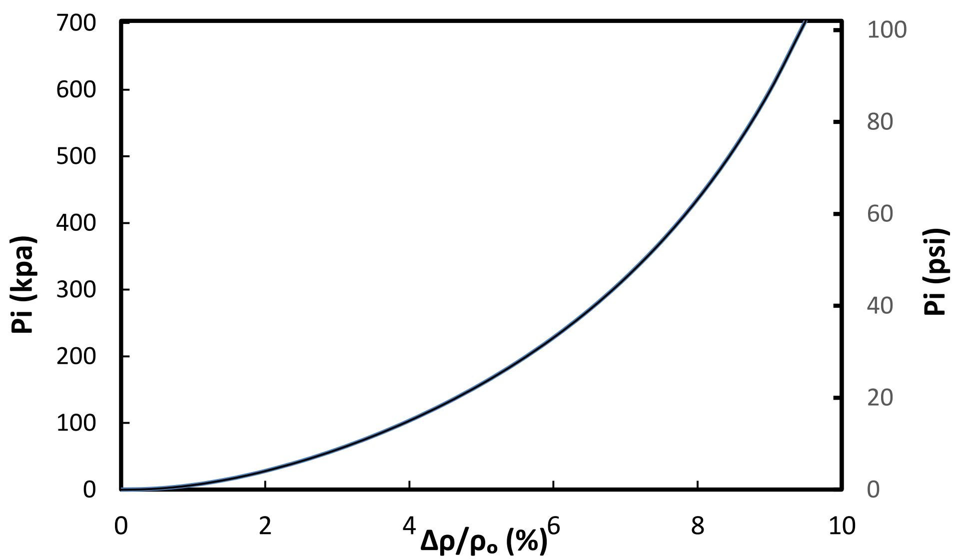

Fig. 2: Pressure versus resistivity changes, p, q Model (Vipulanandan and Mebarkia 1990)

By substituting the pressure from Eq. (37) in displacement Eqs. (35), the radial displacement ur and the vertical displacement uz become the function of resistivity changes Eq.(38).

$$u_r = -\frac{\omega - \frac{(1-\upsilon)}{\upsilon} p_i\left(\frac{\Delta\rho}{\rho_0}\right)}{4(2-\upsilon)G - 2\frac{(1-\upsilon)}{\upsilon}G\left((2\upsilon-1) - \frac{b^2}{a^2}\right)}\left[r - \frac{b^2}{r}\right]$$

$$u_z = \frac{1}{G}\left[\left((1-2\upsilon)3E\left(\frac{\Delta\rho}{\rho_0}\right)z + (1-\upsilon)4A\left(\frac{\Delta\rho}{\rho_0}\right)z - \frac{\gamma r^2}{4}\right) - \frac{(1-2\upsilon)z^2 + (1-\upsilon)r^2}{(1-2\upsilon)H^2 + (1-\upsilon)b^2}\left((1-2\upsilon)3E\left(\frac{\Delta\rho}{\rho_0}\right)H + (1-\upsilon)4A\left(\frac{\Delta\rho}{\rho_0}\right)H - \frac{\gamma b^2}{4}\right)\right] \tag{38}$$

The stresses are shown as following Eq. (39).

$$\sigma_{rr} = p_i\left(\frac{\Delta\rho}{\rho_0}\right) + \left(\frac{(1-2\upsilon)3E\left(\frac{\Delta\rho}{\rho_0}\right)H + (1-\upsilon)4A\left(\frac{\Delta\rho}{\rho_0}\right)H - \frac{\gamma b^2}{4}}{4b^2(1-\upsilon) - 4H^2(1-2\upsilon)}\right)\upsilon z$$
$$- \left(\frac{\omega - \frac{(1-\upsilon)}{\upsilon}p_i\left(\frac{\Delta\rho}{\rho_0}\right)}{2(2-\upsilon) - \frac{(1-\upsilon)}{\upsilon}\left((2\upsilon-1) - \frac{b^2}{a^2}\right)}\right)\left[\frac{b^2}{a^2} - \frac{b^2}{r^2}\right]$$

$$\sigma_{\theta\theta} = p_i\left(\frac{\Delta\rho}{\rho_0}\right) + \left(\frac{(1-2\upsilon)3E\left(\frac{\Delta\rho}{\rho_0}\right)H + (1-\upsilon)4A\left(\frac{\Delta\rho}{\rho_0}\right)H - \frac{\gamma b^2}{4}}{4b^2(1-\upsilon) - 4H^2(1-2\upsilon)}\right)\upsilon z$$
$$+ \left(\frac{\omega - \frac{(1-\upsilon)}{\upsilon}p_i\left(\frac{\Delta\rho}{\rho_0}\right)}{2(2-\upsilon) - \frac{(1-\upsilon)}{\upsilon}\left((2\upsilon-1) - \frac{b^2}{a^2}\right)}\right)\left[\frac{b^2}{a^2} + \frac{b^2}{r^2}\right] \quad \textbf{(39)}$$

$$\sigma_{zz} = \omega + 4(1-\upsilon)\left(\frac{(1-2\upsilon)3E\left(\frac{\Delta\rho}{\rho_0}\right)H + (1-\upsilon)4AH\left(\frac{\Delta\rho}{\rho_0}\right)H - \frac{\gamma b^2}{4}}{b^2(1-\upsilon) - H^2(1-2\upsilon)}\right)z$$

$$\sigma_{rz} = (1-\upsilon)\left(\frac{-\gamma}{2(1-\upsilon)}\right.$$
$$\left. - 12\left[\frac{(1-2\upsilon)3E\left(\frac{\Delta\rho}{\rho_0}\right)H + (1-\upsilon)4A\left(\frac{\Delta\rho}{\rho_0}\right)H - \frac{\gamma b^2}{4}}{b^2(1-\upsilon) - H^2(1-2\upsilon)}\right]\right)(r)$$